

The Pennsylvania State University
The Graduate School
Department of Chemistry

BEYOND MOLECULAR ASSEMBLIES AND
SCANNING TUNNELING MICROSCOPY

A Dissertation in

Chemistry

by

Moonhee Kim

© 2011 Moonhee Kim

Submitted in Partial Fulfillment
of the Requirements
for the Degree of

Doctor of Philosophy

August 2011

The dissertation of Moonhee Kim was reviewed and approved* by the following:

Paul S. Weiss
Distinguished Professor, Departments of Chemistry and Physics
Dissertation Advisor

Scott T. Phillips
Martarano Assistant Professor of Chemistry
Chair of Committee

Christine D. Keating
Associate Professor of Chemistry

Anne M. Andrews
Adjunct Professor of Veterinary and Biological Medicine

Barbara J. Garrison
Shapiro Professor of Chemistry
Head of the Chemistry Department

*Signatures are on file in the Graduate School

Abstract

We introduce the self-assembled monolayers (SAMs) of *n*-alkanethiols on Au{111} as a standard molecular assembly to understand the physical chemistry of organic molecules on solid surfaces. We apply these molecular assemblies to create new interfaces and to exert control over single molecules. Scanning tunneling microscopy (STM) is used to characterize the molecular orientations, structures, phases, and intermolecular interactions within molecular assemblies, in real space, at the sub-nanometer scale. We take advantage of the high spatial resolution of STM to obtain fundamental insight into molecular phenomena. Other surface characterization techniques, including infrared reflection absorption spectroscopy, X-ray photoelectron spectroscopy, and cyclic voltammetry complement and support our STM measurements.

Photon STM is used to investigate optical phenomena of single organic molecules with Ångström-scale precision. Evanescent wave coupling by total internal reflection adds chemical specificity to STM function. High quality, thin Au{111} films deposited on c-cut sapphire prisms efficiently couple light to the tunneling junction. Annealing significantly improves substrate quality of both the sapphire and Au{111} surfaces, providing more stable tunneling junctions. Lock-in detection with light modulation improves the photoresponse registry in the photon STM. One promising candidate for efficient organic solar cells, C₆₀-tethered 2,5-dithienylpyrrole triads, was isolated within a well-ordered *n*-dodecanethiolate monolayer to measure the photocurrent on single triad molecules, which will determine the intrinsic photovoltaic efficiency at the molecular level. Increased photoconductivity of

isolated photovoltaic or photoconductive molecules demonstrates the function and potential of photon STM.

Photoreactions of conjugated organic molecules may be allowed by selection rules but not observed in solution reactions because of unfavorable reaction geometries. We have used defect sites in self-assembled alkanethiolate monolayers on gold surfaces to direct geometrically unfavorable photochemical reactions between individual organic molecules. High conductivity and stochastic switching of anthracene-terminated phenylethynylthiolates within alkanethiolate monolayers, as well as in-situ photochemical transformations, have been observed and distinguished with the STM. Ultraviolet light absorbed during imaging increases the apparent heights of excited molecules in STM images, evidence that we are probing electronically excited states.

The formation of 2-adamantanethiolate SAMs on Au{111} and their displacement by *n*-dodecanethiol are investigated using STM, X-ray photoelectron spectroscopy, and infrared reflection absorption spectroscopy. Well-ordered 2-adamantanethiolate monolayers undergo rapid and significant molecular exchange upon exposure to *n*-dodecanethiol solutions, but their structures and intermolecular interactions template the growth of *n*-dodecanethiolate domains. Annealing 2-adamantanethiolate monolayers at 78 °C decreases the density of vacancy islands, while increasing the overall order and the average domain sizes in the films. This results in slower displacement by *n*-dodecanethiol molecules, as compared to unannealed monolayers. The secondary sulfur position on the adamantyl cage alters the lattice structure and the exchange of 2-adamantanethiolate monolayers by alkanethiols relative to 1-adamantanethiol monolayers.

We report the electrochemically driven phase transformation of a linear nanostructure in amide-containing alkanethiol, 3-mercapto-*N*-nonylpropionamide (**1ATC9**) SAMs. Hydrogen-bonding interactions between buried amide groups cause a multi-step electrochemical desorption, which involves an unusual phase change. This reaction can be exploited to produce a less dense, textured structure. Single-component **1ATC9** SAMs prepared in solution at room temperature for 24 hours consist of two phases with different apparent heights in STM images; these phases are readily manipulated by controlling solution temperature and deposition time. Intermolecular hydrogen-bonding interactions produce films with high thermal stability. The presence of two independent cathodic peaks in **1ATC9** monolayer voltammograms indicates two-step reductive desorption. A monolayer phase transition occurs after the first cathodic peak, transforming a close-packed monolayer into a striped phase that is energetically favored at low surface-thiolate density. Scanning tunneling microscopy, cyclic voltammetry, infrared reflection absorption spectroscopy, and X-ray photoelectron spectroscopy reveal electrochemical nanostructuring, driven by partial reductive desorption and strong interchain hydrogen bonding. The resultant striped, low-coverage phase is inaccessible by other synthetic preparations, except by controlled dosing in ultrahigh vacuum.

Table of Contents

List of Tables.....	ix
List of Figures	x
Acknowledgments.....	xx
Chapter 1. Beyond Molecular Assemblies and Scanning Tunneling Microscopy.....	1
1.1 Introduction	1
1.2 Self-Assembled Monolayers	2
1.2.1 Self-assembly in solution vs. vapor deposition	3
1.2.2 Single-molecule insertion.....	4
1.3 Scanning Tunneling Microscopy	12
1.3.1 Scanning tunneling microscope	15
1.3.2 Besocke scanning tunneling microscope	16
1.3.3 Photon scanning tunneling microscope.....	23
1.4 Thesis Overview.....	25
Chapter 2. Photon Scanning Tunneling Microscopy	27
2.1 Introduction	27
2.2 Theory and Experimental Design.....	29
2.2.1 Evanescent field coupling	29
2.2.2 Photon scanning tunneling microscope.....	33
2.2.3 Substrate preparation.....	42
2.2.4 Light modulation	53
2.3 Results and Discussion.....	54
2.3.1 <i>n</i> -Alkanethiolate self-assembled monolayers on Au{111}/Al ₂ O ₃ (0001)	54
2.3.2 Single-molecule detection	56
2.4 Conclusions and Outlook	61
Chapter 3. Creating Favorable Geometries for Directing Organic Photoreactions in Alkanethiolate Monolayers	64
3.1 Introduction	64
3.2 Experimental Details	67
3.3 Results and Discussion.....	69
3.3.1 Photoreaction of phenylethynylanthracene in solution	69
3.3.2 Photoreaction of phenylethynylanthracene on surfaces	69

3.3.3 Stochastic switching of 9-(4-mercaptophenylethynyl)anthracene	72
3.3.4 Photoexcitation of 9-(4-mercaptophenylethynyl)anthracene	74
3.3.5 Photodimerization of 9-(4-mercaptophenylethynyl)anthracene	77
3.3.6 Calculations	77
3.4 Conclusions and Prospects	78
Chapter 4. Self-Assembled Monolayers of 2-Adamantanethiol on Au{111}: Control of Structure and Displacement	82
4.1 Introduction	82
4.2 Experimental Methods	85
4.2.1 Materials	85
4.2.2 2-Adamantanethiol synthesis	85
4.2.3 Self-assembled monolayer fabrication	86
4.2.4 Scanning tunneling microscopy	86
4.2.5 X-Ray photoelectron spectroscopy	87
4.2.6 Cyclic voltammetry	87
4.2.7 Infrared reflection absorption spectroscopy	88
4.3 Results and Discussion	89
4.3.1 Characterization of 2-adamantanethiolate SAMs on Au{111}	89
4.3.2 Displacement of 2-adamantanethiolate SAMs with <i>n</i> -dodecanethiol	94
4.3.3 Intermolecular interaction strengths and molecular packing	101
4.3.4 Kinetics of displacement in 2-adamantanethiolate SAMs	111
4.4 Conclusions	114
Chapter 5. Hydrogen-Bonding Networks in Amide-Containing Alkanethiolate Monolayers	115
5.1 Introduction	115
5.2 Experimental Section	116
5.2.1 Materials	116
5.2.2 Self-assembled monolayer fabrication and imaging	117
5.2.3 Electrochemistry	117
5.2.4 Infrared reflection absorption spectroscopy	118
5.2.5 X-Ray photoelectron spectroscopy	118
5.3 Results and Discussion	119
5.3.1 Self-assembled monolayers of 3-mercapto- <i>N</i> -nonylpropionamide	119
5.3.2 Thermal stability	125
5.3.3 Reductive desorption	127
5.3.4 Controlled potential electrolysis	128
5.3.5 Electrochemically driven phase transition	139
5.5 Conclusions and Prospects	140

Chapter 6. Conclusions and Future Prospects.....	142
6.1 Summary	142
6.2 Photon Scanning Tunneling Microscopy	143
6.3 Regioselective Photoreaction on Surfaces	144
6.4 Molecular Chemistry on Surfaces	144
6.5 Future Prospects	145
References and Notes	153

List of Tables

Table 4-1 Average cathodic peak potential (E_p), current (I_p), area, and full-width-at-half-maxima (fwhm) from voltammograms of single-component 1-adamantanethiolate (1AD) SAMs, single-component 2-adamantanethiolate (2AD) SAMs, and single-component <i>n</i> -dodecanethiolate (C12) SAMs. All SAMs were prepared by immersing clean Au substrates in 1 mM ethanolic corresponding thiol solution at room temperature for 24 hours.....	103
Table 4-2 Binding energies and the full-width-at-half-maxima (fwhm) of the C 1s peaks in the XPS spectra of single-component 2-adamantanethiolate (2AD) SAMs, single-component <i>n</i> -dodecanethiolate (C12) SAMs, and mixed 2AD/C12 SAMs created by displacement of 2AD SAMs in 1 mM <i>n</i> -dodecanethiol solution for the specified times. The 2AD SAMs were prepared by immersing clean Au substrates in 1 mM 2-adamantanethiol solution at room temperature for 24 hours (RT 2AD SAMs) or by placing Au substrates in 2-adamantanethiol solution at 70 °C for 2 hours, then dry-annealing the samples under nitrogen at 78 °C for 17 hours (DA 2AD SAMs). *Surface fraction of each molecule, estimated from the area ratios of the individual peaks discussed in the text.	107
Table 5-1 Elemental composition of 1ATC9 SAMs on Au{111} by XPS before and after controlled potential electrolysis.	138

List of Figures

- Figure 1.1 Schematics of *n*-dodecanethiolate (**C12**) SAM structure on Au{111}. (A) A side view along the nearest neighbor direction showing the 30° tilt to maximize van der Waals interactions. (B) A top view showing hexagonal close packing of **C12** molecules. 5
- Figure 1.2 A schematic top-down view of the unit cells, $(\sqrt{3} \times \sqrt{3})R30^\circ$ (top) and $c(4 \times 2)$ superlattice (bottom) on underlying (1×1) Au{111} substrate. 6
- Figure 1.3 Molecular-resolution STM images of **C12** SAMs, displaying hexagonally close-packed lattice (red dot in A, and B) and $c(4 \times 2)$ superlattice (blue dot in A, and C). Imaging conditions were sample bias voltage -1.0 V and tunneling current 1.0 pA..... 7
- Figure 1.4 (A) A representative STM image of a **C12** SAM showing domain boundaries (red arrow), vacancy islands (yellow arrow), and substrate step edges (green arrow). Imaging conditions were sample bias voltage -1.0 V and tunneling current 1.0 pA. (B) A STM image of a bare Au{111} substrate displaying the herringbone structure [28]. Imaging conditions were sample bias voltage -1.0 V and tunneling current 10.0 pA..... 8
- Figure 1.5 Scanning tunneling microscopy images of **C12** SAMs prepared in solution (A) at room temperature for 1 hour and (B) for 24 hours, (C) at 70°C for 1 hour, and (D) via vapor deposition at 78°C for 24 hours. The SAM quality (larger domains, fewer defect sites, and better order) can be improved substantially by using increased temperature in solution or vapor deposition. Imaging conditions were sample bias voltage -1.0 V and tunneling current 1.0 pA..... 9
- Figure 1.6 (A) A schematic drawing of the insertion procedure with self-assembly. (B) A STM image of 9-(4-mercaptophenylethynyl)anthracene (**MPEA**) molecules inserted into a **C12** SAM matrix. Imaging conditions were sample bias voltage -1.0 V and tunneling current 1.0 pA. (C) Current-voltage characteristics of isolated **MPEA** molecules taken by scanning tunneling spectroscopy. Isolated single **MPEA** molecule shows negative differential resistance which has not been observed in full coverage monolayers. 11
- Figure 1.7 (A) An energy level diagram for a 1D electron tunneling junction and (B) schematics of a STM tip rastering a sample surface (left) in constant-current mode and (right) in constant-height mode. 14
- Figure 1.8 A schematic of a basic scanning tunneling microscope setup. A small bias voltage is applied between the sample and tip, and the resulting current is recorded and is simultaneously adjusted by the feedback loop to maintain the constant current. 17

- Figure 1.9 Photographs of the STM head configuration and the sample holder in the custom-built Besocke-style scanning tunneling microscope. (A) The tip is connected to the center scanner tube through the copper grounding plane. The three outer tubes are equipped with each metal ball bearing that contacts the ramps below the sample holder. (B) The tip and sample spacing is decreased or increased by the movement of the three outer tubes on the ramps via either clockwise or counterclockwise rotations. (C) The tip scans the sample surface within the center hole. 18
- Figure 1.10 Schematic drawing of piezoelectric tube movement. (A) The piezoelectric has four electrodes outside and one electrode inside. (B) The tip motion in x or y directions can be carried out by anti symmetric voltages between diagonal pairs of the outer quadruple electrode. (C) The z motion is controlled by the inside electrode..... 20
- Figure 1.11 Photographs of the sample holder assembly. (A and B) Thin flat Au/mica substrate is placed between the bottom and the top Au foils for electrical contact. (C and D) The plastic spacer and cover are compressed to ensure electrical contact. The center area should be open for electrical contact to the preamplifier. 21
- Figure 1.12 Photographs of the Au spring attached to the preamplifier and the entire assembly of our Besocke-style scanning tunneling microscope. (A) The Au spring contacts the top Au foil of the sample holder. (B) The copper shield protects the scanning tunneling microscope head component and the sample surface. Stacks of stainless steel plates are placed between elastomeric materials for damping. 22
- Figure 1.13 Kretschmann-Raether configuration in the photon scanning tunneling microscope. A Au {111} substrate on a sapphire prism is back-illuminated, producing the evanescent field in the tunneling junction. This geometry allows the direct observation and measurement of the energy conversion mechanism for individual, isolated photoreactive molecules. 24
- Figure 2.1 Schematic description of Snell's law for a sapphire prism ($n_2 = 1.8$)/air ($n_1 = 1.0$) interface. (A) At $\theta_i = 0^\circ$, light (blue arrows) incident from the sapphire prism normal to the interface transmits normal to the interface as well. (B) As the angle of incidence is increased ($\theta_c > \theta_i > 0^\circ$), the transmitted ray refracts away from the surface normal at a larger angle than the incident angle ($\theta_t > \theta_i$). (C) At the critical angle ($\theta_i = \theta_c \sim 35^\circ$), the transmitted ray skims across the interface. (D) Beyond the critical angle ($\theta_i > \theta_c$), all incident light gets reflected back to the sapphire, total internal reflection. (E) A top-view photograph of total internal reflection of 405 nm light through the cylindrical sapphire prism. 31

- Figure 2.2 The evanescent wave field intensity and the penetration depth exponentially decay and are dependent on the angle of incidence. (A) The evanescent wave intensity of a visible light ($\lambda=635$ nm) generated between the interface between a highly refractive material ($n_2 = 1.76$) and air ($n_1 = 1.00$) depends on the incident angle (red at $\theta_i = 45.0^\circ$ and blue at $\theta_i = 80.0^\circ$). (B) Penetration depth exponentially decreases above the critical angle (θ_c , $\sim 35^\circ$). 32
- Figure 2.3 A schematic of the photon scanning tunneling microscope setup. A tunable laser or a monochromator with a high-power Xe lamp is used to supply monochromatic light at diverse wavelengths over a range of 200 – 1400 nm. Polarized light and frequency modulation enhance the signal-to-noise ratio. Optical coupling in the tunneling junction is optimized with the Kretschmann-Raether total internal reflection geometry..... 35
- Figure 2.4 Photographs of the photon scanning tunneling microscope setup: (A) lasers with optics and (B) the scanning tunneling microscope part in the enclosure. A light beam from a laser or monochromator (1, 2, 3, and 4) transmits through the window (6) of the STM enclosure. The sample holder and the STM head (9) are placed on stacks of stainless steel plates separated by elastomeric materials to absorb vibration caused by the rotation stage (8). The photon STM components are numbered as follows: (1) lasers, (2) polarizers, (3) a chopper, (4) a monochromator with a Xe lamp, (5) a beam shutter, (6) A window in the STM enclosure, (7) a focusing lens with xyz translation stage, (8) a rotation stage, (9) a STM platform, (10) a photodetector, (11) an optical microscope with translation stages, (12) a vibration isolation table, and (13) a Besocke-style scanning tunneling microscope. 36
- Figure 2.5 A one-dimensional schematic drawing of Kretschmann-Raether configuration in the photon STM. The evanescent wave is generated behind the sample via total internal reflection. The STM tip scans this coupled area and detects the tunneling current (I_t), including components due to photoexcitation. 37
- Figure 2.6 Photographs of the sample holder in the photon scanning tunneling microscope. (A) The cylindrical side of the prism is exposed to laser illumination through the prism window. (B) The sapphire prism fits in the machined half-cylindrical relief for high accuracy of rotation and light comes through the prism window for total internal reflection. (C) The flat side of the prism is coated with a Au film and faces the STM head. (D) The holder cover has electrical contact to the Au film surface and the sample area is exposed through the hole to the STM head..... 39
- Figure 2.7 (A) A photograph of the optical microscope with a CCD camera that is attached to a translation stage above the sample holder to monitor light coupling. (B and C) Photographs of light transmission to the STM tip at $\theta_i = 0^\circ$, and the total internal reflection (TIR) spot and its reflection to the tip at $\theta_i = 45^\circ$. (D) Photographs of the TIR spot where the tip is positioned at different incident angles. This spot is carefully aligned to the exact center of the rotation stage so that the spot does not change its position during rotation.

- The STM tip and the TIR spot are rotated in these photographs because the optical microscope is fixed above the rotation stage. At $\theta_i = 90^\circ$, the light is blocked by the sample holder..... 40
- Figure 2.8 Photographs of the photon STM head mounted on the x-z microslides, (A) top view and (B) side view. The STM head faces the sample surface. The top (z) microslide moves the STM tip (circle in A) to the tunneling junction and the bottom (x) microslide adjusts the tip position to the TIR spot..... 41
- Figure 2.9 Photographs of a cylindrical sapphire prism (A) before and (B) after Au film deposition on the c-cut plane. 45
- Figure 2.10 Atomic force microscopy images of as-supplied $\text{Al}_2\text{O}_3(0001)$ prisms. The epi-polished surface is irregularly rough and contains grease contaminants. Imaging parameters: (A) Amplitude set point: 220 mV; Drive frequency: 276 kHz; Scan rate: 2 Hz; (B) Amplitude set point: 220 mV; Drive frequency: 75 kHz; Scan rate: 2 Hz. (C) A line profile was taken along the line indicated in the image B. The steps are difficult to distinguish, and are highly curved..... 46
- Figure 2.11 Atomic force microscopy images of a $\text{Al}_2\text{O}_3(0001)$ prism after annealing at 1100 °C for 24 hours. Imaging parameters: (A and B) Amplitude set point: 195 mV; Drive frequency: 272 kHz; Scan rate: 2.5 Hz. (C) A line profile was taken along the line indicated in the image B. Thermal treatment smoothes the entire surface, producing atomically flat terraces with straight linear steps. 47
- Figure 2.12 Atomic force microscopy images of a $\text{Al}_2\text{O}_3(0001)$ prism annealed at 1400 °C for 18 hours subsequently after annealing at 1100 °C for 24 hours. Imaging parameters: (A and B) Amplitude set point: 420 mV; Drive Frequency: 271 kHz; Scan rate: 2 Hz. (C) A line profile was taken along the line indicated in the image B. Further heat treatment at 1400 °C after 1100 °C annealing doubles the terrace size..... 48
- Figure 2.13 Atomic force microscopy images of a $\text{Al}_2\text{O}_3(0001)$ prism annealed only at 1400 °C for 24 hours. Imaging parameters: (A and B) Amplitude set point: 580 mV; Drive frequency: 276 kHz; Scan rate: 2.5 Hz. Long annealing at 1400 °C creates irregularly shaped step edges. 49
- Figure 2.14 Atomic force microscopy images of a 40-nm-thick $\text{Au}\{111\}$ film deposited on 2-nm-thick Nb on a $\text{Al}_2\text{O}_3(0001)$ prism. Imaging parameters: (A and B) Amplitude set point: 195 mV; Drive frequency: 272 kHz; Scan rate: 2.5 Hz. Small grains and large gaps around grain boundaries are mainly observed. 50
- Figure 2.15 Atomic force microscopy images of a 150-nm-thick $\text{Au}\{111\}$ /mica substrate (Agilent, Santa Clara, CA). Imaging parameters: Amplitude set point: 254 mV; Drive frequency: 75 kHz; Scan rate: 2.5 Hz. The grains are much larger than those for Au films grown on $\text{Al}_2\text{O}_3(0001)$ substrates and the $\text{Au}\{111\}$ terraces are atomically flat..... 51

- Figure 2.16 Atomic force microscopy images of a 40-nm-thick Au{111} film deposited on 2-nm-thick Nb on a Al₂O₃(0001) prism after thermal annealing at 400 °C for 18 hours. Imaging parameters: (A and B) Amplitude set point: 450 mV; Drive frequency: 270 kHz; Scan rate: 2.5 Hz. Thermal annealing at 400 °C increases the grain sizes and generates many large flat terraces. Small round islands between grains are attributed to Au residue from migration during annealing. 52
- Figure 2.17 Scanning tunneling microscopy images of *n*-dodecanethiolate (**C12**) monolayers assembled on Au{111}/Al₂O₃(0001) substrates. Imaging conditions were sample bias voltage –1.0 V and tunneling current 1.0 pA. The average terrace size is much smaller than for typical **C12** SAMs on Au/mica. Terraces appear tilted in random orientations, and narrow terraces with many steps are often observed in large scan areas. Hexagonal close packing and the presence of SAM characteristics including vacancy islands, domain boundaries, and step edges indicate that there are no systematic differences from **C12** SAMs on Au{111}/mica. 55
- Figure 2.18 (A) A schematic drawing and (B to D) STM images of C₆₀-tethered 2,5-dithienylpyrrole triad molecules inserted into **C12** SAM matrices on a Au{111}/ Al₂O₃(0001) prism. **C12** SAM matrices were prepared in solution (B) at room temperature for 30 minutes, (C) at 70 °C for 4 hours, and (D) in vapor phase at 78 °C for 24 hours. The distribution of inserted C₆₀-triad molecules substantially decreases in tight **C12** SAM matrices. Imaging conditions were sample bias voltage –1.0 V and tunneling current 1.0 pA..... 58
- Figure 2.19 Schematic illustration of photovoltaic efficiency measurements on a single triad molecule with photon STM. (A) 2,5-dithienylpyrrole chromophore is excited by the evanescent wave ($\lambda = 405$ nm). Electrons are subsequently transferred to the fullerene after charge separation and can be measured by the STM tip. (B) Light-modulated scanning tunneling spectroscopy can determine illuminated (red line) and dark (blue line) current-voltage characteristics on single triad molecules [122]. 59
- Figure 2.20 (A) A schematic drawing of a 9-(4-mercaptophenylethynyl)anthracene (**MPEA**) molecule inserted into a *n*-dodecanethiolate (**C12**) SAM on a Au{111} surface. (B) Ultraviolet-visible absorption spectrum of **MPEA** (100 μ M) in ethanol solution. (C and D) Scanning tunneling microscope topographic images (top) and simultaneously recorded photoconductance maps (bottom) of isolated **MPEA** molecules in a **C12** monolayer on a Au{111}/Al₂O₃(0001). Molecules along step edges and on lower terraces were more sensitive to the 405 nm light absorption. Imaging conditions were sample bias voltage –1.0 V and tunneling current 1.0 pA..... 60
- Figure 3.1 Structures of 2-anthracenethiol, 10-thiodecyl 2-anthryl ether are compared to structures of 9-(4-mercaptophenylethynyl)anthracene (**1**), 9-phenylethynyl-anthracene disulfide (**2**), and oligo(phenylene ethynylene)thiol (**3**). 66

Figure 3.2 Ultraviolet-visible absorption spectrum of 9-(4-mercaptophenylethynyl)-anthracene (MPEA , 100 μ M) in ethanol solution.	68
Figure 3.3 Schematic view of the photoreaction of 9-phenylethynylantracene in solution [158].	70
Figure 3.4 Schematic view of the photoreaction of 9-(4-mercaptophenylethynyl)-anthracene on a Au{111} surface.	71
Figure 3.5 (A, to C) Sequential STM images of inserted MPEA molecules in a C12 SAM matrix. Yellow and red boxes show the apparent height changes of molecules. (D to I) Cropped sequential STM images of molecular switching. The arrows at the bottoms of images (A to C) highlight molecules that show no substantial conductance changes during imaging. Imaging conditions: $V_{\text{sample}} = -1.0$ V, $I_{\text{tunnel}} = 1.0$ pA.	75
Figure 3.6 (A to C) Scanning tunneling microscopy images of MPEA molecules inserted into a C12 SAM matrix, and then exposed to UV light (~ 365 nm). Images were collected during irradiation after (A) 24 minutes, (B) 124 minutes, and (C) 220 minutes. Imaging conditions: $V_{\text{sample}} = -1.0$ V, $I_{\text{tunnel}} = 1.0$ pA. The UV illumination increases the apparent height of photoreactive molecules and more molecules appear as protrusions at longer irradiation (see arrows). Several pairs of molecules show substantial decreases in apparent height, attributed to photodimerization (boxes in B and C).	76
Figure 3.7 (A) The calculated electronic energy profile and (B) the energy gap between the HOMO and the LUMO of MPEA as the function of relative ring orientations about the ethynyl bond.	80
Figure 3.8 Frontier molecular orbitals and corresponding energy levels (HOMO-1, HOMO, LUMO, LUMO+1) of the planar (0°) and orthogonal (90°) conformations of MPEA . The gap energy between the HOMO and LUMO of the planar MPEA (3.01 eV) is smaller than that of the orthogonal MPEA (3.29 eV).	81
Figure 4.1 (A) The molecular structures of 1-adamantanethiol and 2-adamantanethiol. Sulfur attachments to the tertiary (3°) and secondary (2°) carbon on the adamantyl cage in each thiol are shown by the arrows. (B) The three-dimensional representation of the corresponding thiolates.	84
Figure 4.2 Scanning tunneling microscopy images of 2-adamantanethiolate (2AD) self-assembled monolayers (SAMs) on Au{111} fabricated by immersing substrates in 1 mM 2-adamantanethiol solution at room temperature for 24 hours (RT 2AD SAMs, A and B) or by first exposing clean Au substrates to solution at 70°C for 2 hours, then dry-annealing the samples under nitrogen at 78°C for 17 hours (DA 2AD SAMs, C and D); sample bias 0.80 V, tunneling current 2.0 pA. The round features with high contrast in C correspond to Au adatom islands with measured height of 2.4 \AA , consistent with the Au{111} single-atom step height [14].	91

- Figure 4.3 Scanning tunneling microscopy images of 2-adamantanethiolate (**2AD**) self-assembled monolayers (SAMs) on Au{111} prepared by first placing Au substrates in 1 mM 2-adamantanethiol solution at 70 °C for 2 hours, then dry-annealing the samples under nitrogen at 78 °C for 14, 17, and 22 hours for A, B, and C, respectively (**DA 2AD** SAMs); sample bias 0.80 V, tunneling current 2.0 pA. 92
- Figure 4.4 (A) A scanning tunneling microscopy image of a 2-adamantanethiolate (**2AD**) self-assembled monolayer (SAM) on Au{111} showing several rotational domains. The SAM was prepared by first placing a Au substrate in a 1 mM 2-adamantanethiol solution at 70 °C for 2 hours, then dry-annealing the sample under nitrogen at 78 °C for 17 hours (**DA 2AD** SAM). The lattice in domain B is rotated 30° counterclockwise with respect to domain A, and domain C is rotated 40° clockwise with respect to domain A. The domains A' and C' have the same orientations as domains A and C, respectively. Domain D is disordered. The yellow arrows denote translational domain boundaries; 600 Å × 600 Å; sample bias 0.80 V, tunneling current 2.0 pA. (B) The proposed unit cell for the **2AD** lattice on Au{111}. (C and D) The proposed superlattice $c(4 \times 2)$ structures of alternating heights results from different phases (β and δ), respectively. 93
- Figure 4.5 (A and B) Scanning tunneling microscopy images of mixed SAMs containing 2-adamantanethiolate (**2AD**) and *n*-dodecanethiolate (**C12**) domains fabricated by inserting **2AD** SAMs in 1 mM *n*-dodecanethiol solution for the specified times. (A) The **2AD** SAMs were prepared by immersing clean Au substrates in 1 mM 2-adamantanethiol solution at room temperature for 24 hours (**RT 2AD** SAMs). The small protruding features in the first image correspond to Au adatom islands formed during **2AD** self-assembly. (B) The **2AD** SAMs were prepared by first placing Au substrates in 1 mM 2-adamantanethiol solution at 70 °C for 2 hours, then dry-annealing the samples under nitrogen at 78 °C for 17 hours (**DA 2AD** SAMs); sample bias 0.80 V, tunneling current 2.0 pA. 96
- Figure 4.6 (A to D) Scanning tunneling microscopy images of a mixed SAM composed of 2-adamantanethiolate (**2AD**) and *n*-dodecanethiolate (**C12**) domains on Au{111} fabricated by inserting a **2AD** SAM into a 1 mM *n*-dodecanethiol solution. The **2AD** SAM was prepared by first placing a Au substrate in 1 mM 2-adamantanethiol solution at 70 °C for 2 hours, then dry-annealing the sample under nitrogen at 78 °C for 17 hours (**DA 2AD** SAM); sample bias 1.0 V, tunneling current 2.0 pA. 99
- Figure 4.7 Scanning tunneling microscopy images of *n*-dodecanethiolate (**C12**) phases generated from displacement of a 2-adamantanethiolate (**2AD**) SAM with a 1 mM *n*-dodecanethiol solution for 60 minutes. The **2AD** SAM was fabricated by first placing a Au substrate in 1 mM 2-adamantanethiol solution at 70 °C for 2 hours, then dry-annealing the sample under nitrogen at 78 °C for 17 hours (**DA 2AD** SAM). (A) 715 Å × 615 Å; (B) 996 Å × 477 Å; sample bias 1.0 V, tunneling current 2.0 pA 100

- Figure 4.8 Representative voltammograms showing the reductive desorption of (A) a single-component 1-adamantanethiolate (**1AD**) SAM, (B) a single-component 2-adamantanethiolate (**2AD**) SAM, and (C) a single-component *n*-dodecanethiolate (**C12**) SAM. Baseline correction was applied to account for solution resistance and sample/electrode contact resistance using a straight line subtraction in the first of 100 mV of the sweep in which no faradaic processes occur. The traces are offset for clarity. 102
- Figure 4.9 The C 1s region of XPS spectra of a single-component 2-adamantanethiolate (**2AD**) SAM, a single-component *n*-dodecanethiolate (**C12**) SAM, and binary **2AD/C12** SAMs created by displacement of **2AD** SAMs with 1 mM *n*-dodecanethiol solution for 10 seconds, 1 minute, and 10 minutes. The **2AD** SAMs were prepared by inserting Au substrates in 1 mM 2-adamantanethiol solution at room temperature for 24 hours (**RT 2AD** SAMs). The inset shows the C 1s peak of a single-component **RT 2AD** SAM fit by two Gaussian-Lorentzian line shapes with maxima at 283.8 and 285.0 eV (283.9 and 285.1 eV for a dry-annealed **2AD** SAM), and with a peak area ratio of 9:1. 106
- Figure 4.10 The S 2p regions of XPS spectra of single-component 2-adamantanethiolate (**2AD**) SAMs, a single-component *n*-dodecanethiolate (**C12**) SAM, and mixed **2AD/C12** SAMs created by displacement of **2AD** SAMs in 1 mM *n*-dodecanethiol solution for the specified times. The **2AD** SAMs were fabricated by immersing clean Au substrates in 1 mM 2-adamantanethiol solution at room temperature for 24 hours (**RT 2AD** SAMs) and by first immersing substrates in solution at 70 °C for 2 hours, then dry-annealing the samples under nitrogen at 78 °C for 17 hours (**DA 2AD** SAMs); Each spectrum was fit with Gaussian-Lorentzian line shapes for contributions from **S_A** peak (162.0 and 163.2 eV, red and orange, for S 2p_{3/2} and S 2p_{1/2}, respectively) and **S_B** peak (161.0 and 162.2 eV, dark blue and light blue, for S 2p_{3/2} and S 2p_{1/2}, respectively). 110
- Figure 4.11 (A) Infrared spectra of the C-H stretch region of a 2-adamantanethiolate (**2AD**) SAM and a *n*-dodecanethiolate (**C12**) SAM, showing their spectral overlap (see text for mode assignments). The **2AD** SAMs were prepared by either inserting clean Au substrates in 1 mM 2-adamantanethiol solution at room temperature for 24 hours (**RT 2AD** SAMs) or by placing Au substrates in 2-adamantanethiol solution at 70 °C for 2 hours, then dry-annealing the samples under nitrogen at 78 °C for 17 hours (**DA 2AD** SAMs). (B) Spectral evolution of a **DA 2AD** SAM displaced by **C12** in 1 mM solution as a function of immersion time, 1 minute, 10, 40, and 180 minutes. (C) Plot of **C12** monolayer coverage formed by displacement of **RT 2AD** and **DA 2AD** SAMs by **C12** as a function of the specified periods of displacement time, at every 1 minute interval for **RT 2AD** SAMs, and at 1 minute, 10, 20, 40, 60, 80, 100, 120, and 180 minutes intervals for **DA 2AD** SAMs. 113
- Figure 5.1 Scanning tunneling microscopy images of **1ATC9** self-assembled monolayers (SAMs) on Au{111}. Samples were fabricated in solution either at room temperature (A and B, **1ATC9 RT** SAMs) or at 70 °C (C and D, **1ATC9 70**

- SAMs) for 24 hours; sample bias -1.0 V, tunneling current 1.0 pA. The round features that appear more protruding in (B and C) correspond to Au adatom islands formed during assembly..... 122
- Figure 5.2 A schematic illustration of the molecular orientation in (A) **1ATC9 RT** SAMs and (B) **1ATC9 70** SAMs with difference in Hydrogen-bonding linearity..... 123
- Figure 5.3 Sequential scanning tunneling microscopy images of **1ATC9** self-assembled monolayers (SAMs) on Au{111} prepared by placing Au substrates in 1 mM **1ATC9** solution at 70 °C for 24 hours (**1ATC9 70** SAM); sample bias -1.0 V, tunneling current 1.0 pA. The fast scan direction was rotated counterclockwise by (A) 0° , (B) 30° , and (C) 45° . The oval shape of molecules in one direction is independent of scanning direction, and is attributed to molecular tilt to maximize hydrogen bonding..... 124
- Figure 5.4 Scanning tunneling microscopy images of **1ATC9** self-assembled monolayers on Au{111} after dry-annealing at 120 °C for 18 hours. The samples were fabricated by immersing a clean Au substrate in 1 mM ethanolic solution (A) at room temperature and (B) at 70 °C for 24 hours. Each was then dry-annealed in a N_2 atmosphere: sample bias -1.0 V, tunneling current 1.0 pA. The protruding round features in (B) correspond to Au adatom islands formed during assembly, while depressions are vacancy islands..... 126
- Figure 5.5 (A and B) Cyclic voltammograms of **1ATC9** SAMs and (C) **C12** SAMs on Au{111} with (A) 0.5 M KOH and (B and C) 0.5 M KCl (pH ~ 7) aqueous (aq) solutions at 20 mV/s. The SAMs were prepared by placing clean substrates in 1 mM ethanolic solution of **1ATC9** or **C12** at room temperature and at 70 °C for 24 hours. The appearance of oxidative readsorption only in **C12** SAMs not in **1ATC9** SAMs, indicates that the multistep reduction in **1ATC9** SAMs is not from decreased solubility in KCl (aq). 130
- Figure 5.6 Current vs. time plot during controlled potential electrolysis on **1ATC9 70** SAMs. A reductive potential of -960 mV was applied to the **1ATC9 70** SAM for 120 seconds. The current from desorbed **1ATC9** molecules from the monolayer drops rapidly in the first 10 seconds and remain steady, indicating the surface is no more reductive..... 131
- Figure 5.7 Scanning tunneling microscopy images of electrochemically processed **1ATC9** SAMs on Au{111}. The SAMs were fabricated by inserting clean substrates in 1 mM **1ATC9** solution at 70 °C for 24 hours, then applying a reductive potential of -960 mV for 120 seconds; sample bias -1.0 V, tunneling current 1.0 pA. The round protruding features correspond to Au adatom islands formed during self-assembly. The stripe patterns are oriented in three directions rotated by 120° with respect to each other. 132
- Figure 5.8 The FTIR spectra of **1ATC9** SAMs (A) in the high-frequency C-H region and (B) in the amide region. The SAMs were fabricated by inserting clean substrates in 1 mM **1ATC9** solution at 70 °C for 24 hours (**1ATC9**, red trace),

then applying a reductive potential of -960 mV for 120 seconds (**1ATC9** CPE, black trace). 133

Figure 5.9 C 1s, N 1s, O 1s, S 2p, and Au 4f regions of high-resolution XPS spectra of **1ATC9** SAMs before (red trace) and after (black trace) controlled potential electrolysis (CPE). Elemental components for XPS data analysis were color coded as magenta for the lower binding-energy peak, as cyan for the higher binding-energy peak and as brown for combination of both components (O 1s and S 2p). The SAMs were fabricated by inserting clean substrates in 1 mM **1ATC9** solution at 70°C for 24 hours with application of a -960 mV reductive potential for 120 seconds. Each element (other than Au) decreases in abundance, consistent with reductive desorption of the thiolates. The increase in the peak intensity in the Au 4f region is consistent with effectively thinning the monolayer via desorption. 137

Figure 6.1 (A) Schematic illustration of proposed STM measurements on photocurrent generated at the donor-acceptor interface. The double layer is composed of an electron donor, 2,3,7,8,12,13,17,18-octaethyl-21*H*,23*H*-porphine zinc(II) (**ZnOEP**), and an electron acceptor, fullerene. (B) A STM image of a **ZnOEP** monolayer. (C) A STM image of a C_{60} monolayer assembled on a **ZnOEP** monolayer. 148

Figure 6.2 Schematic illustration of photoinduced [2+2] cycloaddition reaction of fullerenes [321]. 149

Figure 6.3 (A) Molecular structure of dicubyl disulfide (B) A three-dimensional representation of isolated cubanethiolate molecules on Au{111}. The linear features are the Au{111} herringbone reconstruction. 151

Figure 6.4 (A) Schematic representation of molecular-scale interactions within **1ATC9** SAMs on **EGaIn** nanoparticles. (B) Hydrogen-bonding within **1ATC9** SAMs dominates local order and decreases domain size. The combination of strong hydrogen-bonding interactions between **1ATC9** molecules and local order facilitates the nondestructive scission of larger spherical particles into smaller spheres (red arrow). (C) A representative transmission electron microscopy image of **1ATC9**-capped **EGaIn** nanoparticles. 152

Acknowledgments

I am grateful and fortunate to work for my advisor, Paul Weiss. Thank you for all of the fantastic research opportunities that you have given me. I have learned from you not only the many important skills needed to pursue academic research, but also professionalism. You have taught me what it takes to be a great scientist. Thank you for your patience, and for your confidence, in my scientific abilities. You have always encouraged me to realize how important my research is, and not to give up.

I thank my committee members Professors, Christine Keating, Scott Phillips, and Anne Andrews for the time and effort you have put into being on my committee. I acknowledge financial support for my research from the Department of Energy, the National Science Foundation, and the Kavli Foundation. Chapters 3, 4, and 5 have been reproduced in part with permission. Copyrights 2009, 2010, and 2011, the American Chemical Society, and AAAS.

Sang-il Park, you have always cared for me like a daughter. You made me realize that I can look further, and extend my dream, rather than just staying satisfied with my position in Korea. I appreciate that you supported my decision to pursue a Ph.D. in the United States, despite your desire to keep me at Park Systems.

I acknowledge all the Weiss group members that I have encountered during my graduate career for their support and advice. First, I would like to thank my group members at Penn State, Professor Beth Anderson, Drs. Rachel Smith, Arrelaine Dameron, Julia Heetderks, Sanjini Nanayakkara, TJ Mullen, Amanda Moore, Hector Saavedra, Adam

Kurland, Charan Srinivasan, Dongbo Li, Meaghan Blake, Ajeet Kumar, and soon to be Dr. Mitch Shuster, Mr. Jeff Lawrence, and Mr. Daniel Dewey. You are my friends and my partners. Also, thank you, Mr. Steve Bumbarger, you assisted the Weiss group members with more than just logistics. When I am unhappy or exhausted, you make me feel better just by listening to me. After I moved to UCLA and settled in the new Weiss labs, I missed Penn State a lot, but Dr. Shelley Claridge and Mr. David McMillan have been a great help for me inside and outside of the lab to get used to our new location. I cannot imagine our new lab without David, that's for sure. With the Weiss group members who transferred to UCLA or joined, Balakrishna Pathem, Jeffrey Schwartz, John Thomas, Amit Vaish, Garrett Wadsworth, Sarawut Cheunkar, Andrew Guttentag, Dr. Wei-Ssu Liao, Dr. Yuebing Zheng, Huan Cao, Yuxi Zhao, Heidi Bednar, Mya LeThai, and Andrew Serino, it has been a great joy to work with you.

I have made many special life-long friends in graduate school at Penn State. I would like to give special thanks to Dr. Minjeong Kyoung who took such wonderful care of me when I started graduate school. You have always been very close to me, and given me so much advice for everything. I also acknowledge Professors Don Kim and Dongwon Lee for helpful advice for graduate school life and for research as an international student. To my friends in Chemistry department at Penn State, Drs. Sooyoung Kim, Jeeyeon Lee, Jongsik Gam, Songon An, Songyun Cho, Namhwan Chu, Seunghyun Anna Lee, Jaehong Seo, and Ms. Hayoung Back, it was great to have you. We shared happiness, difficulties, worries, and advice.

I am extremely thankful to my gracious husband, J. Nathan Hohman who is also my best friend, partner, and coworker. You helped me with everything more than 100%. I was so

lucky to find you during the most important moment of my life. It is so much fun to discuss our research with you anytime and anywhere. You see so much potential for me and encourage me to try harder. I feel much more comfortable living here, finally, thanks to you.

To my parents who devoted their lives to support their children, especially me, education was always your number one priority. With your strong, tough love, I have come this far. Your hard work and dedication are priceless. Thank you so much for letting me pursue my dream. Also, I miss my two lovely sisters and my little brother so much every day.

Chapter 1. Beyond Molecular Assemblies and Scanning Tunneling Microscopy

1.1 Introduction

We have applied molecular self-assembly to tailor interfaces and to design organic reactions on surfaces. By understanding the chemistry of adsorbed molecules, we can develop a systematic design strategy for the production of diverse interfaces. Structural variation, molecular orientation, and chemical functionalization enable precise tuning of the local and ensemble interfacial properties of supramolecular assemblies and the creation of new nanoscale patterns.

Scanning tunneling microscopy (STM) has been a powerful tool for nanoscience, used to characterize nanoscale features with high resolution in real space. However, this excellent resolution without chemical specificity limits the capabilities of STM. Development of STM with chemical specificity is thus an important goal in science especially chemistry. Although many achievements have been made, it will still be a long journey to accomplish definitive chemical identification with STM.

In this thesis, we emphasize the importance of chemical principles to help elucidate the chemistry of supramolecular assembled systems. We also use these assemblies to conduct chemical reactions of individual organic molecules on surfaces. We observe the underlying physical chemistry of self-assembled monolayers (SAMs) and bimolecular organic reactions with STM. Our newly designed photon STM provides fresh opportunities for the study of

functional molecular candidates for molecular optoelectronics and organic solar cell applications.

1.2 Self-Assembled Monolayers

Organic thiols spontaneously assemble into one-molecule thick layers (monolayers) on diverse substrates such as metals and semiconductors [1-7]. The reaction is spontaneous, driven first by highly strong adsorbate-substrate interactions (the Au-S bond is ~128 kJ/mol) [8,9]. *n*-Alkanethiolate SAMs on Au{111} have been studied extensively because they are easy to prepare, stable, and are well-ordered [3,10]. Nanoscale ordering is driven by the substrate lattice and the attractive van der Waals interactions between alkyl chains (~4 – 8 kcal/mol) and is improved by the diffusion of a Au-S complex during assembly [9-11].

When the Au{111} surface is exposed to *n*-alkanethiols, the thiol head group attaches to the Au surface, achieving nearly complete coverage within seconds. The alkanethiolate molecules tilt with respect to the surface normal by 30° to maximize the van der Waals interactions between neighboring alkyl chains (Figure 1.1A). Molecules assemble to a hexagonally close-packed lattice with nearest neighbor distances of 5.0 Å (Figure 1.1B) [10]. The monolayer lattice is described by a $(\sqrt{3} \times \sqrt{3})R30^\circ$ unit cell with respect to the underlying (1×1) Au{111} lattice. A primitive $c(4 \times 2)$ superlattice is also observed, which has been explained by an alternating azimuthal orientation of one molecule with respect to its neighbors [10,12]. Figure 1.2 illustrates both $(\sqrt{3} \times \sqrt{3})R30^\circ$ and $c(4 \times 2)$ superlattice structures of *n*-alkanethiolate monolayers. A hexagonally closed-packed *n*-dodecanethiolate (**C12**) monolayer and its $c(4 \times 2)$ superlattice structure can be resolved in molecular resolution STM images of **C12** SAMs, as shown in Figure 1.3.

A representative STM image of a **C12** SAM on Au{111} displays the characteristic features, including vacancy islands, domain boundaries, and step edges that are normally observed in *n*-alkanethiolate monolayers (Figure 1.4A). During self-assembly, the herringbone structure of the Au{111} substrate (Figure 1.4B) reconstructs by Au atom ejection, resulting in one-Au-atom deep (2.35 Å) substrate vacancy islands (red arrow in Figure 1.4A) [11,13,14]. Adjacent domains with different translation, rotation, or tilt are separated by characteristic domain boundaries (yellow arrow in Figure 1.4A) [15-18]. Domain boundaries can appear as protrusions or depressions in SAMs. Each Au{111} terrace is separated by substrate step edges, 2.35 Å higher or lower (green arrow in Figure 1.4A). We define any disorder, pinholes, domain boundaries, and vacancy islands as SAM defects that direct the physical, chemical and electrical properties of monolayers.

1.2.1 Self-assembly in solution vs. vapor deposition

n-Alkanethiolate SAMs on gold are commonly prepared by the immersion of freshly prepared, clean substrates, typically 150-nm-thick bare Au{111} film on cleaved mica, into a dilute (~1 mM) ethanolic solution of related thiols at room temperature. During self-assembly at room temperature, the Au substrate is quickly covered with *n*-alkanethiolates from solution within milliseconds to minutes, but the slow reorganization process takes a minimum of several hours to maximize coverage density and to minimize the defect sites (Figure 1.5A and B) [19]. However, the solvent, temperature, concentration, immersion time, purity, cleanliness of the substrate, and the alkyl chain length can affect the overall SAM structure and quality [4].

Solution deposition at somewhat elevated temperature ($\sim 70^\circ\text{C}$) substantially improves SAM quality. Even with short assembly times (70°C for 1 hour, Figure 1.5C), we observe lower defect densities with increased overall order and average domain sizes. The extra thermal energy speeds up the self-assembly process [20]. Alkanethiolate-Au complexes diffuse faster at elevated temperatures and are able to overcome the barrier for the reorganization of kinetically trapped molecules, which enables them to maximize their intermolecular interactions. Noticeably, self-assembly in the vapor phase ($\sim 78^\circ\text{C}$) promotes self-exchange [21], substantially improving monolayer order. Vapor deposition accelerates both assembly and ordering, resulting in high-quality SAMs (Figure 1.5D) [19,22]. Figure 1.5 displays STM images of **C12** SAMs prepared in solution and vapor phase at room temperature (A and B) and mildly elevated temperatures (70°C and 78°C , in C and D, respectively). Longer time, higher temperature, and vapor phase thiols increase domain sizes and decrease the numbers of vacancy islands.

1.2.2 Single-molecule insertion

Ensemble averaging samples from all configurations molecules. Single-molecule spectroscopy allows us to monitor variations in the configurations of single molecules. It provides details of underlying distributions that can be critically important for understanding heterogeneous systems [23,24]. Measurements of time-dependent processes and stochastic behavior, including single-molecule fluctuations or “flickering” have grown to understand unprecedented insight into single-molecule behavior obscured by traditional ensemble averaging [23,25-27].

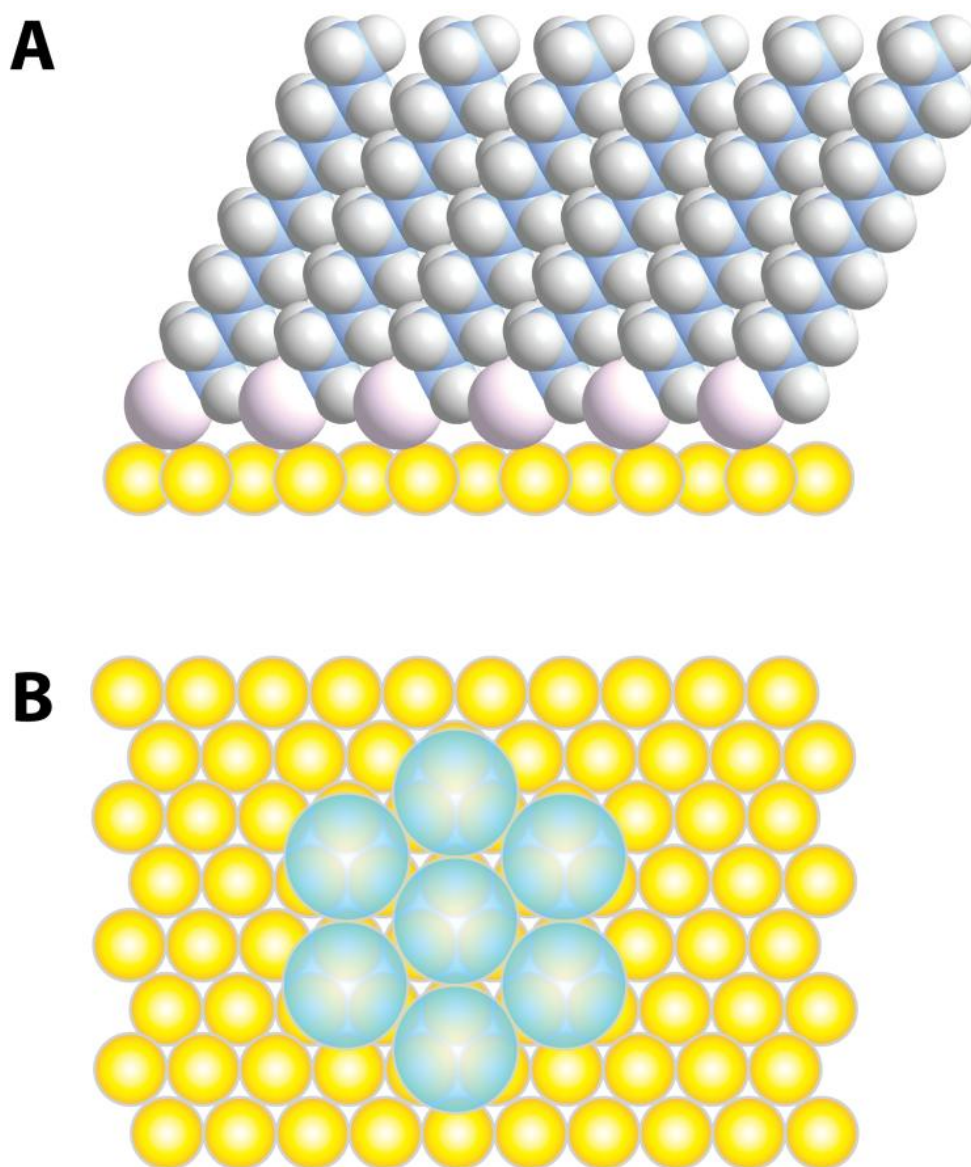


Figure 1.1 Schematics of *n*-dodecanethiolate (**C12**) SAM structure on Au{111}. (A) A side view along the nearest neighbor direction showing the 30° tilt to maximize van der Waals interactions. (B) A top view showing hexagonal close packing of **C12** molecules.

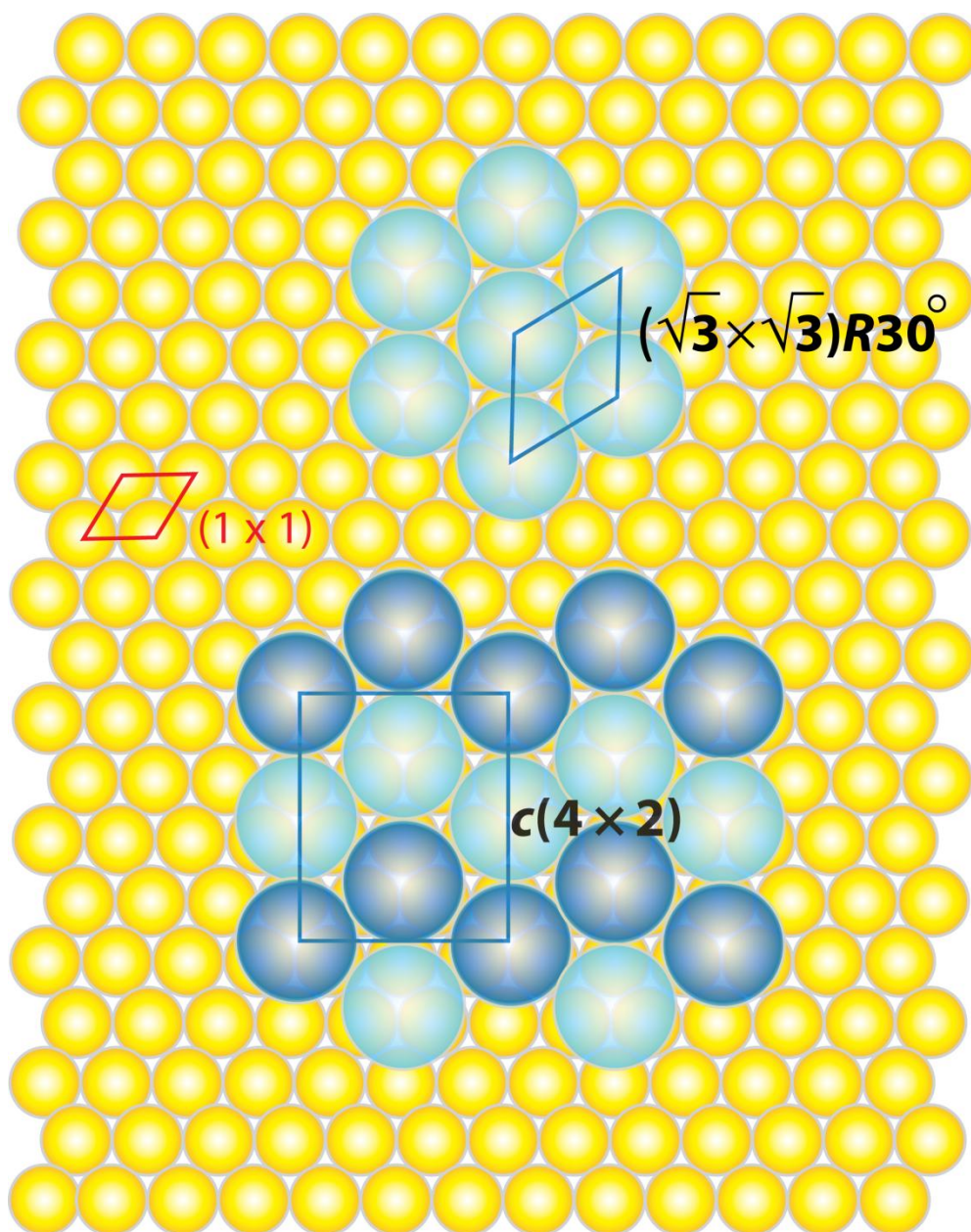


Figure 1.2 A schematic top-down view of the unit cells, $(\sqrt{3} \times \sqrt{3})R30^\circ$ (top) and $c(4 \times 2)$ superlattice (bottom) on underlying (1×1) Au{111} substrate.

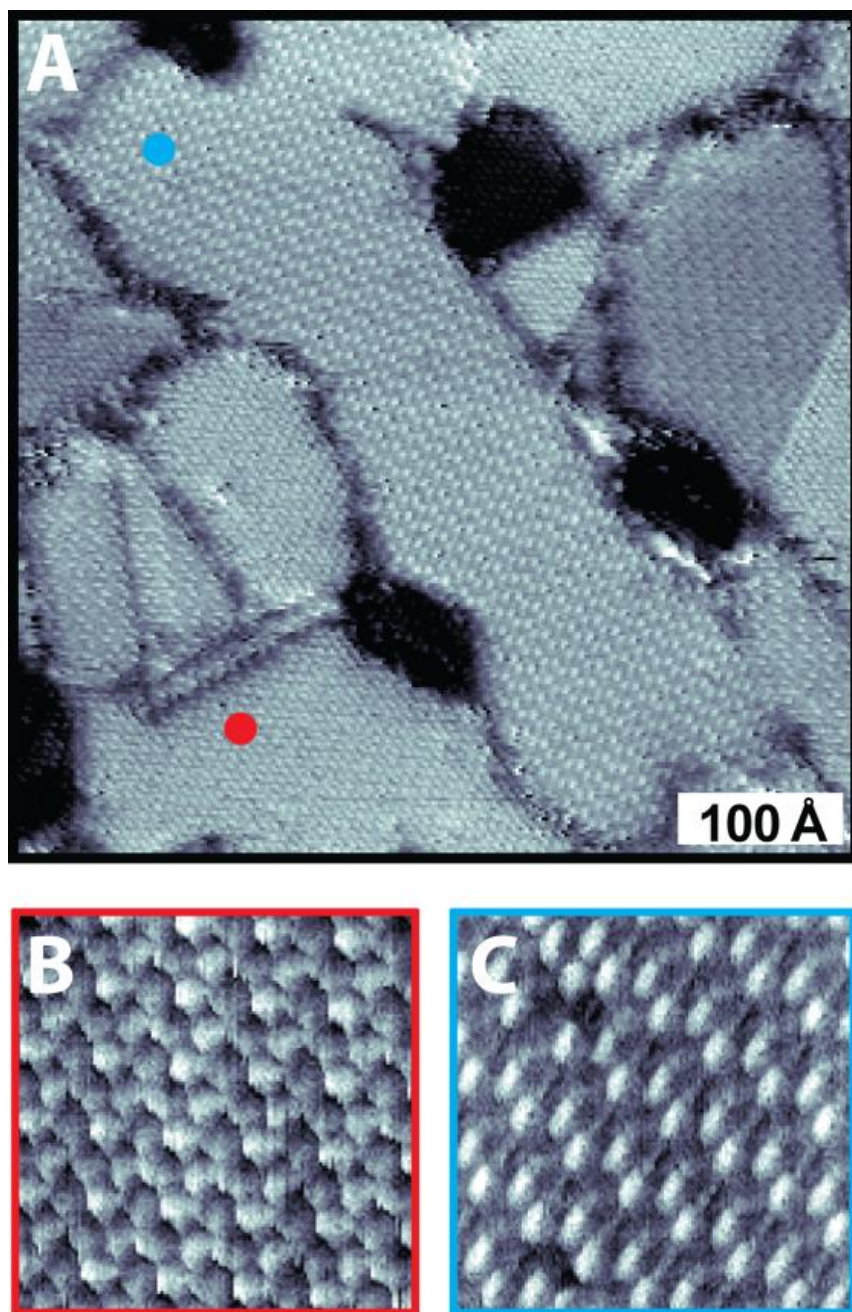


Figure 1.3 Molecular-resolution STM images of **C12** SAMs, displaying hexagonally close-packed lattice (red dot in A, and B) and $c(4 \times 2)$ superlattice (blue dot in A, and C). Imaging conditions were sample bias voltage -1.0 V and tunneling current 1.0 pA.

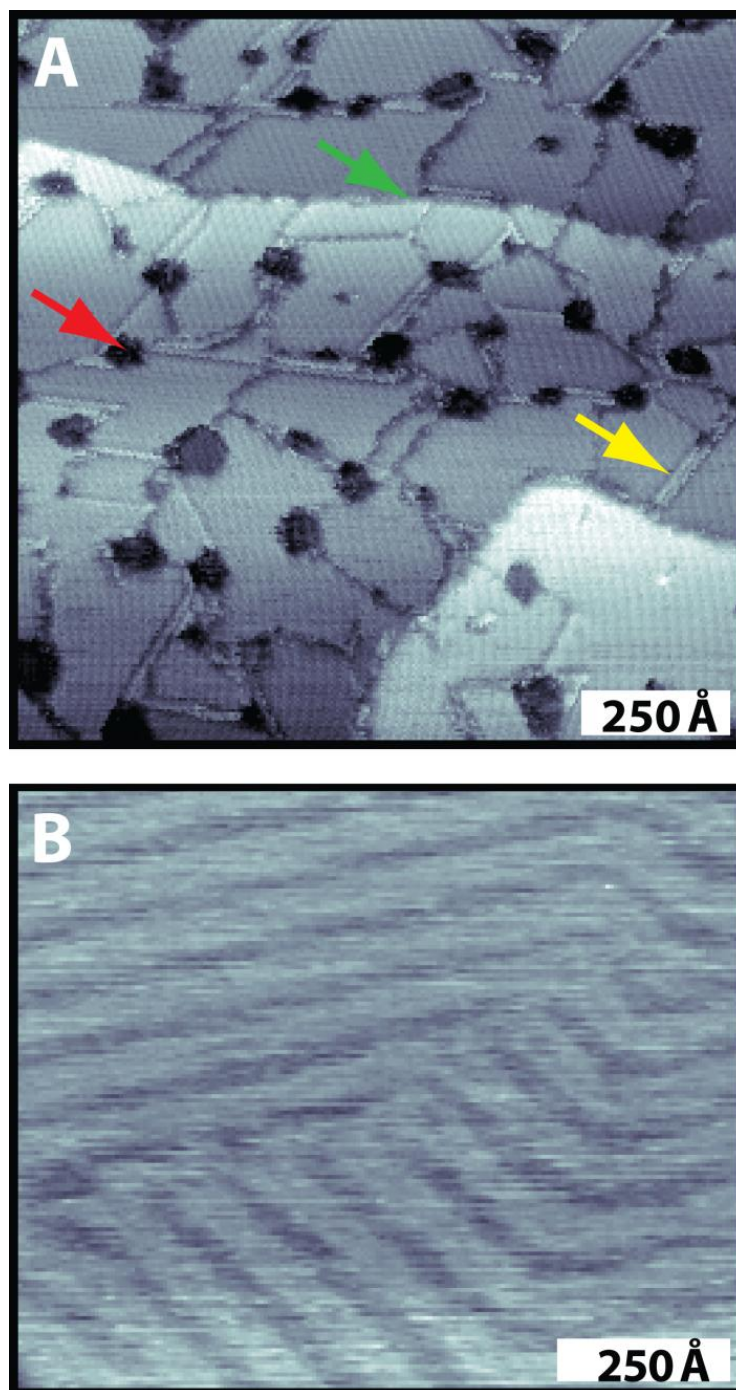


Figure 1.4 (A) A representative STM image of a **C12** SAM showing domain boundaries (red arrow), vacancy islands (yellow arrow), and substrate step edges (green arrow). Imaging conditions were sample bias voltage -1.0 V and tunneling current 1.0 pA. (B) A STM image of a bare Au{111} substrate displaying the herringbone structure [28]. Imaging conditions were sample bias voltage -1.0 V and tunneling current 10.0 pA.

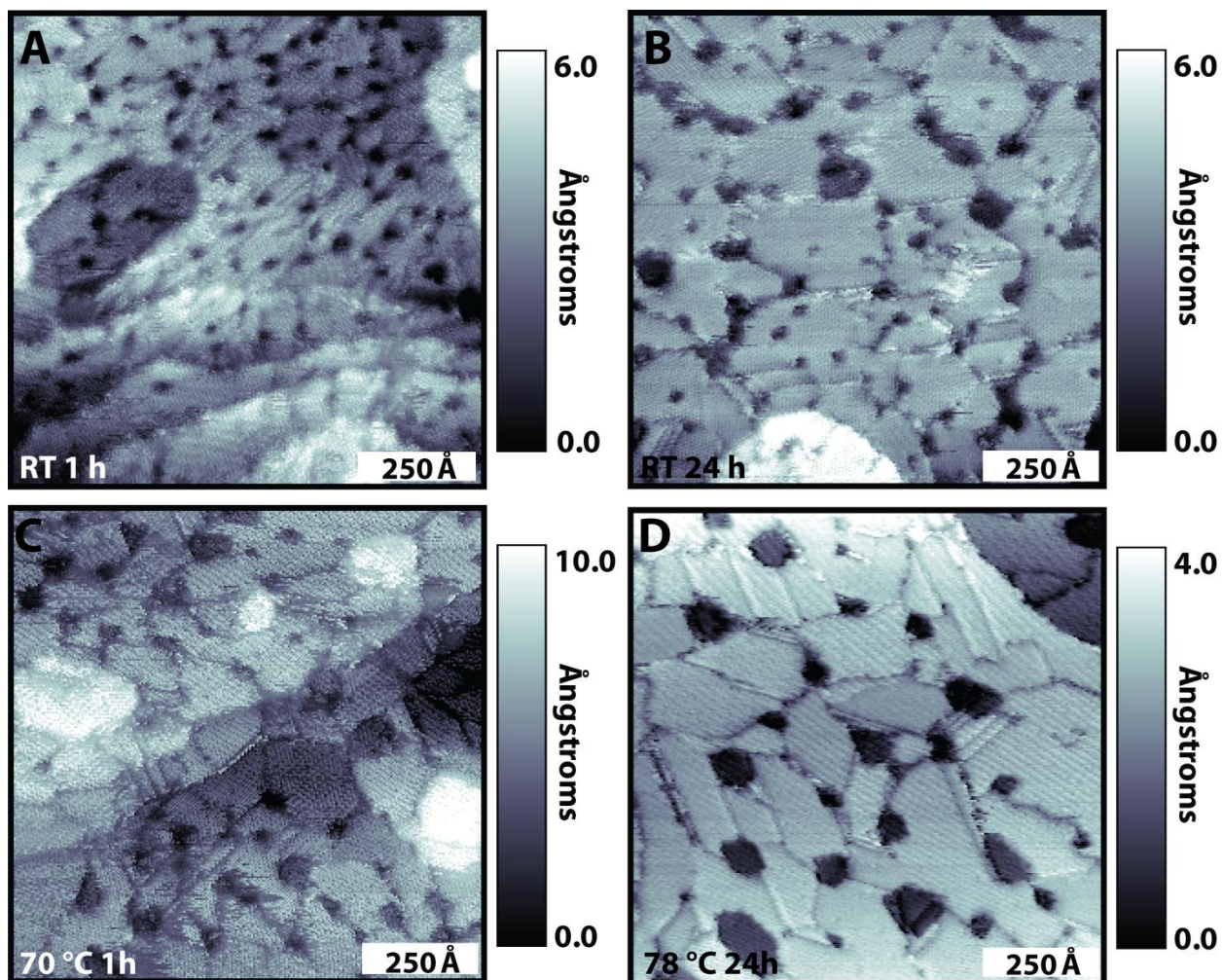


Figure 1.5 Scanning tunneling microscopy images of **C12** SAMs prepared in solution (A) at room temperature for 1 hour and (B) for 24 hours, (C) at 70 °C for 1 hour, and (D) via vapor deposition at 78 °C for 24 hours. The SAM quality (larger domains, fewer defect sites, and better order) can be improved substantially by using increased temperature in solution or vapor deposition. Imaging conditions were sample bias voltage -1.0 V and tunneling current 1.0 pA.

We use *n*-alkanethiolate SAMs on gold surfaces as a stable and well-defined matrix for single-molecule spectroscopy of organic molecules or nanoparticles [29-31]. Small organic molecules or nanoclusters are tethered with thiol functionality and can be isolated within *n*-alkanethiolate monolayers by placing preformed *n*-alkanethiolate SAMs on Au{111} into low concentration ($\sim\mu\text{M}$) solutions of related sulfur-functionalized chemicals. Figure 1.6A illustrates typical molecular insertion into an *n*-alkanethiolate monolayer and Figure 1.6B shows STM images of inserted molecules within an *n*-alkanethiolate monolayer (here, 9-(4-mercaptophenylethynyl)anthracene (**MPEA**) molecules in a **C12** SAM). We are able to isolate molecules singly, in pairs, or in groups within a SAM matrix and to monitor their activities in situ with STM [32].

Stable insulating *n*-alkanethiolate monolayers serve as a homogeneous low-noise background and a test bed for single-molecule measurements by scanning tunneling spectroscopy. Stochastic switching and spectral diffusion [33] caused by molecular motion and conformational changes have been successfully measured and imaged [30,31]. One example of single-molecule spectroscopy on inserted molecules is shown in Figure 1.6C. Conductivity measurements on isolated single **MPEA** molecules exhibit conductivity fluctuations (with negative differential resistance), which have not been observed on full coverage monolayers [34].

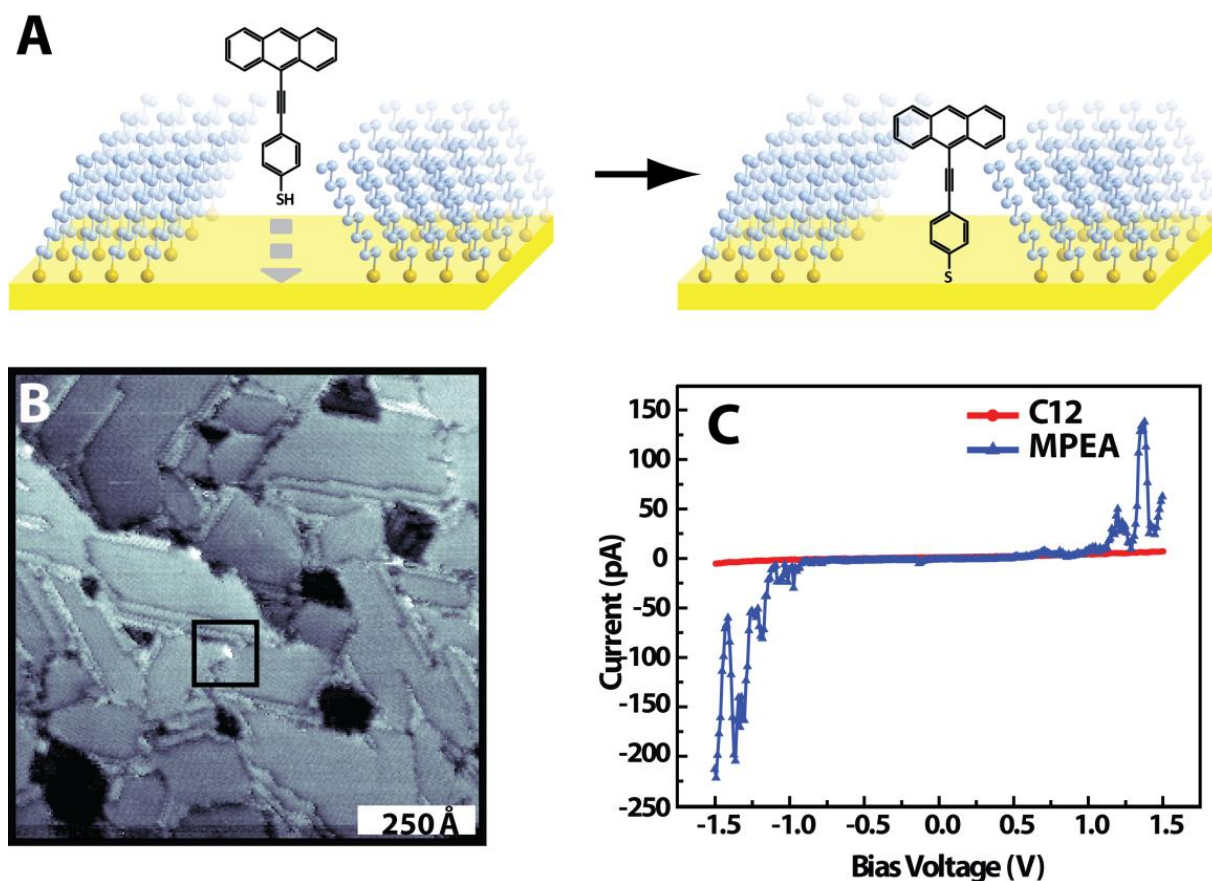


Figure 1.6 (A) A schematic drawing of the insertion procedure with self-assembly. (B) A STM image of 9-(4-mercaptophenylethynyl)anthracene (**MPEA**) molecules inserted into a **C12** SAM matrix. Imaging conditions were sample bias voltage -1.0 V and tunneling current 1.0 pA. (C) Current-voltage characteristics of isolated **MPEA** molecules taken by scanning tunneling spectroscopy. Isolated single **MPEA** molecule shows negative differential resistance which has not been observed in full coverage monolayers.

1.3 Scanning Tunneling Microscopy

Scanning tunneling microscopy has been used to discover diverse electronic properties of metallic and semiconductor surfaces [35,36]. Quantum mechanical electron tunneling across sub-nanometer separations enables the direct measurement of individual atoms or molecular structures in real time and space. Unlike energetic beam microscopes and other surface characterization tools, STM is not limited to high vacuum environments. Also, organic molecules or biological structures can be analyzed without using statistical or diffraction methods [27].

Figure 1.7 schematically describes an overview of STM operation, with a one-dimensional (1D) metal-vacuum-metal tunnel junction. An atomically sharp metallic tip (typically W, or a Pt/Ir alloy) is brought to within Ångströms of an atomically flat, conductive sample surface. At these separations, the wave functions of the tip and the sample begin to overlap. When a small bias voltage (V) is applied between the sample and the tip, a tunneling current can flow due to a shift in equilibrium [37].

When electrons tunnel through the potential barrier, the state of an electron in a 1D junction with rectangular barrier is:

$$\Psi(z) = \Psi(0)e^{-\kappa z},$$

where the electronic wavefunction is Ψ and z is the tip-sample distance and the decay constant κ is defined as:

$$\kappa = \frac{\sqrt{2m(V-E)}}{\hbar},$$

where the mass of an electron, m , is 9.1×10^{-28} g and Plank's constant, \hbar , is 6.626×10^{-34} J.s. The potential barrier and the energy of the tunneling electrons are V and E , respectively. The work functions of both the tip and the sample influence the height of the tunneling barrier. For small biases, the quantity $(V - E)$ can be approximated as the work function of the metal tip ($V - E = -\Phi$). By the Born-Oppenheimer approximation, the square of the wavefunction is proportional to the probability distribution of the electron and thus, the tunneling current (I) can be described as the following equation:

$$z|\Psi(z)|^2 \propto e^{-2\kappa z} \propto I(z).$$

The tunneling current decays exponentially with the tip-sample distance, z ; the tunneling current is highly localized and thereby provides STM with extreme sensitivity to topography laterally and normal to the surface. The exponential relationship between I and z is responsible for resolution normal to the surface.

The two common modes of STM operation are constant-current or constant-height modes (left and right in Figure 1.7B, respectively). In constant-current mode, the tip moves up and down as it scans the surface, responding to the feedback loop (FBL) to keep the tip-sample spacing constant. Constant-current mode is most common because it can be used on rough surfaces with large scan areas. The recorded topography depends on both electronic and physical structures of the tip and the sample. In constant-height mode, the tip does not move up or down during scanning. Changes in distance between the tip and the sample generate changes in the measured current. This mode allows faster scanning because it does not need the FBL, and is typically used for smooth surfaces with atomic resolution.

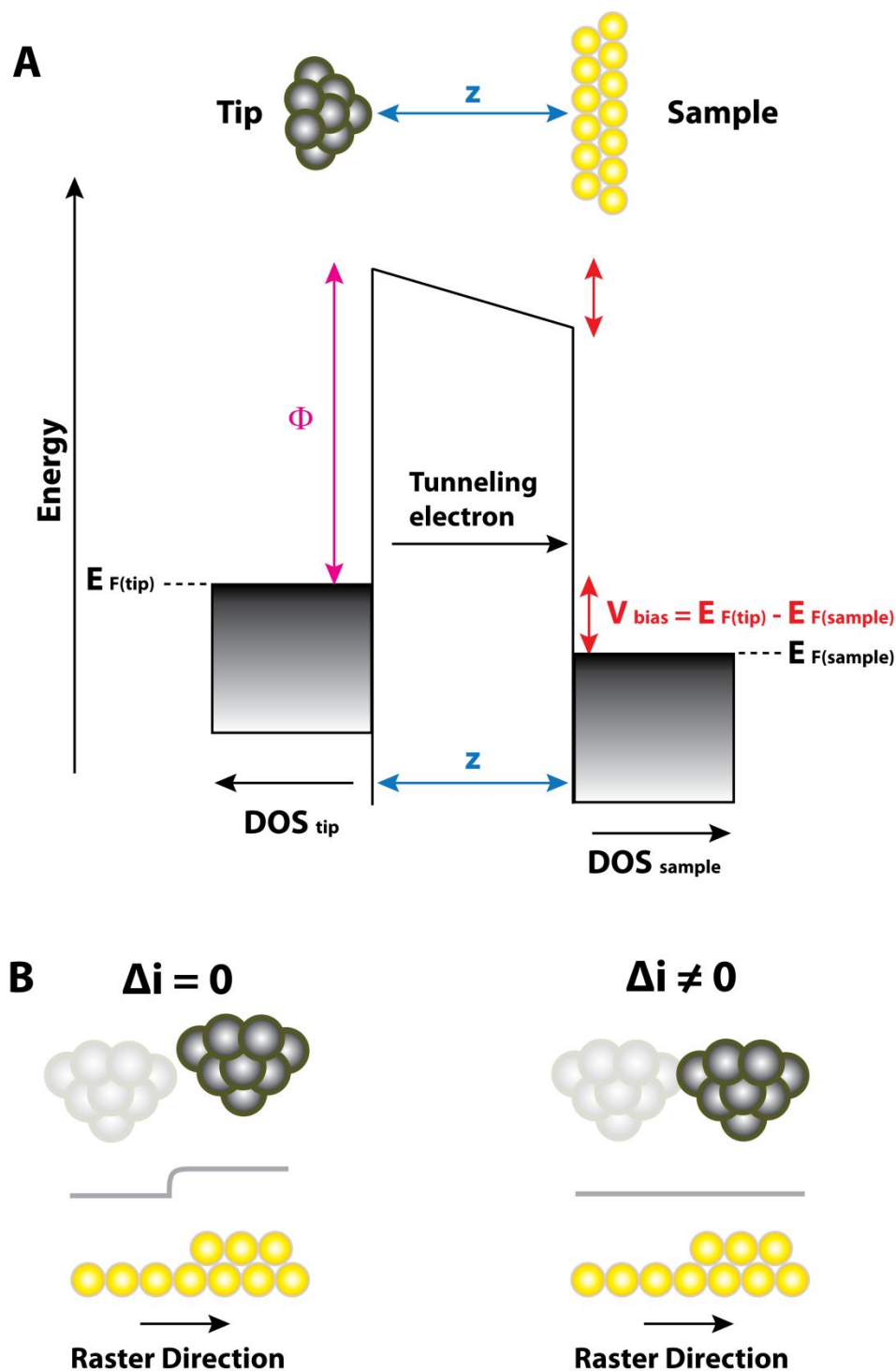


Figure 1.7 (A) An energy level diagram for a 1D electron tunneling junction and (B) schematics of a STM tip rastering a sample surface (left) in constant-current mode and (right) in constant-height mode.

1.3.1 Scanning tunneling microscope

A scanning tunneling microscope is composed of a conductive sample, a scanning tip, a preamplifier, and control electronics with data acquisition hardware and control software (Figure 1.8). An atomically sharp metal tip is brought close to the atomically flat conductive surface for electron tunneling. The small tunneling current, typically between 1 pA and 100 nA, must be amplified for electrical detection. This current signal is routed through control electronics and the data acquisition hardware, and is digitally processed in the computer (here, WinSTM software). The main elements of a scanning tunneling microscope demand rigid construction to fulfill the requirements for stable operation, and to avoid electronic coupling with the environment. The tunneling gap between the tip and the sample (on the order of Ångströms) must be stabilized by a combination of construction elements in the centimeter range. All elements are mechanically coupled to each other, making the tunneling junction sensitive to vibrations and to thermal drift. To prevent undesired motion in the tunneling junction, all components should be miniaturized and held on a rigid support. The support is placed on a damping system to decrease vibrations that negatively affect imaging and spectroscopy.

In order to achieve atomic or molecular resolution of surfaces, the end of the STM tip needs to be atomically sharp; a single atom at the closest point to the surface. Tip shape is a critical concern: double-tip images are often observed due to the presence of multiple atoms protruding on the tip. This sharpness is achieved by skillful cutting of a Pt-Ir wire at a high angle, resulting in an audible snap. Other methods for tip preparation are electrochemical etching with strong base (KOH or NaOH) solution [38-40], or field emission in vacuum [41,42]. The use of piezoelectric materials for the tip scanner provides convenient, low-

voltage control of the position and motion at the atomic scale. Vibrations and acoustic noise can cause serious problems in atomic- and molecular-scale imaging. The instrument should thus be isolated from these noise sources by using a vibration isolation table and a STM enclosure.

1.3.2 Besocke scanning tunneling microscope

Most scanning tunneling microscopes in our group adopted the Besocke-style scanning tunneling microscope [43,44] because of its extraordinary stability, rigid and compact construction, and temperature compensation. The simple, rigid construction and intrinsic thermal compensation of the tip-sample spacing substantially reduce the effects of drift and vibration. Figure 1.9 shows the head configuration of the Besocke-style scanning tunneling microscope. Four identical piezoelectric tubes stand on the Macor base (McMaster-Carr, Elmhurst, IL) on top of a copper support block. The three outer tubes are arranged in a triangular configuration and their top ends are equipped with small metal ball bearings. The Pt/Ir probe wire (80:20) is connected to the central piezoelectric tube for scanning (Figure 1.9A). The ramps below the sample holder rest on the three ball bearings and move clockwise for coarse tip approaching (Figure 1.9B). The only significant force acting on the sample holder is gravity, which further improves tunneling junction stability. The sample surface is exposed to the STM tip through the 5 mm diameter hole for scanning (Figure 1.9C).

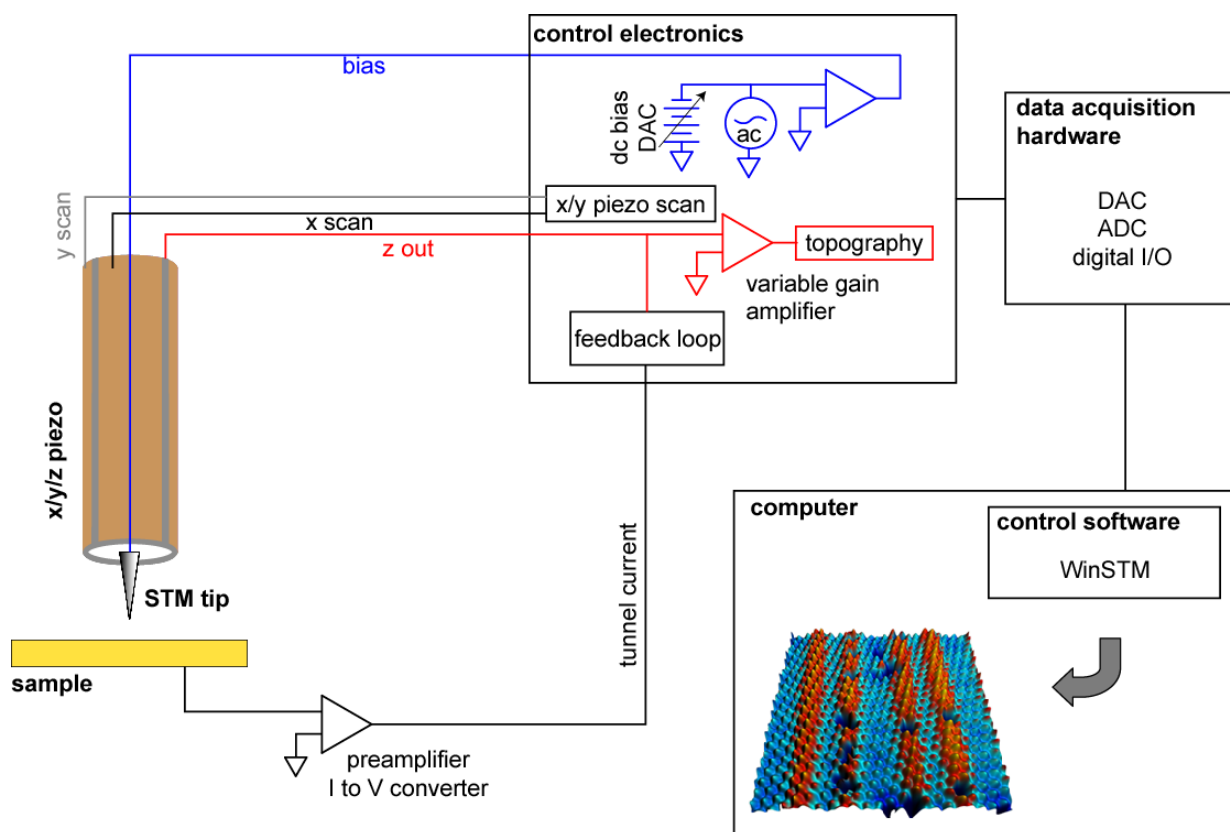


Figure 1.8 A schematic of a basic scanning tunneling microscope setup. A small bias voltage is applied between the sample and tip, and the resulting current is recorded and is simultaneously adjusted by the feedback loop to maintain the constant current.

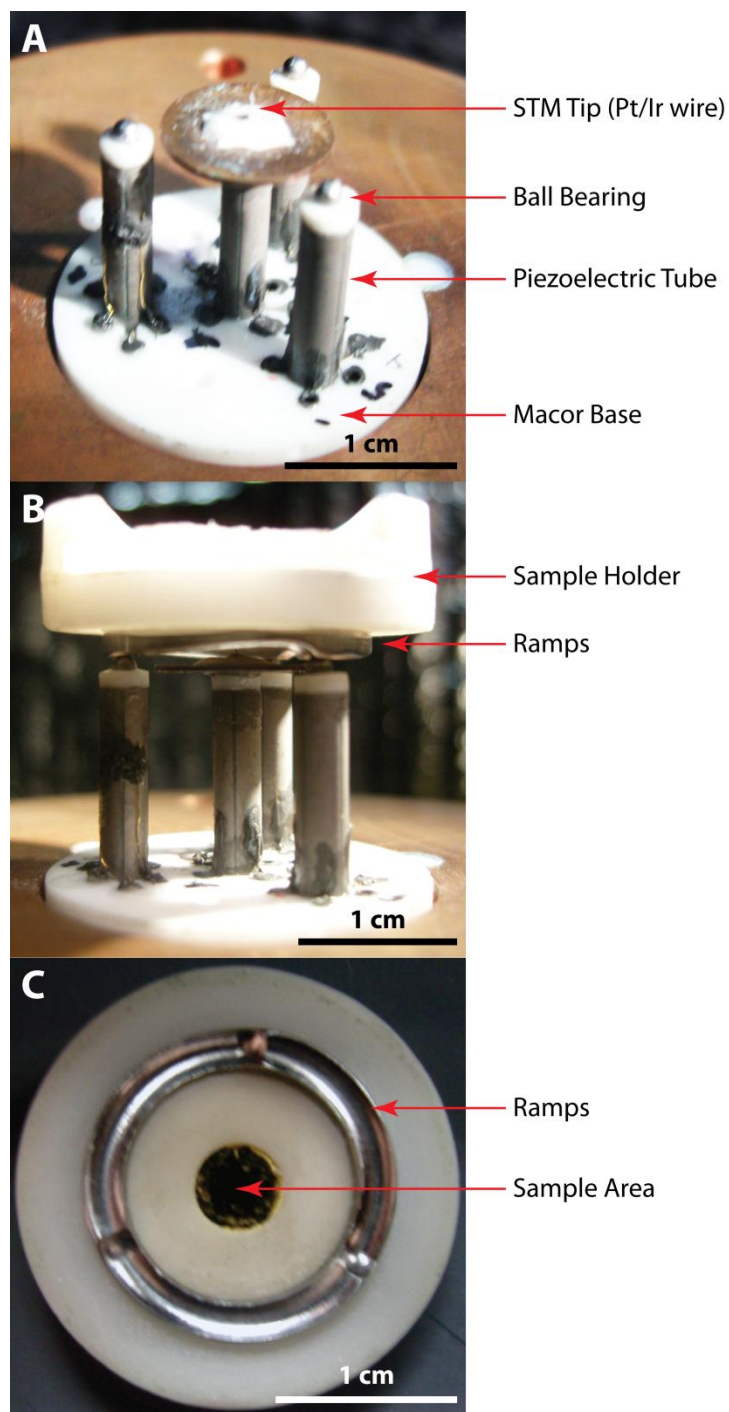


Figure 1.9 Photographs of the STM head configuration and the sample holder in the custom-built Besocke-style scanning tunneling microscope. (A) The tip is connected to the center scanner tube through the copper grounding plane. The three outer tubes are equipped with each metal ball bearing that contacts the ramps below the sample holder. (B) The tip and sample spacing is decreased or increased by the movement of the three outer tubes on the ramps via either clockwise or counterclockwise rotations. (C) The tip scans the sample surface within the center hole.

Piezoelectric materials can stretch or shrink by application of positive or negative voltages. The outer surface of a piezoelectric tube has isolated electrode quadrants and the inner tube is a single electrode (z direction) (see Figure 1.10). One tube thus can achieve movement in any direction via vector combination of x and y motions. This offers superior performance over more conventional independent x-y-z tripod arrangements. Also, the tip-sample spacing is less sensitive to thermal drift because four identical piezoelectric tubes are used. Thermal expansion and contraction of the scanner is thus compensated by identical changes in the three outer tubes. Consequently, this Besocke-style scanning tunneling microscope brings the tip with tunneling range of the sample with no mechanical coupling of the microscope to vibrational noise sources.

The sample holder for a Besocke-style scanning tunneling microscope is shown in Figure 1.11. A flat sample substrate is placed between two Au foils, pressed together by the sample holder cover and the spacer to ensure good electrical contact. This sample holder can accept only thin, flat substrates. As shown in Figure 1.12, the preamplifier is mounted on top of the sample holder and amplifies the tunneling current signal before the control electronics. A thin, flexible Au wire spring touches the top Au foil for electrical contact (Figure 1.12A). This close, direct connection to the sample does not require any extra length of wire, eliminating extraneous noise source. The Au wire spring compensates for shocks from sample approach. Stainless steel plate stacks separated by elastomeric materials decrease the effect of external impact during imaging, improving stability for long duration scanning (Figure 1.12B). Overall, the Besocke design offers high stability operation and easy sample mounting with reduced influence of drift and vibration.

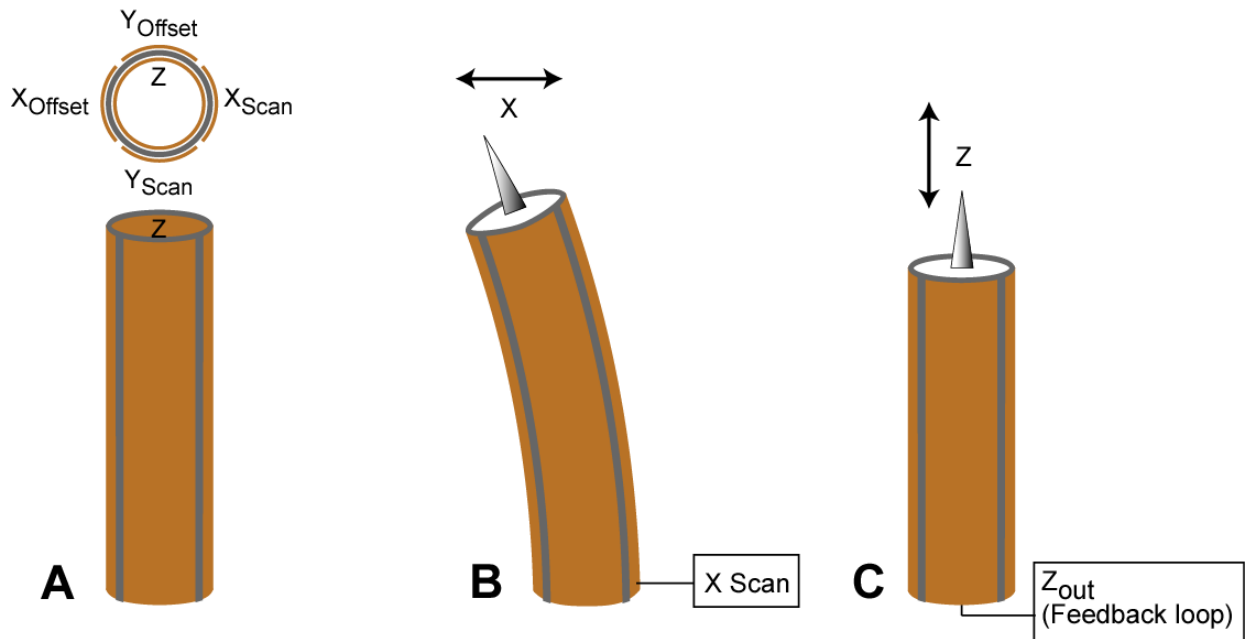


Figure 1.10 Schematic drawing of piezoelectric tube movement. (A) The piezoelectric has four electrodes outside and one electrode inside. (B) The tip motion in x or y directions can be carried out by anti symmetric voltages between diagonal pairs of the outer quadruple electrode. (C) The z motion is controlled by the inside electrode.

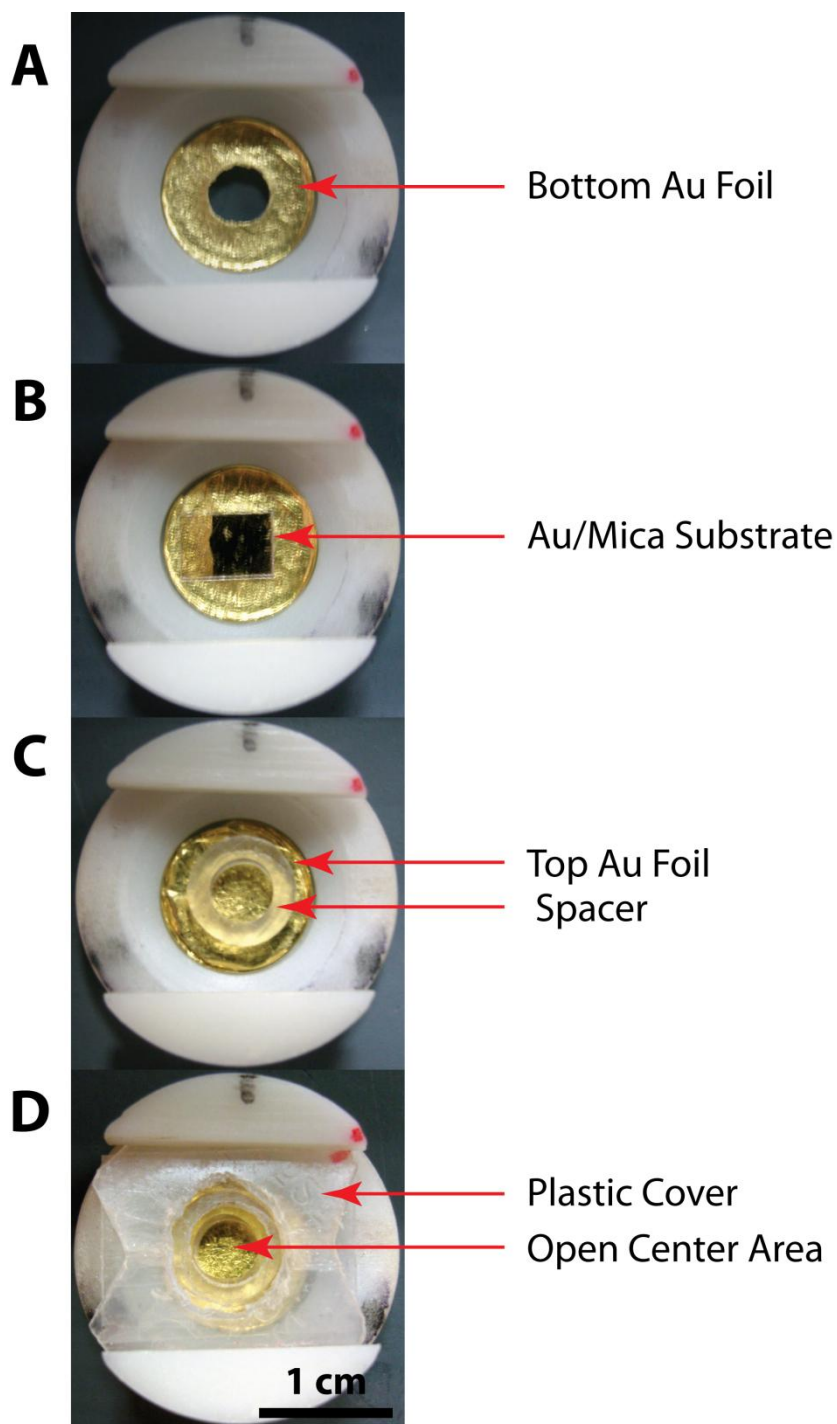


Figure 1.11 Photographs of the sample holder assembly. (A and B) Thin flat Au/mica substrate is placed between the bottom and the top Au foils for electrical contact. (C and D) The plastic spacer and cover are compressed to ensure electrical contact. The center area should be open for electrical contact to the preamplifier.

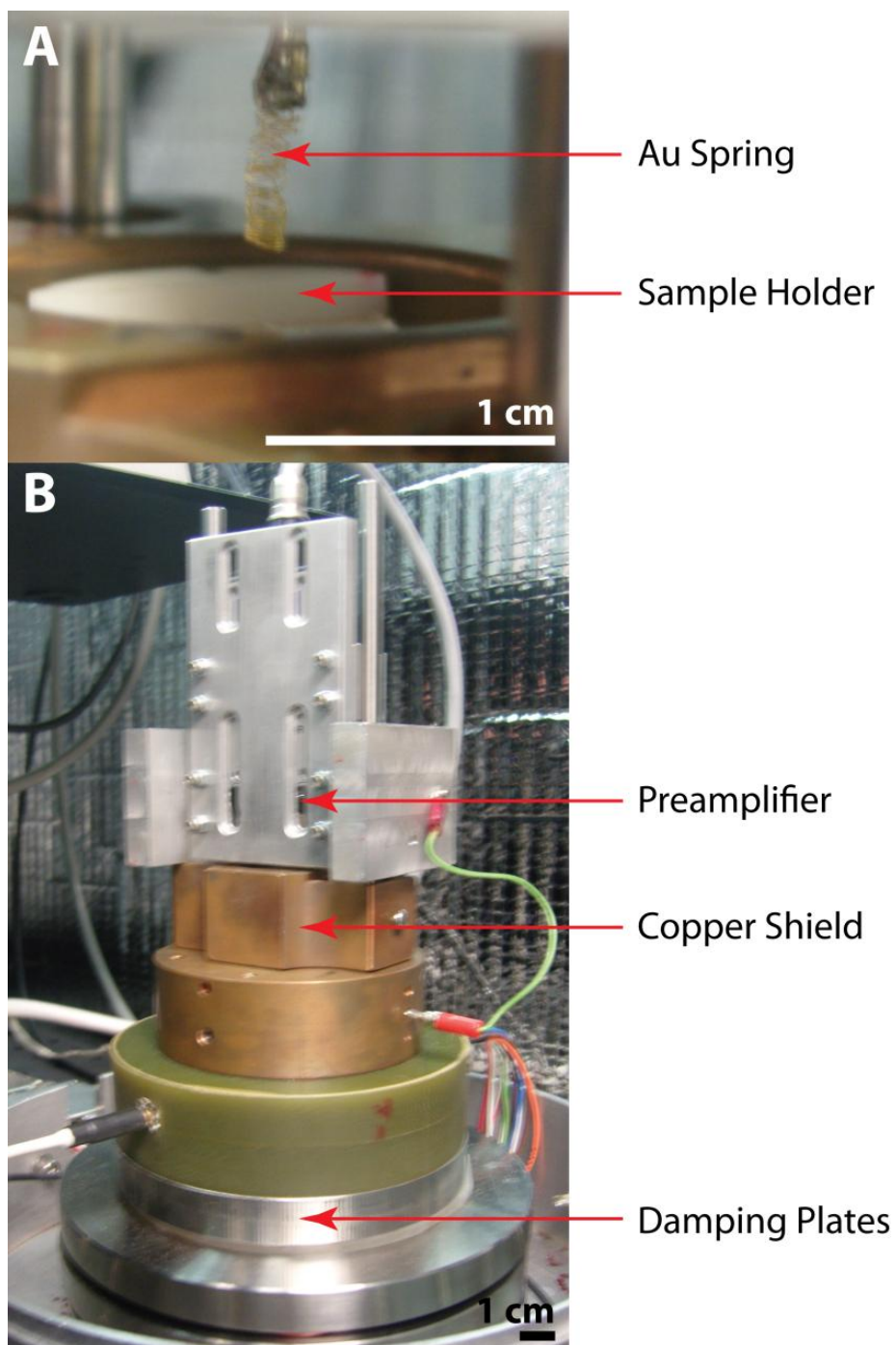


Figure 1.12 Photographs of the Au spring attached to the preamplifier and the entire assembly of our Besocke-style scanning tunneling microscope. (A) The Au spring contacts the top Au foil of the sample holder. (B) The copper shield protects the scanning tunneling microscope head component and the sample surface. Stacks of stainless steel plates are placed between elastomeric materials for damping.

1.3.3 Photon scanning tunneling microscope

The photon scanning tunneling microscope is designed to allow introduction of ultraviolet (UV)-visible light into the tunneling junction during imaging. The photon scanning tunneling microscope requires access of both light and the STM head to the sample surface. Despite its many advantages, the Besocke style STM is incompatible with the photon scanning tunneling microscope in part because its compact design makes it more difficult to bring light into the tunneling junction. With the Besocke style, all four piezoelectric tubes are adjacent and the tip scanner is within ~ 1 cm of the sample surface. Our photon scanning tunneling microscope is configured for a horizontal approach for coarse tip-distance adjustment, rather than sample rotation by three outside sample carriers. The sample is placed a few centimeters away from the tip, enabling the user to check the alignment of the tip with the laser.

We designed our photon scanning tunneling microscope based on the Kretschmann-Raether configuration for evanescent wave coupling by total internal reflection (Figure 1.13) [45,46]. This geometry allows us to use a high-intensity light source without heating the probe tip. The half cylindrical sapphire prism is open for total internal reflection. The flat side is coated with a Au film as a sample substrate where is exposed to the STM head for imaging. The UV-visible light is focused onto the center of the half cylindrical prism and the tip is positioned at the incident spot. The prism can be rotated to adjust the angle of incidence for maximum optical coupling.

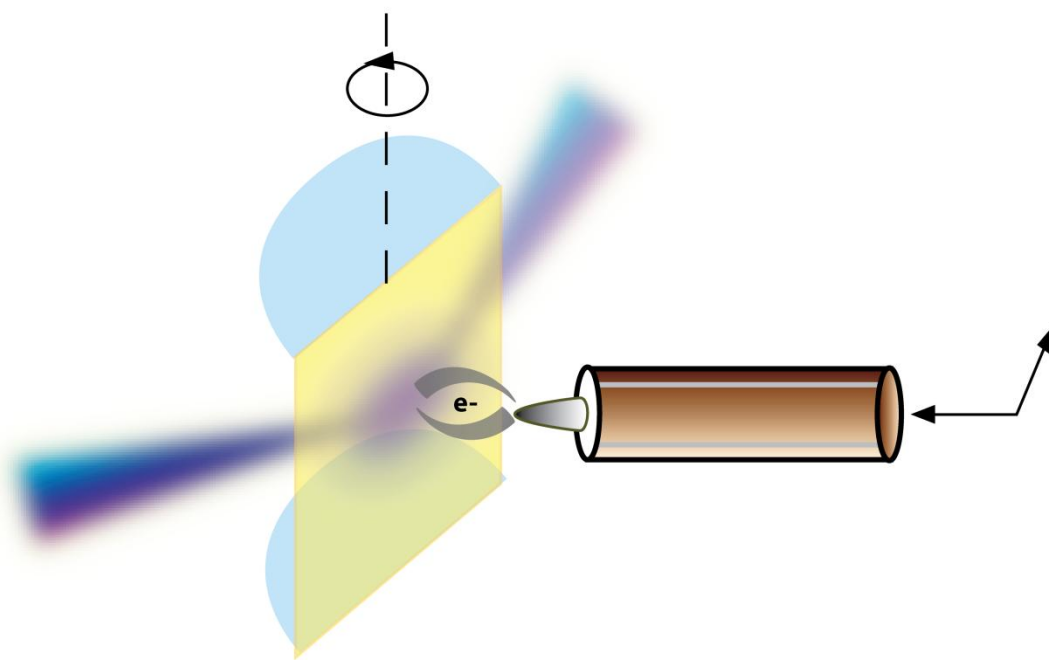


Figure 1.13 Kretschmann-Raether configuration in the photon scanning tunneling microscope. A Au {111} substrate on a sapphire prism is back-illuminated, producing the evanescent field in the tunneling junction. This geometry allows the direct observation and measurement of the energy conversion mechanism for individual, isolated photoreactive molecules.

1.4 Thesis Overview

The following chapters of this thesis will describe the details of the development of the photon scanning tunneling microscopy, single-molecule measurements on photoreactive molecules, and the control of chemistry on interfaces using molecular assemblies. The first two chapters introduce new optical spectroscopic techniques extending STM in new ways. The next two chapters focus on the importance of chemical design principles for supramolecular self-assemblies.

Chapter 2 describes the design of the photon scanning tunneling microscope, including the sample holder, the tip approach system, and the rotation stages. Epitaxial growth of Au{111} film on a c-cut plane of a sapphire prism is discussed. The Kretschmann-Raether configuration for the evanescent coupling by total internal reflection is explained in detail. Preliminary results with light modulation are discussed briefly.

In Chapter 3, we discuss the regioselective control of photochemical reactions on surfaces. We apply molecular self-assembly to direct the allowed but unfavorable photocycloaddition between anthracene moieties of molecules inserted into a SAM. The confined molecules are exposed to UV radiation, and the molecular conformation forces them to undergo [4+4] instead of [4+2] photocycloaddition.

In Chapter 4, we explore the self-assembly of small cage molecules (adamantanethiols) on Au surfaces. This cage system offers new ways of diversifying interface properties. The shape and the size of the cages alter the intermolecular interaction strengths of the monolayers. The different composition of elements (for example, carboranes that are composed of carbon and boron) can tune electrical, optical, physical properties of

SAMs. Finally, the different sulfur position on the cage brings the cage molecules onto the surface in different orientations, changing local and entire SAM structure and morphology.

Chapter 5 is committed to understanding buried hydrogen bonding networks within alkanethiolate monolayers. This hydrogen-bonding network increases overall intermolecular interaction strengths in monolayers, substantially increasing thermal stability. Hydrogen bonding orientation gives different phases, domains, and unusual electrochemistry responses. Using this electrochemical effect, we also bring about nanoscale structural transformations by chemical electrolysis.

Lastly, the summarized results from each project, the key aspects, and future directions are discussed in chapter 6.

Chapter 2. Photon Scanning Tunneling Microscopy

2.1 Introduction

We have been misled for decades by the presumption that identical molecules always behave identically. Most conventional characterization techniques provide an ensemble of averaged molecular characteristics because of the limits of detection. For example, in traditional optical spectroscopy, millions of photons or more pass through a constellation of identical unknown elements or molecules. These unknowns can be identified by measuring sums of their electronic or other excitations. Certainly, these ensemble measurements represent the behavior of *most* molecules. However, when the underlying system is not homogeneous, or if it is impossible to place them in the exact same conditions, we cannot and should not rely on bulk analyses alone [47].

Advances in technology and the invention of highly localized characterization techniques have driven single-molecule studies, and have enabled researchers to explore individual molecules in heterogeneous environments [24,48,49]. Ultrasensitive, time-resolved photodetectors enable single-biomolecule fluorescence spectroscopy [50-52], enabling non-invasive observations. Traditional ensemble measurements are not suitable for time-dependent movements, structural reorganization of enzymes, the dynamics of protein folding [53], and other complex biological machinery [54,55]. Such motion can be tracked using covalently attached fluorescent probes [56,57]. Spatial motion, changes in emission intensity, and radiative lifetime can be monitored simultaneously and in real time with changes in local environment [58]. However, nonradiative quenching and photodegradation often restrict

broader applications. They also give relatively low spatial resolution, at best tenths of nanometers [59].

Scanning probe microscopy experiments have made important contributions to single-molecule studies [48,60,61]. An atomically sharp probe is brought close to a flat sample surface for surface imaging and measures tunneling electrons or tip-sample forces. These imaging techniques offer highly localized, real-space information and high spatial resolution (substantially better than optical detection limits) [62]. However, a lack of chemical information is a trade-off for the otherwise magnificent resolution. Chemical identification is interpretive, and it is challenging to treat chemically complex samples by STM measurements.

Combining the high spatial resolution of the STM with the energy selectivity of optical techniques addresses both of their limitations [63]. By performing optical spectroscopy with the scanning tunneling microscope within the tunneling junction, it is possible to measure the optically excited vibrational and electronic states of single molecules on surfaces. The STM tip serves as a near-field detector, collecting both spatial and optical measurements. Previous attempts have made progress in determining photoconductance [64], photovoltage [65-68], photocurrent [69-71], photothermal effects [72,73], optical rectification [74,75], and surface plasmon resonances [76-78]. Such optically assisted STMs have focused mainly on photonic effects or on optical phenomena of bulk semiconductor surfaces. However, the direct illumination of laser light onto the tunneling junction often causes overwhelming background noise and artifacts from differential heating of the tip and sample [79,80]. Here, we introduce an optically assisted STM (photon STM) that has been developed to achieve single-molecule optical spectroscopy in air. Optical coupling by total internal

reflection eliminates thermal effects on the tunneling junction, resulting in stable imaging conditions with long-duration illumination. We also apply molecular assemblies to isolate and to stabilize single organic molecules.

2.2 Theory and Experimental Design

2.2.1 Evanescent field coupling

For the photon STM, UV-visible light is coupled with the tunneling junction evanescently from beneath a Au surface deposited on the backside of a sapphire prism. Light is converted into an evanescent wave via total internal reflection. This electromagnetic field penetrates the thin metallic film, extends a small distance from the surface, and propagates parallel to the surface in the plane of incidence. This field can optically excite molecules just as direct illumination can [81,82].

2.2.1.1 Total internal reflection

When a light beam passes through a high-refractive index material (*i.e.*, sapphire) and encounters another medium with a lower refractive index (*i.e.*, air), a certain amount of the light will either transmit into the low-index medium (refract) or will reflect back into the high-index material. The ratio of the light transmission or reflection depends on the ratio of the two refraction indices and the incident angle, θ_i , at which the light strikes the dielectric interface. *Snell's law* describes the angle at which the transmitted light refracts into the lower index medium, θ_t :

$$\sin(\theta_t) = \frac{n_1}{n_2} \sin(\theta_i).$$

The angle where the transmitted light beam skims across the interface is called the critical angle, θ_c (Figure 2.1C). Figure 2.1 describes each case of light travel between a high-index medium (sapphire, $n_2=1.8$) and a low-index interface (air, $n_1=1.0$). The light passes through the interface differently depending on the angle of incidence.

When $\theta_i \geq \theta_c$, all incoming light reflects back into the prism, which is called *total internal reflection* (TIR). Total internal reflection produces an electromagnetic field, an *evanescent wave*, which travels along the interface surface and penetrates slightly beyond, into the air. The intensity of the evanescent wave decays exponentially as a function of the angle of incidence along the direction perpendicular to the dielectric interface (Figure 2.2) [83], as described in the following expressions:

$$I(z, \theta) = I(0, \theta)e^{-\gamma z},$$

$$\text{where } \gamma = \frac{4\pi \sqrt{n_2^2 \sin^2 \theta - n_1^2}}{\lambda}.$$

$I(0, \theta)$ is the intensity of the light incidence on the interface ($z = 0$) at angle θ , and λ is the wavelength of the light source in vacuum. The penetration depth of the evanescent wave can be defined by γ , as $d_p = 1/\gamma$. The value d_p represents the distance at which the intensity of the evanescent wave in the z direction drops to a value equal to $1/e$ (~37%) of its original intensity at the interface.

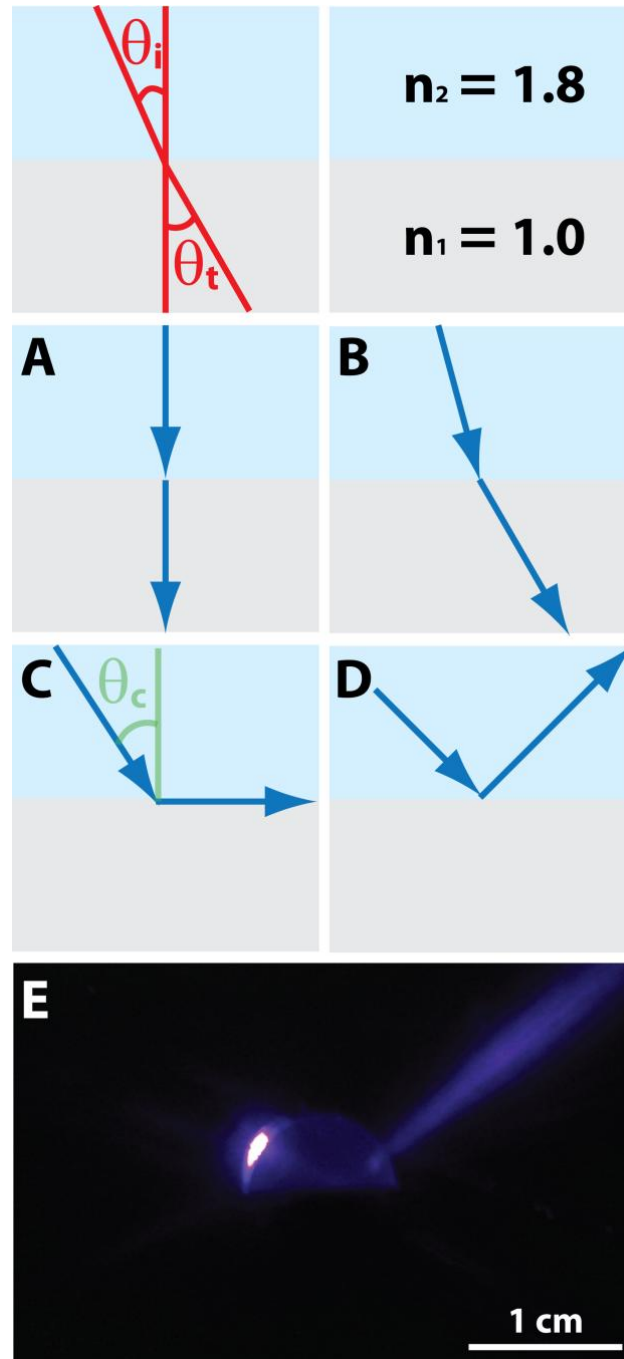


Figure 2.1 Schematic description of Snell's law for a sapphire prism ($n_2 = 1.8$)/air ($n_1 = 1.0$) interface. (A) At $\theta_i = 0^\circ$, light (blue arrows) incident from the sapphire prism normal to the interface transmits normal to the interface as well. (B) As the angle of incidence is increased ($\theta_c > \theta_i > 0^\circ$), the transmitted ray refracts away from the surface normal at a larger angle than the incident angle ($\theta_t > \theta_i$). (C) At the critical angle ($\theta_i = \theta_c \sim 35^\circ$), the transmitted ray skims across the interface. (D) Beyond the critical angle ($\theta_i > \theta_c$), all incident light gets reflected back to the sapphire, total internal reflection. (E) A top-view photograph of total internal reflection of 405 nm light through the cylindrical sapphire prism.

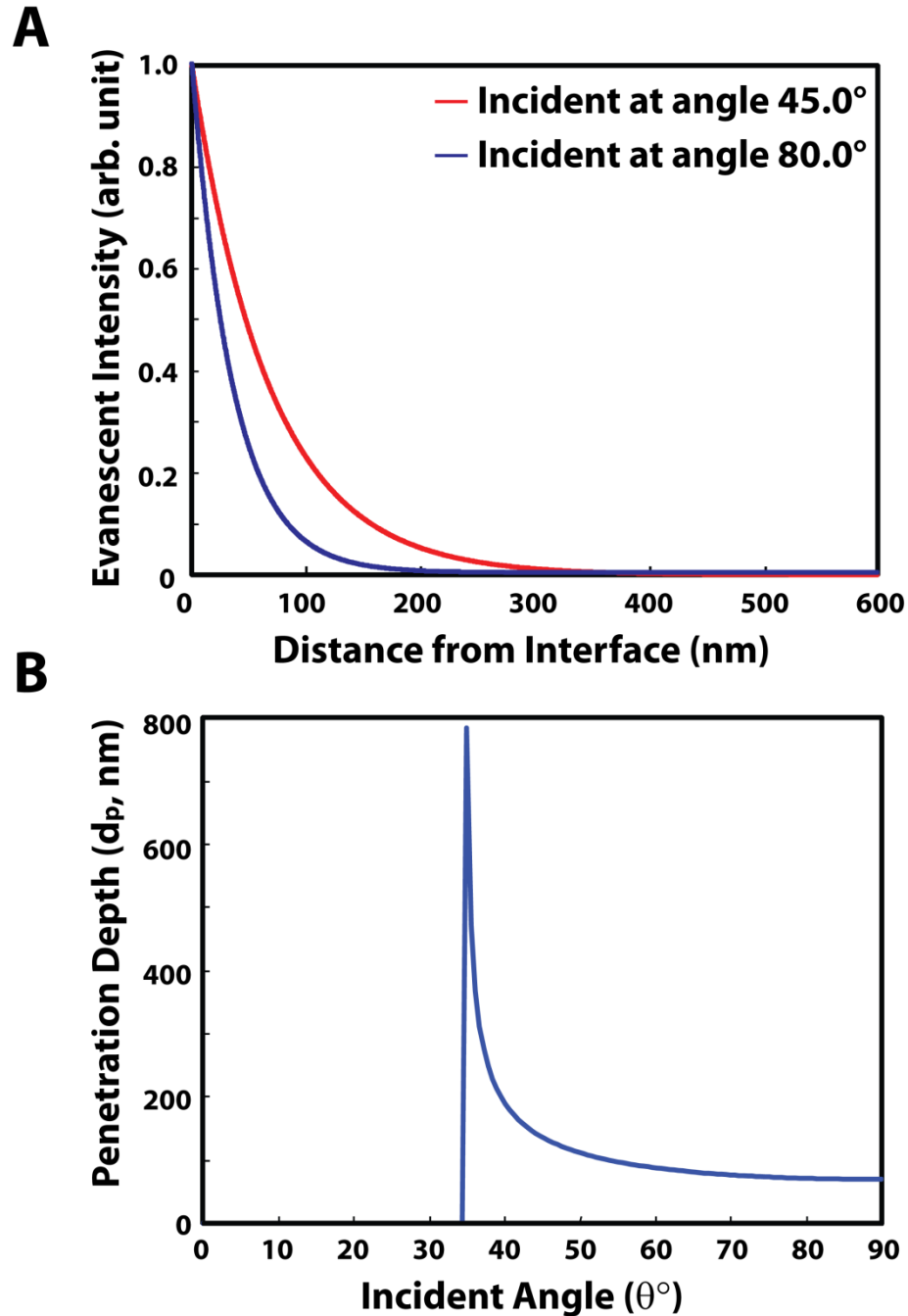


Figure 2.2 The evanescent wave field intensity and the penetration depth exponentially decay and are dependent on the angle of incidence. (A) The evanescent wave intensity of a visible light ($\lambda=635$ nm) generated between the interface between a highly refractive material ($n_2 = 1.76$) and air ($n_1 = 1.00$) depends on the incident angle (red at $\theta_i = 45.0^\circ$ and blue at $\theta_i = 80.0^\circ$). (B) Penetration depth exponentially decreases above the critical angle (θ_c , $\sim 35^\circ$).

2.2.1.2 Evanescent field enhancement

If the TIR interface is coated with a thin layer of a noble metal (with thickness less than the wavelength of the light source), the energy of the electromagnetic field can interact with the free electrons of the metal surface. The monochromatic, *p*-polarized (polarized parallel to the plane of incidence) light couples with the surface electrons and is converted into *surface plasmons*, resulting in decreased reflected light intensity [84]. Surface plasmon resonance occurs when the momentum of the incoming light matches the momentum of the plasmons [85].

The surface plasmon resonance of a thin metal layer enhances the evanescent wave field due to surface propagation [86-88]. The wavelength of the evanescent field is the same as the incident light. Gold is the most practical metal for surface plasmon resonance because it does not generally oxidize and is compatible with chemical modification such as organic thiolate monolayers [89].

2.2.2 Photon scanning tunneling microscope

The photon scanning tunneling microscope is composed of two main parts: a laser source with focusing optics and the STM head on a rotation stage (Figure 2.3). The photon scanning tunneling microscope is based on total internal reflection with Kretschmann-Raether configuration [90,91]. UV-visible light from a laser (or a monochromator) is *p*-polarized through a Glan-Thompson polarizer and is modulated by a mechanical chopper. This polarized light transmits to a cylindrical sapphire prism coated with a thin gold film and then reflects to a photodetector. Total internal reflection can be maximized by adjustment of the incident angle with a rotation stage. The STM tip monitors the evanescently coupled sample

surface on the backside of the prism. The light modulation frequency is confined to the lock-in amplifier to register light-induced signal detection from the sample. Photographs of the photon scanning tunneling microscope setup are shown in Figure 2.4. The scanning tunneling microscope is acoustically isolated by the enclosure shown.

2.2.2.1 Sample holder

Photon scanning tunneling microscopy (Photon STM) utilizes the evanescent wave in order to eliminate heating of the STM tip by direct laser illumination [79,92,93]. The Kretschmann-Rather (KR) geometry is employed for efficient evanescent-wave coupling (Figure 2.5) through a metal layer deposited directly on the TIR interface to prevent energy loss [90,94]. The evanescent field extends only a few hundred nanometers above the Au film (see Figure 2.2), which minimizes the differential thermal expansion of the tip.

We use a half-cylindrical sapphire prism for the sample substrate and for TIR. Total internal reflection occurs on the cylindrical side of the prism. Sapphire transmits in a wide optical range, between ultraviolet (150 nm) and mid-infrared (6000 nm). It is hard, chemically inert, and insoluble in most solvents. The flat side is a c-cut $\text{Al}_2\text{O}_3(0001)$ plane, and serves as the metal evaporation target.

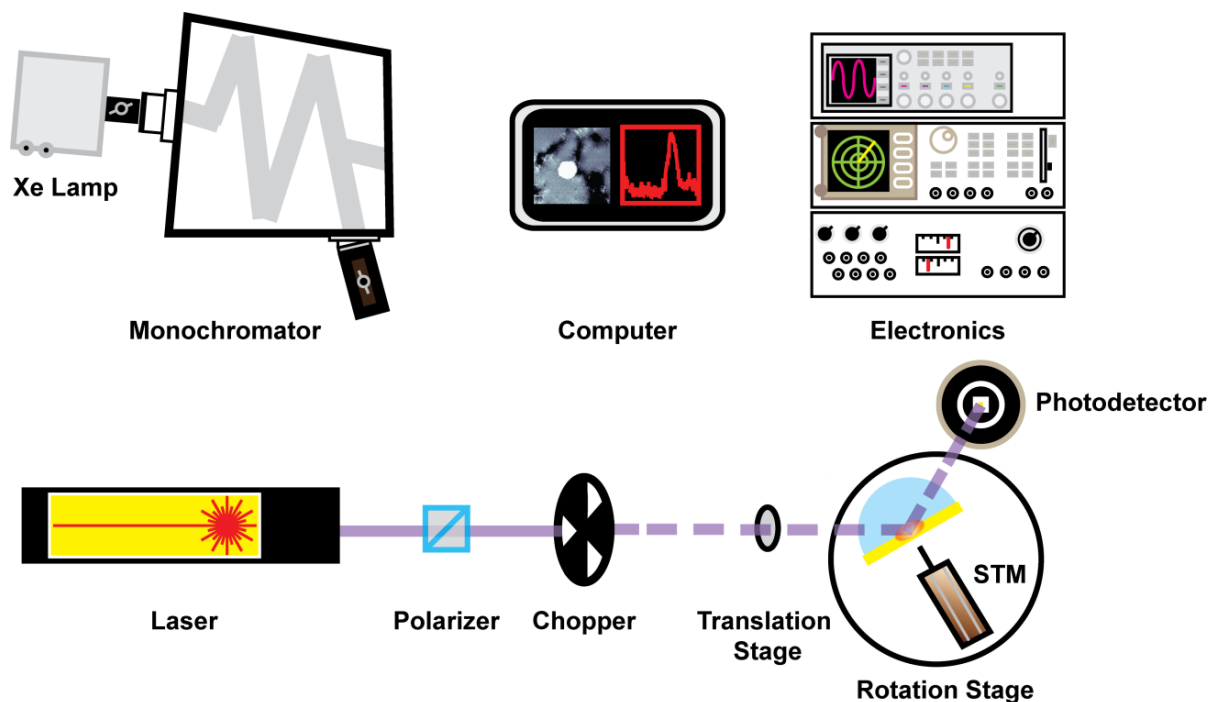


Figure 2.3 A schematic of the photon scanning tunneling microscope setup. A tunable laser or a monochromator with a high-power Xe lamp is used to supply monochromatic light at diverse wavelengths over a range of 200 – 1400 nm. Polarized light and frequency modulation enhance the signal-to-noise ratio. Optical coupling in the tunneling junction is optimized with the Kretschmann-Raether total internal reflection geometry.

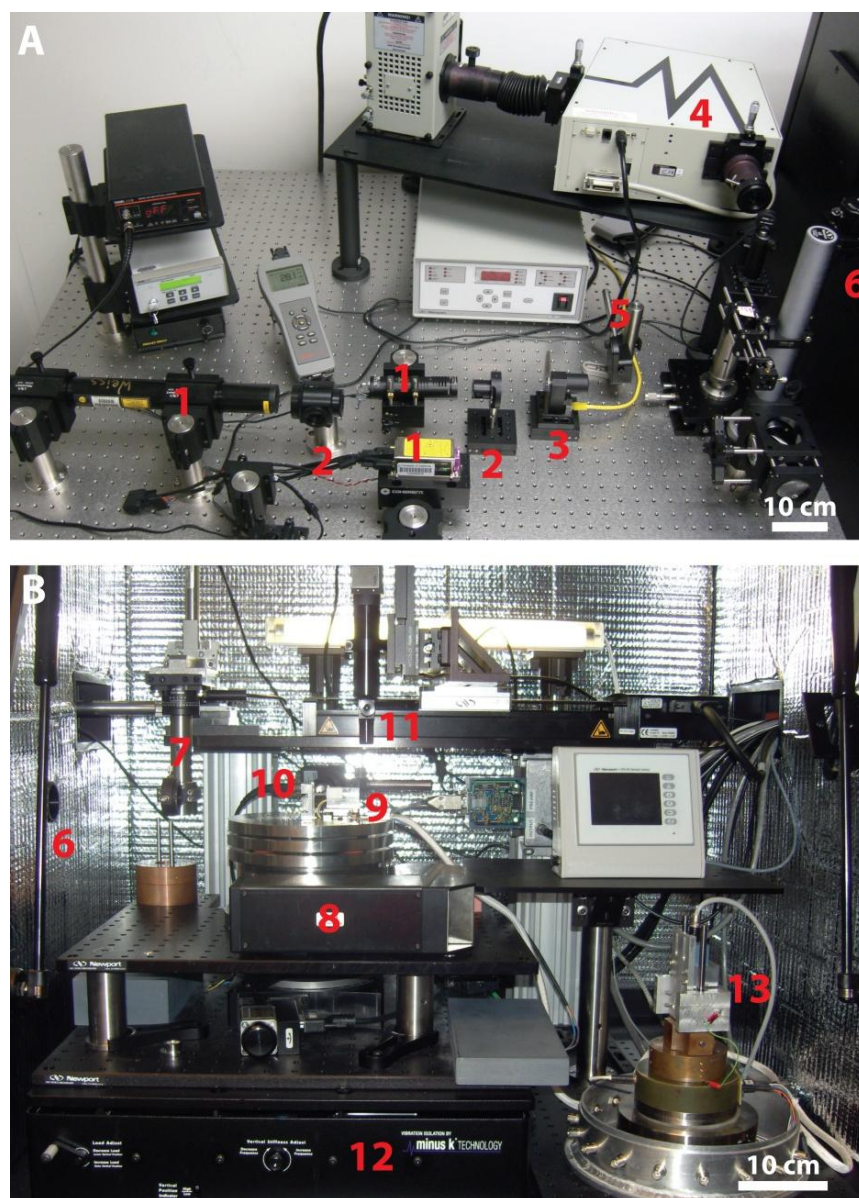


Figure 2.4 Photographs of the photon scanning tunneling microscope setup: (A) lasers with optics and (B) the scanning tunneling microscope part in the enclosure. A light beam from a laser or monochromator (1, 2, 3, and 4) transmits through the window (6) of the STM enclosure. The sample holder and the STM head (9) are placed on stacks of stainless steel plates separated by elastomeric materials to absorb vibration caused by the rotation stage (8). The photon STM components are numbered as follows: (1) lasers, (2) polarizers, (3) a chopper, (4) a monochromator with a Xe lamp, (5) a beam shutter, (6) A window in the STM enclosure, (7) a focusing lens with xyz translation stage, (8) a rotation stage, (9) a STM platform, (10) a photodetector, (11) an optical microscope with translation stages, (12) a vibration isolation table, and (13) a Besocke-style scanning tunneling microscope.

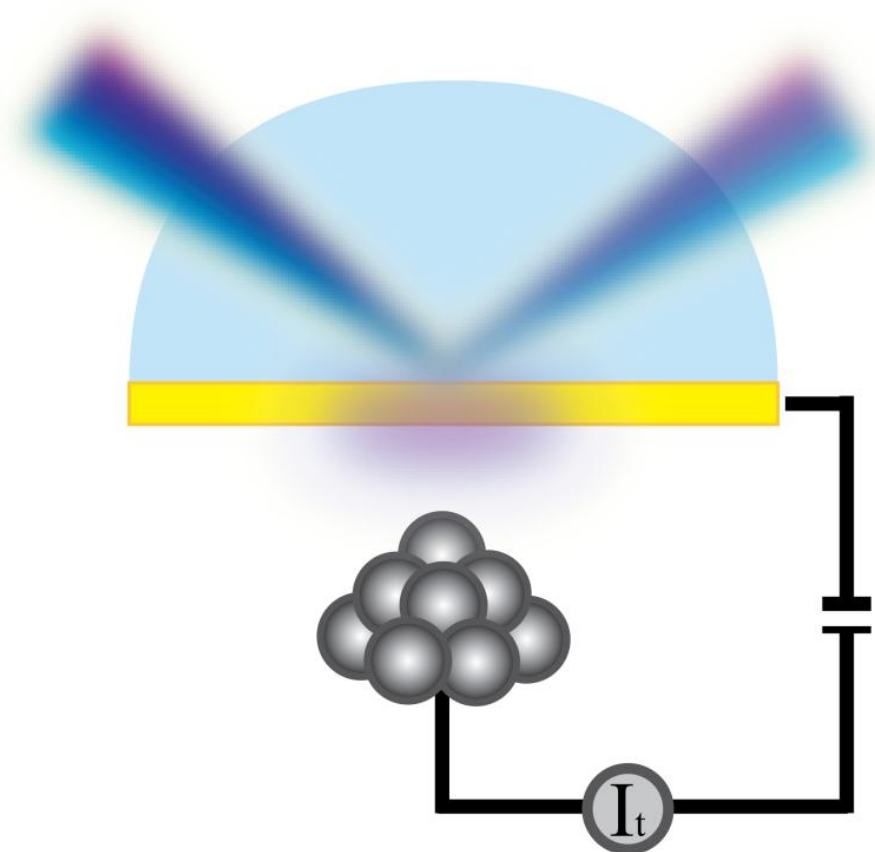


Figure 2.5 A one-dimensional schematic drawing of Kretschmann-Raether configuration in the photon STM. The evanescent wave is generated behind the sample via total internal reflection. The STM tip scans this coupled area and detects the tunneling current (I_t), including components due to photoexcitation.

The sample holder is designed to position the sapphire prism for simultaneous laser irradiation and STM measurements (Figure 2.6). The cylindrical side is open for total internal reflection with the other flat side, Au film exposed to the STM tip for imaging. An optical microscope is placed above the sample holder to monitor laser illumination, and to locate the STM tip at the TIR spot (Figure 2.7). The sample holder is placed on a rotation stage to adjust the angle of incidence. The preamplifier is placed right below the sample holder at the center of the rotation stage to minimize mechanical noise from the sample-stage rotation.

2.2.2.2 STM head

Microslides (Omicron, Taunusstein, Germany) are used for the STM tip approach. The microslide travels up to 5 mm with adjustable step sizes, between 40 and 400 nm. Figure 2.8 shows the STM head mounted on the microslides. The top microslide is for coarse tip approach (z) and the bottom one is for laser spot alignment (x).

A piezoceramic tube (EBL product, East Hartford, CT) is used as the STM tip scanner, and is attached to the front Macor (McMaster, Elmhurst, IL) base of the STM head mount. It is important to have strong attachment between the tube and its base, since we employ a horizontal approach. The head must be carefully balanced - if gravity pulls unevenly on one end, there is substantially increased susceptibility to mechanical noise. Balancing is critical to produce stable tunneling junctions and to reduce mechanical perturbations while scanning.

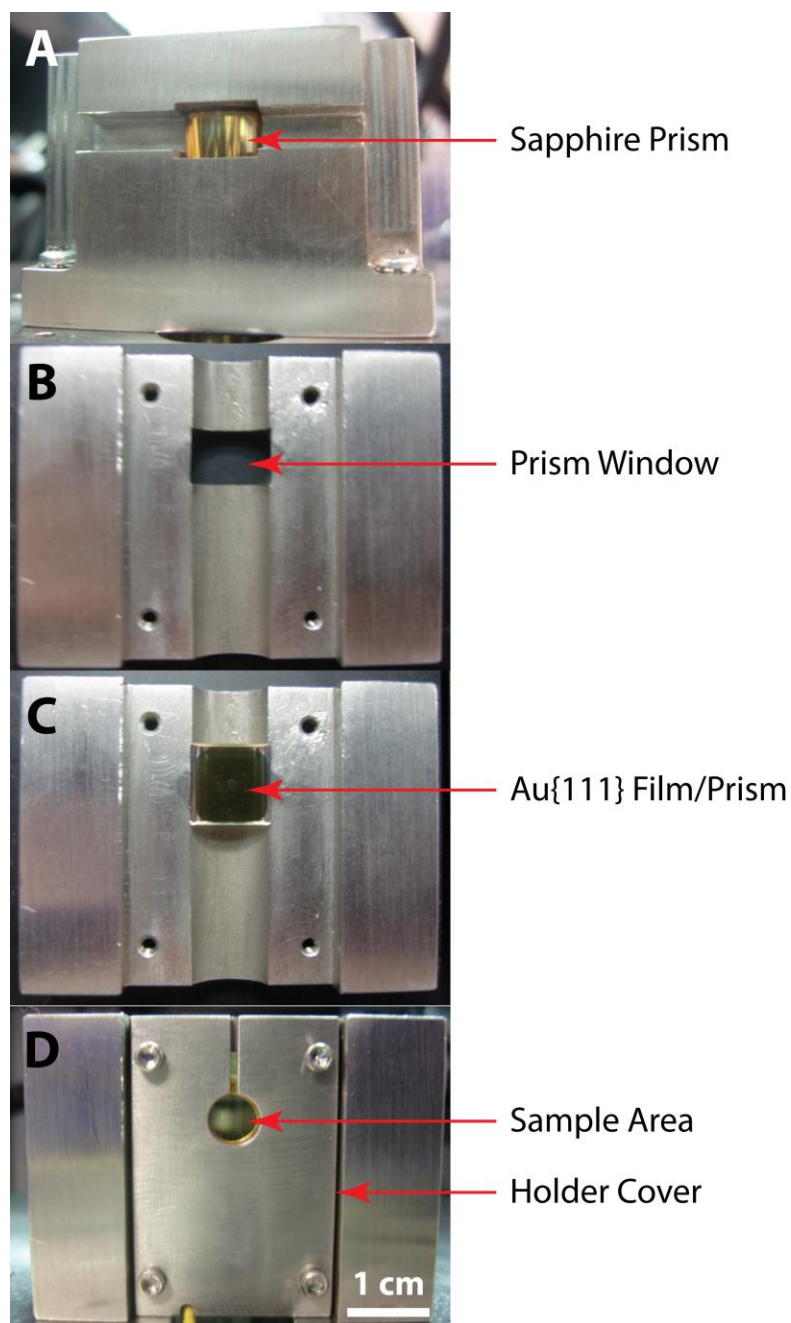
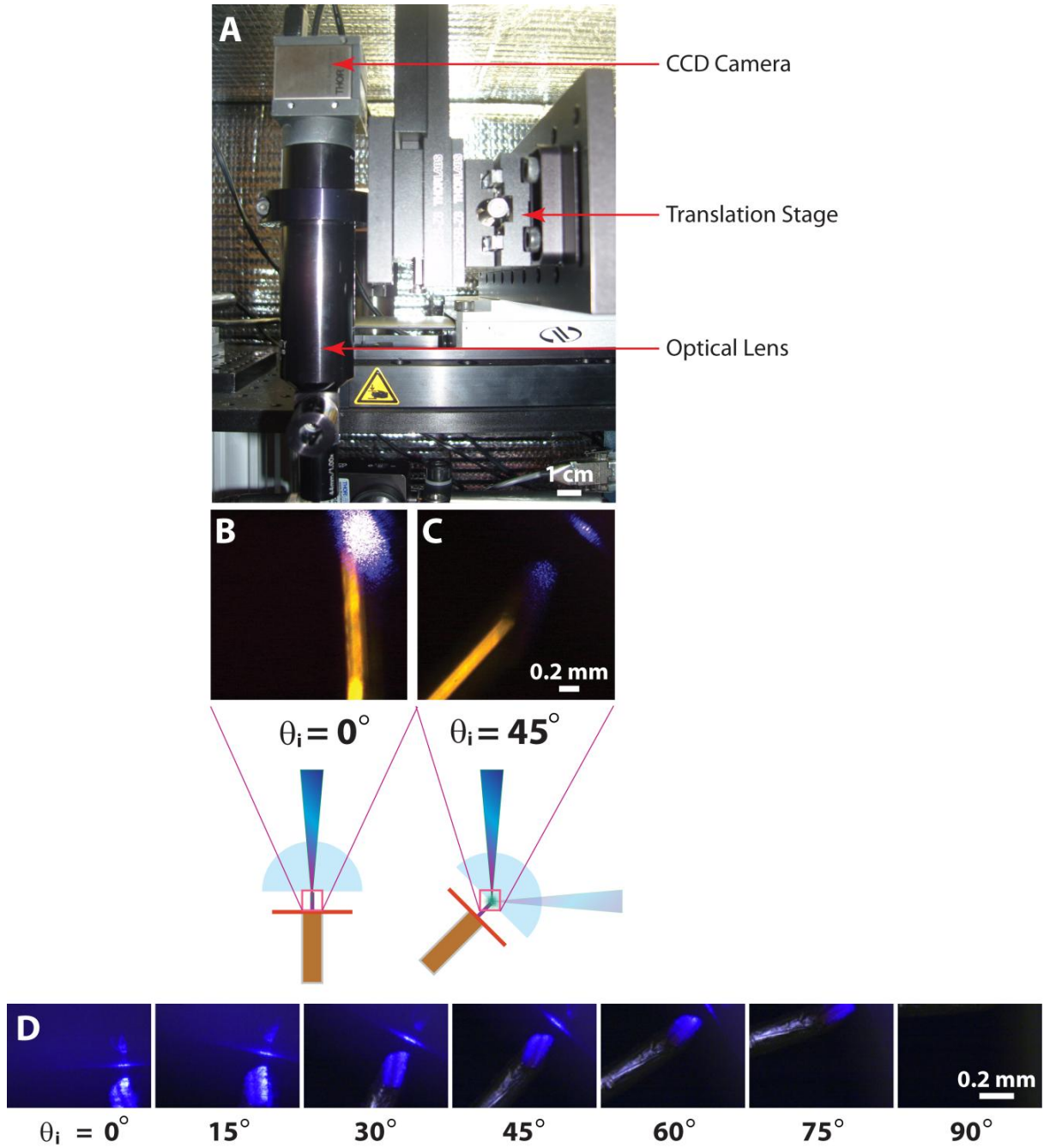


Figure 2.6 Photographs of the sample holder in the photon scanning tunneling microscope. (A) The cylindrical side of the prism is exposed to laser illumination through the prism window. (B) The sapphire prism fits in the machined half-cylindrical relief for high accuracy of rotation and light comes through the prism window for total internal reflection. (C) The flat side of the prism is coated with a Au film and faces the STM head. (D) The holder cover has electrical contact to the Au film surface and the sample area is exposed through the hole to the STM head.



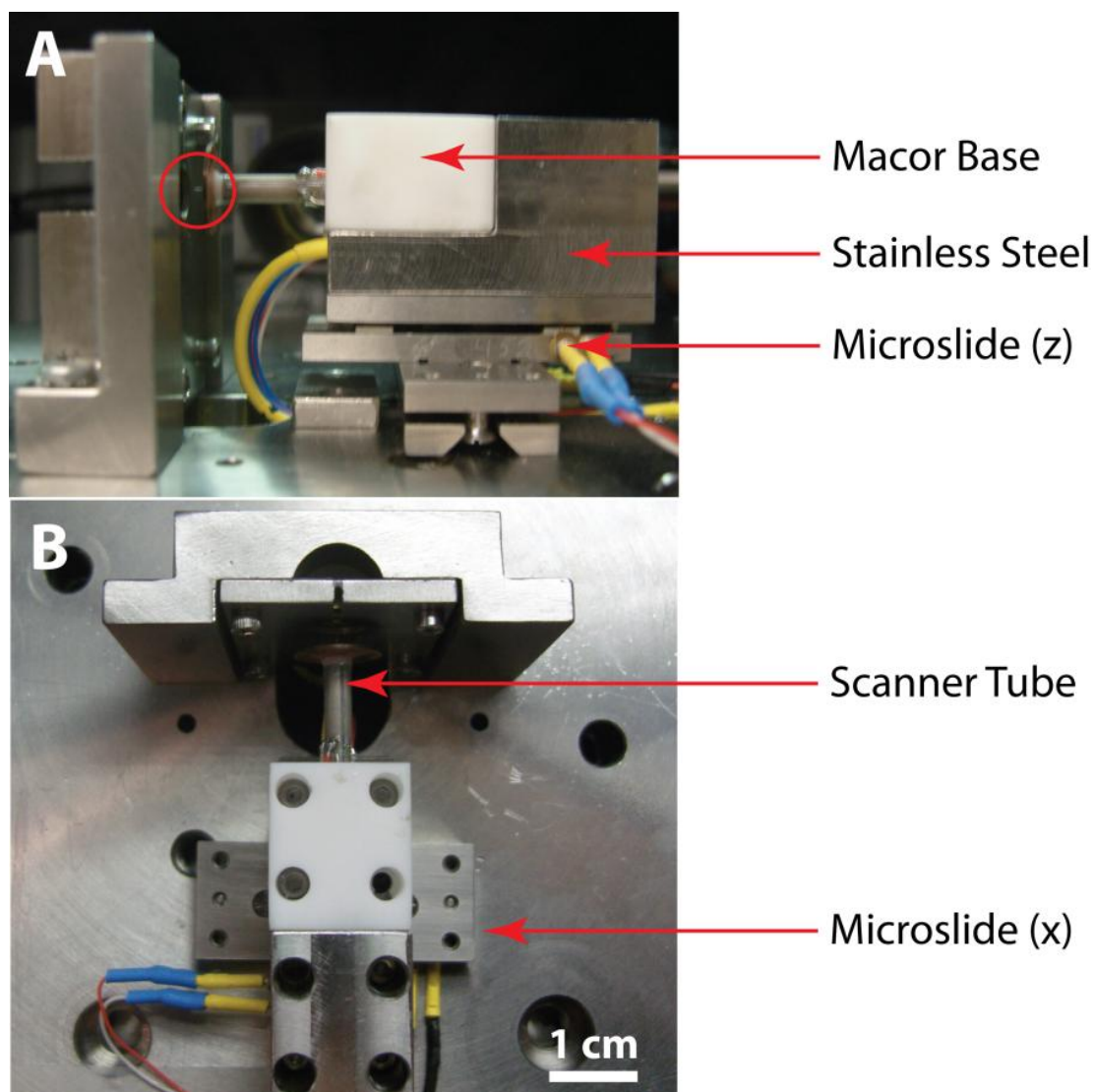


Figure 2.8 Photographs of the photon STM head mounted on the x-z microslides, (A) top view and (B) side view. The STM head faces the sample surface. The top (z) microslide moves the STM tip (circle in A) to the tunneling junction and the bottom (x) microslide adjusts the tip position to the TIR spot.

2.2.3 Substrate preparation

Thin (<50 nm), flat (roughness $\sim 0.3 - 1$ nm_{rms}) epitaxial Au{111} films are deposited on c-cut sapphire cylindrical prisms (Figure 2.9). Half-cylindrical sapphire prisms (1 cm \times 1 cm, 1 cm diameter) with epi-polished c-cut planes, Al₂O₃ (0001) were purchased from Meller Optics (Providence, RI). These substrates were annealed in air at 1100 °C and at 1400 °C for 24 hours in repeated cycles. This thermal annealing cycle heals surface defects from polishing and increases the (0001) terrace size, which substantially affect Au {111} film growth.

2.2.3.1 Thermal annealing on sapphire

Thermal annealing of sapphire substrates at high temperature is a crucial step to obtain atomically flat and ultrasmooth substrates for high-quality thin film fabrication [95]. Single-crystalline α -Al₂O₃ has been used for GaN-thin film growth, as well as for wide-band gap semiconductors for blue-light-emitting diodes [96]. Atomically flat sapphire substrates are expected to enhance epitaxial growth of films with sharp interfaces [97,98]. Among commercially available sapphire substrates with various crystallographic faces, the Al₂O₃ (0001) basal plane is a good candidate substrate for metal and semiconductor thin film growth. Hot thermal treatment tends to decrease the effects of unavoidable miscuts in substrate preparation.

The as-supplied Al₂O₃(0001) substrates show surface irregularity and are contaminated with grease from the commercial epi-polishing procedure (Figure 2.10). Chemical cleaning removes surface contaminants, however such procedures attack surface

defects faster, further roughening surfaces [99]. These sapphire substrates were treated at high temperatures (1100 and 1400 °C) in order to improve the surface flatness.

After heat treatment, c-cut sapphire substrates exhibit a dramatic increase in the prevalence of fine, smooth surfaces with atomically flat terrace (~100 nm wide) and uniform atomic steps (~0.2 nm). Longer annealing (more than 24 hours) at 1100 °C further improves the step edge straightness (Figure 2.11). However, the terrace sizes increase more slowly with the annealing time. Further annealing at 1400 °C doubles the terrace size (Figure 2.12). Annealing only at 1400 °C produces irregular, curved steps, or lopsided terraces (Figure 2.13). Repeated cycling (~10) of annealing at both 1100 and 1400 °C substantially improves the overall substrate quality, including large and atomically flat terraces with uniform atomic steps. Ultimately, the annealed substrates are air stable until metal deposition.

2.2.3.2 Nb seed layer and Au{111} film deposition

Thin Au{111} films were grown on c-cut plane sapphire prisms with using a Nb seed layer [100]. The annealed sapphire substrates were introduced to the ultrahigh vacuum evaporator chamber with a base pressure in the 10^{-10} mbar range, and were outgassed for 1 hour at 150 °C to remove absorbed water. A 2-nm-thick Nb seed layer was evaporated at a rate of 0.15 Å/s at room temperature [101]. The pressure increased to $\sim 5 \times 10^{-9}$ mbar during evaporation. Room temperature deposition favors the Nb(110) orientation over Nb(111), while elevated temperatures (over 800 °C) yield Nb(111) [102,103]. Since the orientation of Au(111) is parallel to Nb(110), the epitaxial relationship between Au, Nb, and c-cut sapphire substrates should follow [101,102,104,105] :

$$Au(111)[0\bar{1}1]||Nb(110)[001]||Al_2O_3(0001)[1\ 0\ \bar{1}0].$$

Thin Au films (40 nm) were then deposited at a substrate temperature of 300 °C and an evaporation rate of 0.5 Å/s. The surface temperature should not exceed 300 °C, to avoid interdiffusion and intermetallic compounds (primarily AuNb₃ and Au₂Nb₃) that occur above 325 °C [106]. The (0001) terraces of α -Al₂O₃ substrate are no longer visible after Au deposition. Figure 2.14 represents a 40-nm-thick Au film deposited on Nb/Al₂O₃(0001). Grains are discontinuous and are much smaller than those observed for Au{111} evaporated on a mica substrate (Figure 2.15).

2.2.3.3 Effect of annealing Au{111}

Substantial improvement of the Au film quality was observed after thermal and hydrogen flame annealing. Thermal annealing of metal films causes diffusion at grain boundaries, allowing them to merge, producing larger grains. Au atoms diffuse during heat treatments between 100 and 400 °C [107]. Evaporated Au layers become smoother, even after annealing at 200 °C in air for 24 hours. This smoothing effect can be maximized by long duration annealing at 400 °C (>15 hours).

Hydrogen flame annealing is another effective way to improve Au film quality [108,109]. Flame annealing removes contaminants from the Au surface and increases the grain size. Flame annealing Au{111}/mica produces contaminant-free Au surfaces with terrace widths increased by a factor of 25 relative to the unannealed films [110]. After Au deposition, Au{111}/Al₂O₃(0001) substrates were routinely annealed at 400 °C for 24 hours, and flame annealed immediately before self-assembly.

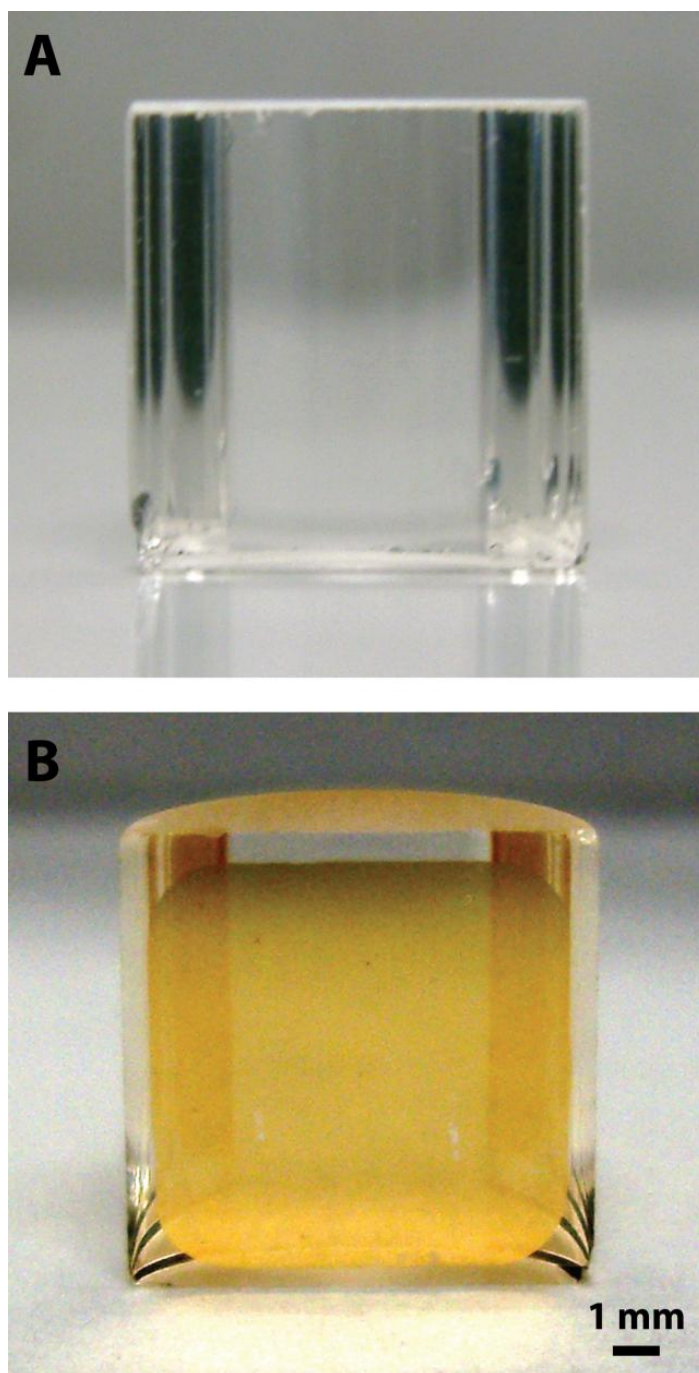


Figure 2.9 Photographs of a cylindrical sapphire prism (A) before and (B) after Au film deposition on the c-cut plane.

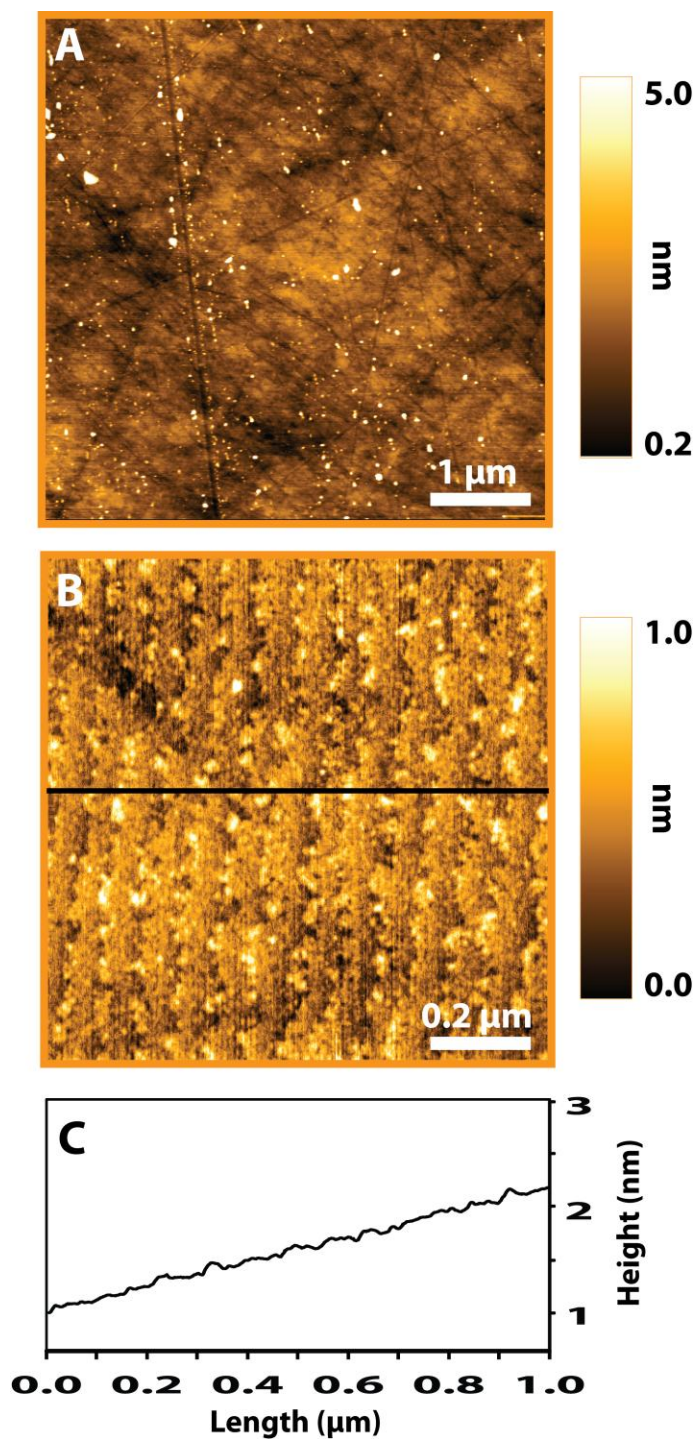


Figure 2.10 Atomic force microscopy images of as-supplied $\text{Al}_2\text{O}_3(0001)$ prisms. The epi-polished surface is irregularly rough and contains grease contaminants. Imaging parameters: (A) Amplitude set point: 220 mV; Drive frequency: 276 kHz; Scan rate: 2 Hz; (B) Amplitude set point: 220 mV; Drive frequency: 75 kHz; Scan rate: 2 Hz. (C) A line profile was taken along the line indicated in the image B. The steps are difficult to distinguish, and are highly curved.

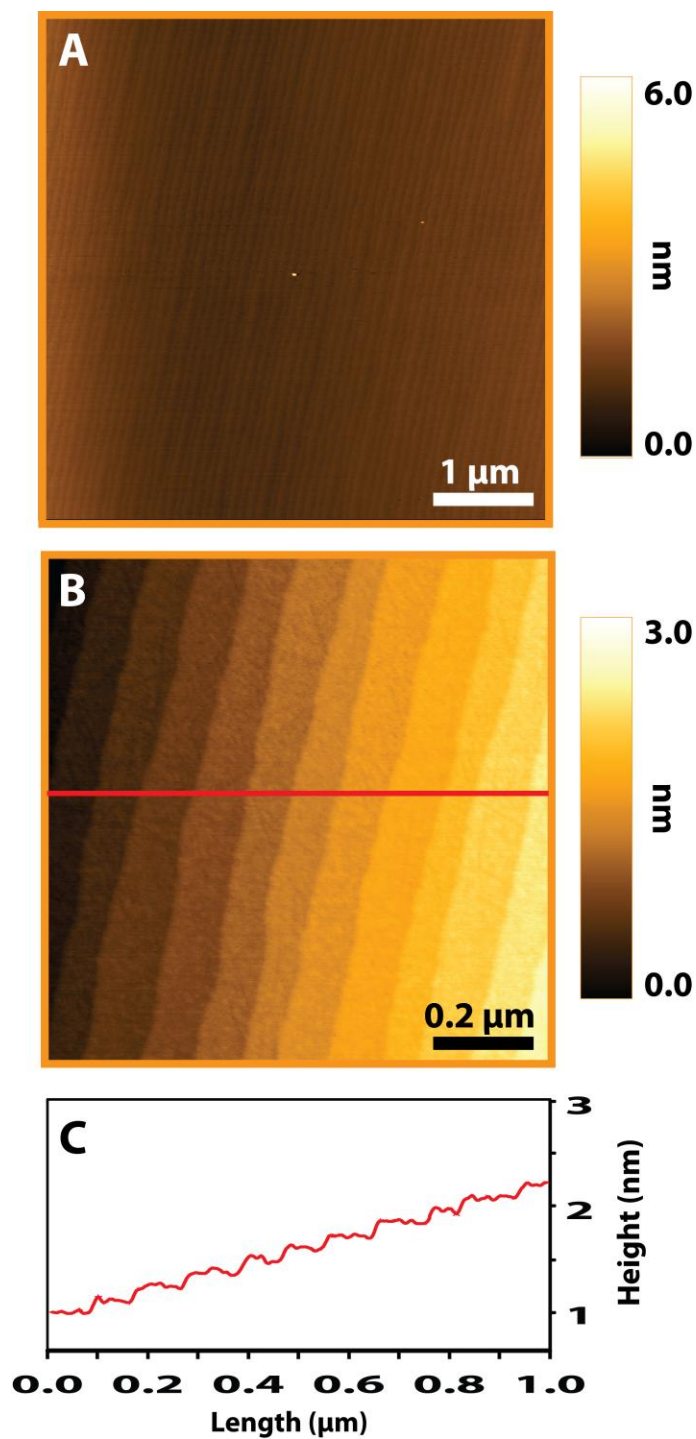


Figure 2.11 Atomic force microscopy images of a $\text{Al}_2\text{O}_3(0001)$ prism after annealing at 1100 °C for 24 hours. Imaging parameters: (A and B) Amplitude set point: 195 mV; Drive frequency: 272 kHz; Scan rate: 2.5 Hz. (C) A line profile was taken along the line indicated in the image B. Thermal treatment smoothes the entire surface, producing atomically flat terraces with straight linear steps.

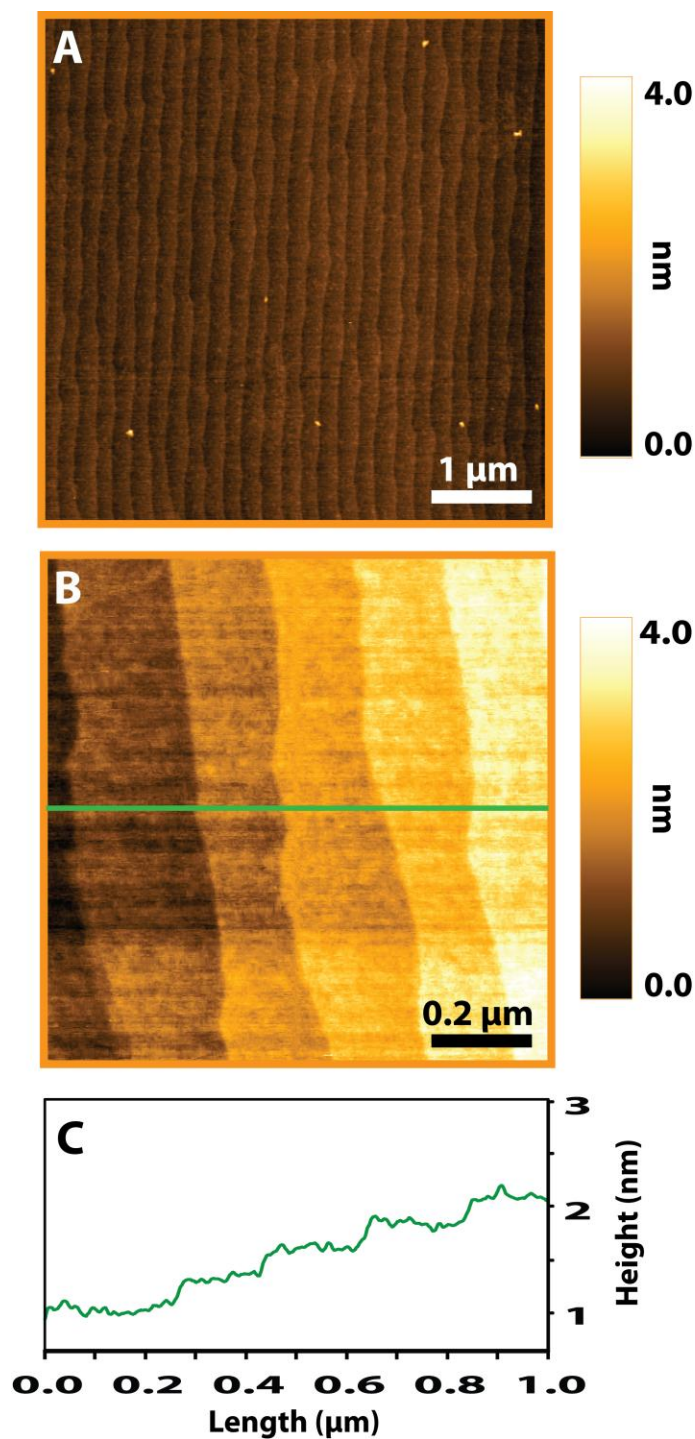


Figure 2.12 Atomic force microscopy images of a $\text{Al}_2\text{O}_3(0001)$ prism annealed at 1400 °C for 18 hours subsequently after annealing at 1100 °C for 24 hours. Imaging parameters: (A and B) Amplitude set point: 420 mV; Drive Frequency: 271 kHz; Scan rate: 2 Hz. (C) A line profile was taken along the line indicated in the image B. Further heat treatment at 1400 °C after 1100 °C annealing doubles the terrace size.

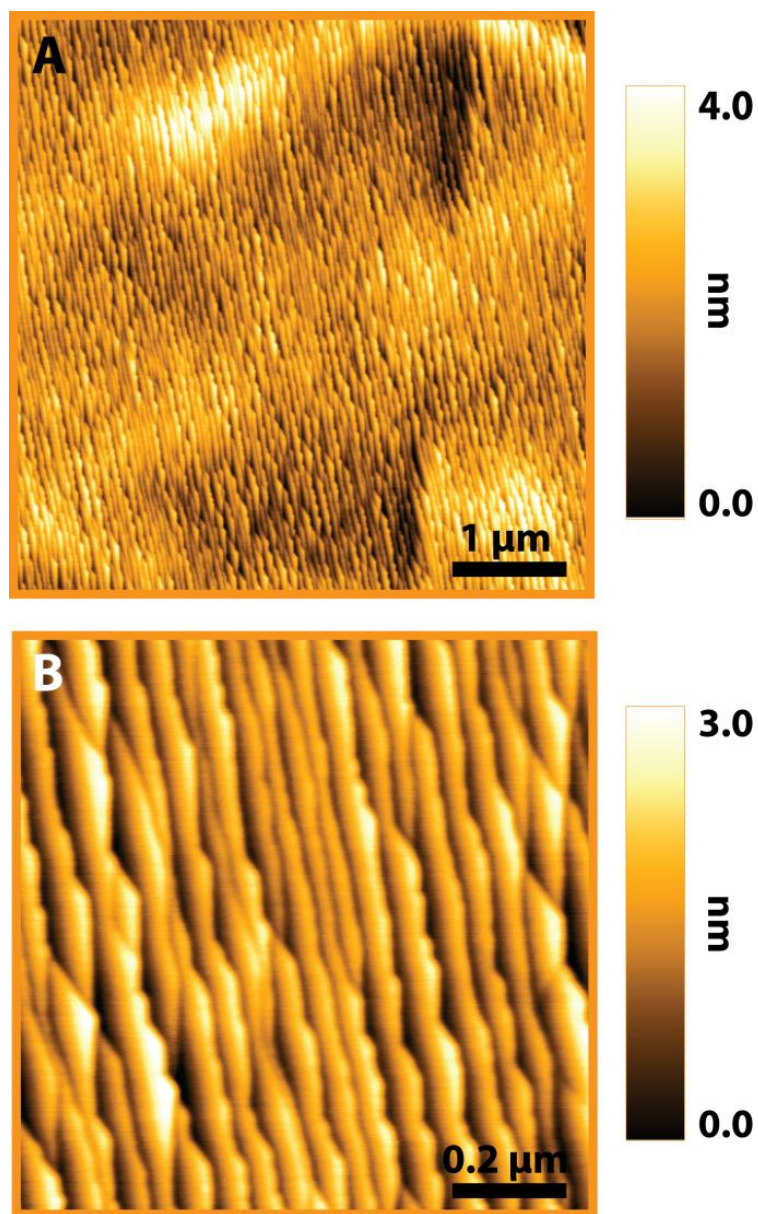


Figure 2.13 Atomic force microscopy images of a $\text{Al}_2\text{O}_3(0001)$ prism annealed only at 1400°C for 24 hours. Imaging parameters: (A and B) Amplitude set point: 580 mV; Drive frequency: 276 kHz; Scan rate: 2.5 Hz. Long annealing at 1400°C creates irregularly shaped step edges.

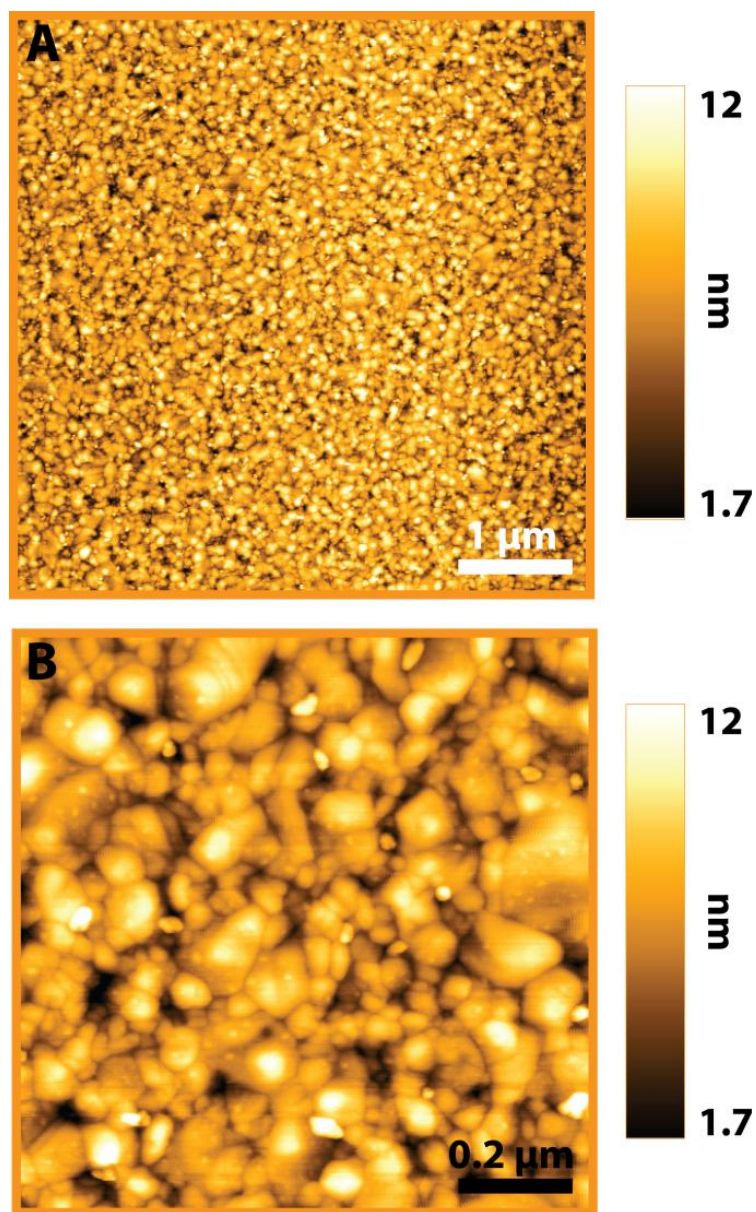


Figure 2.14 Atomic force microscopy images of a 40-nm-thick Au{111} film deposited on 2-nm-thick Nb on a $\text{Al}_2\text{O}_3(0001)$ prism. Imaging parameters: (A and B) Amplitude set point: 195 mV; Drive frequency: 272 kHz; Scan rate: 2.5 Hz. Small grains and large gaps around grain boundaries are mainly observed.

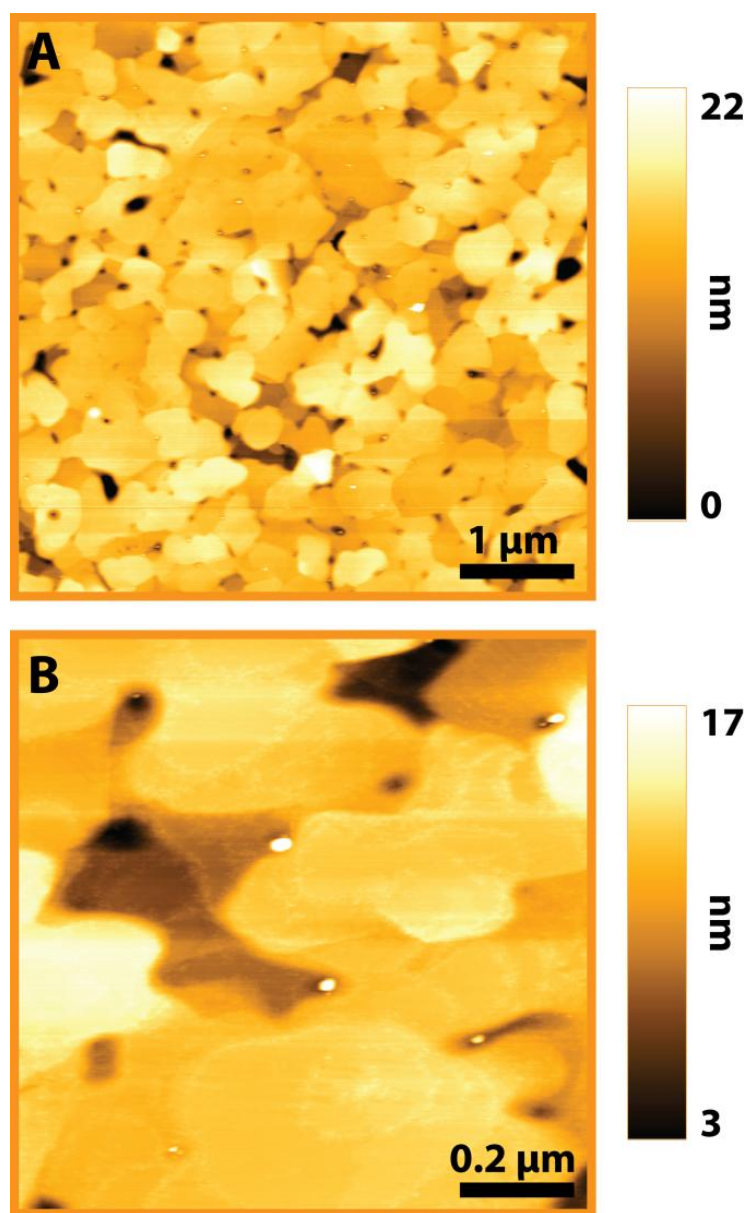


Figure 2.15 Atomic force microscopy images of a 150-nm-thick Au{111}/mica substrate (Agilent, Santa Clara, CA). Imaging parameters: Amplitude set point: 254 mV; Drive frequency: 75 kHz; Scan rate: 2.5 Hz. The grains are much larger than those for Au films grown on Al₂O₃(0001) substrates and the Au{111} terraces are atomically flat.

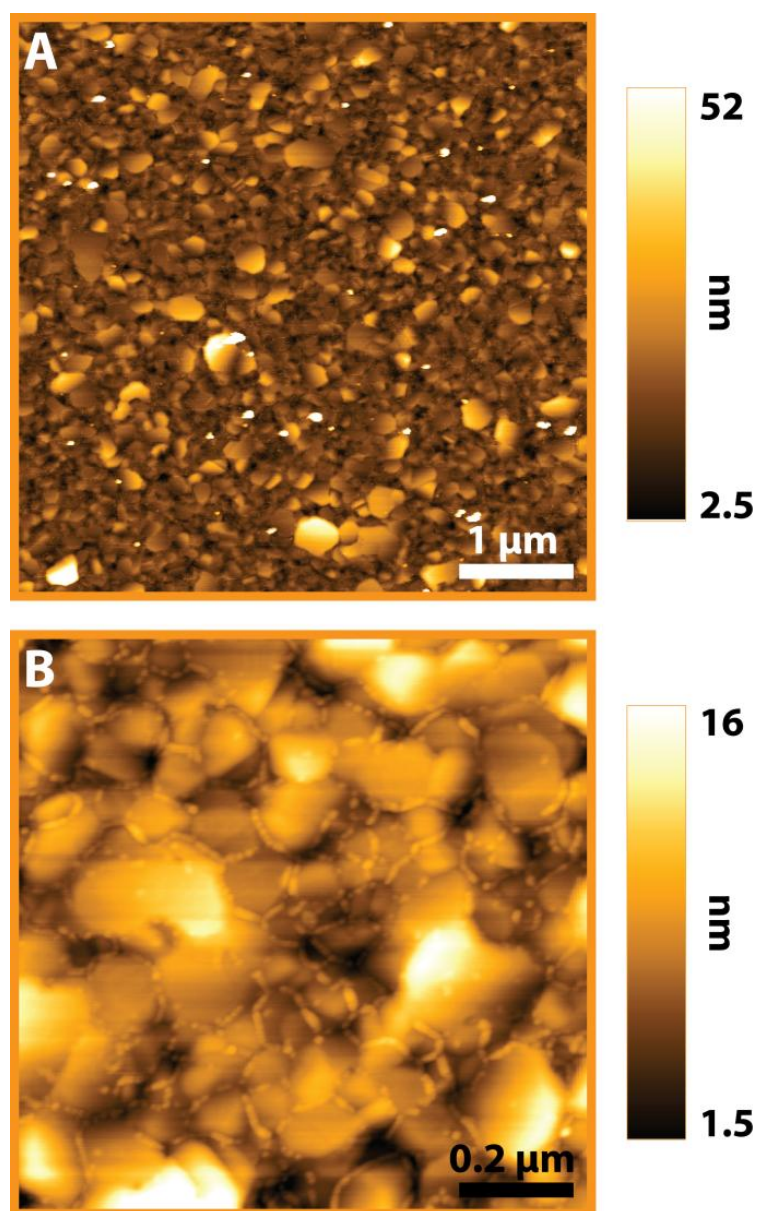


Figure 2.16 Atomic force microscopy images of a 40-nm-thick Au{111} film deposited on 2-nm-thick Nb on a $\text{Al}_2\text{O}_3(0001)$ prism after thermal annealing at 400 °C for 18 hours. Imaging parameters: (A and B) Amplitude set point: 450 mV; Drive frequency: 270 kHz; Scan rate: 2.5 Hz. Thermal annealing at 400 °C increases the grain sizes and generates many large flat terraces. Small round islands between grains are attributed to Au residue from migration during annealing.

2.2.4 Light modulation

Light modulation with lock-in amplification brings significant improvement to detection efficiency by elimination of non-linear system responses to the light, such as photothermal noise [111] or electric field oscillation in the tunneling junction [112]. The laser light is modulated by a mechanical chopper, and the reference signal is locked onto the modulation frequency. In order to avoid tip/sample acoustic mode enhancement by modulation, the modulation frequency was carefully selected by monitoring each tip with a spectrum analyzer over the range 1.8 – 2.4 kHz [113]. At modulation frequencies greater than the 1 kHz or lower bandwidths, the STM feedback system cannot respond, eliminating drift problems or modulation as a noise source [114]. The photoinduced tunneling current was measured using a lock-in amplifier (LIA) X-Y output. Scanning tunneling microscopy imaging is carried out in constant-current mode, simultaneously collecting topography and LIA output from each scan.

Imaging is typically performed at a -1.0 V sample bias voltage with a 1 pA tunneling current. The LIA time constant is set to be 3 ms with the same point delay for imaging. The probe tip condition determines the optical LIA parameters including sensitivity (fs), amplitude (V_{rms}), and dynamic reserve (dB). The tip was left in tunneling range for several hours prior to light modulation experiments to stabilize the piezoelectric drift due to hysteresis.

2.3 Results and Discussion

2.3.1 *n*-Alkanethiolate self-assembled monolayers on Au{111}/Al₂O₃(0001)

Self-assembled monolayers of *n*-dodecanethiol on Au{111} films on sapphire prisms show typical *n*-alkanethiolate SAM features such as substrate vacancy islands, step edges, and domain boundaries. However, the average terrace size is ~ 500 Å, which is much smaller than that for high-quality Au on mica (~ 1500 Å). Even after thermal and flame annealing, the sample roughness, especially between individual grains, is relatively high. Small terraces with many steps are frequently observed (Figure 2.17A). This reduces tunneling junction stability, reducing image quality and causing a higher incidence of tip crashes. However, high resolution STM images (Figures 2.17B and C) show that C12 SAM features and its molecular packing are identical to those on Au{111}/mica.

We utilize *n*-alkanethiolate monolayers on Au{111}/Al₂O₃(0001) as a matrix for photoconductance or photocurrent measurements of single organic molecules. The height of the matrix can be tuned by altering the alkyl chain length to support the light absorbing organic molecules properly, at which the matrix is slightly lower than the inserted molecules. The stability of the SAM matrix is critical to resolve their intrinsic photoinduced activities, excluding any outside systematic effects such as heating, electric field, and non-linear harmonic oscillation. Two examples of photon STM applications are described in the following chapter.

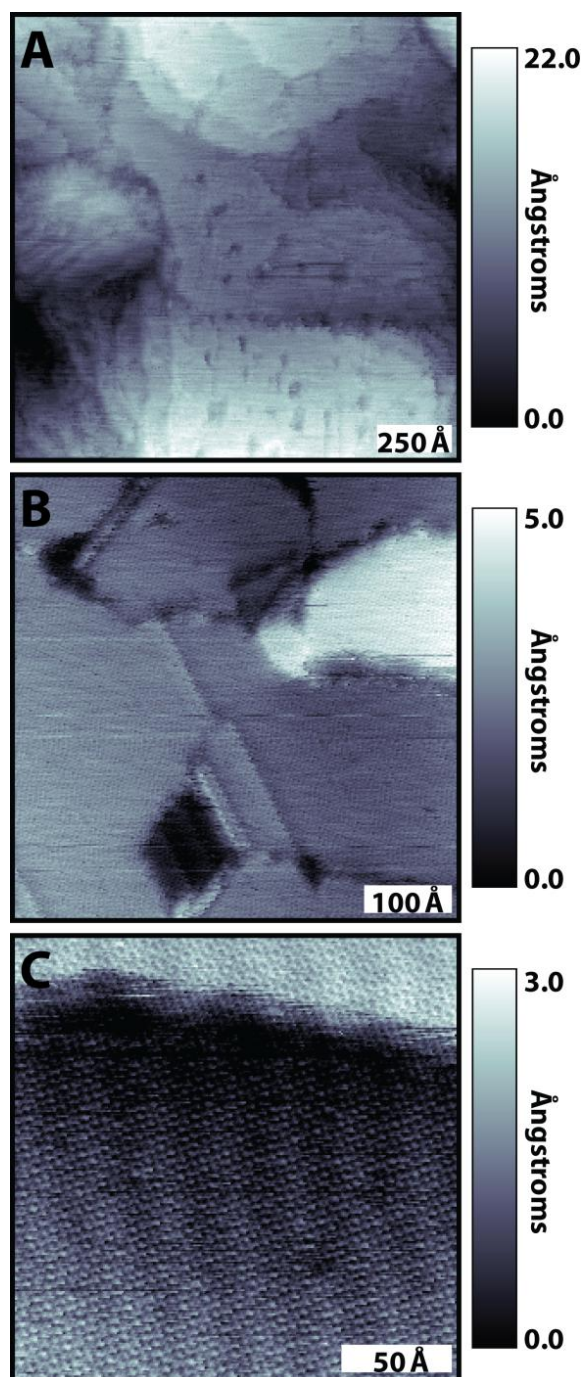


Figure 2.17 Scanning tunneling microscopy images of *n*-dodecanethiolate (**C12**) monolayers assembled on Au{111}/Al₂O₃(0001) substrates. Imaging conditions were sample bias voltage -1.0 V and tunneling current 1.0 pA. The average terrace size is much smaller than for typical **C12** SAMs on Au/mica. Terraces appear tilted in random orientations, and narrow terraces with many steps are often observed in large scan areas. Hexagonal close packing and the presence of SAM characteristics including vacancy islands, domain boundaries, and step edges indicate that there are no systematic differences from **C12** SAMs on Au{111}/mica.

2.3.2 Single-molecule detection

2.3.2.1 C₆₀-tethered 2,5-dithienylpyrrole triad

A rigid C₆₀-tethered 2,5-dithienylpyrrole triad (its molecular structure is shown in thiolate form in Figure 2.18A) is designed for efficient photocurrent generation [115]. The electron-rich π -conjugated 2,5-dithienylpyrrole acts as an electron donor after light absorption, with extended lifetime of the charge-separated state, due to its low oxidation potential [116,117]. The phenylethynyl moiety provides a rigid framework for a stable and conducting connection to a Au substrate (or other contact). Two fullerenes were attached to both ends of the electron-rich chromophore to act as electron acceptors. This arrangement prevents C₆₀ from blocking the chromophore for light absorption. The two C₆₀ acceptors and the 2,5-dithienylpyrrole chromophore are spatially separated, improving light conversion efficiency.

The C₆₀-tethered 2,5-dithienylpyrrole triads are inserted into well-ordered **C12** SAMs on Au{111}/Al₂O₃(0001) substrates (Figure 2.18B to D). Molecules are isolated singly, in pairs, and in groups depending on the order of the SAM matrix [118]. The loosely packed **C12** SAM matrix is prepared by short-duration self-assembly at room temperature, and contains more defect sites where groups of molecules are inserted (Figure 2.17B). Fewer molecules insert into more tightly packed **C12** matrices (assembled at high temperatures, Figure 2.17C and D). A compact matrix ensures a stable molecular conformation. Frequent conductivity changes are attributed to molecular motion, Au-S bond hybridization changes, and substrate place-exchange [30,119].

Photon STM enables us to map photocurrent generation of isolated triad molecules on surfaces [120]. We can position the STM tip at single triads, and measure current responses on variation of the sample bias voltage (scanning tunneling spectroscopy). The current-voltage (I/V) spectra can be obtained when the light is off and on, producing dark current and photocurrent plots for the same molecule in the same environment. Consequently, the quantum efficiency of photovoltaic activity on single C₆₀-triad molecules will be determined. This experiment is ongoing and is described schematically in Figure 2.19.

2.3.2.2 9-(4-Mercaptophenylethynyl)anthracene

The anthracene derivative, 9-(4-mercaptophenylethynyl)anthracene (**MPEA**), shown in Figure 2.20A, is a candidate for a molecular electronic device. This highly conjugated molecule contains a delocalized π network, which provides a pathway for electron conduction. This rigid molecular wire can be easily assembled onto Au substrates and is highly ordered by strong π -stacking interactions [34,121].

To measure **MPEA** photoconductance, **MPEA** molecules were inserted into a **C12** SAM on Au{111}/Al₂O₃(0001) (Figure 2.20A). Insertion is restricted to step edges and domain boundaries due to the highly ordered and compact **C12** matrix (prepared via vapor deposition at 78 °C for 24 hours). In STM images, inserted molecules appear to protrude from the surrounding **C12** SAM matrix, both because they are longer than the matrix molecules and because of their higher conductivity [34]. The UV-visible absorption spectrum of **MPEA** shows a strong absorption at 405 nm (Figure 2.20B). A 405-nm diode laser was coupled evanescently to the photon STM junction. The STM tip was then translated to the evanescent coupling spot. The STM platform, including the sample holder, was rotated to $\theta = 45^\circ$ where

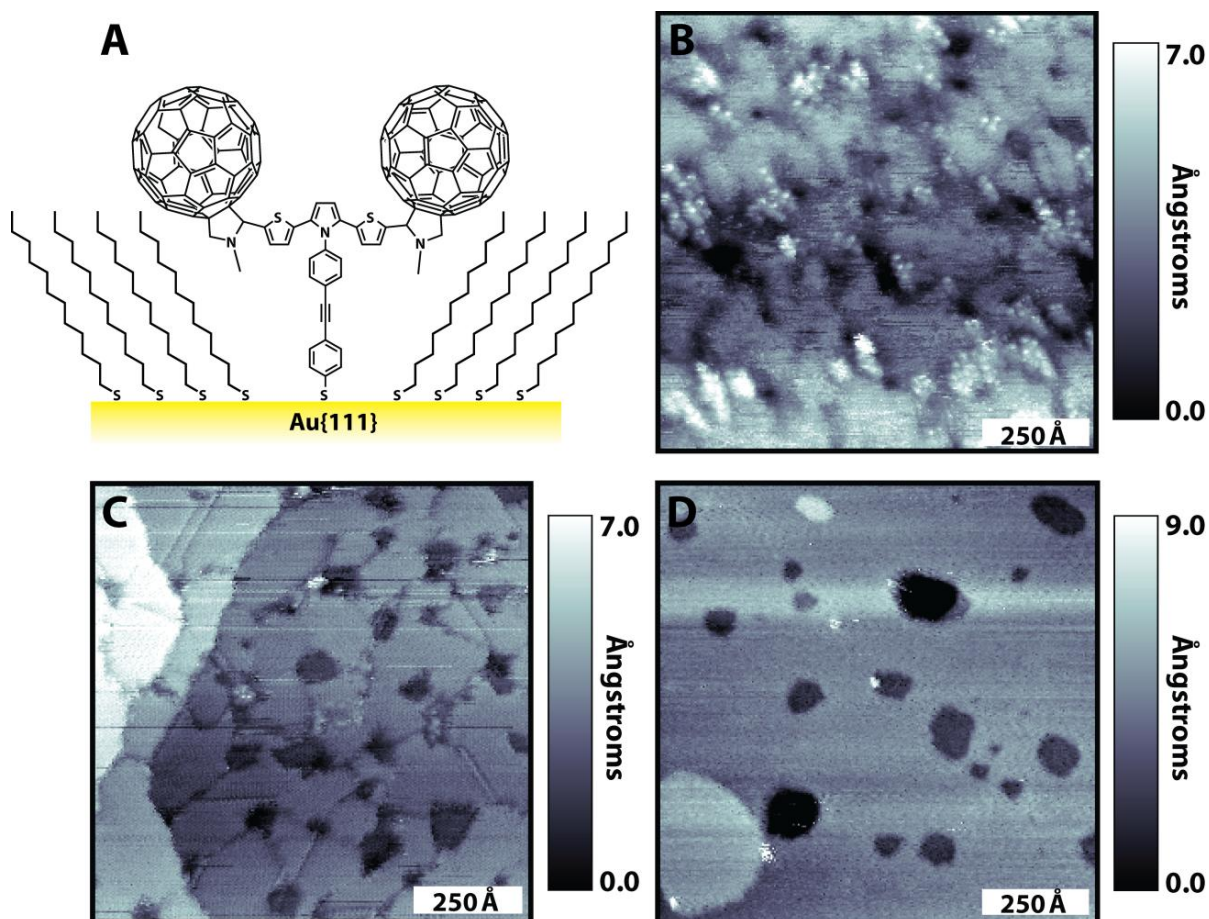


Figure 2.18 (A) A schematic drawing and (B to D) STM images of C₆₀-tethered 2,5-dithienylpyrrole triad molecules inserted into **C12** SAM matrices on a Au{111}/Al₂O₃(0001) prism. **C12** SAM matrices were prepared in solution (B) at room temperature for 30 minutes, (C) at 70 °C for 4 hours, and (D) in vapor phase at 78 °C for 24 hours. The distribution of inserted C₆₀-triad molecules substantially decreases in tight **C12** SAM matrices. Imaging conditions were sample bias voltage –1.0 V and tunneling current 1.0 pA.

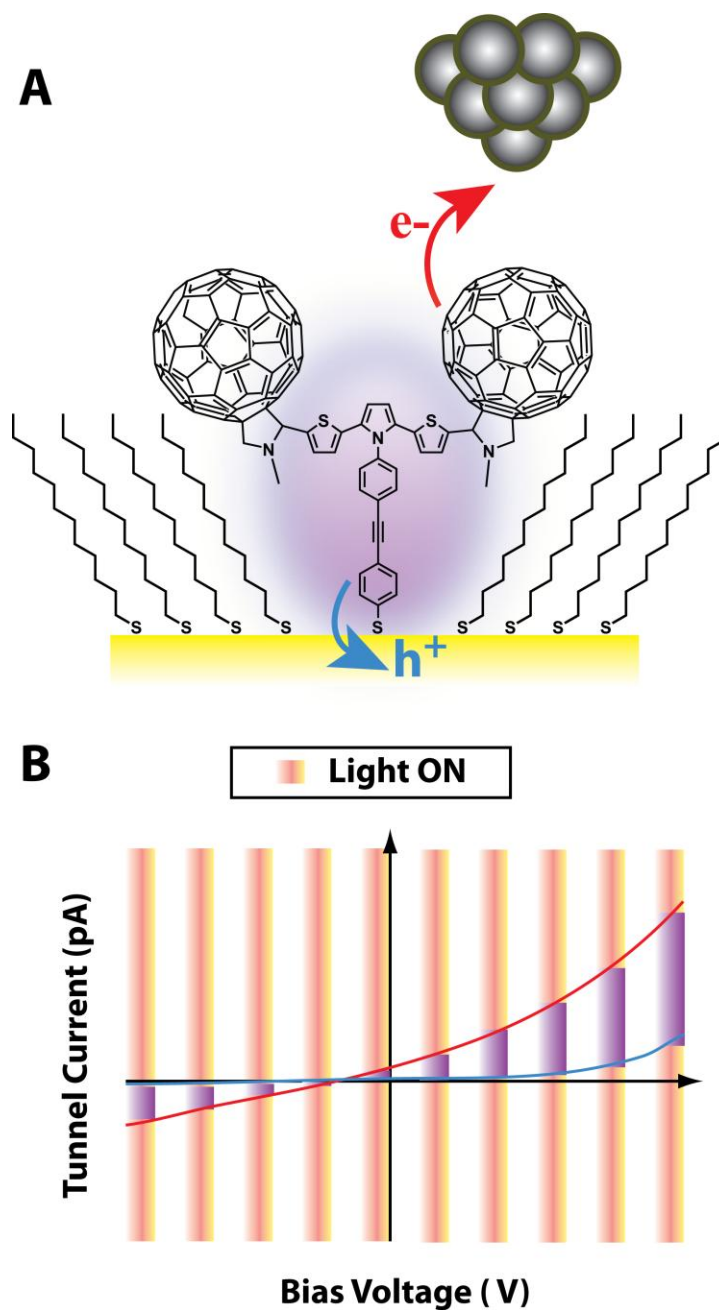


Figure 2.19 Schematic illustration of photovoltaic efficiency measurements on a single triad molecule with photon STM. (A) 2,5-dithienylpyrrole chromophore is excited by the evanescent wave ($\lambda = 405$ nm). Electrons are subsequently transferred to the fullerene after charge separation and can be measured by the STM tip. (B) Light-modulated scanning tunneling spectroscopy can determine illuminated (red line) and dark (blue line) current-voltage characteristics on single triad molecules [122].

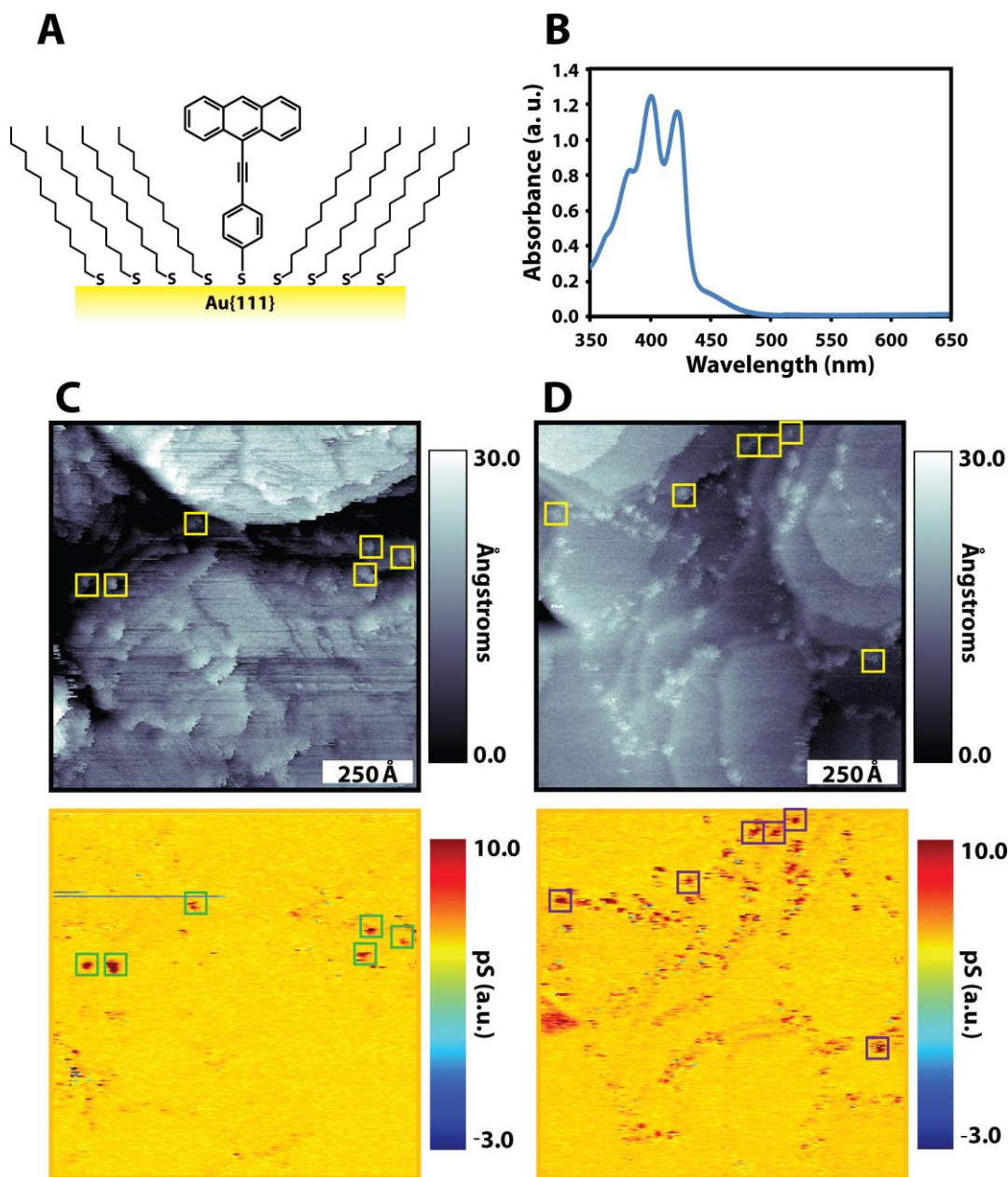


Figure 2.20 (A) A schematic drawing of a 9-(4-mercaptophenylethynyl)anthracene (**MPEA**) molecule inserted into a *n*-dodecanethiolate (**C12**) SAM on a Au{111} surface. (B) Ultraviolet-visible absorption spectrum of **MPEA** (100 μM) in ethanol solution. (C and D) Scanning tunneling microscope topographic images (top) and simultaneously recorded photoconductance maps (bottom) of isolated **MPEA** molecules in a **C12** monolayer on a Au{111}/Al₂O₃(0001). Molecules along step edges and on lower terraces were more sensitive to the 405 nm light absorption. Imaging conditions were sample bias voltage −1.0 V and tunneling current 1.0 pA.

the maximum evanescent field enhancement occurs on the sample substrate. Resultant electronic excitation of isolated **MPEA** molecules within the **C12** SAM matrix resulted in significant increases in photoconductance. No equivalent increase was found for the matrix providing an internal control for artifacts due to thermal effects.

While the STM tip is imaging the surface, the sample surface is illuminated by the laser at 405 nm (1.4 mWcm^{-2}) modulated at 1.8 kHz. The topography (Figure 2.20C and D, top) and the photoconductance map (Figure 2.20C and D, bottom) were measured simultaneously. Isolated **MPEA** molecules respond to illumination by 405 nm light. The increase in the modulated signal is attributed to the electronic excitation of **MPEA** molecules by UV irradiation. More intense absorption was observed along step edges (see colored boxes in Figure 2.20C), attributed to enhanced charge transfer across the step edges [123,124]. Molecules embedded in lower Au terraces tend to show higher signal intensities, while the terrace height does not affect the lock-in image contrast (see colored boxes in Figure 2.20D). Molecules on the same terrace will be examined to test the effects of the possible near-field enhancement of the evanescent wave [125].

2.4 Conclusions and Outlook

The photon STM presented here is uniquely designed to measure photocurrent or photoconductance of isolated organic molecules on surfaces. It also allows us to conduct photochemical reactions of organic molecules in controlled and stable environments, which will be discussed in detail in Chapter 3. Preliminary data show that the system is stable and can resolve the photoinduced effect of single molecules by phase-sensitive lock-in detection.

Improvements in Au{111} substrate quality and piezoelectric thermal drift will improve imaging characteristics.

This microscope is universal and can be easily modified to add further capabilities. For example, it is possible to study the surface plasmon resonances of individual metal nanoobjects including nanoclusters [31,126], nanotriangles [127,128], and nanocages [129,130]. Photon STM can detect local details of topographic and optoelectronic differences with sub-nanometer precision. It can also be applied to liquid systems to study biological specimens. Photon STM measurements do not require fluorescence tags and can be used to measure photoinduced charge transport within single biomolecules, such as DNA [131,132].

Most importantly, photon STM can serve as a diagnostic tool to measure the intrinsic photovoltaic efficiency of single organic molecules for solar cell applications. Among the most promising candidates for efficient organic photovoltaic devices are dyads and triads, in which light harvesting electron donors are covalently attached to electron acceptors [133,134]. By investigating those molecules with photon STM, we can obtain fundamental insight into the photovoltaic effect with molecular resolution and provide direct figures of merit for energy conversion. These studies will provide important design principles and feedback for organic chemists, and help to determine key components for efficient light conversion. Candidate molecules must first be fundamentally understood and objectively compared at the molecular level for photovoltaic efficiency prior to device fabrication. Using photon STM, we optimize molecular design, diagnose intrinsic problems, and separate them from other extrinsic efficiency factors such as charge recombination, hole-electron mobility differences, and charge collection. As interfaces dominate complete photovoltaic devices, using this strategy we can address and optimize specific designs of molecules before device assembly.

Other light sources can be used to expand the capabilities of the photon STM, such as infrared light for vibrational information of molecules. Multiple wavelengths of light can be introduced simultaneously to resolve samples that contain mixtures of molecules. Two-photon and time-resolved pulse-probe experiments are also accessible. Photon STM can thus be used to improve our understanding of a wide range of chemical systems.

Our instrument configuration takes advantage of full access to the sample surface. Light illumination is isolated from the sample side. This facile access to the sample surface will enable multi-probe experiments to characterize simultaneously photothermal effects, fluorescence, and light scattering in the near field [135-137].

Chapter 3. Creating Favorable Geometries for Directing Organic Photoreactions in Alkanethiolate Monolayers

3.1 Introduction

Regioselectivity of organic reactions is critically important for organic synthesis, and a wide variety of strategies are used to restrict the geometry of approaching reactants in solution to favor the preferred products (for example, bulky ligands on metal complex catalysts to direct incoming reactants). Geometric control can also be exerted in solution by encapsulating reactants in host-guest complexes. In the context of surface reactions, the formation of adsorbed monolayers can restrict the relative motion of molecules and may afford a route to regioselective chemistry. For example, *n*-alkanethiolate self-assembled monolayers (SAMs) on gold surfaces have been used to prepare well-defined matrices for studying molecules or nanoparticles in locally controlled environments [29,31,138]. The stability, simple fabrication, and fundamental understanding of alkanethiolate SAMs provide an excellent system to control the placement, orientation, and reactions of molecules. Here, we detail our strategy to control molecular placement and environment, enabling selection of a photocycloaddition reaction that is geometrically unfavorable in solution yet allowed by selection rules, the [4+4] between adjacent 9-(4-mercaptophenylethynyl)anthracene (**MPEA**, Figure 3.1) molecules on a Au surface. A thiol form of 9-phenylethynylanthracene (**PEA**) is readily inserted singly, in pairs, or in groups into the defects of preformed alkanethiolate SAMs [119,139,140]. The rigid spacer, phenylethynyl backbone was buried with Au-S surface attachment, leaving anthracene exposed at the surface of the alkanethiolate monolayer. Precise control over the

molecular assembly enables us to trap molecules in an environment where they are constrained to undergo a regioselective [4+4] cycloaddition under ultraviolet (UV) illumination, and imaging with a scanning tunneling microscope (STM) enables us to screen for molecules in well-defined environments.

Using the STM to track reactions between upright, photoreactive molecules inserted in SAMs in situ is complicated by the dynamics of the individual molecules. Inserted molecules display frequent changes in apparent height, commonly referred to as stochastic switching [118,141], while imaging under illumination can cause electronic excitation or reactions in the molecule [142-145]. The aromaticity and photoreactivity of anthracene make it an important candidate material for organic electronics, optoelectronics, and surface photochemistry [146-149]. Detailed studies of 2-anthracenethiolate (Figure 3.1, shown as the thiol) SAMs on gold emphasize the importance of structure, phase, and stability [150]. Exposure to ultraviolet (UV) light induces distinct structural changes by dimerization within the monolayer [151]. However, the close proximity of the anthracene moiety to the Au surface and the perpendicular orientation of the anthracene moiety to the substrate limit SAM ordering and stability, and trap molecules in unfavorable arrangements for photodimerization. Photolysis on thioalkyl 2-anthryl ether (Figure 3.1, shown as the thiol) monolayers has shown reversible photodimerization of adjacent anthracene moieties, as confirmed by ensemble techniques, including infrared spectroscopy, contact angle, and X-ray photoelectron spectroscopy [152].

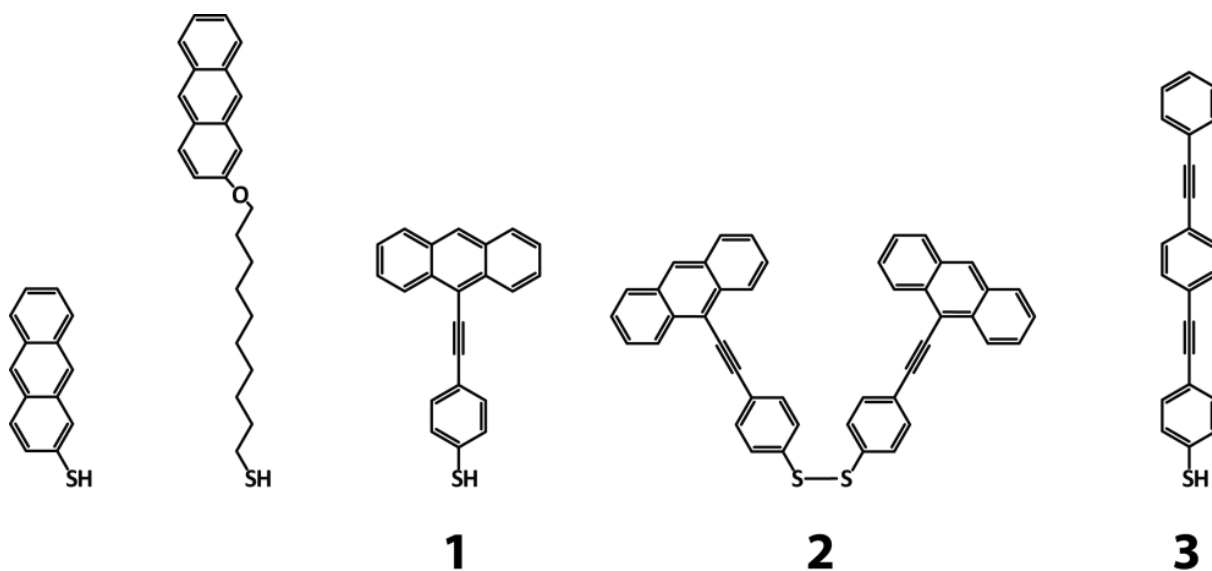


Figure 3.1 Structures of 2-anthracenethiol, 10-thiodecyl 2-anthryl ether are compared to structures of 9-(4-mercaptophenylethynyl)anthracene (**1**), 9-phenylethynylantracene disulfide (**2**), and oligo(phenylene ethynylene)thiol (**3**).

3.2 Experimental Details

Well-ordered, *n*-dodecanethiolate (**C12**) monolayers were assembled on Au{111} substrates by vapor annealing, where substrates were held above 100 μL of 1 mM ethanolic *n*-dodecanethiol solution at 78 $^{\circ}\text{C}$ for 24 hours. These conditions lead to the formation of high-quality, tightly packed SAMs with large, ordered domains [153]. The SAM matrix was placed in a solution containing $\sim 1\ \mu\text{M}$ **MPEA** (**1**) or the disulfide form of **PEA** (**2**, Figure 3.1), allowing insertion and exchange at defects. Insertion of the disulfide molecules assured adjacent placement of molecules [30,154,155]. We note that the same strategy can be used with asymmetric disulfides to place two different molecules in proximity by insertion. Images were collected under ambient conditions with our custom-built STM. Samples were imaged continuously at $-1\ \text{V}$ sample bias and 1 pA tunneling current. The tunneling junction was illuminated with low-power 365 nm Ultraviolet (UV) light ($\sim 1\ \text{mWcm}^{-2}$) and inserted molecules were monitored in situ for reactions between and excitations of **MPEA** thiolates (see UV-visible absorption spectra of **1** in Figure 3.2).

9-(4-Mercaptophenylethynyl)anthracene and disulfide **PEA** were synthesized as described previously [121,156,157]. Ultraviolet-visible spectra of **MPEA** (100 μM in ethanol) and disulfide **PEA** (100 μM in tetrahydrofuran) in solutions were collected by using a Evolution 600 UV-Vis spectrometer (Thermo scientific, West Palm Beach, FL). Disulfide **PEA** shows only a single absorbance at 280 nm (spectra not shown), in contrast to three peaks (383, 401, and 421 nm) of **MPEA** as shown in Figure 3.2.

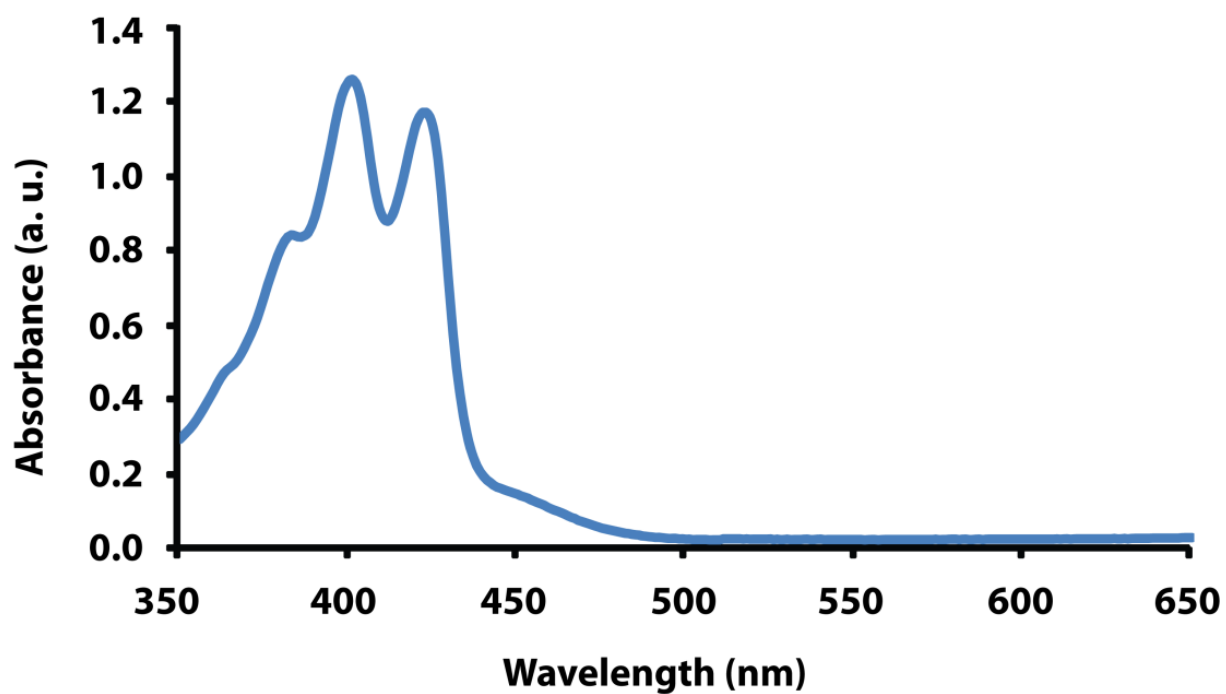


Figure 3.2 Ultraviolet-visible absorption spectrum of 9-(4-mercaptophenylethynyl)anthracene (MPEA, 100 μ M) in ethanol solution.

3.3 Results and Discussion

3.3.1 Photoreaction of phenylethynylanthracene in solution

In solution, anthracene and its 9-substituted derivatives undergo UV-activated dimerization at the 9 and 10 positions via [4+4] cycloaddition [146,158,159]. The reaction is reversible by irradiation at 254 nm or by mild heating [146]. However, irradiation of **PEA** in solution triggers a [4+2] Diels-Alder addition reaction between the ethynyl moiety and the central ring of the other anthracene system (Figure 3.3) [159]. The regiochemistry of this reaction is governed by the more favorable centrosymmetric-oriented complex. Electronic excitation is not limited only to the anthracene chromophore [146,158]. Connecting a phenylethynyl backbone to anthracene substantially increases electron delocalization through the ethynyl group. Thus, photodimerization between one anthracene and one ethynyl moiety are more favorable in solution.

3.3.2 Photoreaction of phenylethynylanthracene on surfaces

To investigate photoreactions between adjacent **PEA** molecules on surfaces, **MPEA** (**1**) was designed; a rigid spacer, phenylethynyl backbone introduces separation between the anthracene moiety and the gold. 9-(4-mercaptophenylethynyl)anthracene was inserted into preformed **C12** SAMs (Figure 3.5). The calculated length of **MPEA** is slightly greater than the thickness of **C12** molecular layer [34]. Because of the steric hindrance between the bulky anthracene and surrounding methyl groups, upright orientation of **MPEA** with the anthracene parallel to the substrate is the most stable configuration [121].

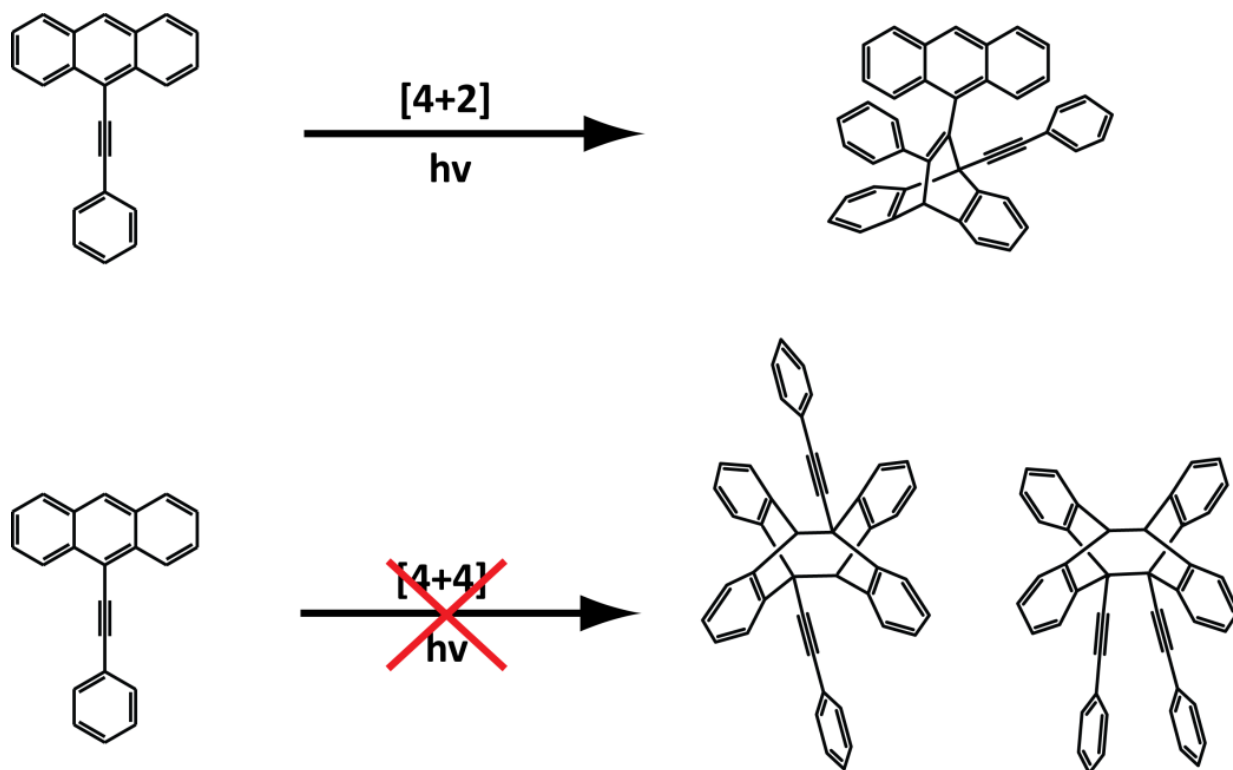


Figure 3.3 Schematic view of the photoreaction of 9-phenylethynylantracene in solution [160].

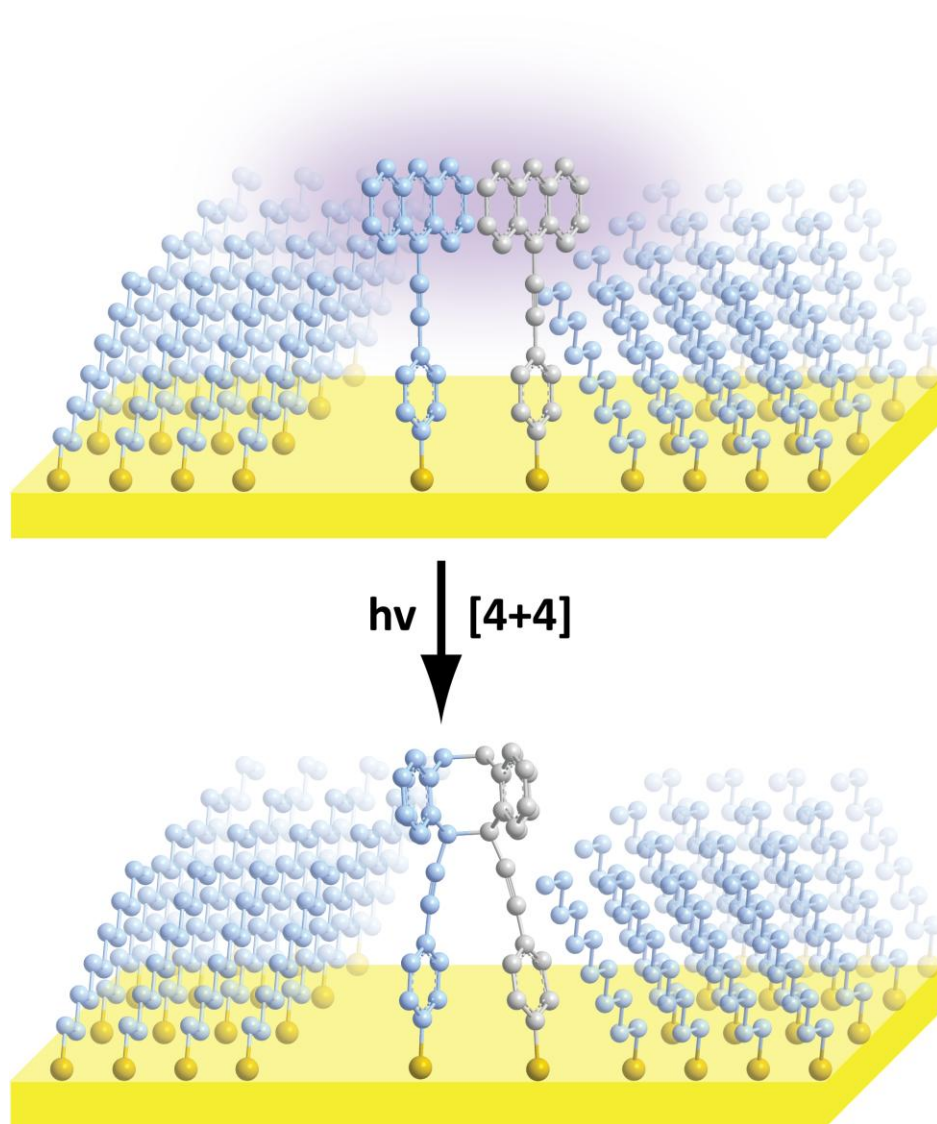


Figure 3.4 Schematic view of the photoreaction of 9-(4-mercaptophenylethynyl)anthracene on a Au{111} surface.

If two upright **MPEA** molecules are adjacent on the surface, UV illumination can drive the dimerization of anthracene moieties via [4+4] photocycloaddition, rather than the [4+2] reaction favored in solution, as shown schematically in Figure 3.4. For the reaction to occur, **MPEA** molecules must be parallel [161] and sufficiently close for strong π - π stacking interactions [34]. This conformation and the limited mobility forced by a compact matrix increase the likelihood of the [4+4] photocycloaddition between two adjacent anthracenes. Long-wave UV irradiation at 365 nm does not cause rapid photooxidation in the host SAMs, although exposure to short-wave UV light (254 nm) rapidly damages the alkanethiolate matrix before the reverse reaction can progress appreciably [162].

3.3.3 Stochastic switching of 9-(4-mercaptophenylethynyl)anthracene

Inserted **MPEA** molecules in STM images appear to protrude from their surrounding host matrices both as a result of their higher conductivity and their geometric height differences. Insertion occurs at defects, predominantly in SAM domain boundaries, around substrate vacancy islands, and along substrate step edges [139,140]. The number of inserted molecules is limited by using tightly packed **C12** matrices, short insertion times (~5 minutes), and low insertion solution concentration (~1 μ M).

Isolated **MPEA** molecules displayed stochastic switching activity during imaging. Similar molecules are well known to undergo transitions between the more conductive state (“ON”) and the less conductive state (“OFF”) in sequential STM imaging. The ON-state molecules appear as protrusions, and the OFF-state molecules appear as depressions relative to the surrounding matrix (or at the same apparent height as the matrix) in STM images. Images were screened for switching activity [118,119]. The observed number of transitions

from the ON state to the OFF state and from the OFF state to the ON state were 76 and 65, respectively from 148 selected images with $1000 \text{ \AA} \times 1000 \text{ \AA}$ scan areas containing an average of 10 isolated **MPEA** molecules per imaged area. The limited amount of stochastic switching observed is attributed to the tight SAM matrices used [118,140,163].

Two typical sequences of conductance switching are highlighted in Figure 3.5. One pair of molecules on the left are observed initially (Figure 3.5A, yellow box). Second pair of switches are ON in the subsequent image (Figure 3.5B, yellow box). The OFF-state molecules appear at nearly the same apparent height as surrounding **C12** domains. The measured apparent height change between the ON and the OFF conductance states was $\sim 2 \text{ \AA}$ at these tunneling conditions. Inserted groups of molecules can appear with larger apparent height depending on the number of molecules, which is attributed to intermolecular π - π interactions [164]. Then, the second pair changed shape in the next image (Figure 3.5C, yellow box). This pair was more active than the other in this area. Some molecules do not appear to switch over the experimental time scale (Figure 3.5, arrows). Distortion in molecular shape by a sudden contrast change was also detected (Figure 3.5B, red box), attributed to molecular switching in the presence of the STM tip. Later, this molecule returned to the ON state (Figure 3.5C, red box). Stochastic conductance switching occurs spontaneously at moderate sample bias, $\pm 1.0 \text{ V}$, and occurs on time scales faster than typical STM image acquisition [141,165].

We anticipated that, as in our earlier work on functionalized oligo(phenylene ethynylene)thiols (**3**, Figure 3.1), switching is the result of changes in the hybridization of the Au-thiolate bond as the molecules tilt [30,118,140]. All data recorded are consistent with this observation [166]. Inserted **MPEA** molecules were irradiated with long-wave ultraviolet light ($\sim 365 \text{ nm}$) for ~ 4 hours of 1 mWcm^{-2} . In-situ time-lapse STM images were collected during

irradiation. Heating induced by direct illumination introduces noise and thermal drift. So, relatively large scan areas ($1500 \text{ \AA} \times 1500 \text{ \AA}$) were monitored to track the changes in many molecules simultaneously, and to ease the required compensation for thermal drift. Figure 3.6 shows photoreactivity of isolated **MPEA** molecules at longer illumination time. Measurements were restricted to one atomically flat substrate terrace to maintain a consistent background height. Several sets of STM image frames containing $\sim 20 - 30$ **MPEA** molecules were used to measure apparent height changes by photodimerization of anthracene moieties.

3.3.4 Photoexcitation of 9-(4-mercaptophenylethynyl)anthracene

Ultraviolet irradiation stimulates molecules to switch to the ON state (see arrows in Figure 3.6), and leads to substantial increases in conductivity; **MPEA** molecules appear more protruding under illumination relative to the surrounding matrix. The apparent height difference between the isolated **MPEA** molecules and the surrounding **C12** matrix doubles to $\sim 4 \text{ \AA}$, compared to the ON-state apparent height without illumination. Since topographic STM images represent a convolution of the physical and electronic structures of the molecules [118,167], and conformation is restricted by the matrix, this change is attributed to a steady-state fraction of molecules in an electronically excited state (see Figure 3.8). Continuous illumination makes molecules appear protruding, despite the short time scale of individual excitation events; the calculated absorption cross section of the anthracene moiety with a molar extinction coefficient of $9,700 \text{ M}^{-1}\text{cm}^{-1}$ at 356.25 nm is $3.7 \times 10^{-17} \text{ cm}^2$ [168]. As the illumination time increases, more molecules switch on, although the rate of appearance does not strongly correlate with increased illumination time. Light-induced electronic excitation can be detected with single-molecule resolution, without appreciable quenching by gold, and it may be distinguished from switching events characteristic of such molecules.

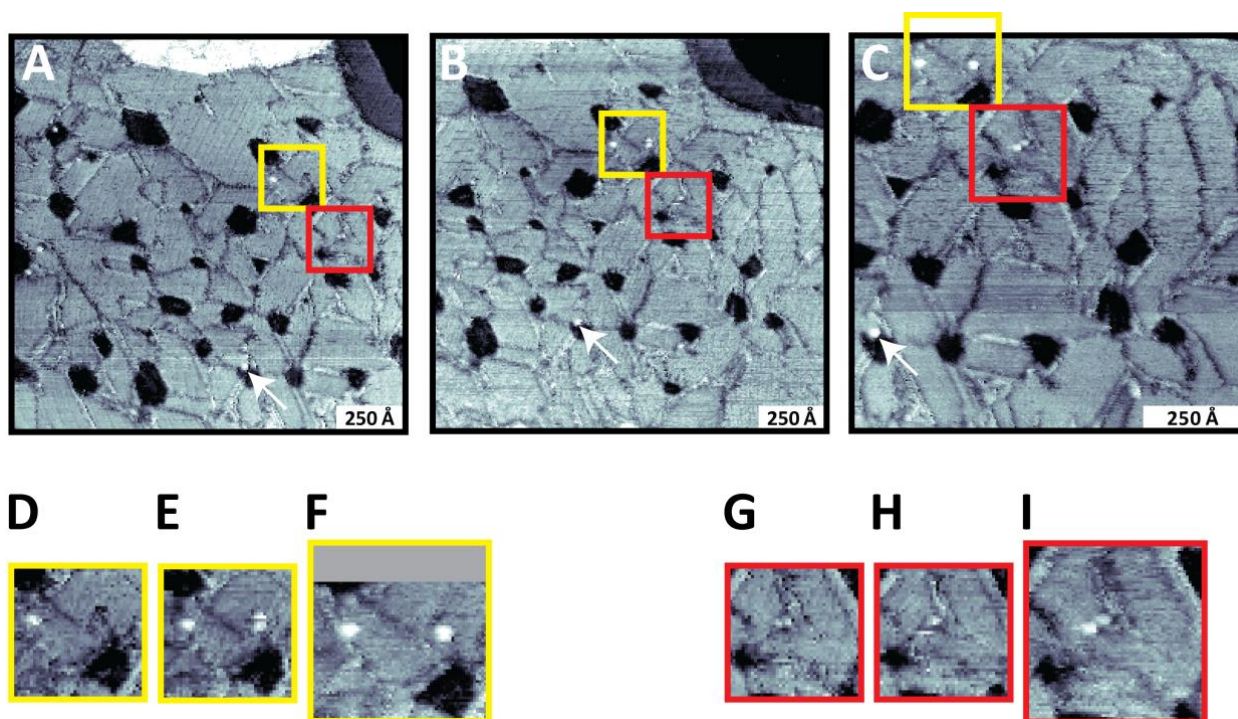


Figure 3.5 (A, to C) Sequential STM images of inserted **MPEA** molecules in a **C12** SAM matrix. Yellow and red boxes show the apparent height changes of molecules. (D to I) Cropped sequential STM images of molecular switching. The arrows at the bottoms of images (A to C) highlight molecules that show no substantial conductance changes during imaging. Imaging conditions: $V_{\text{sample}} = -1.0$ V, $I_{\text{tunnel}} = 1.0$ pA.

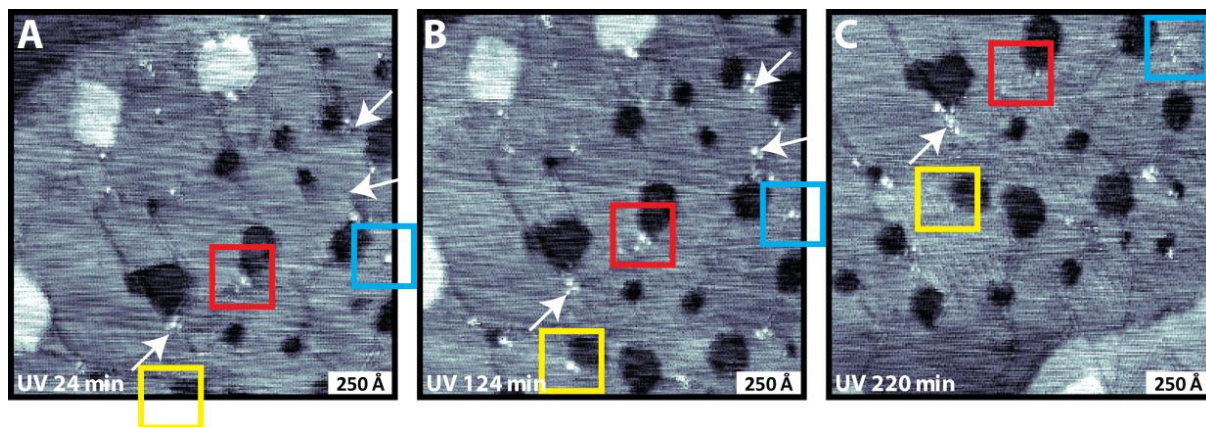


Figure 3.6 (A to C) Scanning tunneling microscopy images of **MPEA** molecules inserted into a **C12** SAM matrix, and then exposed to UV light (~ 365 nm). Images were collected during irradiation after (A) 24 minutes, (B) 124 minutes, and (C) 220 minutes. Imaging conditions: $V_{\text{sample}} = -1.0$ V, $I_{\text{tunnel}} = 1.0$ pA. The UV illumination increases the apparent height of photoreactive molecules and more molecules appear as protrusions at longer irradiation (see arrows). Several pairs of molecules show substantial decreases in apparent height, attributed to photodimerization (boxes in B and C).

3.3.5 Photodimerization of 9-(4-mercaptophenylethynyl)anthracene

Irradiation also induces permanent apparent height decreases in groups of molecules (colored boxes in Figure 3.6B and C). We attribute this change to the photodimerization of adjacent anthracene moieties, shown schematically in Figure 3.4. This reaction breaks the extended π conjugation network, resulting in a significant decrease in conductivity. By constraining the degrees of freedom in orientation in photodimerized molecules, conductance switching is inhibited. This photodimerization can be reversed by exposure to 254 nm light (or mild heat), but such illumination appreciably damages the surrounding **C12** SAM. (The photooxidation of anthracene can be discounted, as it usually occurs in substituted anthracenes at both the 9 and 10 positions [169,170]).

3.3.6 Calculations

Density functional theory calculations to determine the stable geometry and relative energies of **MPEA** in gas phase were performed with the Gaussian 03 program [171]. Geometries for different dihedral angles of molecular conformations in the **MPEA** were optimized using the density functional theory with the B3LYP functional and the 6-31G(d) basis set [172].

9-(4-Mercaptophenylethynyl)anthracene is composed of three π systems; anthracene, acetylene, and thiophenol. The anthracene moiety and the mercaptophenyl ring are rotated about the ethynyl bond into the planar and orthogonal configurations between the planar (0°) and the orthogonal (90°) molecular conformations of **MPEA**.

Energy and conductivity vary as the anthracene and the mercaptophenyl rings rotate around the ethynyl bond. The relevant dihedral angle was scanned from 0° to 90° in steps of 10° and the geometry was optimized without further restrictions. Figure 3.7 shows the relative electronic energies and the energy gap between the highest occupied molecular orbital (HOMO) and the lowest unoccupied molecular orbital (LUMO). The planar conformation has the lowest relative electronic energy and the smallest gap. The rotational barrier from the planar to the orthogonal conformations is 1.0 kcal/mol.

The calculated frontier molecular energy levels and corresponding orbital energies of **MPEA** in planar and orthogonal conformations are shown in Figure 3.8. The energy gap between the HOMO and the LUMO for the planar **MPEA** (3.01 eV) is slightly smaller than for the orthogonal conformation (3.29 eV). The frontier molecular orbitals of the planar **MPEA** are fully delocalized along the entire molecule. In contrast, the frontier molecular orbitals of the orthogonal **MPEA** remain localized in either the anthracene (HOMO and LUMO) or the mercaptophenylethynyl backbone (HOMO-1 and LUMO+1).

3.4 Conclusions and Prospects

We observe three distinct phenomena on anthracene-terminated phenylethynyl thiolates molecules on Au{111}: stochastic switching, increased conductance for molecules in excited states, and drops in conductance attributed to photochemical reaction. The change in molecular configuration and conformation modulate the conductivity by changing the π conjugation and the electron distributions in the HOMO and LUMO energy levels. Scanning tunneling microscope imaging under illumination probes photoinduced conductance. Long illumination (~ 3 hours) drives molecules to photodimerize between two

anthracene moieties in adjacent **MPEA** molecules, resulting in apparent depressions in STM images. Molecular orientation, packing, and the proximity of other molecules all influence the photoreaction efficiency.

Exercising control over molecular reactivity by confinement has great potential for both understanding and measuring complex chemical reactions [173,174]. Regioselective photoreactions between individual molecules by molecular design and self-assembly with in-situ monitoring are powerful demonstrations of chemical control via the local environment [118,175,176]. The extraordinary resolution of the STM enables monitoring molecular motions and reactions. Controlling the chemical environment and monitoring such selective reactions between individual molecules will be important elements in directing chemistry with this approach.

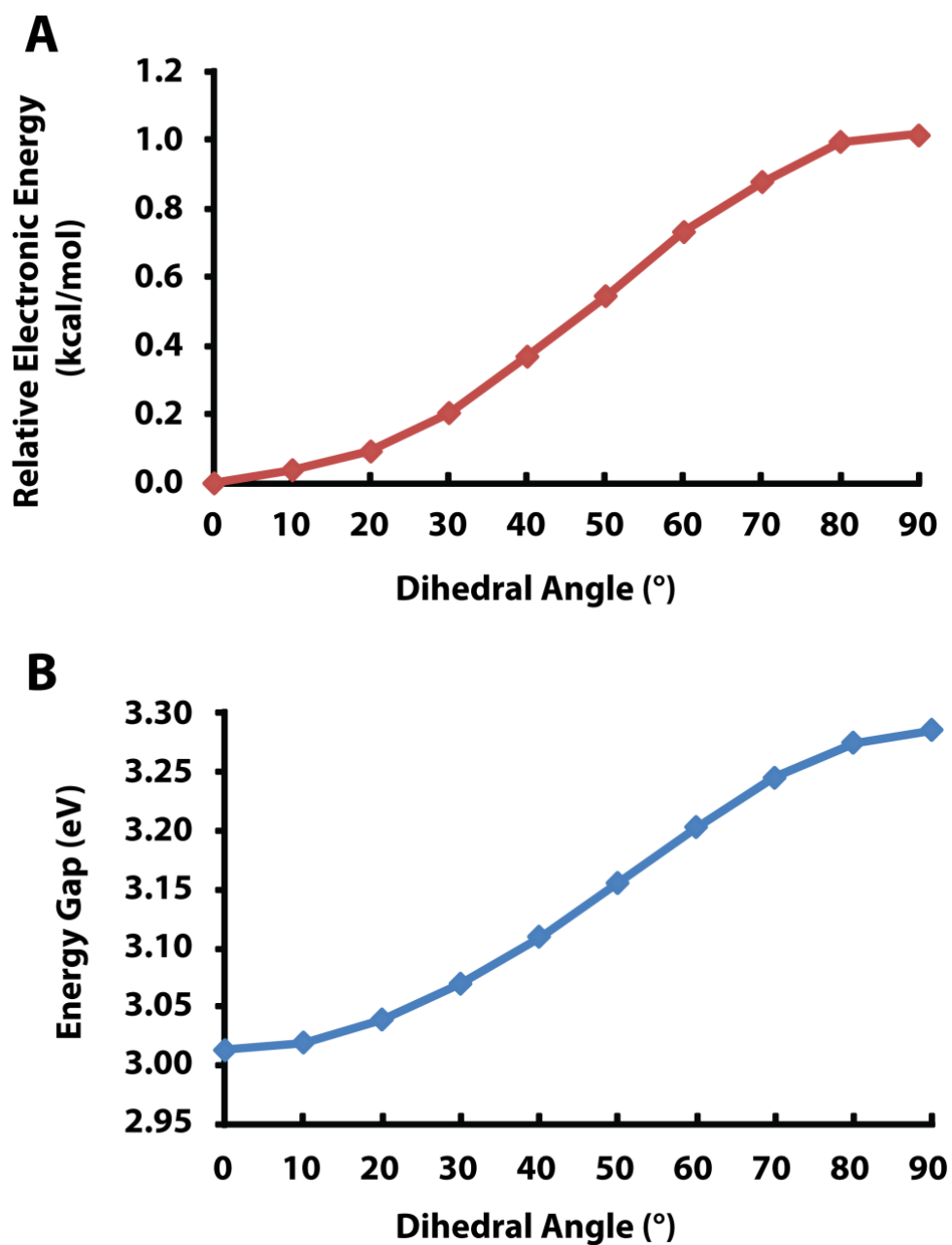


Figure 3.7 (A) The calculated electronic energy profile and (B) the energy gap between the HOMO and the LUMO of **MPEA** as the function of relative ring orientations about the ethynyl bond.

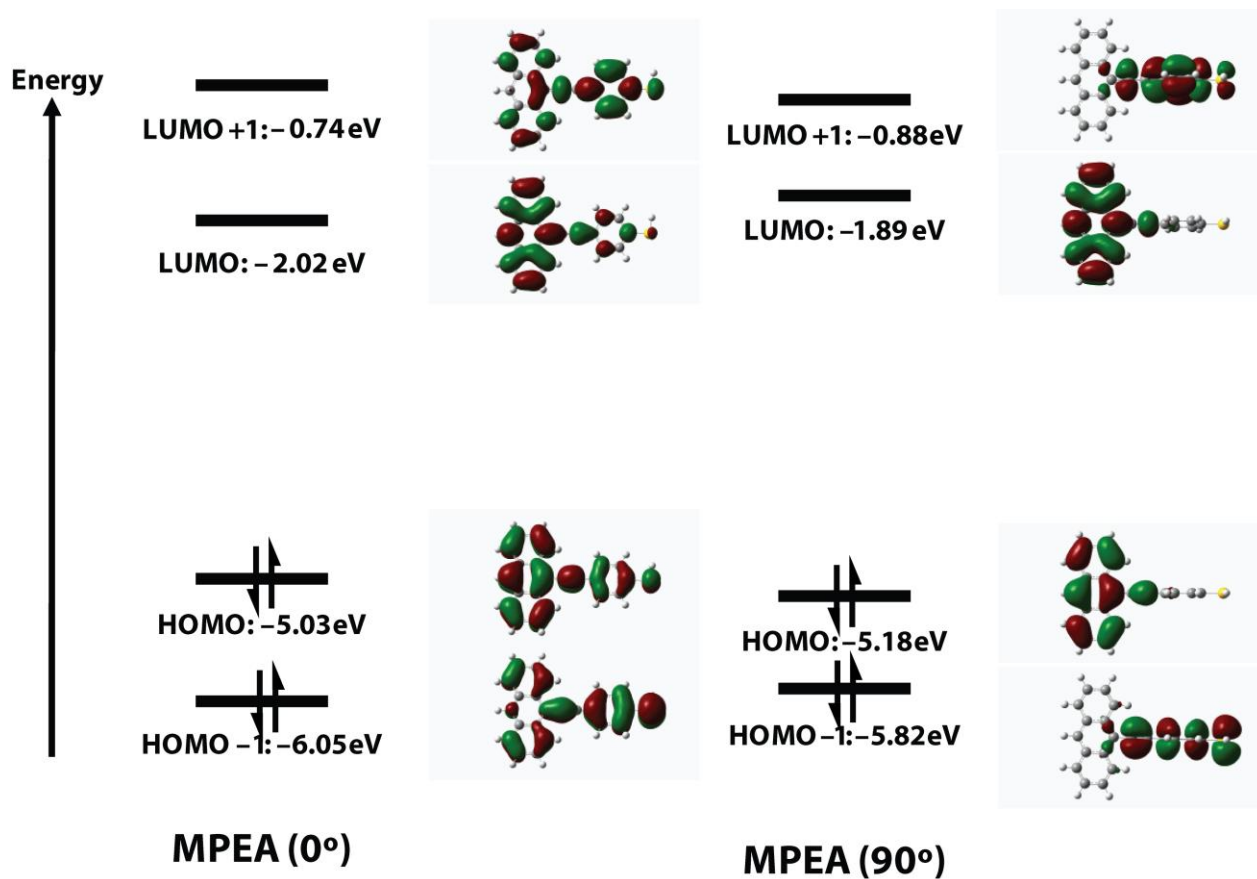


Figure 3.8 Frontier molecular orbitals and corresponding energy levels (HOMO-1, HOMO, LUMO, LUMO+1) of the planar (0°) and orthogonal (90°) conformations of **MPEA**. The gap energy between the HOMO and LUMO of the planar **MPEA** (3.01 eV) is smaller than that of the orthogonal **MPEA** (3.29 eV).

Chapter 4. Self-Assembled Monolayers of 2-Adamantanethiol on Au{111}: Control of Structure and Displacement

4.1 Introduction

Alkanethiolate SAMs on Au{111} form well-defined crystalline structures due to the spontaneous formation of strong gold-sulfur bonds and attractive van der Waals forces between adjacent alkyl chains [1,177]. However, characteristic domain boundaries and defects generated during assembly [4,10,178,179] limit their applicability for patterning and device fabrication [3-5].

One solution for improving control over patterning in SAMs is to design molecules with tailored intermolecular interactions that impart tunability to surface properties [20,31,32,118,141,180,181]. For instance, self-assembly of amide-containing alkanethiols results in highly stable films due to strong hydrogen-bonding interactions between buried amide functional groups [182,183]. In contrast, adamantanethiols with their rigid 10-carbon adamantane cage (Figure 4.1) [184] produce SAMs with larger intermolecular distances and thus smaller intermolecular interaction strengths, as compared to *n*-alkanethiols. Thiol-based adamantane [185-187] and polymantane [188-190] SAMs on Au{111} have been prepared with a variety of assemblies on gold surfaces by altering the number and position of thiol functionalities on the diamondoid cage. Recent STM studies on 1-adamantanethiolate (**1AD**) SAMs on Au{111} revealed highly ordered, hexagonally close-packed lattices that were readily displaced by short-chain alkanethiols [191]. The labile nature of **1AD** SAMs has also been exploited to develop an improved soft lithography technique, microdisplacement

printing, wherein alkanethiolate ink molecules displace a preexisting **1AD** SAM only in stamped (contacted) regions [192-195]. With this technique, the remaining **1AD** SAM in unstamped areas acts as a diffusion barrier, preventing pattern dissolution. This creates high-quality patterns with sharp edges.

The decreased molecular packing density and the lower intermolecular interaction strengths in **1AD** SAMs facilitate their rapid and complete displacement by other thiol molecules at room temperature and at millimolar concentrations [196,197]. By designing the intermolecular interactions in SAMs, we are able to control the rate and extent of molecular exchange in SAMs, making microdisplacement printing technique flexible and robust. Here, we demonstrate that 2-adamantanethiol forms well-ordered, hexagonally close-packed monolayers on Au{111} with a $c(4 \times 2)$ superlattice. We also show the geometric influence of the adsorbates on the final SAM structure by comparing differences in SAMs of two structural isomers. In 1-adamantanethiol and 2-adamantanethiol, sulfur is attached to the tertiary or secondary carbon, respectively, on the adamantyl cage (Figure 4.1). We posit that this alteration changes the orientation of molecules within the respective SAMs, resulting in different superlattice structures. Further, in a 2-adamantanethiolate (**2AD**) monolayer, asymmetry in the adamantyl cage with respect to the gold-sulfur bond axis should modulate the strength of the intermolecular interactions within the SAM, allowing us to control the rate and extent of displacement.

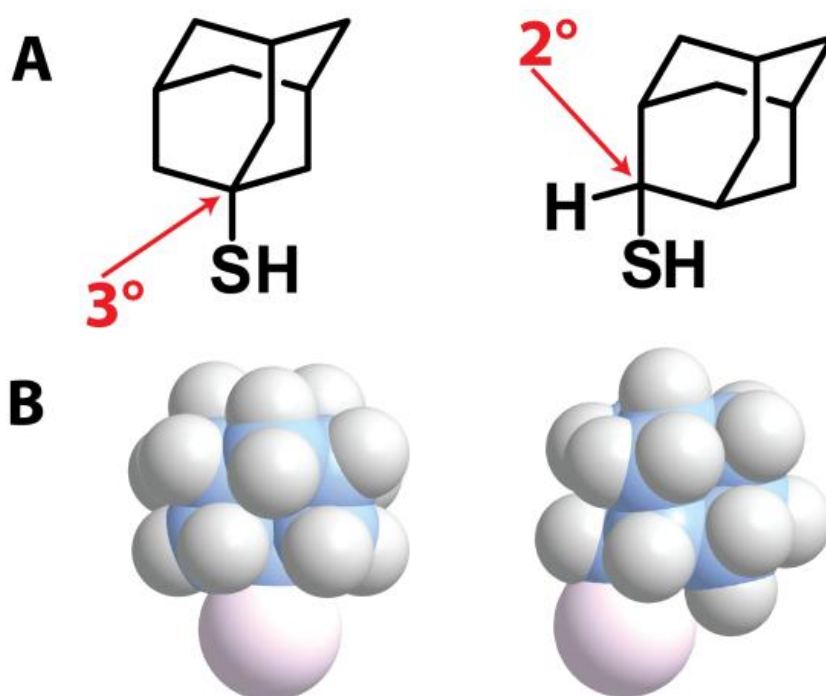


Figure 4.1 (A) The molecular structures of 1-adamantanethiol and 2-adamantanethiol. Sulfur attachments to the tertiary (3°) and secondary (2°) carbon on the adamantyl cage in each thiol are shown by the arrows. (B) The three-dimensional representation of the corresponding thiolates.

4.2 Experimental Methods

4.2.1 Materials

The chemicals *n*-dodecanethiol, thiourea, diethyl ether, anhydrous magnesium sulfate, sodium hydroxide, silica gel (70 – 230 mesh), anhydrous hexanes, potassium thioacetate (KSAc), dimethylformamide (DMF), 2-bromoadamantane (Sigma-Aldrich, St. Louis, MO), 1-bromododecane-*d*₂₅ (Cambridge Isotopes, Andover, MA), and 200-proof ethanol (Pharmaco, Brookfield, CT) were used as received. 1-dodecanethiol-*d*₂₅ was prepared as described previously [198].

4.2.2 2-Adamantanethiol synthesis

2-Adamantanethiol was synthesized by modifying a previously reported method [199] using KSAc and 2-bromoadamantane. In a three-neck flask, 10.7 g (50 mmol) of 2-bromoadamantane was added to a stirred solution of 10 g (87 mmol) of KSAc in 100 mL of DMF. The mixture was refluxed at 130 °C under Ar until 2-adamantanethiol was formed. The resulting solution was allowed to cool to room temperature and was partitioned between H₂O and hexane. The hexane was dried over anhydrous magnesium sulfate, the magnesium sulfate was removed by filtration and the hexane was evaporated under Ar gas. 2-Adamantanethiol was purified using flash column chromatography and vacuum sublimation [200]. The purified product was characterized by infrared spectroscopy, nuclear magnetic resonance (NMR), and mass spectroscopy [201-204]. Infrared absorptions in CCl₄ were observed at 2910, 2850, 1465, 1455, and 2580 cm⁻¹ (S-H, very weak). Nuclear magnetic resonance features in CDCl₃ were found as follows: ¹H NMR: δ = 1.41 (d, 1H, J = 6 Hz), 1.47 (broad s, 1H), 1.53 (broad s, 1H), 1.72 (broad s, 2H), 1.79 (broad, 8H), 2.15 (broad s, 1H), 2.20 (broad, 1H), and 3.30

(broad d, 1H, $J = 7$ Hz); ^{13}C NMR: $\delta = 45.90, 36.05, 28.17, 27.37$ for primary and tertiary carbons, $\delta = 39.28, 38.25, 31.27$ for secondary carbons. Mass spectral features with assigned fragments and relative intensities were observed at mass/charge ratios of: 168 ($\text{C}_{10}\text{H}_{15}\text{SH}^+$, 70%), 135 ($\text{C}_{10}\text{H}_{15}^+$, 85%), 93 (C_7H_9^+ , 80%), 91 (C_7H_7^+ , 90%), 79 (C_6H_7^+ , 100%), 77 (C_6H_5^+ , 70%), 67 (C_5H_7^+ or $\text{C}_{10}\text{H}_{15}^{2+}$, 70%), 41 (C_3H_5^+ , 30%), and 334 ($\text{C}_{20}\text{H}_{30}\text{S}_2$, 20%).

4.2.3 Self-assembled monolayer fabrication

All **2AD** monolayers were assembled on flame-annealed Au{111} on mica substrates (Agilent Technologies, Tempe, AZ) inserted in 1 mM ethanolic 2-adamantanethiol solution. After annealing the Au substrates with a hydrogen flame, clean substrates were placed in 1 mM 2-adamantanethiol solution either at room temperature (**RT**) for 24 hours (**RT 2AD** SAMs) or at 70 °C for 2 hours with subsequent dry-annealing (**DA**) under nitrogen at 78 °C for 17 hours (**DA 2AD** SAMs) in sealed glass v-shaped vials. Following deposition, each sample was removed from solution, rinsed with ethanol and blown dry with nitrogen 3 times. Displacement of **2AD** SAMs with *n*-dodecanethiol was carried out by immersing preassembled **2AD** SAMs into 1 mM *n*-dodecanethiol solutions for the specified time periods.

4.2.4 Scanning tunneling microscopy

All STM measurements were performed under ambient conditions using a custom-built Besocke-style STM [20,43,44]. The samples were scanned within 24 hours of fabrication and were stored under nitrogen prior to any other measurements. The **2AD** lattice spacing was measured from Fourier transforms of STM images of **2AD** SAMs after being calibrated using the Fourier transforms of images of the *n*-dodecanethiolate (**C12**) SAM lattice. Lattice spacings were also determined from binary SAMs, which contained distinct ordered domains

of both **2AD** and **C12**. In this way, the same tip was used to obtain the lattice spacings of both components simultaneously. The apparent corrugations of the SAMs were calibrated using the known height of the step edges of the Au{111} substrate in **C12** SAMs.

4.2.5 X-Ray photoelectron spectroscopy

Samples for X-ray photoelectron spectroscopy were stored under nitrogen and transferred to the vacuum chamber within 1 hour. Spectra were acquired using a Kratos Axis Ultra photoelectron spectrometer with a monochromatic Al K α source (20 mA, 14 kV), base pressure of 1×10^{-9} torr, and a spot size of $300 \mu\text{m} \times 700 \mu\text{m}$. Survey spectra were acquired at a pass energy of 80 eV and high-resolution spectra of the C 1s, S 2p, and Au 4f regions were collected at a pass energy of 20 eV. The binding energies were referenced to the Au 4f_{7/2} peak at 83.98 eV [205]. All of the peaks from the spectra were fit using Gaussian-Lorentzian (GL) line shapes (CasaXPS analysis software [206]) using a linear background when necessary.

4.2.6 Cyclic voltammetry

A custom-built electrochemical cell [207] and a BAS Epsilon potentiostat (Bioanalytical Systems Inc., West Lafayette, IN) were used to perform electrochemical measurements using methods described previously [208]. The working electrode was defined by a perfluoroelastomer O-ring (McMaster Carr, Cleveland, OH) mounted on top of the Au{111} substrates inside the electrochemical cell. The area of the working electrode was $\sim 0.5 \text{ cm}^2$, electrochemically determined using the Randles-Sevcik equation [209].

The potential of the cell was controlled by employing a Ag/AgCl saturated KCl reference electrode (Bioanalytical Systems Inc., West Lafayette, IN) and a Pt wire counter

electrode (Bioanalytical Systems Inc., West Lafayette, IN). An aqueous solution of 0.5 M KOH (99.99%, semiconductor grade, Sigma-Aldrich, St. Louis, MO) prepared with deionized water (18.2 M Ω) was used for the supporting electrolyte, after being sparged with ultrahigh purity Ar for 20 minutes. Cyclic voltammograms were acquired from -200 to -1500 mV at a sweep rate of 20 mV/s and were baseline-corrected using a straight line subtraction in the first of 100 mV of the sweep in which no faradaic processes occur [197].

4.2.7 Infrared reflection absorption spectroscopy

All infrared spectra were acquired using a Nicolet 6700 Fourier transform infrared (FTIR) spectrometer (Thermo Electron Corp., Waltham, MA) equipped with a liquid-nitrogen-cooled mercury-cadmium-telluride detector and a Seagull variable-angle reflection accessory (Harrick Scientific Inc., Ossining, NY). The spectrometer was purged with dry CO₂-free air prepared by a FTIR Pure Gas Generator (Parker-Balston, Cleveland, OH). The data were collected at grazing incidence reflection (82° relative to surface normal) with *p*-polarized light and a mirror speed of 1.27 cm/s with a resolution of 2 cm⁻¹. All SAM spectra were transformed using N-B Medium apodization and were normalized with data recorded for perdeuterated *n*-dodecanethiolate monolayers on Au{111}. Spectra were acquired for each **2AD** SAM to verify the absence of impurities and the presence of the characteristic CH₂ stretch at 2913 ± 1 cm⁻¹, which is indicative of well-ordered **2AD** SAMs. The samples were placed in 1 mM ethanolic *n*-dodecanethiol solutions for displacement. After every specified time frame, the SAMs were rinsed with ethanol and blown dry with nitrogen. Each FTIR spectrum was recorded, and the sample was returned to the *n*-dodecanethiol solution for further exposure. In the case of **DA 2AD** SAM displacement, the displacement interval was increased as the rate of change diminished. In order to achieve saturation coverage, the

samples were placed in a *n*-dodecanethiol solution for a total of 24 hours to allow additional growth and ordering. Subsequently, a final spectrum was recorded for each sample to determine the saturation coverage.

4.3 Results and Discussion

4.3.1 Characterization of 2-adamantanethiolate SAMs on Au{111}

Molecular exchange with a SAM strongly depends upon the defect densities and domain sizes of the films [197,210,211]. Thus, we first established conditions for controlling domain sizes (and thus defect densities) in **2AD** SAMs. Small-domain **2AD** SAMs with higher defect densities were prepared by placing clean Au{111} substrates in 1 mM ethanolic 2-adamantanethiol solution at room temperature (**RT**) for 24 hours (**RT 2AD** SAMs, Figures 4.2A and B). Large-domain **2AD** SAMs with lower defect densities were fabricated by first placing clean Au substrates in 1 mM ethanolic 2-adamantanethiol solution at 70 °C for 2 hours, then dry-annealing (**DA**) the samples under nitrogen at 78 °C for 17 hours (**DA 2AD** SAMs, Figures 4.2C and D). The samples prepared from solution at 70 °C formed **2AD** SAM surfaces with greater degrees of long-range order than the samples prepared at room temperature. Other temperatures (50 and 60 °C) accelerate ordering. Annealing at 78 °C gives further access to slow ordering, extending to large domains. The annealing time used is not critical; however, we observed evidence of desorption or oxidation including molecular vacancies, disorientation or disordering and clustering for annealing times over 17 hours [212,213]. As shown in Figure 4.2, domain boundaries in STM images appear as slight protrusions. The domain sizes of **RT 2AD** SAMs were observed to be < 200 Å, with a large number of disordered molecules in domain boundaries, vacancy islands, and step edges

(Figure 4.2A). High-resolution STM images of **RT 2AD** SAMs (*e.g.*, Figure 4.2B) reveal distinct domain boundaries separating rotational domains. In contrast, annealing at moderately elevated temperature (78 °C) results in **2AD** SAMs with larger domain sizes, typically >500 Å across, and substantial decreases in disordered regions and vacancy islands (Figure 4.2C) [16,214-216]. During annealing, thermal energy allows molecules in disordered regions to change orientation, forming highly ordered monolayers over large areas (Figure 4.2D). However, disordered regions still remain proximate to vacancy islands, between domains, and along step edges (Figure 4.3).

In molecularly resolved images, we observe that rows of molecules change direction between domains, even without apparent depressions or protrusions at rotational domain boundaries. The relative orientation angles between rotational domains were measured, although the exact rotation with respect to the underlying Au substrate cannot be determined by imaging only the adlayer. Figure 4.4A shows four rotational domains in a **DA 2AD** SAM. Slight apparent protrusions observed in region A (arrows in Figure 4.4A) indicate translational domain boundaries in the same rotational domain. The relative rotational angles of domains B and C were measured from domain A; the angle for domain D was not measured due to disorder. The angle from domain A to domain B was 30° counterclockwise, whereas the angle from domain A to domain C was 40° clockwise. Other rotational domains were also observed in other STM images. All measured rotational angles between domains were close to 30°, within a standard deviation of 10° due to errors resulting from thermal drift in our ambient STM. The restricted variation in relative rotational angles between domains in **2AD** SAMs is consistent with our proposed lattice structure (*vide infra*).

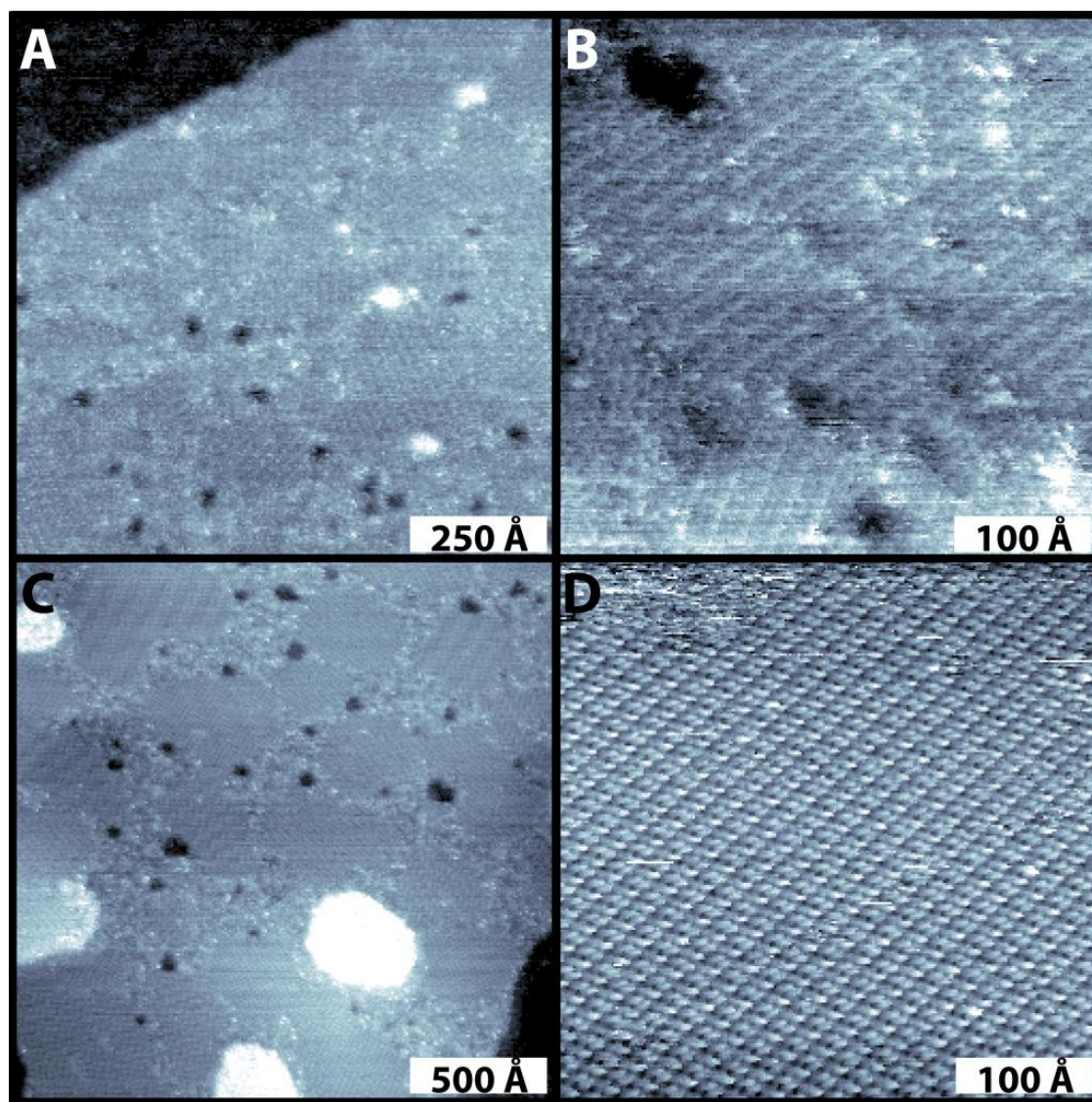


Figure 4.2 Scanning tunneling microscopy images of 2-adamantanethiolate (**2AD**) self-assembled monolayers (SAMs) on Au{111} fabricated by immersing substrates in 1 mM 2-adamantanethiol solution at room temperature for 24 hours (**RT 2AD** SAMs, A and B) or by first exposing clean Au substrates to solution at 70 °C for 2 hours, then dry-annealing the samples under nitrogen at 78 °C for 17 hours (**DA 2AD** SAMs, C and D); sample bias 0.80 V, tunneling current 2.0 pA. The round features with high contrast in C correspond to Au adatom islands with measured height of 2.4 Å, consistent with the Au{111} single-atom step height [14].

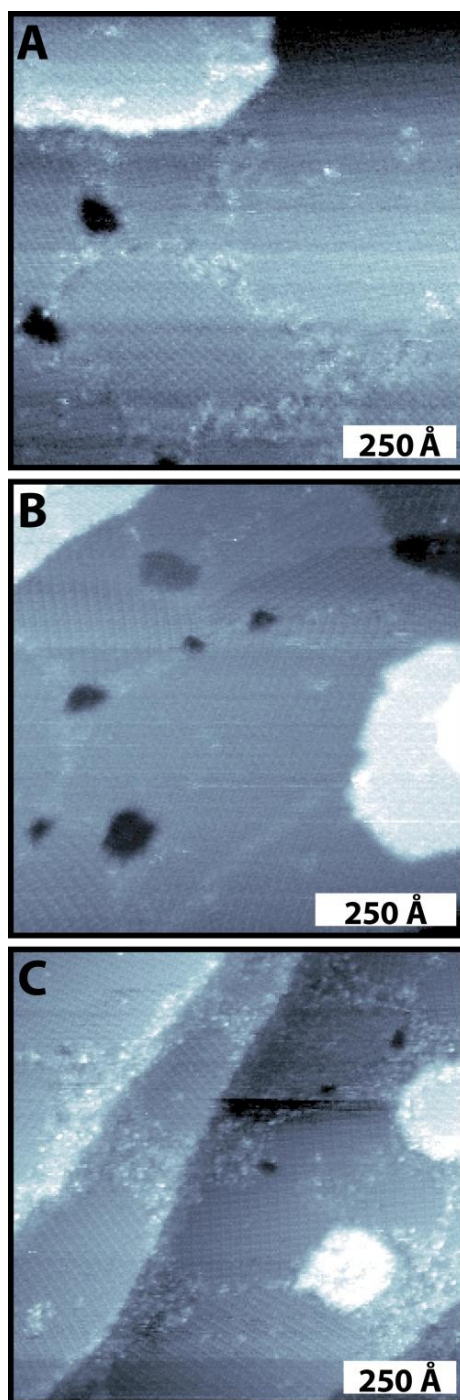


Figure 4.3 Scanning tunneling microscopy images of 2-adamantanethiolate (**2AD**) self-assembled monolayers (SAMs) on Au{111} prepared by first placing Au substrates in 1 mM 2-adamantanethiol solution at 70 °C for 2 hours, then dry-annealing the samples under nitrogen at 78 °C for 14, 17, and 22 hours for A, B, and C, respectively (**DA 2AD** SAMs); sample bias 0.80 V, tunneling current 2.0 pA.

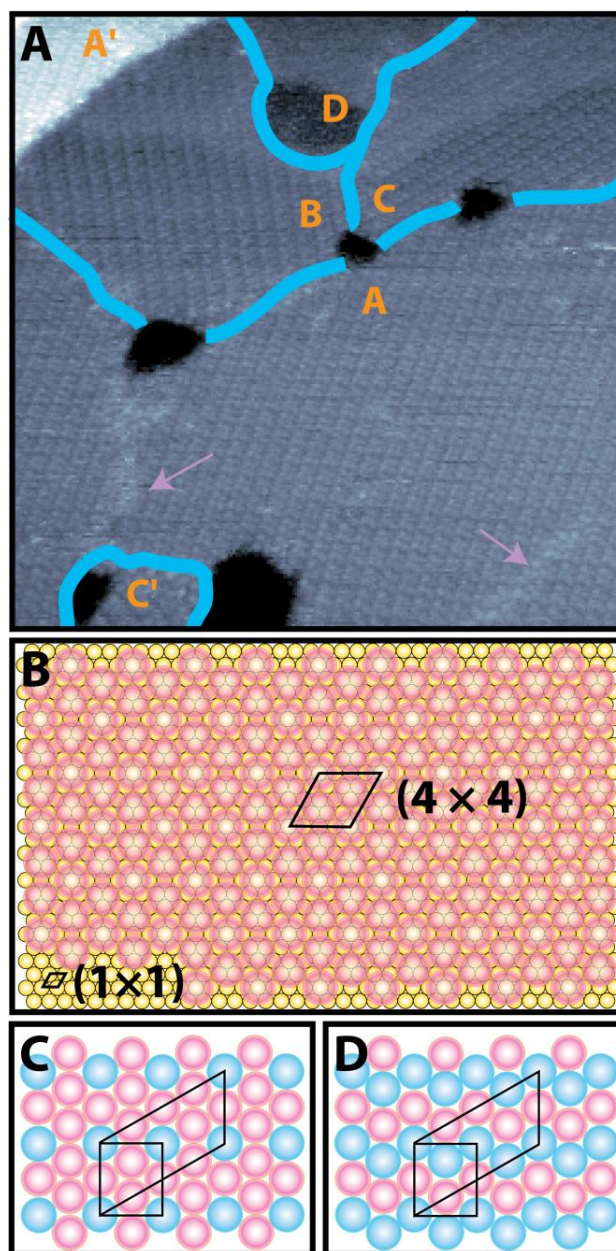


Figure 4.4 (A) A scanning tunneling microscopy image of a 2-adamantanethiolate (**2AD**) self-assembled monolayer (SAM) on Au{111} showing several rotational domains. The SAM was prepared by first placing a Au substrate in a 1 mM 2-adamantanethiol solution at 70 °C for 2 hours, then dry-annealing the sample under nitrogen at 78 °C for 17 hours (**DA 2AD SAM**). The lattice in domain B is rotated 30° counterclockwise with respect to domain A, and domain C is rotated 40° clockwise with respect to domain A. The domains A' and C' have the same orientations as domains A and C, respectively. Domain D is disordered. The yellow arrows denote translational domain boundaries; 600 Å × 600 Å; sample bias 0.80 V, tunneling current 2.0 pA. (B) The proposed unit cell for the **2AD** lattice on Au{111}. (C and D) The proposed superlattice $c(4 \times 2)$ structures of alternating heights results from different phases (β and δ), respectively.

Individual molecules in **2AD** SAMs are arranged in a hexagonally close-packed formation with a $c(4 \times 2)$ superlattice structure [15,217]. The distance between hexagonal points in reciprocal space corresponds to measured nearest neighbor distances of 6.9 ± 0.4 Å and next nearest neighbor distances of 11.6 ± 0.4 Å, which are close to the nearest neighbor distances of 6.67 ± 0.01 Å for three-dimensional adamantane crystals [218]. Based on the above observations, we propose that the most likely unit cell assignment is (4×4) with respect to the Au{111} substrate, as shown in Figure 4.4B [185]. Using a gold spacing of 2.88 Å, a (4×4) unit cell has a lattice constant of 11.52 Å and comprises three molecules per unit cell. The phases of the $c(4 \times 2)$ superlattice with respect to the proposed (4×4) unit cell observed in **2AD** SAMs are β and δ phases [219], consisting of molecules with two different apparent heights (Figure 4.4C and D). We observed ellipsoids at molecular resolution and linear features in large scanning areas (Figure 4.2) depending on the tip condition. This might have been caused by the convolution of $c(4 \times 2)$ phases or different molecular interactions between molecules driven by the flexible molecular orientation of **2AD** (e. g., tilt or twist). However, it was not possible to determine tilt or twist angles of the adamantyl cage from the Au-S bond axis by STM.

4.3.2 Displacement of 2-adamantanethiolate SAMs with *n*-dodecanethiol

Scanning tunneling microscopy allows us to monitor the molecular exchange of **2AD** monolayers with other alkanethiols at the nanoscale. Figure 4.5 shows STM images of **2AD** SAMs containing **C12** domains generated by displacement with 1 mM ethanolic *n*-dodecanethiol solution. In order to correlate exchange kinetics with the domain sizes and defect densities in **2AD** SAMs, both **RT 2AD** and **DA 2AD** SAMs were immersed in 1 mM ethanolic *n*-dodecanethiol solutions for the controlled time periods. Figure 4.5A shows the

results of displacement of **RT 2AD** SAMs by **C12** for 2, 10, and 60 seconds from top to bottom. Figure 4.5B depicts the displacement of **DA 2AD** SAMs by **C12** for 10, 40, and 120 minutes from top to bottom.

As expected, small-domain **RT 2AD** SAMs undergo much faster molecular exchange with **C12** than large-domain **DA 2AD** SAMs. After 2 seconds of displacement, the remaining lower areas correspond to well-ordered **2AD** domains, while the dots and lines with high contrast are assigned as less-ordered **C12** molecules. In the early stages of displacement, rapid molecular exchange primarily occurs in disordered regions such as domain boundaries, vacancy islands, and step edges; adsorbed **C12** molecules in these regions are disordered. After 10 seconds of displacement, corrugated rod-like structures begin to appear in the SAM, oriented in different directions; we attribute these features to the **C12** areas that displace ordered **2AD** molecules in different rotational domains. After 60 seconds of displacement, **C12** molecules start forming small domains of hexagonally close-packed lattices; well-organized **2AD** domains were still present (not shown). We ascribe depressed lines observed in some **C12** regions (arrows in Figure 4.5A) to missing rows caused by the size disparity between **C12** and **2AD** after exchange. During the displacement process, a **C12** molecule replaces a relatively large **2AD** molecule, leaving room for additional **C12** insertion. This lattice mismatch is a key feature of successful and complete displacement. More **C12** molecules eventually backfill these rows, optimizing hexagonally close-packing. As insertion time increased, the fraction of the surface covered by **2AD** domains decreased and displacement was essentially complete after 40 minutes. At very long displacement times, molecular exchange continued at the boundaries between **C12** islands until they eventually coalesced into large domains [197].

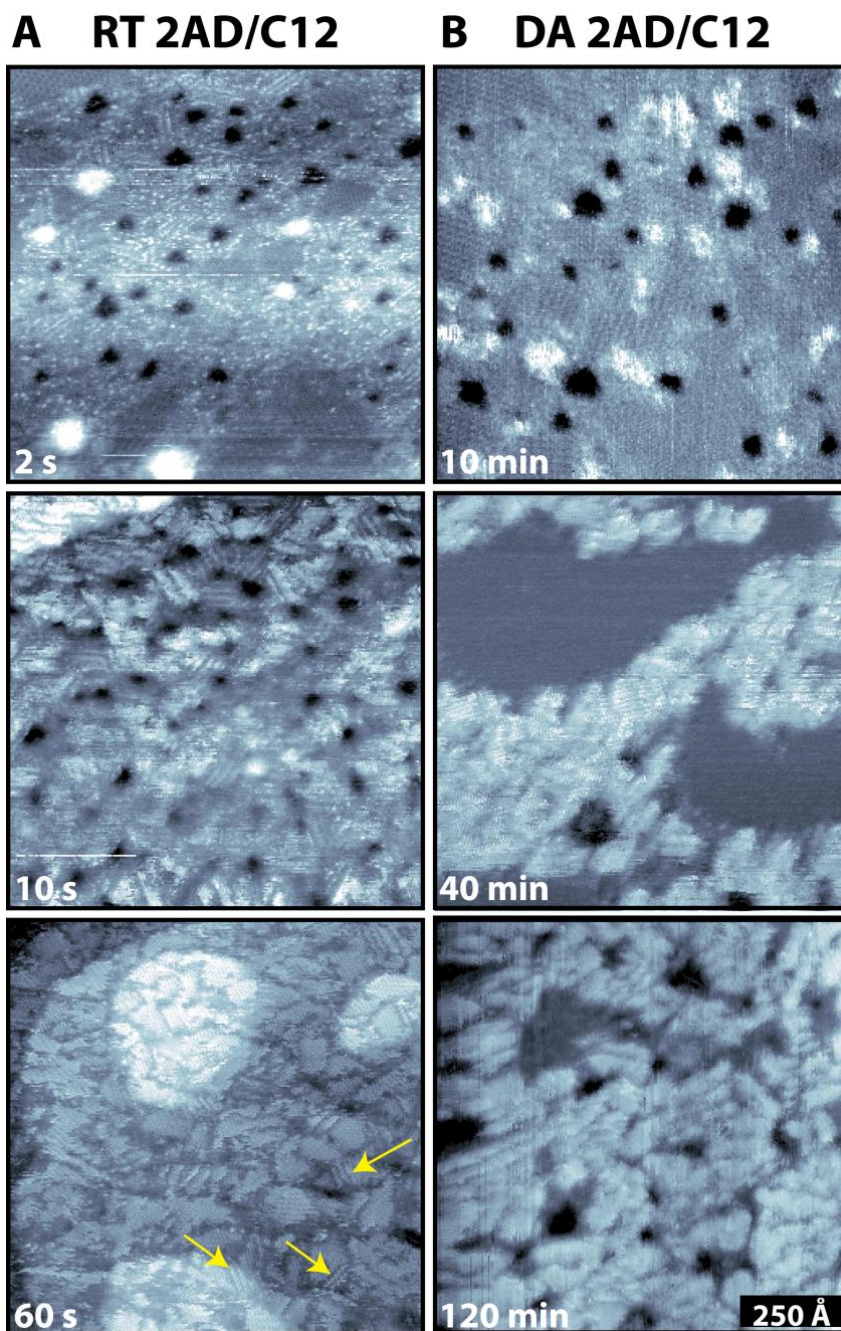


Figure 4.5 (A and B) Scanning tunneling microscopy images of mixed SAMs containing 2-adamantanethiolate (**2AD**) and *n*-dodecanethiolate (**C12**) domains fabricated by inserting **2AD** SAMs in 1 mM *n*-dodecanethiol solution for the specified times. (A) The **2AD** SAMs were prepared by immersing clean Au substrates in 1 mM 2-adamantanethiol solution at room temperature for 24 hours (**RT 2AD** SAMs). The small protruding features in the first image correspond to Au adatom islands formed during **2AD** self-assembly. (B) The **2AD** SAMs were prepared by first placing Au substrates in 1 mM 2-adamantanethiol solution at 70 °C for 2 hours, then dry-annealing the samples under nitrogen at 78 °C for 17 hours (**DA 2AD** SAMs); sample bias 0.80 V, tunneling current 2.0 pA.

As expected, the more ordered **DA 2AD** SAMs with larger domain sizes exhibit slower **C12** exchange kinetics. The displacement process for **DA 2AD** SAMs was much slower than for **RT 2AD** SAMs (Figure 4.5B). However, the initial rapid molecular exchange of disordered **2AD** regions also occurred quickly (first image of Figure 4.5B). At longer exchange times, the difference in kinetics is evident; even after 40 minutes of insertion in *n*-dodecanethiol solution, **DA 2AD** SAMs still contained large, well-ordered **2AD** domains, and 120 minutes was required to cover most of the surface with **C12**.

Important differences are observed between the displacement of SAMs of **2AD** and SAMs of its structural isomer, **1AD**. The **C12** regions in mixed SAMs formed by the short-time displacement of **RT 2AD** SAMs showed rod-like structures that grew linearly (see Figure 4.5A). In contrast, alkanethiolate regions resulting from the solution displacement of **1AD** SAMs with *n*-octanethiol, *n*-decanethiol, and *n*-dodecanethiol appear as clusters of molecules that grow radially. The different growth patterns of **C12** domains in **2AD** SAMs suggest their displacement mechanism is not precisely the same as the displacement in **1AD** SAMs; we attribute this to the different lattice structures of the original labile SAMs.

Apparent height differences in mixed **2AD/C12** SAMs can be used to infer the apparent height of the **2AD** monolayer. The apparent heights are used along with the lattice spacings (and surface coverages) to help identify molecules in mixed monolayers [220-223]. Figure 4.6 shows STM images of a binary SAM composed of both **2AD** and **C12** domains, fabricated by 40 minutes of displacement of a **DA 2AD** SAMs in 1 mM *n*-dodecanethiol solution. In Figure 4.6A, the low-contrast depressed areas correspond to **2AD** domains and the high-contrast protruding patches correspond to **C12** domains. The measured apparent height differences between **2AD** and **C12** are 3.5 ± 0.2 Å. Based on the previously measured

apparent height of **C12** regions as $12.0 \pm 0.2 \text{ \AA}$ [221], the measured apparent height of **2AD** SAMs under these conditions should be $8.7 \pm 0.2 \text{ \AA}$.

Figure 4.6B shows a highly ordered mixed SAM with **2AD** and **C12** domains, in good agreement with the expectation that well-ordered **2AD** domains are strongly resistant to **C12** exchange. On careful inspection, **C12** regions consist of several rotational domains, attributed to separate nucleation of these domains during displacement (Figure 4.6C). At high resolution (Figure 4.6D), **C12** domains show individual **C12** molecules in a hexagonally close-packed lattice in addition to the aforementioned linear patterns.

After displacement reaches completion, the predominant **C12** phase is the saturated phase where the linear hydrocarbon chains are aligned with a $(\sqrt{3} \times \sqrt{3})R30^\circ$ lattice. However, at shorter displacement times, other **C12** SAM phases were observed. Figure 4.7 shows STM images of **C12** domains after 60 minutes of exchange with a **DA 2AD** SAM. These phases resemble those previously observed for low coverage *n*-alkanethiolate SAMs [17,224-226]. Unsaturated striped phases of linear alkyl chains known as δ and χ phases (see in Figure 4.7A) are initially formed and are eventually replaced by a saturated ϕ phase (Figure 4.7B) upon continued exposure. We propose that molecular exchange between **2AD** and **C12** occurs initially at a 1:1 ratio [21,227,228], resulting in unsaturated phases due to the size disparity between **2AD** and **C12**, and that vacancies are later backfilled by additional **C12** molecules.

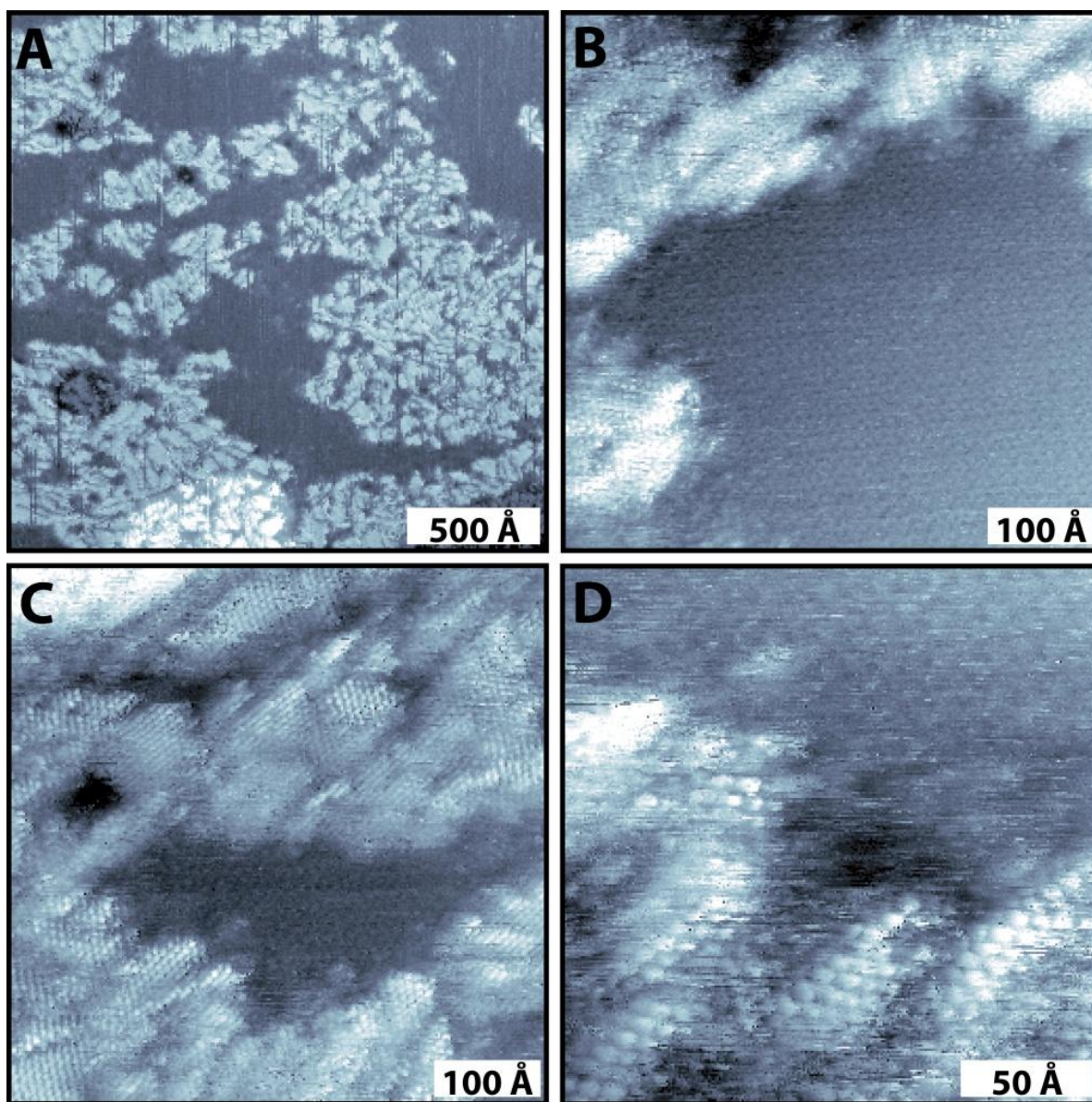


Figure 4.6 (A to D) Scanning tunneling microscopy images of a mixed SAM composed of 2-adamantanethiolate (**2AD**) and *n*-dodecanethiolate (**C12**) domains on Au{111} fabricated by inserting a **2AD** SAM into a 1 mM *n*-dodecanethiol solution. The **2AD** SAM was prepared by first placing a Au substrate in 1 mM 2-adamantanethiol solution at 70 °C for 2 hours, then dry-annealing the sample under nitrogen at 78 °C for 17 hours (**DA 2AD** SAM); sample bias 1.0 V, tunneling current 2.0 pA.

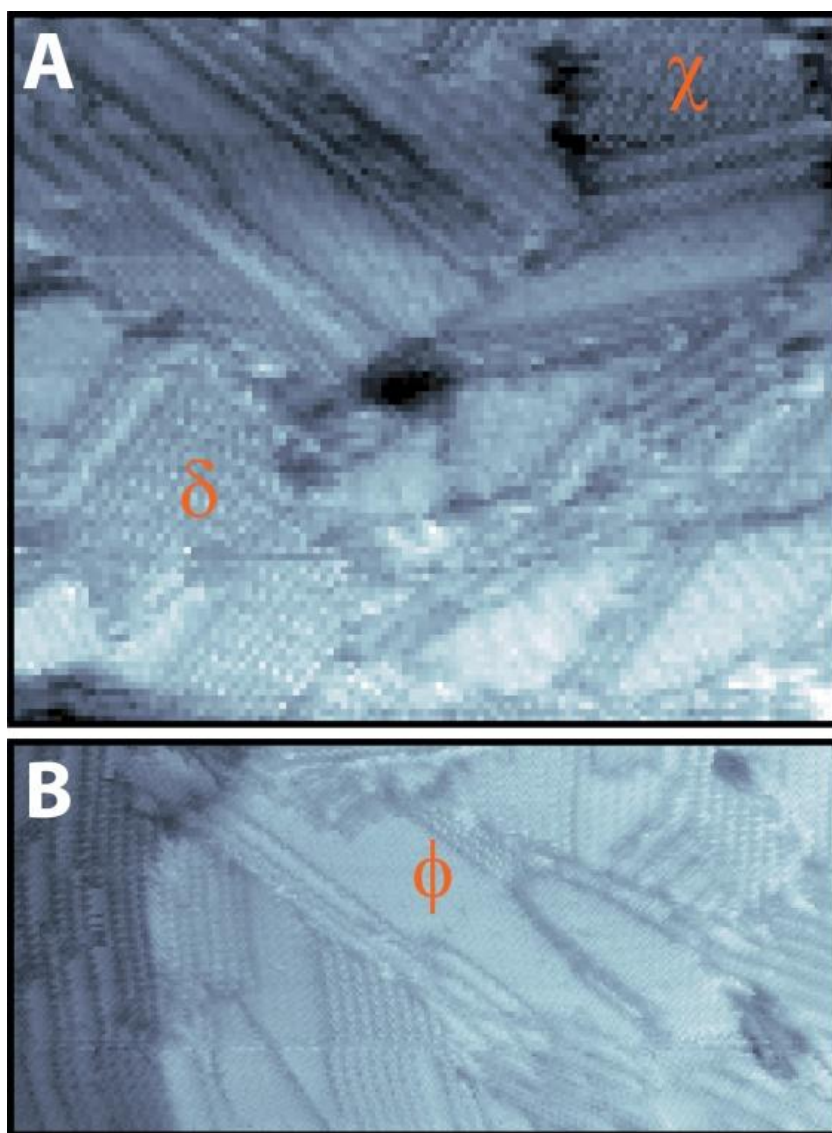


Figure 4.7 Scanning tunneling microscopy images of *n*-dodecanethiolate (**C12**) phases generated from displacement of a 2-adamantanethiolate (**2AD**) SAM with a 1 mM *n*-dodecanethiol solution for 60 minutes. The **2AD** SAM was fabricated by first placing a Au substrate in 1 mM 2-adamantanethiol solution at 70 °C for 2 hours, then dry-annealing the sample under nitrogen at 78 °C for 17 hours (**DA 2AD** SAM). (A) 715 Å × 615 Å; (B) 996 Å × 477 Å; sample bias 1.0 V, tunneling current 2.0 pA

4.3.3 Intermolecular interaction strengths and molecular packing

Weak intermolecular interactions and low molecular packing density in **1AD** SAMs were the main thermodynamic driving forces for displacement by *n*-alkanethiols. These two factors for **2AD** monolayers were quantified using cyclic voltammetry and X-ray photoelectron spectroscopy. Samples for these experiments were prepared in the same way as those used for STM studies.

The cathodic peak potential (E_p) in cyclic voltammetry offers insight into the strength of intermolecular interactions in SAMs [229-234]. Figure 4.8 shows representative voltammograms of single-component **1AD**, **2AD**, and **C12** SAMs. Respective average E_p , cathodic peak current (I_p), peak area, and the full-width-at-half-maxima (fwhm) from several voltammograms are listed in Table 4.1. The one-electron reductive desorption of the thiol from the gold electrode generates the cathodic peaks in the voltammograms. As shown in Table 4.1, the average E_p for single-component **2AD** SAMs appeared at -1076 ± 12 mV, which is slightly more positive than the average E_p for **C12** SAMs (-1113 ± 9 mV) [235], but far more negative than that observed for **1AD** SAMs (-996 ± 4 mV) [196]. A more positive E_p for the SAM implies that less energy is required to desorb each molecule reductively from the Au surface. Since the Au-S bond strength is similar for the three species described here, this suggests that the intermolecular interactions in **2AD** SAMs are weaker than in **C12** SAMs, but are apparently stronger than in **1AD** SAMs. The asymmetry in the adamantyl cage with respect to the Au-S bond provides a degree of freedom to **2AD** molecules, which evidently leads to stronger intermolecular interactions, perhaps due to different intermolecular distances of closest approach. The larger standard deviation of the average E_p for **2AD** SAMs

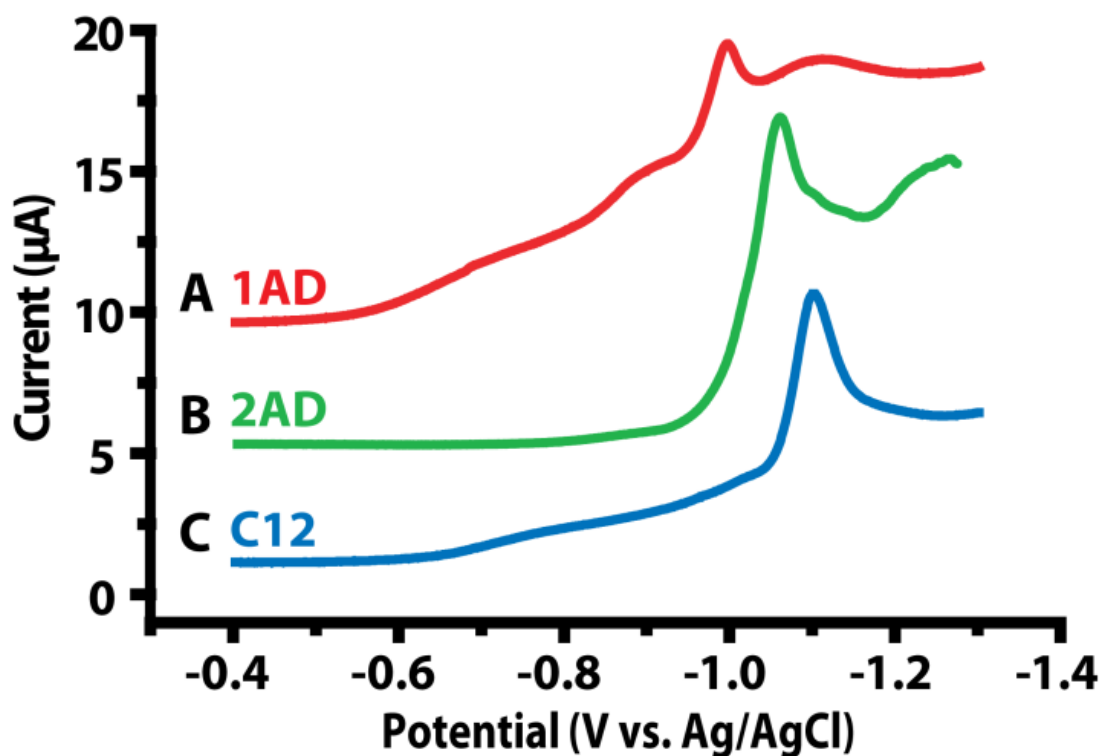


Figure 4.8 Representative voltammograms showing the reductive desorption of (A) a single-component 1-adamantanethiolate (**1AD**) SAM, (B) a single-component 2-adamantanethiolate (**2AD**) SAM, and (C) a single-component *n*-dodecanethiolate (**C12**) SAM. Baseline correction was applied to account for solution resistance and sample/electrode contact resistance using a straight line subtraction in the first of 100 mV of the sweep in which no faradaic processes occur. The traces are offset for clarity.

	Average peak potential (mV)	Average peak current (μ A)	Average peak area (μ C)	Average peak fwhm (mV)
1AD	-996 ± 4	3.2 ± 0.4	8.5 ± 1.8	58 ± 11
2AD	-1076 ± 12	5.0 ± 0.7	9.3 ± 3.0	35 ± 8
C12	-1113 ± 9	6.0 ± 1.0	14.2 ± 0.8	45 ± 9

Table 4-1 Average cathodic peak potential (E_p), current (I_p), area, and full-width-at-half-maxima (fwhm) from voltammograms of single-component 1-adamantanethiolate (**1AD**) SAMs, single-component 2-adamantanethiolate (**2AD**) SAMs, and single-component *n*-dodecanethiolate (**C12**) SAMs. All SAMs were prepared by immersing clean Au substrates in 1 mM ethanolic corresponding thiol solution at room temperature for 24 hours.

may be caused by disordered regions in **2AD** SAMs [236]. The very narrow fwhm of the cathodic peak in **2AD** SAMs may also reflect increased intermolecular interaction strengths relative to **1AD** SAMs [237,238].

The **C12/2AD** ratios for both the I_p (1.2) and the cathodic peak area (1.5) reflect the differences in molecular packing density between **C12** and **2AD** SAMs, since each molecule loses one electron during electrochemical desorption [234,239]. The smaller average I_p and cathodic peak area for **2AD** SAMs on Au{111} compared to **C12** SAMs indicate that the absolute surface coverage (number of molecules per unit area) of **2AD** SAMs is lower than for **C12** SAMs. If we consider only the unit cell of each SAM, a **C12** SAM (one molecule in a $(\sqrt{3} \times \sqrt{3})R30^\circ$ unit cell) contains 1.8 (16/9) times more molecules in the same area than a **2AD** SAM (three molecules in a (4×4) unit cell) [208]. However, disordered molecules in the **2AD** SAMs strongly influence the uncertainty in the I_p and the peak area, making direct comparisons difficult. Also, the larger average I_p and peak area of **2AD** SAMs than those of **1AD** SAMs indicate that the average number of molecules per unit area of **2AD** SAMs is slightly higher than for **1AD** SAMs. This can be rationalized by the difference of intermolecular distances between **2AD** SAMs (6.65 Å) and **1AD** SAMs (6.72 Å or 6.87 Å) [185].

Changes in XPS spectra of the mixed **2AD/C12** SAMs generated by displacement compared to single-component **2AD** and **C12** SAMs allow us to quantify the extent of displacement in exchange reactions and to monitor the change in local electronic properties of the interface between the organic layer and the underlying Au substrate. Importantly, this technique provides us with an ensemble measurement to complement the molecular-scale information obtained by STM. Figure 4.9 shows the C 1s region of the XPS spectra for single-

component **2AD** and **C12** SAMs, as well as binary **2AD/C12** SAMs created by the displacement of **RT 2AD** SAMs with a 1 mM *n*-dodecanethiol solution for 10 seconds, 1 minute, and 10 minutes. All C 1s spectra for each sample were calibrated using the Au 4f_{7/2} peak at 83.98 eV. The Au photoelectron peaks for each sample (not shown) did not change in shape or fwhm, indicating that these electrons come from the bulk gold [189]. The C 1s peaks from the spectra of the mixed **2AD/C12** SAMs shift from the lower **2AD** binding energy to the higher **C12** binding energy as the exposure time increases (see Table 4.2); a similar trend is observed for **DA 2AD** SAMs at long displacement times.

For each **2AD** SAM measurement, the observed peak is a convolution of two peaks, with an area ratio of approximately 9:1 (Inset in Figure 4.9). The smaller peak component at 285.0 ± 0.1 eV corresponds to the carbon with the thiol substituent. The larger peak component at 283.8 ± 0.1 eV corresponds to the other nine adamantyl carbons [196]. These peaks are different than the **C12** peak positions of 286.5 ± 0.1 eV and 284.9 ± 0.1 eV [240,241]. The larger intensity, lower binding-energy peak corresponds to the **C12** hydrocarbon tail. The lower binding energy of the C 1s peak in a single-component **2AD** SAM relative to a single-component **C12** SAM is attributed to the adamantyl cage structure rather than chemical shift. This binding energy difference is substantially larger than typically observed chemical shift (usually 0.1 – 0.3 eV) and the C 1s peak shifts closer to the C 1s binding energies found for graphite and diamond [205,242]. The binding energy of the C 1s peak from **2AD** SAMs, 283.8 ± 0.1 eV, is slightly lower than for **1AD** SAMs, 284.4 ± 0.1 eV [196]. This could originate from the structural flexibility of the molecule caused by tilting or twisting for stronger intermolecular interactions. Based on previous results and discussions, 2-adamantanethiolates on Au{111} may be in a more tilted orientation rather than upright on

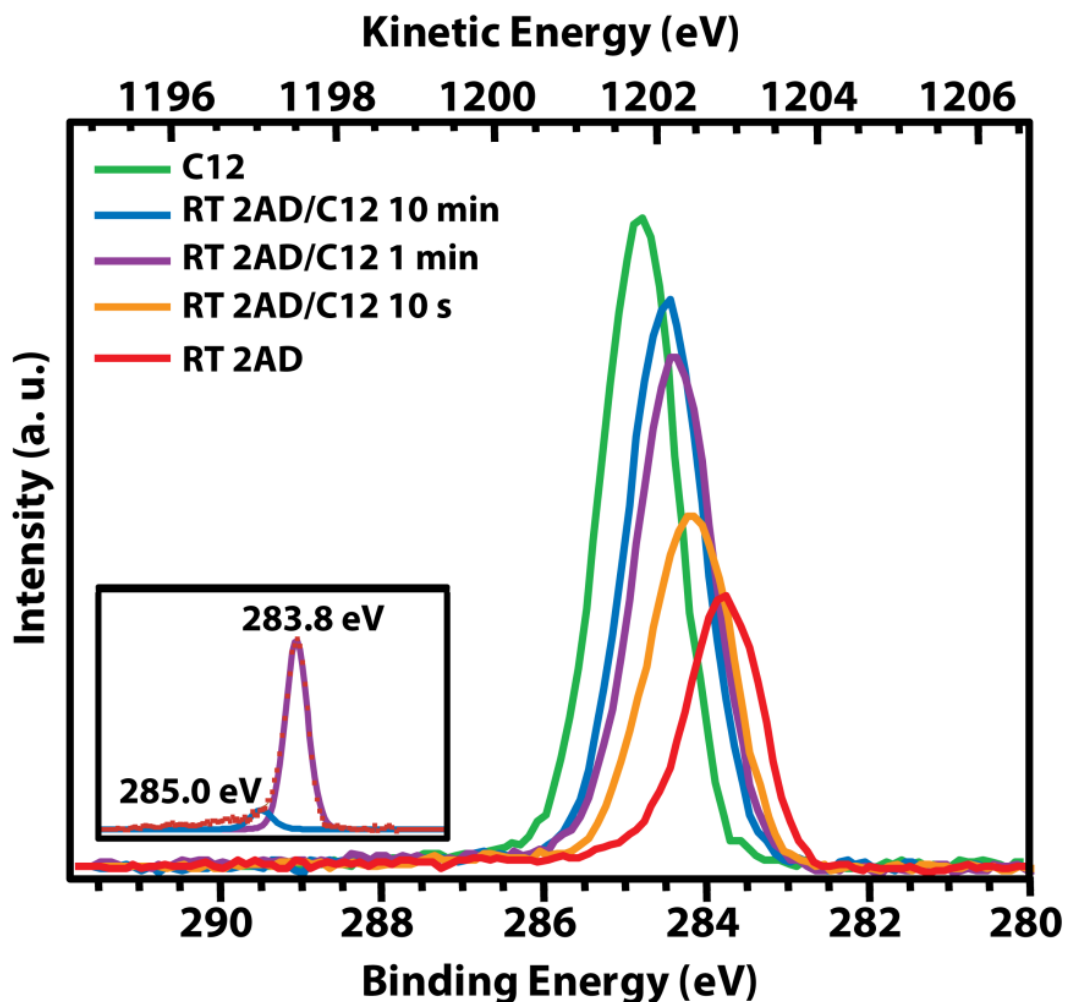


Figure 4.9 The C 1s region of XPS spectra of a single-component 2-adamantanethiolate (**2AD**) SAM, a single-component *n*-dodecanethiolate (**C12**) SAM, and binary **2AD/C12** SAMs created by displacement of **2AD** SAMs with 1 mM *n*-dodecanethiol solution for 10 seconds, 1 minute, and 10 minutes. The **2AD** SAMs were prepared by inserting Au substrates in 1 mM 2-adamantanethiol solution at room temperature for 24 hours (**RT 2AD** SAMs). The inset shows the C 1s peak of a single-component **RT 2AD** SAM fit by two Gaussian-Lorentzian line shapes with maxima at 283.8 and 285.0 eV (283.9 and 285.1 eV for a dry-annealed **2AD** SAM), and with a peak area ratio of 9:1.

	C 1s binding energy (eV)	C 1s fwhm (eV)	molecular species (%)*	
			2AD	C12
RT 2AD	283.8	1.09	100	0
RT 2AD 10 seconds	284.2	1.19	70	30
RT 2AD 1 minute	284.4	1.15	31	69
RT 2AD 10 minutes	284.5	1.13	20	80
C12	284.9	1.11	0	100
DA 2AD	283.9	1.00	100	0
DA 2AD 10 minutes	284.3	1.19	65	35
DA 2AD 40 minutes	284.4	1.21	51	49
DA 2AD 120 minutes	284.5	1.24	43	57
C12	284.9	1.11	0	100

Table 4-2 Binding energies and the full-width-at-half-maxima (fwhm) of the C 1s peaks in the XPS spectra of single-component 2-adamantanethiolate (**2AD**) SAMs, single-component *n*-dodecanethiolate (**C12**) SAMs, and mixed **2AD/C12** SAMs created by displacement of **2AD** SAMs in 1 mM *n*-dodecanethiol solution for the specified times. The **2AD** SAMs were prepared by immersing clean Au substrates in 1 mM 2-adamantanethiol solution at room temperature for 24 hours (**RT 2AD** SAMs) or by placing Au substrates in 2-adamantanethiol solution at 70 °C for 2 hours, then dry-annealing the samples under nitrogen at 78 °C for 17 hours (**DA 2AD** SAMs). *Surface fraction of each molecule, estimated from the area ratios of the individual peaks discussed in the text.

the surface. Interestingly, the C 1s binding energy range of **DA 2AD** SAMs (283.9 – 284.0 eV) is slightly higher than for **RT 2AD** SAMs (283.7 – 283.8 eV), which we attribute to the different local environment in the SAM. We infer that better ordering on large scales gives higher C1s binding energy.

The coverages of **2AD** and **C12** domains in binary SAMs were estimated from the peak areas of the C 1s region of the XPS spectra and are given in Table 4.2. The coverage of each molecule in binary SAMs was determined by comparing the peak areas of the mixed monolayers to those of the single-component **2AD** and **C12** SAMs. Calculations using Gaussian-Lorentzian fits to the spectra for the original monolayers were not applicable [196], due to the changes in the work functions of the local surface [243]. These changes can be directly observed by the change in the C 1s peak positions for mixed **2AD/C12** SAMs vs. **2AD** SAMs while maintaining similar peak widths. As shown in Table 4.2, the displacement of **DA 2AD** SAMs with **C12** is much slower compared to that of **RT 2AD** SAMs, principally resulting from the higher SAM quality - large domain sizes and fewer defects. Another factor is higher molecular coverage indicated by the relatively larger C 1s peak area in **DA 2AD** SAM.

Figure 4.10 shows the S 2p regions of the X-ray photoelectron spectroscopy (XPS) spectra for each single-component **C12**, **RT 2AD**, **DA 2AD** SAMs, and binary **2AD/C12** SAMs. In all SAMs, strong doublet peaks at 162.0 (S 2p_{3/2}) and 163.2 eV (S 2p_{1/2}) with a fixed area ratio of 2:1 (denoted as **S_A** in Figure 4.10) were observed, which are characteristic of alkanethiol or alkyldisulfide SAMs [244,245]. We observed another type of S 2p doublet peak in both **RT 2AD** and **DA 2AD** SAMs. These doublet peaks have lower binding energies (denoted as **S_B** in Figure 4.10), and were resolved into 161.0 ± 0.2 eV and 162.2 ± 0.2 eV

peaks. The S_B peak showed higher intensity in the spectra of the **RT 2AD** SAM than in the spectra of the **DA 2AD** SAM. This peak was previously observed in low-coverage *n*-alkanethiolate SAMs [246], some aromatic derivative thiol SAMs [247], and thiophene SAMs [248]. It has previously been assigned to atomic sulfur formed by C-S cleavage or another type of bound sulfur without molecular decomposition [249-253]. The presence of atomic sulfur is unlikely, given the high molecular stability and mild treatment of **2AD** SAMs, even during dry-annealing processing [254]. Based on previous studies, the presence of the S_B peak suggests that **2AD** SAMs may have another type of bound sulfur without molecular decomposition in SAMs. This low binding energy doublet peak could originate from low molecular packing density and/or the contribution of disordered molecules at domain boundaries. The work by Sabatani *et al.* showed that the peak intensity of the S_B peak observed in the spectra of aromatic thiol SAMs decreased dramatically as the number of phenyl rings increased in the SAM, increasing the molecular packing density [255,256]. Another possible explanation is that disordered **2AD** molecules may have a strong interaction between the sulfur orbital and Au atom [247]. This could also explain why the S_B peak of **RT 2AD** SAMs has higher intensity than that of **DA 2AD** SAMs; as shown in Figure 4.10. We must also consider a possible impurity effect, although we attempt to minimize the possibility of contamination by using highly pure material, careful sample preparation, and annealing samples in sealed v-vials filled with inert gas (N_2).

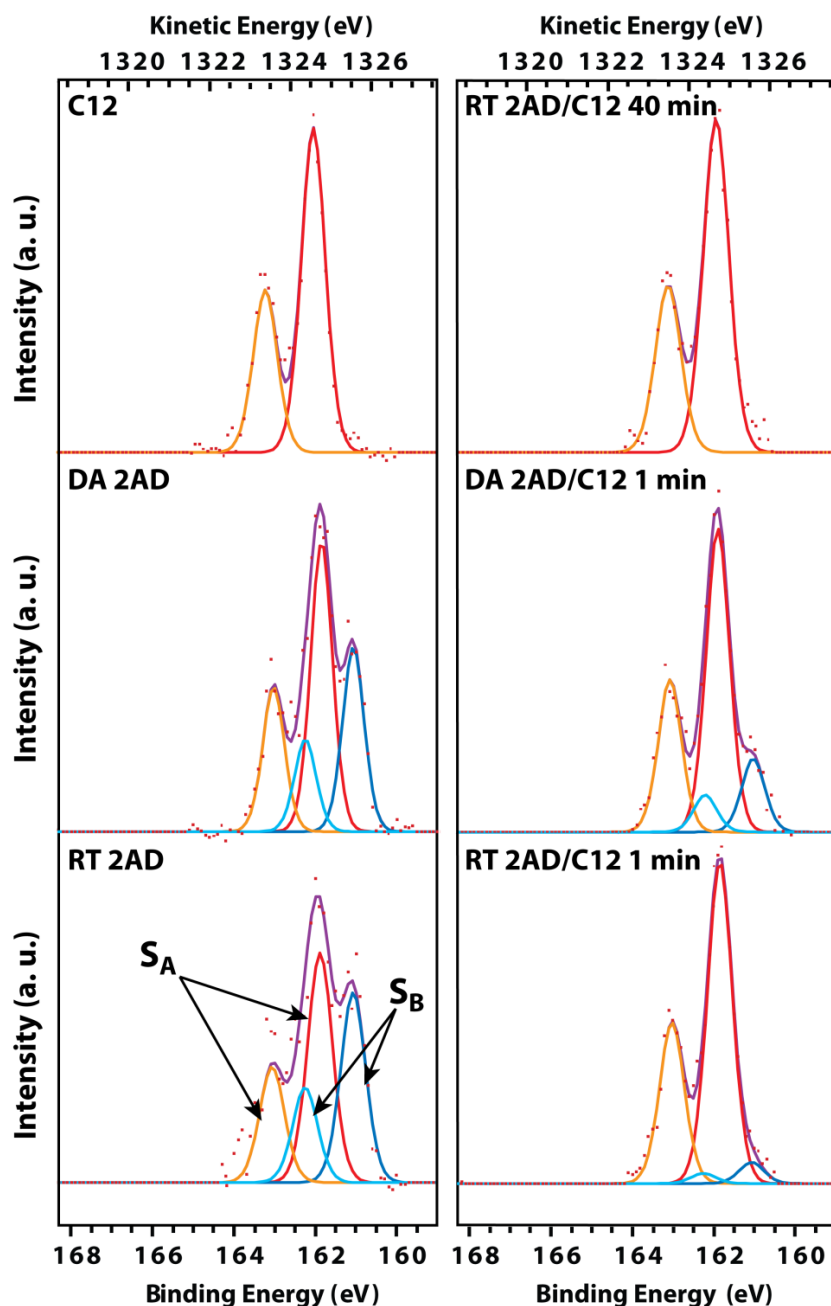


Figure 4.10 The S 2p regions of XPS spectra of single-component 2-adamantanethiolate (**2AD**) SAMs, a single-component *n*-dodecanethiolate (**C12**) SAM, and mixed **2AD/C12** SAMs created by displacement of **2AD** SAMs in 1 mM *n*-dodecanethiol solution for the specified times. The **2AD** SAMs were fabricated by immersing clean Au substrates in 1 mM 2-adamantanethiol solution at room temperature for 24 hours (**RT 2AD** SAMs) and by first immersing substrates in solution at 70 °C for 2 hours, then dry-annealing the samples under nitrogen at 78 °C for 17 hours (**DA 2AD** SAMs); Each spectrum was fit with Gaussian-Lorentzian line shapes for contributions from **S_A** peak (162.0 and 163.2 eV, red and orange, for S 2p_{3/2} and S 2p_{1/2}, respectively) and **S_B** peak (161.0 and 162.2 eV, dark blue and light blue, for S 2p_{3/2} and S 2p_{1/2}, respectively).

For all of the SAMs, the XPS data did not show any characteristic peaks caused by oxidation, sulfinates, or sulfonates [257,258], or unbound thiols/disulfides [259]. The peak intensity of **S_B** during early stages of both **RT 2AD** and **DA 2AD** SAMs was decreased dramatically, which we attribute to relatively rapid displacement on disordered **2AD** regions by *n*-dodecanethiol. Densely packed *n*-dodecanethiolate islands become dominant in the mixed SAMs, predominantly showing the **S_A** peak.

4.3.4 Kinetics of displacement in 2-adamantanethiolate SAMs

We utilized Fourier transform infrared (FTIR) spectrometry to monitor the SAM displacement reactions through completion, and thus the quantitative kinetics of solution displacement of **2AD** SAMs by **C12**. Grazing incidence FTIR spectra of **2AD** and **C12** SAMs were obtained from 800 to 4000 cm⁻¹. Characteristic spectra of each adsorbate are shown in Figure 4.11A. The **2AD** spectra display two main peaks and two shoulders attributed to C-H stretching in the region from 2750 to 3050 cm⁻¹. The 2850 and 2913 cm⁻¹ peaks are associated with symmetric and asymmetric CH₂ stretch modes, respectively [211,260]. The shoulders at 2899 and 2934 cm⁻¹ are associated with C-H stretches [261,262]. The CH₂ symmetric and asymmetric stretch modes of the **C12** spectra were positioned at 2850 and 2919 cm⁻¹, nearly overlapping those of **2AD** in the same spectral region. The CH₃ symmetric and asymmetric stretches were resolved well at 2877 and 2963 cm⁻¹, respectively [240].

The displacement of **2AD** SAMs by **C12** was studied by monitoring the emergence of the well-resolved 2877 cm⁻¹ CH₃ symmetric stretch as a function of *n*-dodecanethiol solution exposure time [211]. Both **RT 2AD** and **DA 2AD** SAMs were prepared and immersed in 1 mM ethanolic *n*-dodecanethiol solution for the specified time periods. The process was

interrupted between time intervals for analysis by FTIR and samples were then returned to the *n*-dodecanethiol solution for the next displacement cycle. Figure 4.11B shows the spectral evolution of a **DA 2AD** SAM at representative time intervals (1 minute, 10, 40, and 180 minutes) during displacement. After 180 minutes of exposure, the sample was left in solution for a total of 24 hours to reach saturation. The final spectrum was collected in order to determine the maximum **C12** coverage. The fractional coverage of **C12** was determined by taking the ratio of the interval and final peak area of the 2877 cm^{-1} CH_3 symmetric stretch of **C12**. Figure 4.11C shows the **C12** coverage as a function of displacement time for the **RT 2AD** and **DA 2AD** SAMs. As a result, **RT 2AD** SAMs were rapidly displaced, approaching saturation with **C12** in less than 20 minutes. However, **DA 2AD** SAMs were replaced by **C12** more slowly, requiring over 180 minutes to approach completion. Both results are consistent with the STM images and C 1s XPS spectral analyses.

As explained above, displacement is driven by three major factors: access to the substrate at defect sites susceptible to insertion and island nucleation, lower density of Au-S bonds relative to the displacing alkanethiolate SAM, and lattice mismatch that allows the SAM to continue to completion. While the internal domain structures of **RT 2AD** and **DA 2AD** SAMs are identical, we observed significant differences in the defect densities and the domain sizes for the two preparations (*vide supra*). Manipulating these factors, *via* annealing, influences the overall displacement process. Numerous defect sites and disordered regions in **RT 2AD** SAMs allow rapid exchange, while the improved quality of **DA 2AD** SAMs in terms of ordering, domain sizes, and smooth domain boundaries limit exchange, resulting in slower overall rates of displacement.

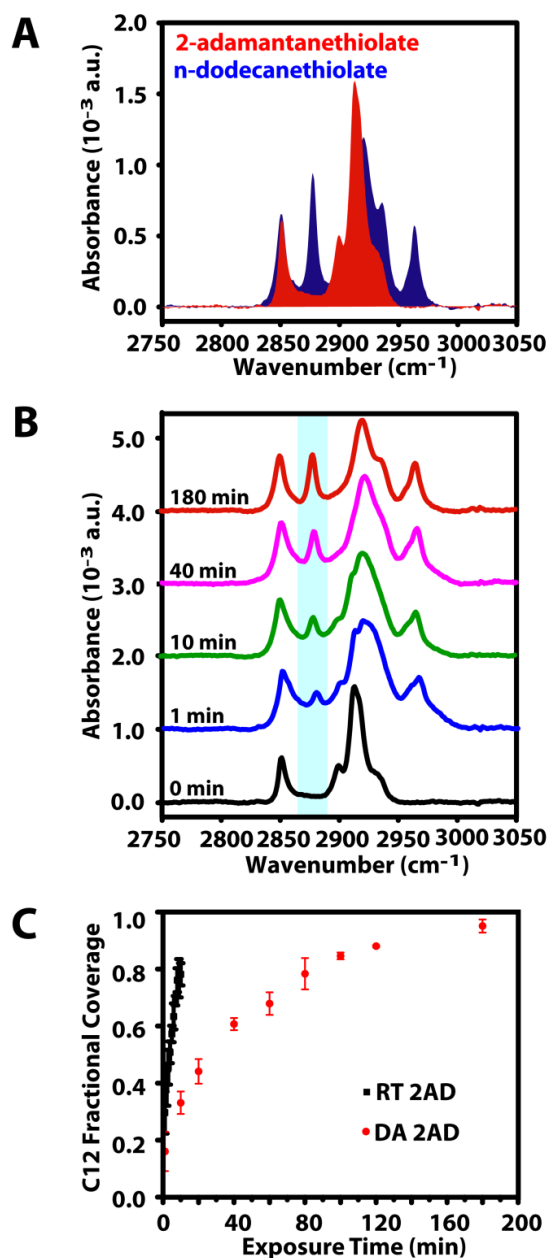


Figure 4.11 (A) Infrared spectra of the C-H stretch region of a 2-adamantanethiolate (**2AD**) SAM and a *n*-dodecanethiolate (**C12**) SAM, showing their spectral overlap (see text for mode assignments). The **2AD** SAMs were prepared by either inserting clean Au substrates in 1 mM 2-adamantanethiol solution at room temperature for 24 hours (**RT 2AD** SAMs) or by placing Au substrates in 2-adamantanethiol solution at 70 °C for 2 hours, then dry-annealing the samples under nitrogen at 78 °C for 17 hours (**DA 2AD** SAMs). (B) Spectral evolution of a **DA 2AD** SAM displaced by **C12** in 1 mM solution as a function of immersion time, 1 minute, 10, 40, and 180 minutes. (C) Plot of **C12** monolayer coverage formed by displacement of **RT 2AD** and **DA 2AD** SAMs by **C12** as a function of the specified periods of displacement time, at every 1 minute interval for **RT 2AD** SAMs, and at 1 minute, 10, 20, 40, 60, 80, 100, 120, and 180 minutes intervals for **DA 2AD** SAMs.

4.4 Conclusions

The study of **2AD** SAMs with STM offers insight into the relationships between molecular geometry and intermolecular interactions in SAMs. In **2AD** SAMs, the different position of sulfur on the adamantyl cage changes the orientations of the molecules on the surface as well as the Au-S bond configuration in comparison with previously reported **1AD** SAMs. This results in stronger and directional intermolecular interactions, which also affect substrate-molecule interactions. In the molecular exchange between **2AD** SAMs and *n*-dodecanethiols in solution, the $c(4 \times 2)$ molecular arrangement directs the linear growth of **C12** domains during initial displacement, which modulates the local work function of mixed SAMs. Increased intermolecular interactions in the ordered **2AD** domains result in resistance to displacement by **C12**. Significantly, the kinetics of molecular exchange in **2AD** SAMs can be tuned by changing the domain sizes and densities of disordered molecules. The different kinetics and structures of these SAMs offer control over molecular exchange and also indicate the importance of directional interactions in patterning surfaces at the nanoscale.

Chapter 5. Hydrogen-Bonding Networks in Amide-Containing Alkanethiolate Monolayers

5.1 Introduction

Self-assembled monolayers of alkanethiols on Au{111} continue to draw interest for the rational design of supramolecular assemblies, as well as nanoscale patterning in two or three dimensions [4,194,195,263]. Strong gold-sulfur bonds (~ 168 kJ/mol) drive spontaneous thiolate-gold adsorption [8,9,264,265], while the van der Waals interactions between hydrocarbon chains lead to monolayer ordering. These intermolecular interactions depend on the molecular shape, length, dipole moment, and functional groups [6,7,22,138,266,267]. Varying molecular structure, for example, by altering chemical functionality or geometry, changes the physical, chemical, and/or electrical properties of the SAM. Chemical patterning at the supramolecular (less than 100 Å) scale is becoming more attractive as structures and devices are miniaturized [3,4,268-270]. Generating and controlling emergent structures of nanosized objects, while modulating both local and global surface properties, continue to be important steps in advancing nanotechnology [192,193,271-276].

Incorporating amide groups into an organic backbone of a thiolate generates a robust, stable, and chemically inert SAM, which is further stabilized by a buried interchain hydrogen-bonding network [182,183,277-279]. Such assemblies have been explored as fundamental model systems for understanding electron transfer [280] and protein assemblies [278]. Detailed studies on SAMs with molecules containing one or more buried amide groups have been performed using IR spectroscopy, XPS, contact angle, electrochemistry, and STM

[277-279,281-284]. The delicate interplay between hydrogen-bonding interactions in the amide stratum and the van der Waals interactions in the hydrocarbon layer complicates the SAM structure laterally and vertically. Electrochemical reduction in an alkaline aqueous solution can be utilized to help understand these effects.

Here, we report electrochemical restructuring during the reductive desorption of SAMs containing one internal amide group, 3-mercapto-*N*-nonylpropionamide ($\text{CH}_3(\text{CH}_2)_8\text{NHCOCH}_2\text{CH}_2\text{SH}$, henceforth **1ATC9**) [279]. Electrochemical experiments on SAMs are often conducted to investigate film coverage, order, and characteristic intermolecular interactions [234,235]. Applying cathodic potentials removes carbonaceous contamination from alkanethiolate SAMs [285], or selectively eliminates one or more components in mixed SAMs [208,229,231,232,234,286-290]. In this case, electrochemical treatment modifies the local structure within SAMs; strong intermolecular hydrogen bonding results in an ordered striped phase. The electrochemical measurements also provide easy access to quantitative analysis and monitor the process in situ. Scanning tunneling microscopy supplements understanding and characterization of electrochemically induced structural changes in the hydrogen-bonding networks of these SAMs. We describe the resultant structures and discuss the mechanism of this process by which SAM structures are changed.

5.2 Experimental Section

5.2.1 Materials

The 3-mercapto-*N*-nonylpropionamide (**1ATC9**) and perdeuterated *n*-dodecanethiol (d_{12}) were purchased from Sigma-Aldrich (St. Louis, MO) and Asemblon (Redmond, WA), respectively, and used as received.

5.2.2 Self-assembled monolayer fabrication and imaging

All **1ATC9** SAMs were prepared by submersing flame-annealed Au{111} on mica substrates (Agilent Technologies, Tempe, AZ) in a 1 mM ethanolic **1ATC9** solution. The hydrogen-flame-annealed surface presents predominantly the {111} crystal face, with atomically flat terraces on the order of thousands of Ångströms. Clean substrates were placed in solution at room temperature or at 70 °C for 24 hours. Following deposition, each sample was removed from solution, rinsed with neat ethanol (200 proof, Pharmaco, Brookfield, CT), and blown dry with nitrogen gas, with rinse/dry cycles repeated 3 times. The samples were immediately used for STM imaging, electrochemical measurements, infrared spectroscopy, or X-ray photoelectron spectroscopy. All STM images were collected under ambient conditions (in air at room temperature) with a custom-built Besocke-style STM [43,44]. Thermal annealing at high temperature (>100 °C) was performed in N₂ environment overnight (18 hours) at different temperatures, 10 °C intervals up to 150 °C.

5.2.3 Electrochemistry

A custom-built electrochemical cell and a BASi Epsilon potentiostat (Bioanalytical Systems Inc., West Lafayette, IN) were used to perform electrochemical measurements as described previously [22,208]. The area of the working electrode was ~0.5 cm², defined by a perfluoroelastomer O-ring (McMaster Carr, Cleveland, OH) mounted on top of the Au{111} substrates inside the electrochemical cell and was electrochemically determined by using the Randles-Sevcik equation [209].

The electrochemical cell potential was applied with a Ag/AgCl saturated KCl reference electrode and a Pt wire counter electrode. The supporting electrolyte, an aqueous

solution of 0.5 M KOH or KCl (99.99 %, Sigma-Aldrich, St. Louis, MO) was prepared with deionized water (18.2 M Ω , Millipore Corp., Billerica, MA) and sparged with ultrahigh purity Ar for 20 min. Cyclic voltammetry was performed at reductive potentials of -200 to -1300 mV with a sweep rate of 20 mV/s. Baseline correction of voltammograms was done in the same manner as previously described [22,196]. Six representative cyclic voltammograms were selected to calculate the peak area with standard deviations for the first peak. For controlled potential electrolysis, a reductive potential of -960 mV was applied to the samples for 120 seconds. Then, the samples were rinsed with 1:1 mixture of deionized H₂O and ethanol, and subsequently ethanol separately 3 times, prior to further characterization.

5.2.4 Infrared reflection absorption spectroscopy

A Nicolet FTIR spectrometer (Thermo Electron Corp., Waltham, MA) was used to acquire all infrared spectra. The spectrometer was equipped with a liquid-nitrogen-cooled mercury-cadmium-telluride detector and a Seagull variable-angle reflection accessory (Harrick Scientific Inc., Pleasantville, NY). Dry CO₂-free air is delivered in a FTIR Pure Gas Generator (Parker-Balston, Cleveland, OH) to purge the spectrometer during spectral acquisition. The data were collected at grazing incidence reflection at 82° relative to surface normal with *p*-polarized light and a mirror speed of 1.27 cm/s with a resolution of 2 cm⁻¹. All spectra were transformed using N-B Medium apodization. The data recorded for perdeuterated *n*-dodecanethiolate (*d*₁₂) SAMs on Au{111} were used for normalization.

5.2.5 X-Ray photoelectron spectroscopy

Samples for XPS were stored under nitrogen until being transferred to the vacuum chamber, usually within 1 hour. A Kratos Axis Ultra photoelectron spectrometer with a

monochromatic Al K α source (20 mA, 14 kV) was used for acquiring spectra at a base pressure of 1×10^{-9} torr and a spot size of $300 \mu\text{m} \times 700 \mu\text{m}$. Survey spectra for each sample were taken at a pass energy of 80 eV, and high-resolution spectra of the C 1s, N 1s, O 1s, S 2p, and Au 4f regions were collected at a pass energy of 20 eV. The binding energies were calibrated to the Au 4f $_{7/2}$ peak at 83.98 eV [205]. Each peak was fit using Gaussian-Lorentzian (GL) line shapes using linear backgrounds in CasaXPS analysis software.

5.3 Results and Discussion

5.3.1 Self-assembled monolayers of 3-mercapto-*N*-nonylpropionamide

Amide group functionality within the molecular backbones plays a central role in molecular packing and orientation during self-assembly. Clegg *et al.* have demonstrated the effects of the number of amide groups and alkyl chain length on intermolecular interactions in molecular assemblies [277-279,283]. Also, phase separation spontaneously occurs in mixed SAMs of alkanethiols and amide-group-containing alkanethiols [182,183]. Two possible molecular orientations in SAMs were predicted by interchain hydrogen bonding incorporating with van der Waals forces between hydrocarbon chains [282].

Scanning tunneling microscopy images reveal two phases with different apparent heights. Figure 5.1A and B show representative STM images of single-component **1ATC9** SAMs prepared from solution at room temperature (**1ATC9 RT**) for 24 hours. The two distinct domains with a measured topographic height difference of $\sim 1 \text{ \AA}$ in a **1ATC9 RT** SAM (for the conditions indicated) are attributed to different tilt angles of the molecules within the monolayer, with regions of lower topographic height having a larger tilt angle (Figure 5.2A).

Both phases are sufficiently stable that they coexist at room temperature. Molecules are more upright in the more protruding domains that appear in STM images (domain type A, Figure 5.1A), attributed to non-linear hydrogen bonding. Molecules in the less protruding domains that appear in STM images (domain type B, Figure 5.1A) tilt to form linear hydrogen-bonding networks [282]. We note that the more protruding domain type A is dominant along step edges, substrate vacancy islands (one-atom-deep depressions in the Au substrate) that are produced during SAM deposition [10,14], and around small Au adatom islands [291]. Small disordered regions are commonly observed in domains of type A (Figure 5.1B). Domain type B is expected to be more stable than domain type A due to more favorable tilt with linear hydrogen-bonding interactions, and thus is expected to dominate in competitive environments. We note that SAMs are not equilibrium structures and are typically trapped in or can be driven into metastable states [3,20,197,270].

Substrate vacancy islands in **1ATC9** SAMs are less uniform in terms of shape, when compared to the predominantly round substrate vacancy islands present in *n*-alkanethiolate SAMs [14,215,292]. We postulate that the intermolecular hydrogen bonds kinetically slow underlying Au atom and vacancy diffusion, and thus retard Ostwald ripening of substrate vacancy islands [293-295]; further, hydrogen bond networks for **1ATC9** only form for linear networks so that there is a driving force to have straight rather than rounded edges for these substrate defects [182,183]. For **1ATC9 RT** films, most vacancies are surrounded by more protruding domains A (Figure 5.1A). We presume that such regions are sites of more frequent exchange from **1ATC9** thiols in solution. Upright molecules in type A domains are less stable and are more susceptible to molecular exchange than the tilted and linearly hydrogen-bonded

molecules in type B domains. Thus, more stable domain type B is dominant in annealed films (*vide infra*).

Solution deposition at elevated temperature (~70 °C) significantly improves the overall SAM quality; only one phase is present, the domain sizes increase, ordering improves, and the number of defect sites decreases (**1ATC9 70** SAMs, Figure 5.1C and D) [20,22,216]. Such **1ATC9 70** SAMs are predominantly in the linearly hydrogen-bonded phase, such as domain B in **1ATC9 RT** SAMs, less protruding than the surrounding matrix in STM images (Figure 5.1C and 5.2B) [10,191]. Vacancy islands are larger than those in **1ATC9 RT** SAMs, a function of Ostwald ripening at elevated temperatures [296-298]. Molecularly resolved images, such as the one shown in Figure 5.1D, reveal individual **1ATC9** molecules in hexagonally close-packed lattices [182]. All molecules adopt a uniform orientation within a single domain. Hydrogen-bonding interactions can improve registry between domains, where adjacent domains with unmatched directionality appear to interact without distinct domain boundaries. The inset in Figure 5.1D shows individual molecules with features that appear extended in one direction. This shift is independent of scanning direction, indicating that it is a manifestation of the linear hydrogen-bonding (rather than thermal drift or an imaging artifact, see Figure 5.3). The linear hydrogen bonding in amide regions affects molecular shapes in STM images and SAM structures. Molecules tilt and twist to maximize hydrogen-bonding; this yields oval shapes in STM images. This distortion originates from molecular orientation in self-assembly rather than piezoelectric drift during STM imaging [187]. Various scanning directions did not affect the molecular shapes in images, as shown in Figure 5.3.

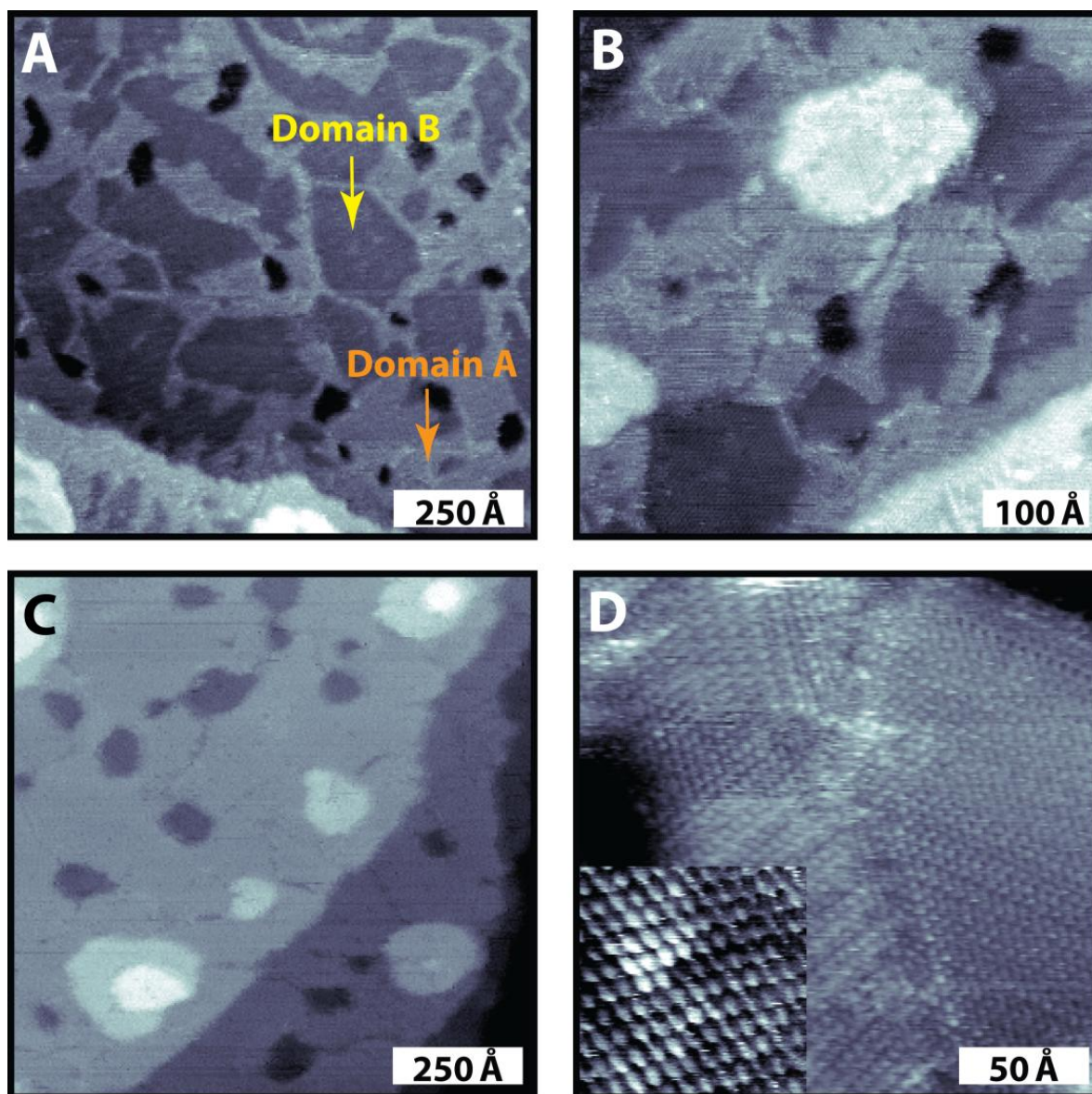


Figure 5.1 Scanning tunneling microscopy images of **1ATC9** self-assembled monolayers (SAMs) on Au{111}. Samples were fabricated in solution either at room temperature (A and B, **1ATC9 RT** SAMs) or at 70 °C (C and D, **1ATC9 70** SAMs) for 24 hours; sample bias -1.0 V, tunneling current 1.0 pA. The round features that appear more protruding in (B and C) correspond to Au adatom islands formed during assembly.

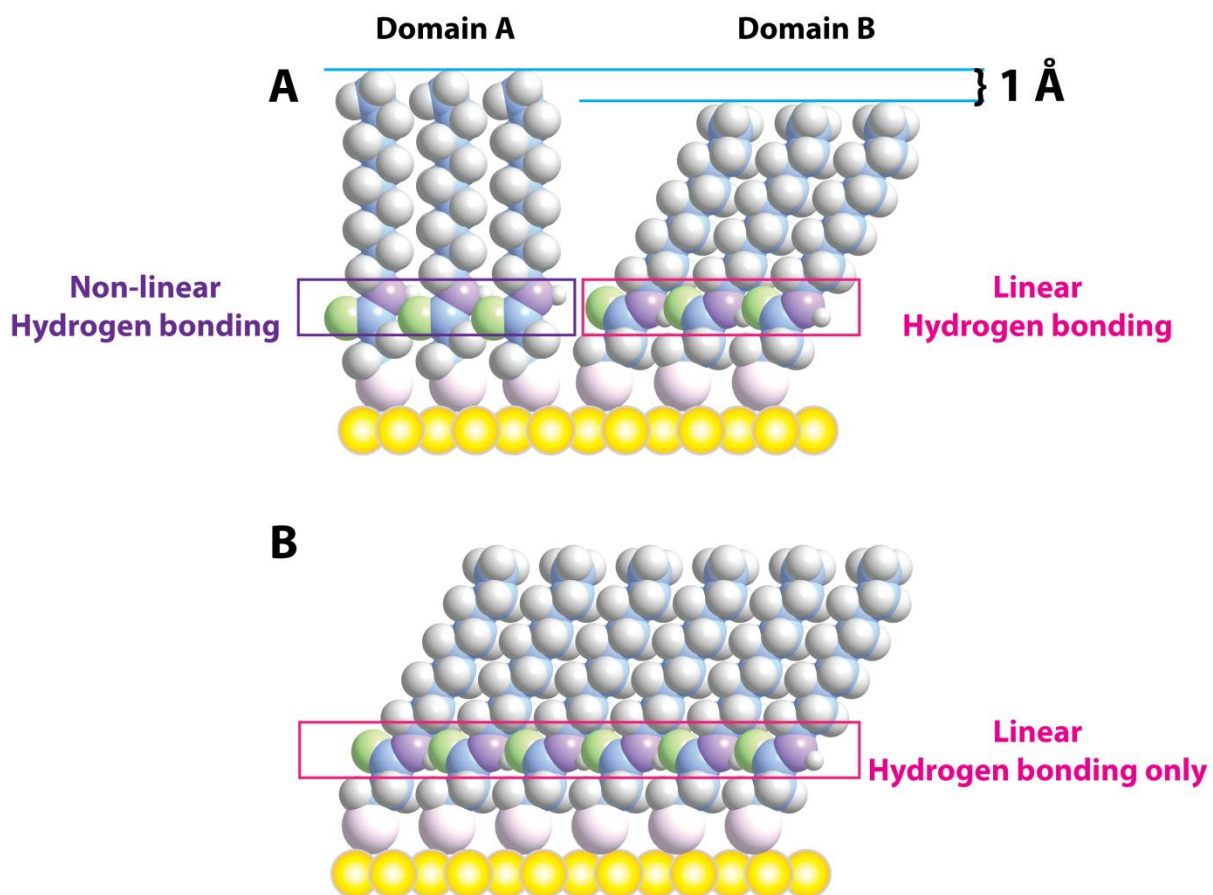


Figure 5.2 A schematic illustration of the molecular orientation in (A) **1ATC9 RT** SAMs and (B) **1ATC9 70** SAMs with difference in Hydrogen-bonding linearity.

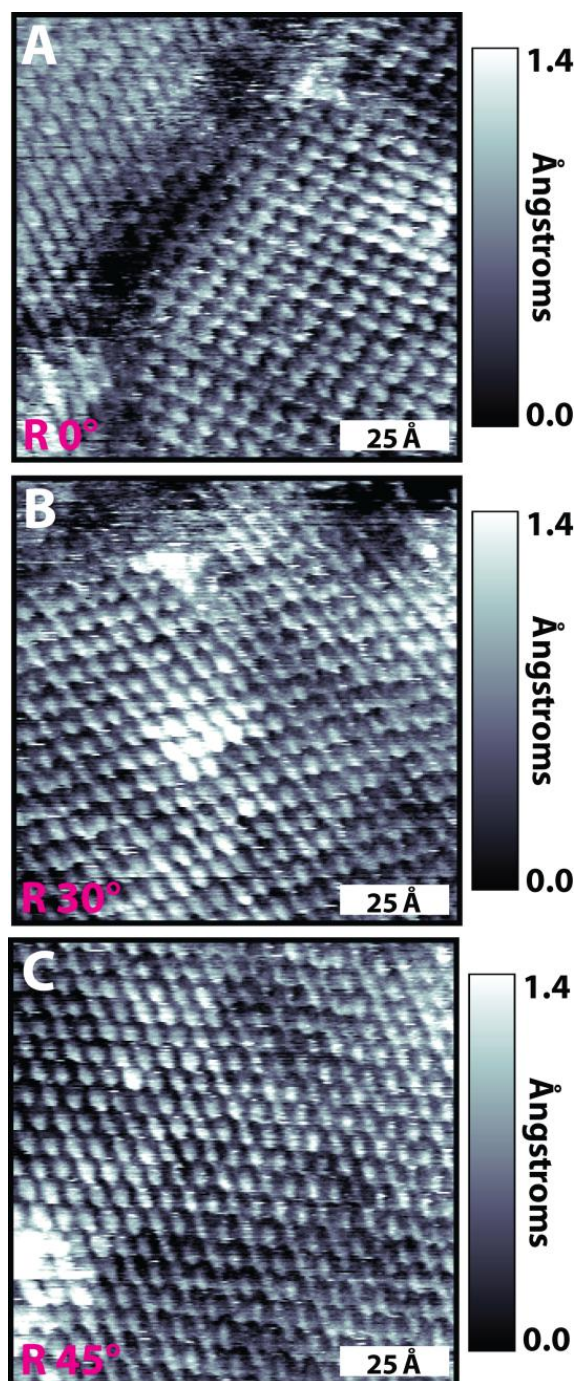


Figure 5.3 Sequential scanning tunneling microscopy images of **1ATC9** self-assembled monolayers (SAMs) on Au{111} prepared by placing Au substrates in 1 mM **1ATC9** solution at 70 °C for 24 hours (**1ATC9 70 SAM**); sample bias -1.0 V, tunneling current 1.0 pA. The fast scan direction was rotated counterclockwise by (A) 0° , (B) 30° , and (C) 45° . The oval shape of molecules in one direction is independent of scanning direction, and is attributed to molecular tilt to maximize hydrogen bonding.

5.3.2 Thermal stability

The linear hydrogen-bonding network of buried amide functionality in crystalline **1ATC9** monolayers provides high thermal stability. Figure 5.4 shows STM images of dry-annealed **1ATC9** SAMs at 120 °C for 18 hours after solution deposition at room temperature (Figure 5.4A) and at 70 °C (Figure 5.4B) for 24 hours. Such annealing conditions generally cause catastrophic thermal desorption for *n*-alkanethiolate SAMs [214]. Domains of dry-annealed **1ATC9** SAM remain intact at this temperature, and in well-ordered arrangements. The protruding straight molecular rows (arrows in Figure 5.4A) on dry-annealed **1ATC9 RT** SAMs indicate a structural change within the SAMs that is evident after thermal treatment.

The absence of such features in dry-annealed **1ATC9 70** SAMs (Figure 5.4B) suggests that the linear hydrogen-bonding network is robust, and is not perturbed by annealing at this temperature. Some molecules at domain boundaries were desorbed when the film was held at 130 °C for 18 hours, but otherwise no substantial differences were observed. Catastrophic desorption occurs after dry-annealing at 145 °C for 18 hours, leaving small patches of molecules with exposed bare gold surfaces (image not shown) [20]. As the number of internal hydrogen bonds increases, the threshold temperature for thermal desorption goes up. For example, Hutchison and coworkers showed that thermal desorption of alkanethiolate SAMs containing three amide groups occurs above 175 °C in argon [278].

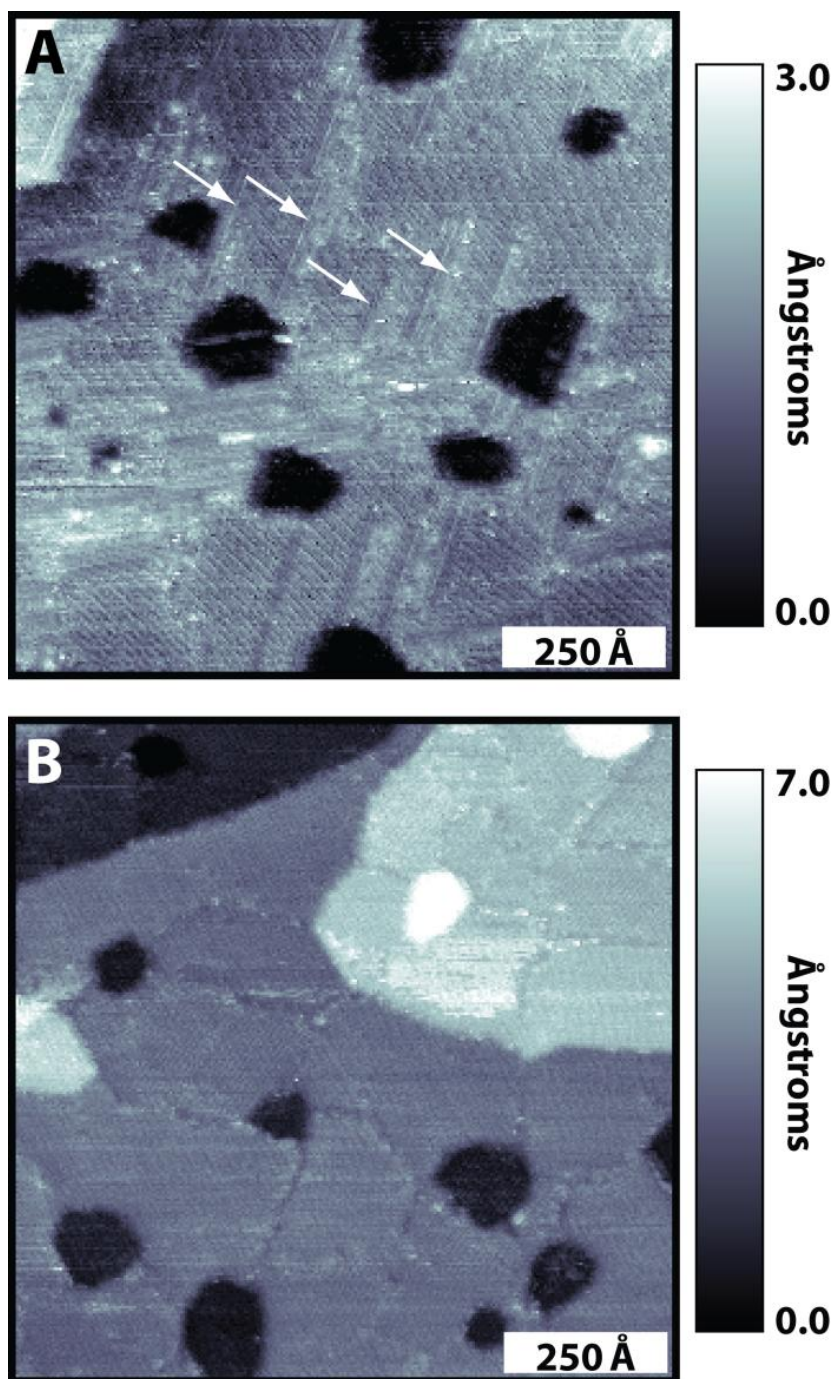


Figure 5.4 Scanning tunneling microscopy images of **1ATC9** self-assembled monolayers on Au{111} after dry-annealing at 120 °C for 18 hours. The samples were fabricated by immersing a clean Au substrate in 1 mM ethanolic solution (A) at room temperature and (B) at 70 °C for 24 hours. Each was then dry-annealed in a N₂ atmosphere: sample bias -1.0 V, tunneling current 1.0 pA. The protruding round features in (B) correspond to Au adatom islands formed during assembly, while depressions are vacancy islands.

5.3.3 Reductive desorption

Cyclic voltammetry is an effective analytical tool to measure the intermolecular interaction strength, degree of molecular order, and molecular coverage of SAMs [20,196,197]. Figure 5.5A displays representative cyclic voltammograms of single-component **1ATC9** SAMs formed on Au{111} with 0.5 M KOH aqueous solution at 20 mV/s scan rate. The SAMs were deposited from solution at room temperature (**1ATC9 RT** SAMs, blue trace) and at 70 °C (**1ATC9 70** SAMs, red trace) for 24 hours. The **1ATC9** SAM shows two reductive peaks, rather than the single peak observed in one-electron desorption of short alkanethiolate SAMs. The first peaks around ~900 mV have a ~40 mV full-width-at-half-maxima (fwhm), while the second peaks have much larger fwhm, at ~100 mV. Although **1ATC9 RT** SAMs consist of two phases, these two peaks do not correlate to the two individual phases in SAMs (*vide infra*), as the single-phase **1ATC9 70** SAMs also have two cathodic peaks.

The monolayer structure directly influences the first peak in voltammograms (Figure 5.5A); the first peak is centered at -920 and -950 mV for **1ATC9 RT** and **1ATC9 70** SAMs, respectively. Also, the -950 mV peak area of the **1ATC9 70** SAM (peak area $3.1 \pm 0.5 \mu\text{C}$) is nominally smaller than that for the **1ATC9 RT** SAM (peak area $4.1 \pm 0.2 \mu\text{C}$). The higher long-range order and increased intermolecular interaction strength by better packing and linear hydrogen bonding in **1ATC9 70** SAMs create a higher reduction threshold compared to **1ATC9 RT** SAMs. The smaller area of the first peak in the **1ATC9 70** SAM indicate that fewer molecules were desorbed at the first reduction than for the **1ATC9 RT** SAM. The second reductive desorption in both SAMs occurs around -1100 mV with broad

potential range. Substantially broad second peaks on both SAMs likely originate from reductive desorption of molecules in less-ordered and loosely packed structures [236].

Two cathodic peaks have been observed in long-chain alkanethiolates in KOH(aq) solution [239,299,300] and was attributed to their lower solubility or to pH decreases in electrolyte solution [299,301]. The absence of an oxidative readsorption peak in Figure 5.5A indicates that **1ATC9** thiolates are sufficiently soluble in 0.5 M KOH (aq) solution to eliminate this possibility. The presence of hydroxide (OH^-) ions is a key feature of the multistep electrochemical reaction in **1ATC9** SAMs, rather than an effect of low solubility. Interestingly, in 0.5 M KCl (aq), the reductive desorption only occurs at -870 mV, and displays no oxidative readsorption peak (Figure 5.5B), in contrast to the voltammetric cycle of **C12** SAMs (Figure 5.5C) [302]. Dodecanethiolates are less soluble in 0.5 M KCl (aq) solution, remaining near the surface, and oxidatively readsorbing to the surface.

5.3.4 Controlled potential electrolysis

Controlled potential electrolysis was used in the reductive desorption of **1ATC9** molecules from the monolayer. The potential is held constant and sufficiently negative to cause rapid reduction and is maintained at this value until only the reduced species is present in solution [303]. Based on the controlled potential electrolysis (CPE) results, the current passed in molecular desorption occurs primarily in the first 10 seconds and then reaches steady state (Figure 5.6).

The structural response of the **1ATC9 70** SAM to the first step of the electrochemical reduction was investigated by STM, infrared absorption spectroscopy (IRRAS), and XPS. Scanning tunneling microscopy enables high-resolution imaging of structural changes. A

reductive potential of -960 mV was applied to **1ATC9 70** SAMs for 120 seconds and the SAM was then immediately imaged by STM (Figure 5.7). The monolayer structure is transformed into a striped pattern in a lying-down phase, with a measured corrugation spacing of ~ 10 Å; in agreement with a $(5 \times \sqrt{3})$ lattice [215,304,305]. Protruding stripes in STM images correspond to two rows of adjacent sulfurs, with **1ATC9** molecules laying down perpendicular to the rows (a corrugation depth is ~ 1.5 Å). The depressed gap indicates that the entire alkyl chains are physically bound to the Au surface. Stripe length appears consistent with average annealed **1ATC9** domain size. We cannot determine analytically whether linear hydrogen bonds in untreated domains correspond to stripe direction. The stripe patterns reflect the three-fold symmetry of the Au{111} surface (arrows in Figure 5.7A). The high-resolution STM image in Figure 5.7B shows the presence of an unstable, mobile, disordered phase, and bare gold surface around substrate vacancy islands [20].

Infrared reflectance absorption spectroscopy provides complementary details of SAM structure including molecular conformation, packing and overall uniformity [306-309]. Grazing incidence FTIR spectra were collected for **1ATC9** SAMs before and after the CPE experiments described above. Figure 5.8 shows an overlay of spectra in the characteristic regions for aliphatic ($2800 - 3000\text{ cm}^{-1}$) and amide ($1100 - 1800\text{ cm}^{-1}$) absorptions, respectively. Both regions of the untreated **1ATC9** SAMs are similar to those in previous reports [279,282], while CPE causes large changes in relative intensities.

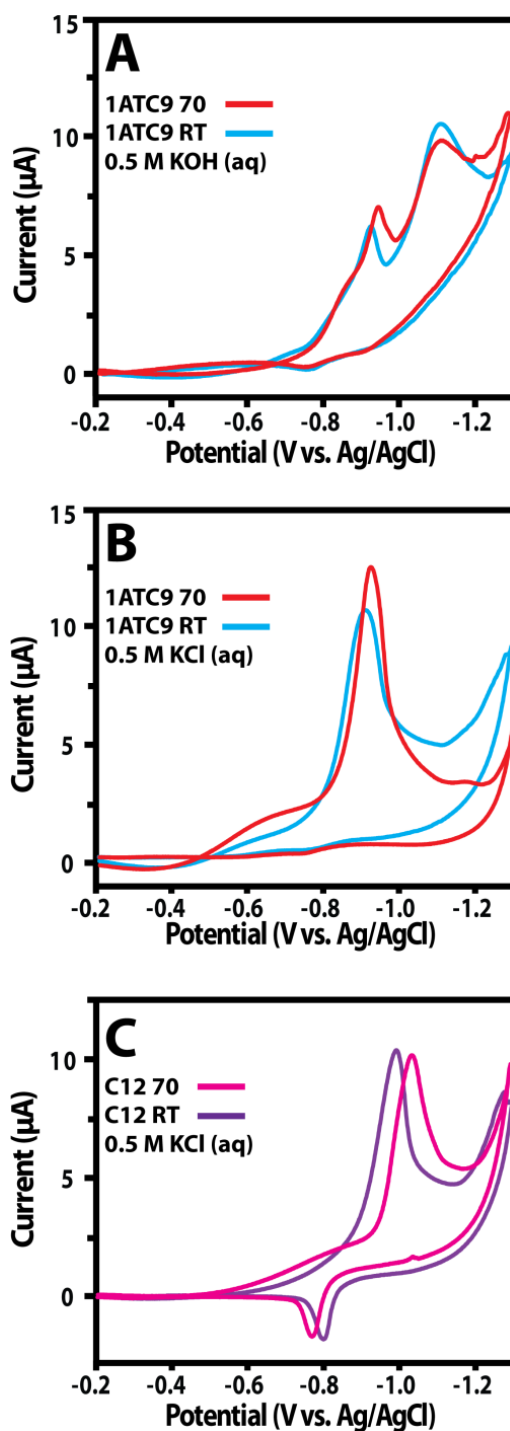


Figure 5.5 (A and B) Cyclic voltammograms of **1ATC9** SAMs and (C) **C12** SAMs on Au{111} with (A) 0.5 M KOH and (B and C) 0.5 M KCl (pH \sim 7) aqueous (aq) solutions at 20 mV/s. The SAMs were prepared by placing clean substrates in 1 mM ethanolic solution of **1ATC9** or **C12** at room temperature and at 70 °C for 24 hours. The appearance of oxidative readsorption only in **C12** SAMs not in **1ATC9** SAMs, indicates that the multistep reduction in **1ATC9** SAMs is not from decreased solubility in KCl (aq).

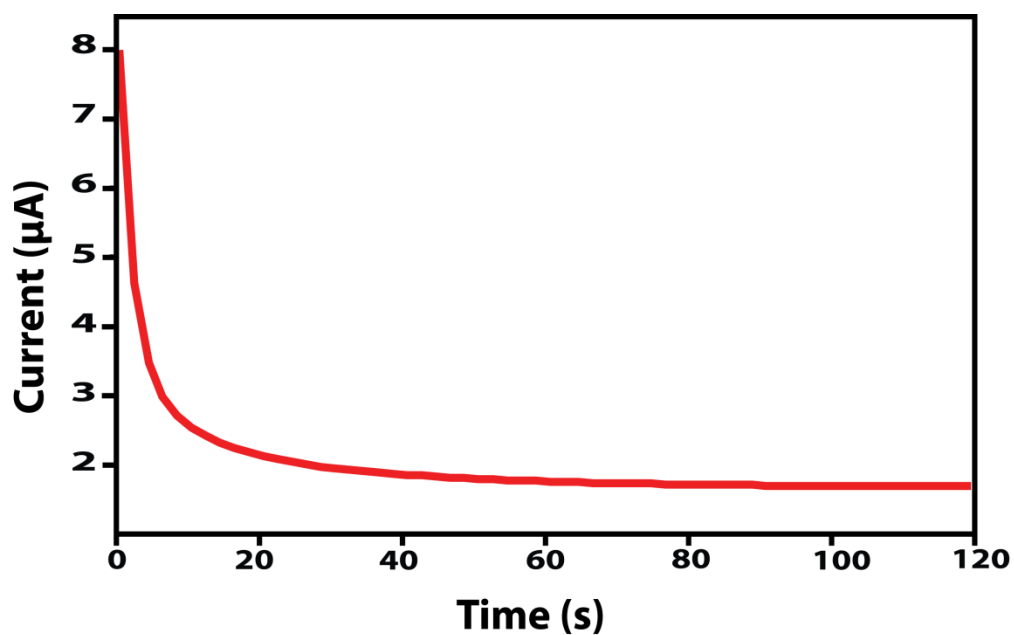


Figure 5.6 Current vs. time plot during controlled potential electrolysis on **1ATC9 70** SAMs. A reductive potential of -960 mV was applied to the **1ATC9 70** SAM for 120 seconds. The current from desorbed **1ATC9** molecules from the monolayer drops rapidly in the first 10 seconds and remain steady, indicating the surface is no more reductive.

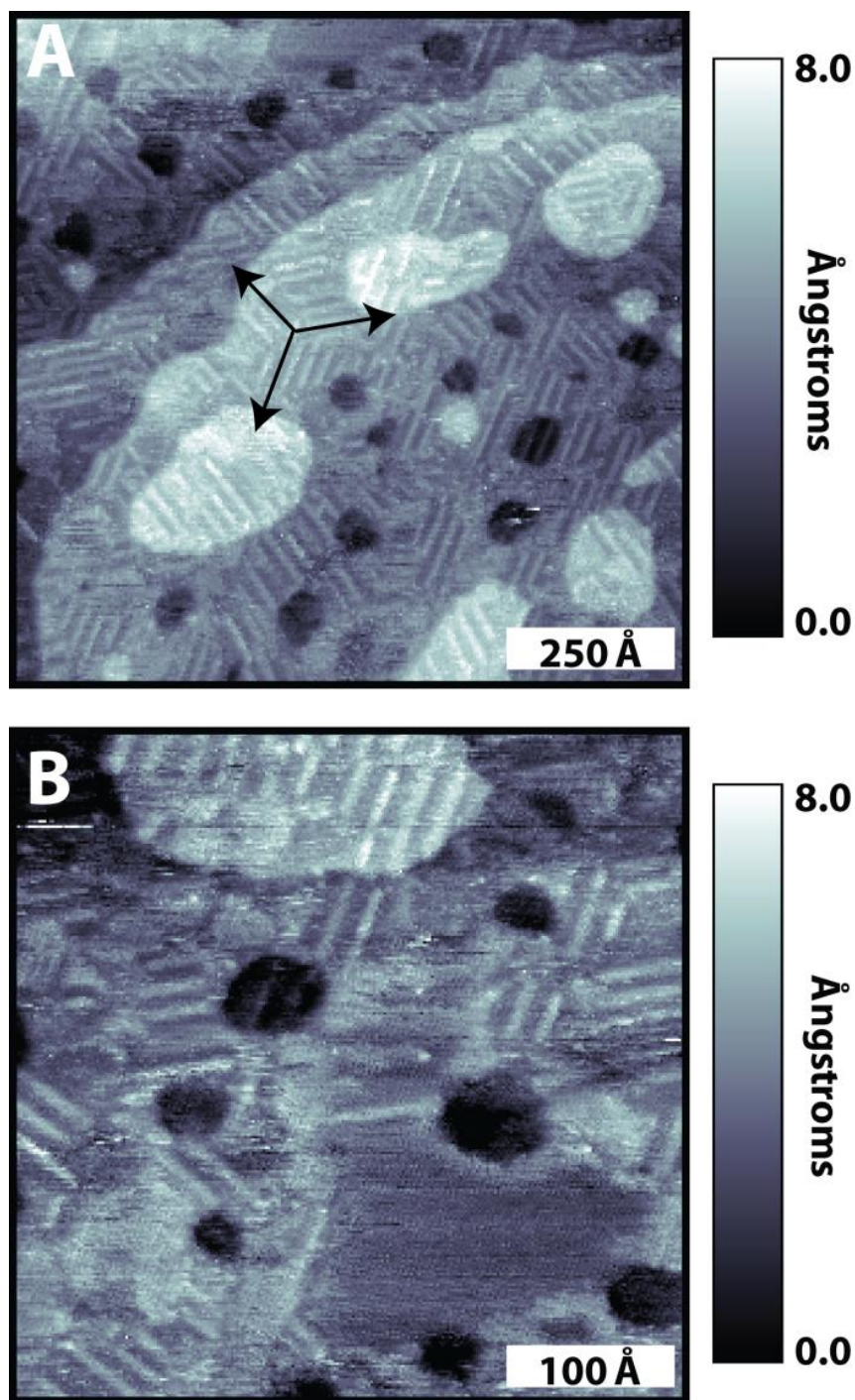


Figure 5.7 Scanning tunneling microscopy images of electrochemically processed **1ATC9** SAMs on Au{111}. The SAMs were fabricated by inserting clean substrates in 1 mM **1ATC9** solution at 70 °C for 24 hours, then applying a reductive potential of -960 mV for 120 seconds; sample bias -1.0 V, tunneling current 1.0 pA. The round protruding features correspond to Au adatom islands formed during self-assembly. The stripe patterns are oriented in three directions rotated by 120° with respect to each other.

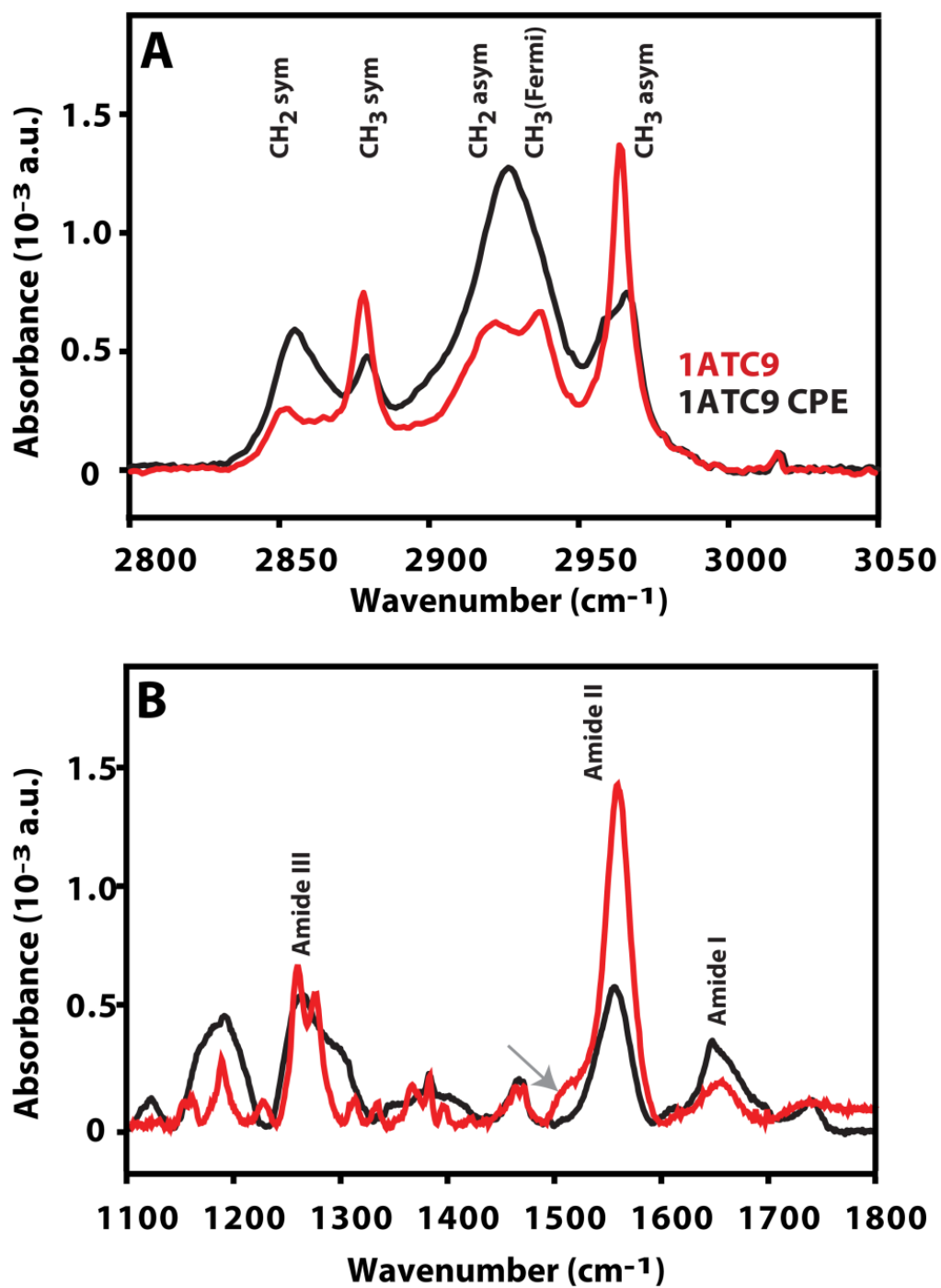


Figure 5.8 The FTIR spectra of **1ATC9** SAMs (A) in the high-frequency C-H region and (B) in the amide region. The SAMs were fabricated by inserting clean substrates in 1 mM **1ATC9** solution at 70 °C for 24 hours (**1ATC9**, red trace), then applying a reductive potential of -960 mV for 120 seconds (**1ATC9** CPE, black trace).

The IR spectra collected between 2800 and 3000 cm^{-1} (Figure 5.8A, red trace) show characteristic peaks similar to those reported for both *n*-alkanethiolate and amide-containing alkanethiolate films; CH_2 symmetric and asymmetric stretches at 2852 and 2919 cm^{-1} , respectively, and CH_3 symmetric and asymmetric stretches at 2877 and 2963 cm^{-1} , respectively. The peak at 2934 cm^{-1} is commonly attributed to a Fermi resonance of CH_3 [240].

The relative intensities of these SAM absorption peaks provide insight into the orientation of the alkyl chains and the positions of the terminal groups, a function of the selection rules for IR absorption of molecules adsorbed on metal surfaces (although quantitative analysis of chain orientation is hampered due to the uncertainty of the ethylene linker orientation below the amide functionality) [243]. A pristine **1ATC9** film shows weak CH_2 absorption, for both symmetric and asymmetric stretches. The low CH_2 peak intensity, despite the high coverage of alkyl chains, is interpreted as the film being highly ordered, with the CH_2 bonds nearly parallel with respect to the gold surface. The CH_3 symmetric stretch has been used as an indicator of coverage, as it has a weaker dependence on orientation than the methylene stretches [240]. Methyl intensities in **1ATC9** SAMs closely match those reported for *n*-alkanethiolate SAMs, indicating well-packed monolayers.

After conducting CPE experiments, the relative intensities of all peaks were dramatically altered (Figure 5.8A, black trace). The CH_3 symmetric stretch (2877 cm^{-1}) decreases in intensity, consistent with decreased coverage in the film. This seems, at first, inconsistent with the large *increase* in the intensity of the CH_2 asymmetric stretch. After CPE, the high order of the film collapses, allowing the alkyl stretches more orientational freedom, resulting in more intense absorption despite lower absolute coverage.

Insight into the amide layer, including the hydrogen-bonding network in **1ATC9** SAMs, comes from carbonyl stretches in the region from 1100 to 1800 cm^{-1} . For the pristine film, the peak assigned as amide I (C=O stretch, $\sim 1640 \text{ cm}^{-1}$), Figure 5.8B, is weak and broad, a result of the selection rules that mask the near-parallel C=O bond in a linear hydrogen-bond configuration [279,283]. The intense, sharp amide II peak (N-H in-plane bend, $\sim 1560 \text{ cm}^{-1}$) reflects hydrogen bonding and *trans* conformation of amide moieties. A weak signature of the non-hydrogen-bonded state is observed at $\sim 1510 \text{ cm}^{-1}$ (an arrow in Figure 5.8B) [282]. The amide III doublet (N-H in-plane bend and C-N stretch at 1287 and 1251 cm^{-1}) is another signature of the *trans* conformation of the amide functionality, expected for a secondary amide group [282,306,308].

The intensity of the amide I peak increases after CPE; carbonyl orientational freedom increases after partial desorption, enhancing the sensitivity of the group to IR. The amide II peak is substantially reduced after electrochemical treatment, but the hydrogen bonding network remains in its *trans* conformation. The torsional motion between the N-H and C-H moieties was restricted after CPE, showing a broad amide III peak with no splitting.

X-ray photoelectron spectroscopy determines the elemental composition of **1ATC9** SAMs, as well as the chemical changes induced by electrochemical processing. Figure 5.9 shows a collection of high-resolution XPS spectra for the C 1s, N 1s, O 1s, S 2p, and Au 4f regions for **1ATC9** SAMs before and after CPE. As expected, XPS data indicate the presence of carbon, nitrogen, oxygen, and sulfur. Table 5.1 summarizes the binding energy of each peak before and after CPE as well as the peak area ratio (%) in which each peak area for spectra acquired following CPE was divided by the peak area observed prior to CPE. The intense C 1s (alkyl) peak at 285.1 eV is due to the alkyl layer predominantly present on top of

the film. The higher binding energy peak in C 1s (287.5 eV) and the energy peak in N 1s (399.3 eV) are from the carbonyl carbon and the nitrogen in the amide group. While the O 1s peak from the carbonyl group appears at 530.9 eV, the small peak at 533.0 eV in the O 1s region corresponds to hydroxyl oxygen possibly from adsorbed ethanol or water remaining after sample preparation. The S 2p peaks at 162.0 eV (S 2p_{3/2}) and 163.2 eV (S 2p_{1/2}) with a 2:1 ratio, indicate sulfur bound to gold, as typically observed for alkanethiol and alkyldisulfide SAMs [247].

The CPE experiment generally results in XPS peak intensity decreases, with the exception of the Au 4f peak. Peaks shift to the lower binding energy in all cases, except S 2p and Au 4f. The peak intensity decreases in the C 1s, O 1s, and N 1s regions and the increased intensity in the Au 4f region are consistent with monolayer thinning, though all elements observed prior to CPE are still detected (see Table 5.1), indicating molecules remain on the surface. The peak shifts to lower binding energy for the C 1s, O 1s, and N 1s are a result of the change in the dipole-dipole interactions in the new structure [145,243,310]. The C 1s binding energy 284.4 eV was mainly assigned to striped alkyl chains [246]. The minor shift in both the N 1s and O 1s regions relative to the larger C 1s shift reveals that hydrogen bonding interactions between amides remain after CPE. We do not observe new chemical signatures after CPE, indicating no chemical reactions in the remaining molecules. These XPS results are consistent with a striped phase of **1ATC9** SAMs, as shown in Figure 5.9. Full details of the mechanism of reorganization remain open to interpretation.

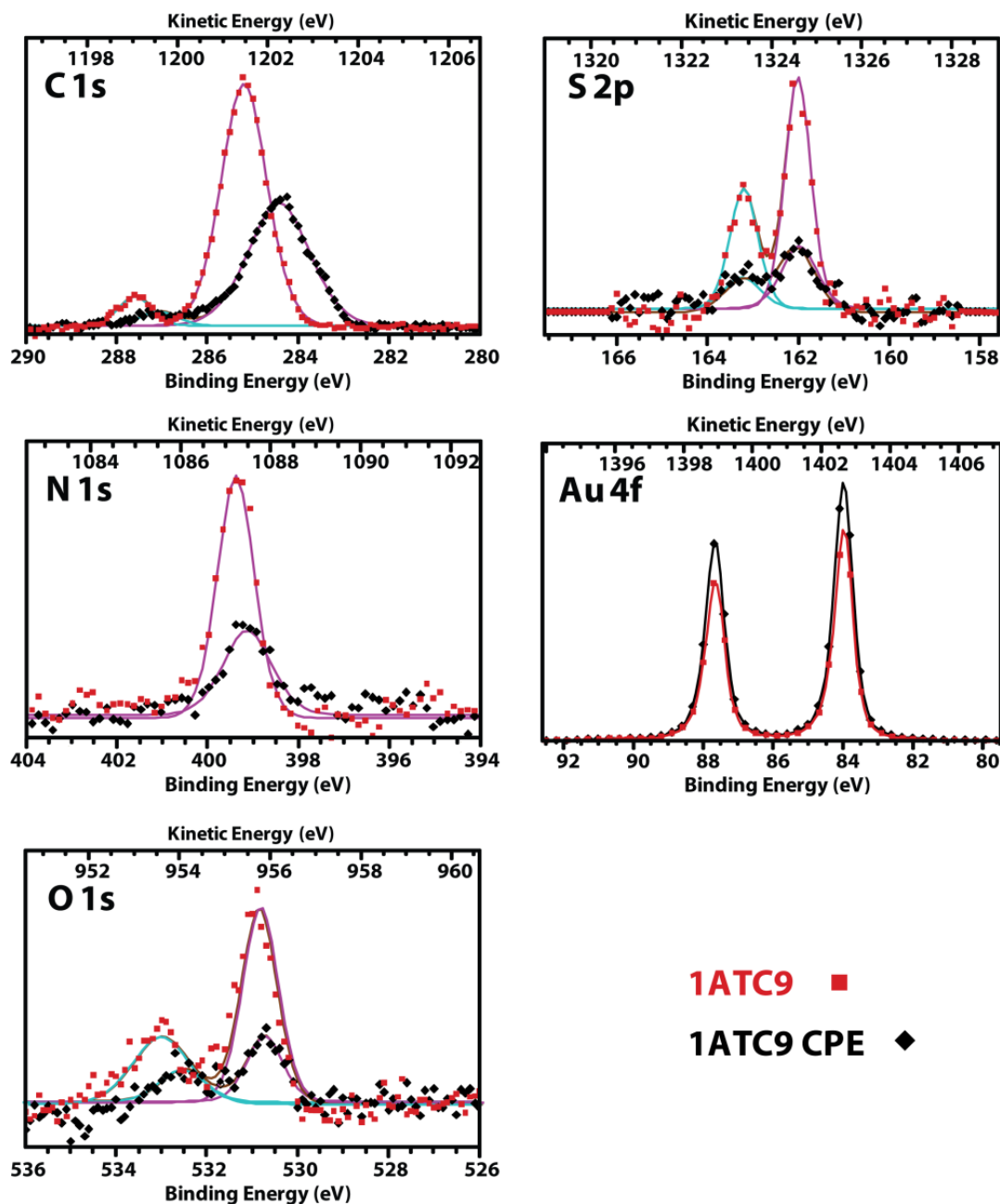


Figure 5.9 C 1s, N 1s, O 1s, S 2p, and Au 4f regions of high-resolution XPS spectra of **1ATC9** SAMs before (red trace) and after (black trace) controlled potential electrolysis (CPE). Elemental components for XPS data analysis were color coded as magenta for the lower binding-energy peak, as cyan for the higher binding-energy peak and as brown for combination of both components (O 1s and S 2p). The SAMs were fabricated by inserting clean substrates in 1 mM **1ATC9** solution at 70 °C for 24 hours with application of a –960 mV reductive potential for 120 seconds. Each element (other than Au) decreases in abundance, consistent with reductive desorption of the thiolates. The increase in the peak intensity in the Au 4f region is consistent with effectively thinning the monolayer via desorption.

	Binding energy (eV) before CPE	Binding energy (eV) after CPE	Peak area ratio (%) $= \frac{\text{Peak area after CPE}}{\text{Peak area before CPE}} \times 100$
C 1s (alkyl, C=O)	285.1, 287.5	284.4, 287.0	69
N 1s	399.3	399.1	46
O 1s (C=O, O-H)	530.9, 533.0	530.7, 532.4	33
S 2p _{3/2} , S 2p _{1/2}	162.0, 163.2	162.0, 163.2	40
Au 4f _{7/2} , Au 4f _{5/2}	83.98, 87.65	83.98, 87.65	125

Table 5-1 Elemental composition of **1ATC9** SAMs on Au{111} by XPS before and after controlled potential electrolysis.

5.3.5 Electrochemically driven phase transition

We have characterized both the initial and nanostructured phases of **1ATC9** SAMs by a variety of techniques, but these methods have not revealed the underlying physical process responsible for this reaction. There are several possibilities for the two-step reductive desorption of **1ATC9** SAMs. The first reduction at lower potential may result from desorption of molecules that are not involved in linear hydrogen-bonding interactions; it is unlikely that all molecules are equally available for interactions in a hexagonally close-packed lattice. Molecules without hydrogen bonding interactions lose 42 kJ/mol per pair in stabilization energy compared to those molecules in ideal hydrogen-bonding configurations [183]. Molecules with weaker interactions could be ejected more easily from the monolayer at lower reductive potentials. The number of desorbed molecules does not necessarily correspond to the number of molecules without hydrogen bonding interactions. Once partial desorption frees space in the lattice, remaining molecules move to disordered regions by surface diffusion, loss of the van der Waals interactions between neighboring alkyl chains, and the exothermicity of desorption.

A second possible explanation of the two-step reductive desorption is electrochemically assisted hydrolysis on amide groups in *isolated* molecules that cannot attain linear hydrogen-bonding interactions between domains. An applied cathodic potential (−960 mV) could drive base-catalyzed hydrolysis of the amide groups in 0.5 M KOH (aq) solution. The enthalpy change for this reaction can be derived from the bond dissociation energy differences between reactants and products for such reactions and is 77 kJ/mol [311]. Also, the calculated activation energy barrier for hydroxide-assisted hydrolysis is 66 ± 12 kJ/mol [312,313]. Controlled potential electrolysis provides 0.96 eV (97 kJ/mol)

energy to the reactants, individual single **1ATC9** molecules attached to a Au electrode [314]. This energy is sufficient to *overcome* the energy barrier to break hydrogen-bonding and van der Waals interactions between molecules as well as to activate hydrolysis. Then, OH⁻ ions react by nucleophilic addition at the amide carbonyl, hydrolyzing the amide. Consequently, adsorbed molecules dissociate into two products and desorb irreversibly, diffusing into solution. In this case, incomplete hydrolysis of the monolayer remains to be explained. The negative potential reduces the surface concentration of the anions, such as OH⁻, and is likely to retard hydrolysis [209].

The observed structural change of electrochemically treated **1ATC9** SAMs likely occurred during CPE without Au reconstruction [315]. The striped $(5 \times \sqrt{3})$ structure has a lower packing density compared to the $(\sqrt{3} \times \sqrt{3})R30^\circ$ lattice previously observed in short-chain or annealed long-chain SAMs [215,304]. Exclusive loss of molecules from exposure to CPE results in structural transformation to the energetically favored phase at low coverage.

The phase transition in these **1ATC9** SAMs is initiated by electrochemical reductive desorption, not by the electrochemical potential effects [305,316-318]. In potential-induced structural changes, the applied electrode potential changes the mobility of thiolate-Au complexes. This is normally performed in acidic aqueous solution in the non-reductive potential range to keep molecules and assemblies intact on Au surfaces.

5.5 Conclusions and Prospects

Hydrogen-bonding interactions between neighboring **1ATC9** molecules have important impact on the structure, ordering, orientation, and stability of SAMs. Assembly from solution at elevated temperatures facilitates molecular rearrangement toward favorable

linear hydrogen-bonding networks with maximized van der Waals interactions in the monolayer. Confining amide groups within monolayers on Au{111} leads to a two-step electrochemical desorption mechanism. Controlled electrolysis at the low-potential step results in a structural transformation to compensate for the desorptive loss of molecules. Strong hydrogen-bonding interactions remain in the lying-down phase, and desorption occurs at more negative reductive potentials. Electrolysis of amide-alkanethiolates confined on Au surfaces enables the synthesis of non-traditional supramolecular assemblies by simple potential control. Understanding the mechanism and kinetics of electrochemically driven nanostructuring could open new routes for the preparation of nanotextured and patterned surfaces. We will gain further insight into this mechanism by exploiting molecular design to alter the number and position of amide and other groups in the molecular backbone.

Chapter 6. Conclusions and Future Prospects

6.1 Summary

This dissertation is focused on understanding the chemical principles that dictate the behavior of molecules assembled on surfaces, and to the expansion of STM capabilities for chemical specification. In Chapter 1, we introduced *n*-alkanethiolate-based molecular assemblies on Au{111}, the principles and instrumentation used for STM, and the key requirements for a photon scanning tunneling microscope. In Chapter 2, we discussed total internal reflection and evanescent coupling, the underlying principles for the photon STM. The design of the photon scanning tunneling microscope, sample preparation, and the measurement of the photoconductance of isolated organic molecules with the photon STM were presented in detail. In Chapter 3, we described regioselective photoreactions between anthracene analogues on surfaces. Pairs of molecules were inserted into a stable *n*-dodecanethiolate SAM matrix to direct organic reactions toward unfavorable, but allowed pathways. Chapters 4 and 5 involve interpretation of the role of chemistry in the structure and properties of self-assembled monolayers. In Chapter 4, we explored monolayers of adamantanethiol, a new building block for molecular assemblies. Cage molecules allow variation of molecular size, orientation, and elemental heterogeneity, which offer new opportunities to tune the physical, chemical, electrical, and optical properties of molecular assemblies. In Chapter 5, hydrogen-bonding interactions affect molecular packing and van der Waals interactions in monolayers, controlling the structure, thermodynamic stability, and electrochemical reactions of amide-containing alkanethiolate monolayers.

6.2 Photon Scanning Tunneling Microscopy

Photon STM achieves chemical specificity with nanometer-scale precision, bridging optical spectroscopy and STM. The Kretschmann-Raether geometry is used for efficient evanescent coupling and a thin Au{111} film is directly deposited on a Al₂O₃(0001) prism. We isolate single molecules using a stable, well-ordered alkanethiolate monolayer and then perform single-molecule spectroscopy to observe long time-scale dynamics (hours) in real time with high spatial resolution.

For highly efficient organic solar cell photocurrent generation, dyad or triad molecules (in which electron donors are attached covalently to electron acceptors) must be understood at the molecular level, to guide organic chemistry and device fabrication. Using the photon STM, we can investigate the molecular orientations, bonding characteristics (covalent, dative, or multiple bonds), π -conjugation, and the roles of bridge functionality between electron donors and electron acceptors. All of these experiments complement computational results. Photon STM can measure the photovoltaic efficiency of individual candidate molecules, and enables determination of the key factors of molecular structure for improving intrinsic quantum efficiency. We demonstrated photoconductivity increases in the semiconducting molecular wire **MPEA**, demonstrating a new paradigm for molecular optoelectronics. The work described in Chapter 2 will result in the following manuscript:

Single-Molecule Optical Spectroscopy with Ångström-Scale Precision: Chemical Specificity Revealed in Scanning Tunneling Microscopy, M. Kim, J. Nathan Hohman, G. A. Wadsworth, and P. S. Weiss, *in preparation*.

6.3 Regioselective Photoreaction on Surfaces

Monitoring stochastic conductance switching of **MPEA** reveals the importance of π -conjugation interactions and electron delocalization for molecular conductivity. Absorption of UV light optically excites molecular electronic states, which manifests as conductance increases. Light absorption opens new channels for charge transport, which can be controlled in time (pulsed lasers) and energy (different wavelengths).

We utilize defect sites in *n*-alkanethiolate monolayers as confinement sites for the study of photoreactions. Molecular conformation and orientation can be controlled via strong Au-S bonds in the assemblies, creating geometrically favorable environments for regioselective reactions. The phenylethynyl moiety is buried within **C12** monolayer. Exposed anthracene moieties were oriented parallel to each other by strong π -stacking interactions, and the applied photons triggered [4+4] photodimerization of the adjacent molecules. As a result, the conductance in photodimerized **MPEA** decreased permanently, attributed to disrupted π conjugation. The work is described in Chapter 3 and resulted in the following publication:

Creating Favorable Geometries for Directing Organic Photoreactions in Alkanethiolate Monolayers, M. Kim, J. N. Hohman, Y. Cao, K. N. Houk, H. Ma, A. K.-Y. Jen, and P. S. Weiss, *Science* 331, 1312-1315 (2011).

6.4 Molecular Chemistry on Surfaces

Self-assembly of cage molecules introduces new diversity to molecular interfaces. Compared to *n*-alkanethiolate assemblies, cage molecules are round, bulky, and short. Thus, cage assemblies contain fewer molecules per unit area, weaker aggregate intermolecular interactions, and loose packing. There are multiple anchoring points for the sulfur attachment

resulting in diverse molecular orientations, which affects molecular packing and monolayer structure. The sulfur atom in 2-adamantanethiol is attached at a secondary carbon, forcing tilt when assembled on gold surfaces. This changes the SAM morphology and physical properties, which distinguishes 2-adamantanethiolate monolayers from 1-adamantanethiolate SAMs.

Incorporating functional groups in the hydrocarbon tail of self-assembling molecules alters the SAM properties. Amide-containing alkanethiolate SAMs show high thermal stability because of the increased intermolecular interactions from hydrogen-bonding networks. Hydrogen-bonding interactions exert strong influences on the structures and electrochemical reduction of the SAMs. By manipulating hydrogen-bonding interactions with electrochemical reactions, we achieved emergent nanoscale patterning that is otherwise kinetically and thermodynamically unfavorable.

The work described in Chapters 4 and 5 resulted in the following publications:

Self-Assembled Monolayers of 2-Adamantanethiol on Au{111}: Control of Structure and Displacement, M. Kim, J. N. Hohman, E. I. Morin, T. A. Daniel, and P. S. Weiss, *Journal of Physical Chemistry A* **113**, 3895-3903 (2009)

Cage Molecules for Assembly, J. N. Hohman, S. A. Claridge, M. Kim, and P. S. Weiss, *Materials Science and Engineering R: Reports* **70**, 188-208 (2010)

Structural Manipulation of Hydrogen-Bonding Networks in Amide-Containing Alkanethiolate Monolayers via Electrochemical Processing, M. Kim, J. N. Hohman, A. C. Serino, and P. S. Weiss, *Journal of Physical Chemistry C* **114**, 19744-19751 (2010)

6.5 Future Prospects

The research themes presented in this dissertation demonstrate chemical principles of molecular interfaces. We have also shown that we can apply these principles for measuring

single molecules and conducting chemical reactions on surfaces. It is now possible to design, to develop, and to control matter, and its assembly. Pseudo-solid molecular assemblies are governed by their characteristic interactions, including van der Waals attractions, dipole-dipole interactions, and hydrogen-bonding forces. We can control the molecular spacing, orientation, composition, and dimensionality of these assemblies, which will lead to further advances in molecular self-assembly.

It is important to develop the right tools to achieve specific goals in science. Without the right scientific tools, it is challenging to identify important problems and questions and to solve them. The STM can be used to monitor, to manipulate, to control, to measure, to diagnose, and to determine single molecules in real space at the sub-nanometer scale. Photon STM allows additional questions to be posed and addressed; Photon STM is chemically sensitive, no special sample preparation such as fluorescent dye attachment is required, and is accessible to biological environments. The theory and principle of optically assisted STM have developed progressively for years, however, scientific interest was narrowly focused and the design was not generalized for diverse fields [63]. Our system configuration in the photon STM will be broadly useful as a research and commercial tool.

Photocurrent measurements on the electron donor-acceptor multilayer can provide close insight to photovoltaic processes at donor-acceptor interfaces (Figure 6.1A). Such interfaces are formed simply by solution deposition [319,320]. An electron acceptor layer, comprised of fullerenes, can be assembled on top of an electron donor monolayer, in this case, 2,3,7,8,12,13,17,18-octaethyl-21*H*,23*H*-porphine zinc(II) (**ZnOEP**) (Figure 6.1B and C). Photocurrent generation can be monitored by photon STM with Ångström-scale precision. This will provide the highest spatial resolution yet obtained for the study of photoinduced

charge separation at donor-acceptor interfaces. By creating mixed electron donor monolayers, composed of both Zinc(II) phthalocyanine (**ZnPc**) and **ZnOEP**, we can manipulate the fullerene arrangement to determine the effective configurations or orientations of electron acceptors, relative to electron donors [320].

Fullerene photopolymerization will be studied with photon STM. Fullerenes undergo a [2 + 2] photocycloaddition on exposure to visible laser light ($\lambda = 633$ nm) (Figure 6.2) [321]. Fullerenes and fullerene derivatives are key components of future solar cell [322-324] and transistor [325-327] devices. They can be solution-processed and patterned, and exhibit desirable electronic properties including high electron mobility and efficient fluorescence, ideal for organic electronics. Photoinduced imprinted fullerene polymer layers show higher stability for further device processing and improved performance for field-effect transistor devices [328,329]. However, the degree and orientation of C_{60} polymers strongly affect the charge transport properties [330-332], which can be understood at the molecular level using photon STM.

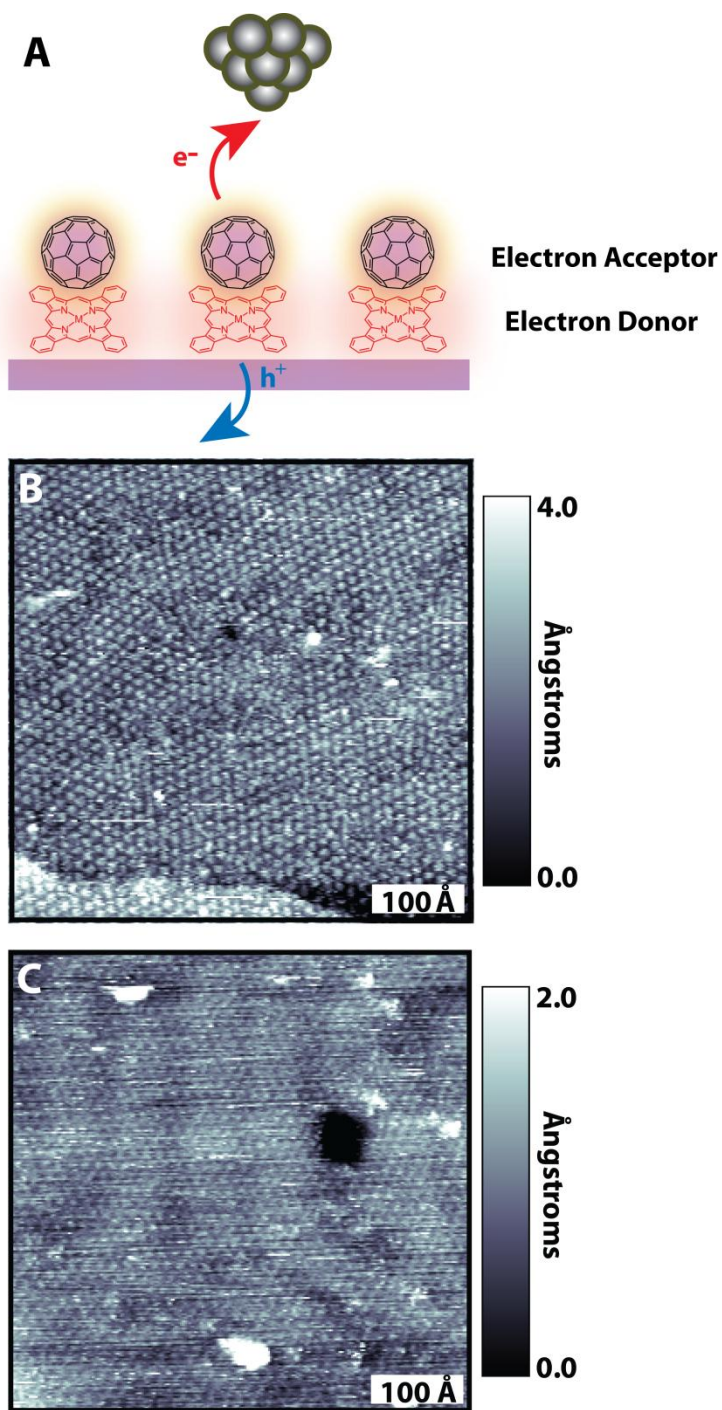


Figure 6.1 (A) Schematic illustration of proposed STM measurements on photocurrent generated at the donor-acceptor interface. The double layer is composed of an electron donor, 2,3,7,8,12,13,17,18-octaethyl-21*H*,23*H*-porphine zinc(II) (**ZnOEP**), and an electron acceptor, fullerene. (B) A STM image of a **ZnOEP** monolayer. (C) A STM image of a C₆₀ monolayer assembled on a **ZnOEP** monolayer.

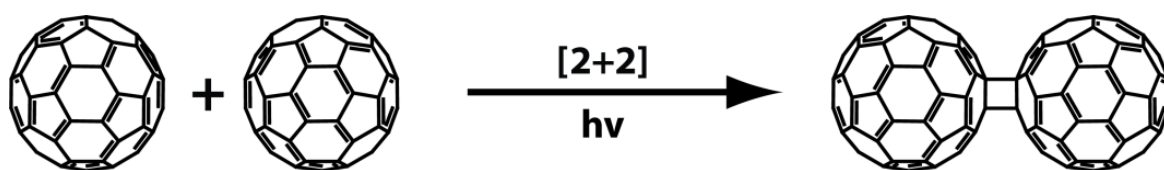


Figure 6.2 Schematic illustration of photoinduced [2+2] cycloaddition reaction of fullerenes [321].

We are also actively studying monolayers based on other cage systems, including polar carboranes [6], and most recently, cubane. The cubane cage (C_8H_8) is the fundamentally smallest practical hydrocarbon cage molecule: highly strained, but stable at room temperature and chemically functionalizable. Monolayers based on cubanethiolates provide an opportunity to test our assumptions regarding the roles of geometry and structure in determining monolayer properties and reactivities. Cubanethiol is susceptible to unimolecular rearrangement reactions, while the oxidized dicubyl disulfide is stable (Figure 6.3) [333]. Of interest is the exploitation of cubane molecular strain [334]. Cubanes have been used as precursors for polyacetylene. Isolated cubanes are susceptible to ring-opening reactions, leading to cyclooctatetraene [335,336]. Ring-opening metathesis reaction produces polyacetylene.

We have exploited the strong hydrogen-bonding interactions in **1ATC9** monolayers to prepare liquid-metal alloy nanoparticles [337]. Eutectic gallium-indium (**EGaIn**) alloy particles are capped with a **1ATC9** monolayer, and can be divided into smaller nanoparticles via ultrasonication. Ultrasound forces disrupt the domain boundaries of hydrogen-bonded **1ATC9** monolayers, cleaving the particles (Figure 6.4). Alloy particles are spherical, and stabilized when protected by **C12** or **1ATC9** monolayers. The presence of extra hydrogen-bonding interactions effectively assists particle division, resulting in high yields of nanoparticles than **C12** capped alloy particles.

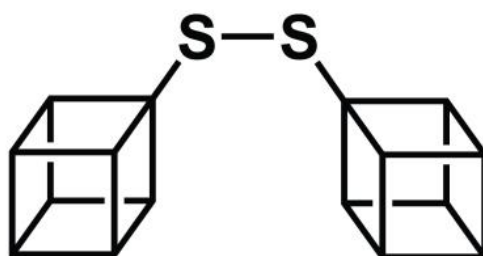
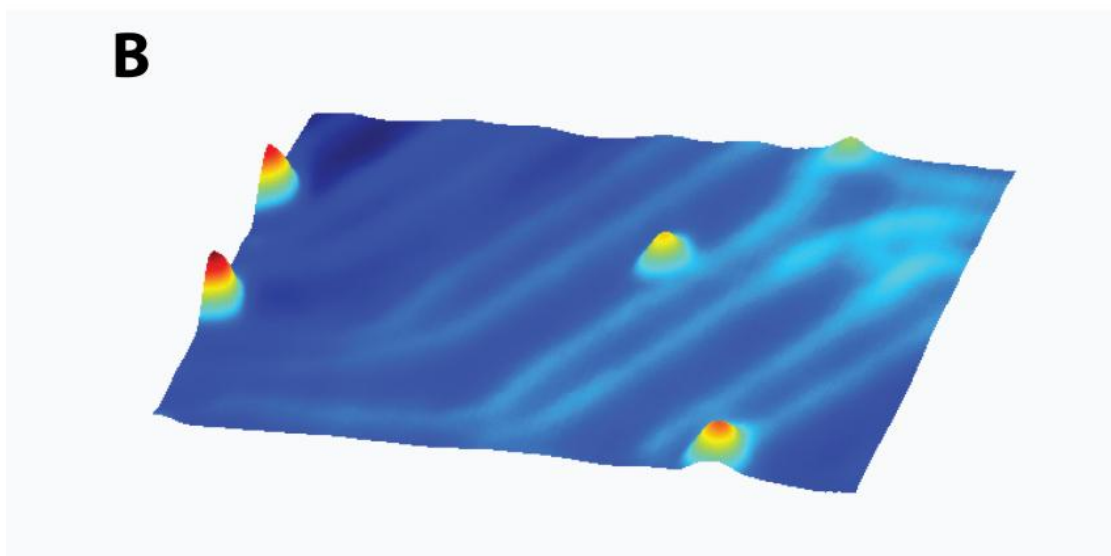
A**B**

Figure 6.3 (A) Molecular structure of dicubyl disulfide (B) A three-dimensional representation of isolated cubanethiolate molecules on Au{111}. The linear features are the Au{111} herringbone reconstruction.

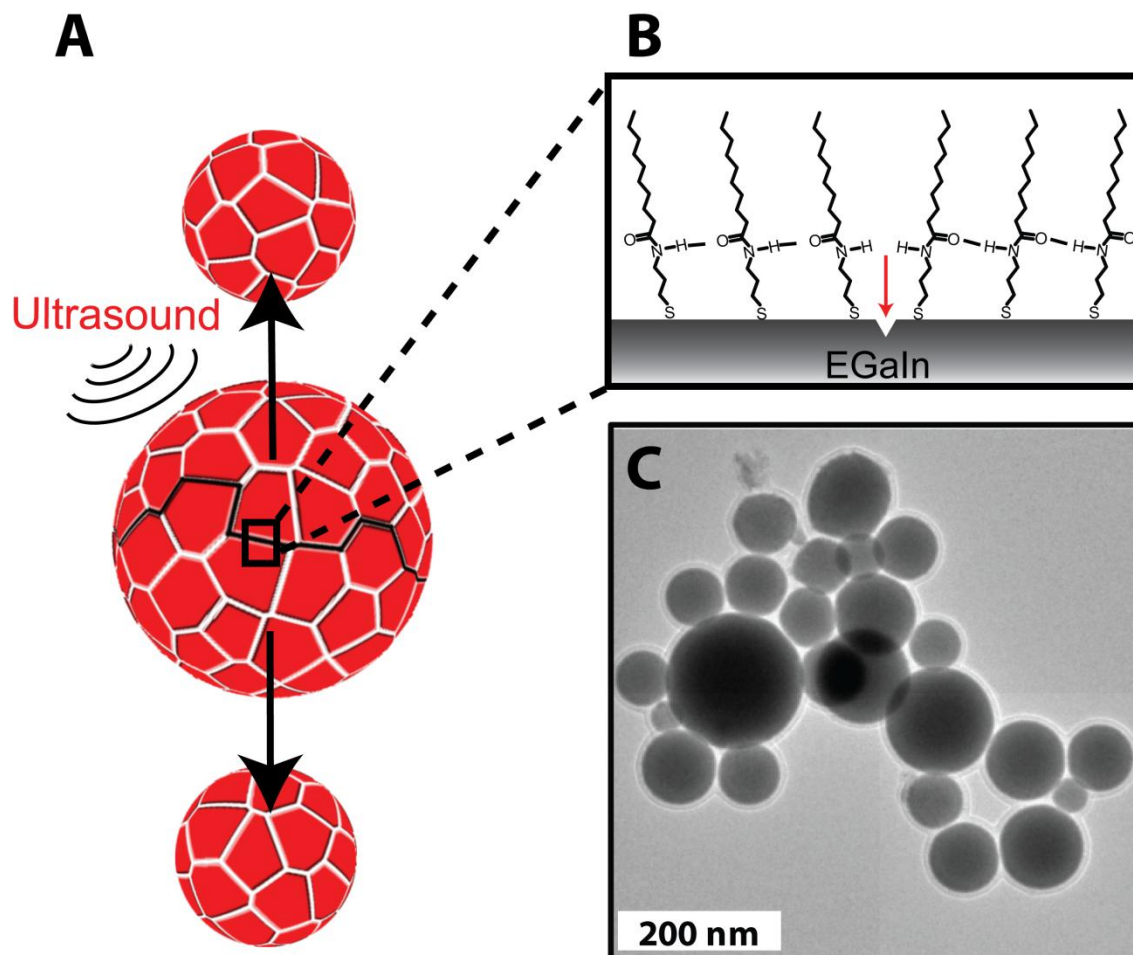


Figure 6.4 (A) Schematic representation of molecular-scale interactions within **1ATC9** SAMs on **EGaIn** nanoparticles. (B) Hydrogen-bonding within **1ATC9** SAMs dominates local order and decreases domain size. The combination of strong hydrogen-bonding interactions between **1ATC9** molecules and local order facilitates the nondestructive scission of larger spherical particles into smaller spheres (red arrow). (C) A representative transmission electron microscopy image of **1ATC9**-capped **EGaIn** nanoparticles.

References and Notes

- [1] R. G. Nuzzo and D. L. Allara, *Adsorption of Bifunctional Organic Disulfides on Gold Surfaces*, J. Am. Chem. Soc. **105**, 4481 (1983).
- [2] P. E. Laibinis, G. M. Whitesides, D. L. Allara, Y. T. Tao, A. N. Parikh, and R. G. Nuzzo, *Comparison of the Structures and Wetting Properties of Self-Assembled Monolayers of Normal-Alkanethiols on the Coinage Metal-Surfaces, Cu, Ag, Au*, J. Am. Chem. Soc. **113**, 7152 (1991).
- [3] R. K. Smith, P. A. Lewis, and P. S. Weiss, *Patterning Self-Assembled Monolayers*, Prog. Surf. Sci. **75**, 1 (2004).
- [4] J. C. Love, L. A. Estroff, J. K. Kriebel, R. G. Nuzzo, and G. M. Whitesides, *Self-Assembled Monolayers of Thiolates on Metals as a Form of Nanotechnology*, Chem. Rev. **105**, 1103 (2005).
- [5] S. F. Bent, *Heads or Tails: Which Is More Important in Molecular Self-Assembly?*, ACS Nano **1**, 10 (2007).
- [6] J. N. Hohman, P. P. Zhang, E. I. Morin, P. Han, M. Kim, A. R. Kurland, P. D. McClanahan, V. P. Balema, and P. S. Weiss, *Self-Assembly of Carboranethiol Isomers on Au{111}: Intermolecular Interactions Determined by Molecular Dipole Orientations*, ACS Nano **3**, 527 (2009).
- [7] J. N. Hohman, S. A. Claridge, M. Kim, and P. S. Weiss, *Cage Molecules for Self-Assembly*, Mater. Sci. Eng., R **70**, 188 (2010).
- [8] C. D. Bain, E. B. Troughton, Y. T. Tao, J. Evall, G. M. Whitesides, and R. G. Nuzzo, *Formation of Monolayer Films by the Spontaneous Assembly of Organic Thiols from Solution onto Gold*, J. Am. Chem. Soc. **111**, 321 (1989).
- [9] A. Ulman, *Formation and Structure of Self-Assembled Monolayers*, Chem. Rev. **96**, 1533 (1996).
- [10] G. E. Poirier, *Characterization of Organosulfur Molecular Monolayers on Au(111) Using Scanning Tunneling Microscopy*, Chem. Rev. **97**, 1117 (1997).
- [11] G. E. Poirier and E. D. Pylant, *The Self-Assembly Mechanism of Alkanethiols on Au(111)*, Science **272**, 1145 (1996).
- [12] N. Camillone, C. E. D. Chidsey, G. Y. Liu, and G. Scoles, *Superlattice Structure at the Surface of a Monolayer of Octadecanethiol Self-Assembled on Au(111)* J. Chem. Phys. **98**, 3503 (1993).
- [13] J. A. M. Sondaghuethorst, C. Schonenberger, and L. G. J. Fokkink, *Formation of Holes in Alkanethiol Monolayers on Gold*, J. Phys. Chem **98**, 6826 (1994).
- [14] G. E. Poirier, *Mechanism of Formation of Au Vacancy Islands in Alkanethiol Monolayers on Au(111)*, Langmuir **13**, 2019 (1997).

- [15] E. Delamarche, B. Michel, C. Gerber, D. Anselmetti, H. J. Guntherodt, H. Wolf, and H. Ringsdorf, *Real Space Observation of Nanoscale Molecular Domains in Self-Assembled Monolayers*, *Langmuir* **10**, 2869 (1994).
- [16] C. Schonenberger, J. Jorritsma, J. A. M. Sondaghuethorst, and L. G. J. Fokkink, *Domain-Structure of Self-Assembled Alkanethiol Monolayers on Gold*, *J. Phys. Chem* **99**, 3259 (1995).
- [17] G. E. Poirier, *Coverage-Dependent Phases and Phase Stability of Decanethiol on Au(111)*, *Langmuir* **15**, 1167 (1999).
- [18] P. Han, A. R. Kurland, A. N. Giordano, S. U. Nanayakkara, M. M. Blake, C. M. Pochas, and P. S. Weiss, *Heads and Tails: Simultaneous Exposed and Buried Interface Imaging of Monolayers*, *ACS Nano* **3**, 3115 (2009).
- [19] D. K. Schwartz, *Mechanisms and Kinetics of Self-Assembled Monolayer Formation*, *Annu. Rev. Phys. Chem.* **52**, 107 (2001).
- [20] L. A. Bumm, J. J. Arnold, L. F. Charles, T. D. Dunbar, D. L. Allara, and P. S. Weiss, *Directed Self-Assembly to Create Molecular Terraces with Molecularly Sharp Boundaries in Organic Monolayers*, *J. Am. Chem. Soc.* **121**, 8017 (1999).
- [21] J. B. Schlenoff, M. Li, and H. Ly, *Stability and Self-Exchange in Alkanethiol Monolayers*, *J. Am. Chem. Soc.* **117**, 12528 (1995).
- [22] M. Kim, J. N. Hohman, E. I. Morin, T. A. Daniel, and P. S. Weiss, *Self-Assembled Monolayers of 2-Adamantanethiol on Au{111}: Control of Structure and Displacement*, *J. Phys. Chem. A* **113**, 3895 (2009).
- [23] W. E. Moerner, *A Dozen Years of Single-Molecule Spectroscopy in Physics, Chemistry, and Biophysics*, *J. Phys. Chem. B* **106**, 910 (2002).
- [24] W. E. Moerner and M. Orrit, *Illuminating Single Molecules in Condensed Matter*, *Science* **283**, 1670 (1999).
- [25] J. M. Tour, *Molecular Electronics. Synthesis and Testing of Components*, *Acc. Chem. Res.* **33**, 791 (2000).
- [26] A. R. Pease, J. O. Jeppesen, J. F. Stoddart, Y. Luo, C. P. Collier, and J. R. Heath, *Switching Devices Based on Interlocked Molecules*, *Acc. Chem. Res.* **34**, 433 (2001).
- [27] S. A. Claridge, J. J. Schwartz, and P. S. Weiss, *Electrons, Photons, and Force: Quantitative Single-Molecule Measurements from Physics to Biology*, *ACS Nano* **5**, 693 (2011).
- [28] W. Chen, V. Madhavan, T. Jamneala, and M. F. Crommie, *Scanning Tunneling Microscopy Observation of an Electronic Superlattice at the Surface of Clean Gold*, *Phys. Rev. Lett.* **80**, 1469 (1998).
- [29] D. I. Gittins, D. Bethell, D. J. Schiffrin, and R. J. Nichols, *A Nanometre-Scale Electronic Switch Consisting of a Metal Cluster and Redox-Addressable Groups*, *Nature* **408**, 67 (2000).
- [30] A. M. Moore, A. A. Dameron, B. A. Mantooth, R. K. Smith, D. J. Fuchs, J. W. Ciszek, F. Maya, Y. X. Yao, J. M. Tour, and P. S. Weiss, *Molecular Engineering and*

- Measurements to Test Hypothesized Mechanisms in Single Molecule Conductance Switching*, J. Am. Chem. Soc. **128**, 1959 (2006).
- [31] R. K. Smith, S. U. Nanayakkara, G. H. Woehrle, T. P. Pearl, M. M. Blake, J. E. Hutchison, and P. S. Weiss, *Spectral Diffusion in the Tunneling Spectra of Ligand-Stabilized Undecagold Clusters*, J. Am. Chem. Soc. **128**, 9266 (2006).
- [32] P. A. Lewis, Z. J. Donhauser, B. A. Mantooth, R. K. Smith, L. A. Bumm, K. F. Kelly, and P. S. Weiss, *Control and Placement of Molecules via Self-Assembly*, Nanotechnology **12**, 231 (2001).
- [33] shifting in the energies of the conductance resonance.
- [34] M. H. Zareie, H. Ma, B. W. Reed, A. K. Y. Jen, and M. Sarikaya, *Controlled Assembly of Conducting Monomers for Molecular Electronics*, Nano Lett. **3**, 139 (2003).
- [35] G. Binnig, H. Rohrer, C. Gerber, and E. Weibel, *Surface Studies by Scanning Tunneling Microscopy*, Phys. Rev. Lett. **49**, 57 (1982).
- [36] G. Binnig and H. Rohrer, *Scanning Tunneling Microscopy-from Birth to Adolescence*, Rev. Mod. Phys. **59**, 615 (1987).
- [37] P. Avouris, *Atom-Resolved Surface-Chemistry Using the Scanning Tunneling Microscope*, J. Phys. Chem **94**, 2246 (1990).
- [38] I. Ekvall, E. Wahlstrom, D. Claesson, H. Olin, and E. Olsson, *Preparation and Characterization of Electrochemically Etched W Tips for STM*, Meas. Sci. Technol. **10**, 11 (1999).
- [39] Y. C. Kim and D. N. Seidman, *An Electrochemical Etching Procedure for Fabricating Scanning Tunneling Microscopy and Atom-Probe Field-Ion Microscopy Tips*, Met. Mater. Int. **9**, 399 (2003).
- [40] Y. C. Kim and D. N. Seidman, *A Scanning Tunneling Microscopy Tip with a Stable Atomic Structure*, Met. Mater. Int. **10**, 97 (2004).
- [41] H. W. Fink, *Mono-Atomic Tips for Scanning Tunneling Microscopy*, IBM J. Res. Dev. **30**, 460 (1986).
- [42] J. A. Meyer, I. D. Baikie, E. Kopatzki, and R. J. Behm, *Preferential Island Nucleation at the Elbows of the Au(111) Herringbone Reconstruction through Place Exchange*, Surf. Sci. **365**, L647 (1996).
- [43] K. Besocke, *An Easily Operable Scanning Tunneling Microscope*, Surf. Sci. **181**, 145 (1987).
- [44] J. Frohn, J. F. Wolf, K. Besocke, and M. Teske, *Coarse Tip Distance Adjustment and Positioner for a Scanning Tunneling Microscope*, Rev. Sci. Instrum. **60**, 1200 (1989).
- [45] E. Kretschmann, *Scattering of Light at Rough Surfaces Due to Excitation of Surface Plasmons* Z. Phys. **227**, 412 (1969).
- [46] E. Kretschmann, *ATR Method with Focused Light - Application to Guide Waves on a Grating*, Opt. Commun. **26**, 41 (1978).

- [47] W. E. Moerner, *New Directions in Single-Molecule Imaging and Analysis*, Proc. Natl. Acad. Sci. U. S. A. **104**, 12596 (2007).
- [48] J. K. Gimzewski and C. Joachim, *Nanoscale Science of Single Molecules Using Local Probes*, Science **283**, 1683 (1999).
- [49] L. Gross, *Recent Advances in Submolecular Resolution with Scanning Probe Microscopy*, Nature Chemistry **3**, 273 (2011).
- [50] S. Weiss, *Fluorescence Spectroscopy of Single Biomolecules*, Science **283**, 1676 (1999).
- [51] E. J. G. Peterman, H. Sosa, and W. E. Moerner, *Single-Molecule Fluorescence Spectroscopy and Microscopy of Biomolecular Motors*, Annu. Rev. Phys. Chem. **55**, 79 (2004).
- [52] X. Michalet, O. H. W. Siegmund, J. V. Vallerga, P. Jelinsky, J. E. Millaud, and S. Weiss, *Detectors for Single-Molecule Fluorescence Imaging and Spectroscopy*, J. Mod. Opt. **54**, 239 (2007).
- [53] M. Jager, X. Michalet, and S. Weiss, *Protein-Protein Interactions as a Tool for Site-Specific Labeling of Proteins*, Protein Sci. **14**, 2059 (2005).
- [54] X. W. Zhuang, L. E. Bartley, H. P. Babcock, R. Russell, T. J. Ha, D. Herschlag, and S. Chu, *A Single-Molecule Study of RNA Catalysis and Folding*, Science **288**, 2048 (2000).
- [55] C. Bustamante, Y. R. Chemla, N. R. Forde, and D. Izhaky, *Mechanical Processes in Biochemistry*, Annu. Rev. Biochem. **73**, 705 (2004).
- [56] H. Yang, G. B. Luo, P. Karnchanaphanurach, T. M. Louie, I. Rech, S. Cova, L. Y. Xun, and X. S. Xie, *Protein Conformational Dynamics Probed by Single-Molecule Electron Transfer*, Science **302**, 262 (2003).
- [57] N. K. Lee, A. N. Kapanidis, Y. Wang, X. Michalet, J. Mukhopadhyay, R. H. Eubright, and S. Weiss, *Accurate FRET Measurements within Single Diffusing Biomolecules Using Alternating-Laser Excitation*, Biophys. J. **88**, 2939 (2005).
- [58] N. K. Lee, A. N. Kapanidis, H. R. Koh, Y. Korlann, S. O. Ho, Y. Kim, N. Gassman, S. K. Kim, and S. Weiss, *Three-Color Alternating-Laser Excitation of Single Molecules: Monitoring Multiple Interactions and Distances*, Biophys. J. **92**, 303 (2007).
- [59] J. J. Sieber, K. I. Willig, C. Kutzner, C. Gerding-Reimers, B. Harke, G. Donnert, B. Rammner, C. Eggeling, S. W. Hell, H. Grubmüller, and T. Lang, *Anatomy and Dynamics of a Supramolecular Membrane Protein Cluster*, Science **317**, 1072 (2007).
- [60] R. P. Andres, T. Bein, M. Dorogi, S. Feng, J. I. Henderson, C. P. Kubiak, W. Mahoney, R. G. Osifchin, and R. Reifengerger, *"Coulomb Staircase" at Room Temperature in a Self-Assembled Molecular Nanostructure*, Science **272**, 1323 (1996).
- [61] F. Oesterhelt, D. Oesterhelt, M. Pfeiffer, A. Engel, H. E. Gaub, and D. J. Müller, *Unfolding Pathways of Individual Bacteriorhodopsins*, Science **288**, 143 (2000).
- [62] R. Wiesendanger, *Scanning Probe Microscopy and Spectroscopy*; Cambridge University Press: Cambridge, 1994.
- [63] S. Grafstrom, *Photoassisted Scanning Tunneling Microscopy*, J. Appl. Phys. **91**, 1717 (2002).

- [64] J. K. Viljas, F. Pauly, and J. C. Cuevas, *Photoconductance of Organic Single-Molecule Contacts*, Phys. Rev. B **76** (2007).
- [65] Y. Kuk, R. S. Becker, P. J. Silverman, and G. P. Kochanski, *Optical Interactions in the Junction of a Scanning Tunneling Microscope*, Phys. Rev. Lett. **65**, 456 (1990).
- [66] R. J. Hamers and K. Markert, *Surface Photovoltage on Si(111)-(7 × 7) Probed by Optical Pumped Scanning Tunneling Microscopy*, J. Vac. Sci. Technol., A **8**, 3524 (1990).
- [67] R. J. Hamers and K. Markert, *Atomically Resolved Carrier Recombination at Si(111)-(7 × 7) Surfaces*, Phys. Rev. Lett. **64**, 1051 (1990).
- [68] Y. Kuk, R. S. Becker, P. J. Silverman, and G. P. Kochanski, *Photovoltage on Silicon Surfaces Measured by Scanning Tunneling Microscopy*, J. Vac. Sci. Technol. B **9**, 545 (1991).
- [69] L. Q. Qian and B. W. Wessels, *Scanning Tunneling Optical Spectroscopy of Semiconductors*, Appl. Phys. Lett. **58**, 1295 (1991).
- [70] F. R. F. Fan and A. J. Bard, *Photoassisted Scanning Tunneling Microscopy and Tunneling Spectroscopy of n-Type Tungsten Diselenide (n-WSe₂) Single Crystals*, J. Phys. Chem **97**, 1431 (1993).
- [71] M. W. J. Prins, R. Jansen, R. H. M. Groeneveld, A. P. van Gelder, and H. van Kempen, *Photoelectrical Properties of Semiconductor Tips in Scanning Tunneling Microscopy*, Phys. Rev. B **53**, 8090 (1996).
- [72] D. Fournier, C. Boccard, A. Skumanich, and N. M. Amer, *Photothermal Investigation of Transport in Semiconductors - Theory and Experiment*, J. Appl. Phys. **59**, 787 (1986).
- [73] J. M. R. Weaver, L. M. Walpita, and H. K. Wickramasinghe, *Optical-Absorption Microscopy and Spectroscopy with Nanometer Resolution*, Nature **342**, 783 (1989).
- [74] A. V. Bragas, S. M. Landi, J. A. Coy, and O. E. Martinez, *Spectroscopic Response of Photoinduced Currents in a Laser-Assisted Scanning Tunneling Microscope*, J. Appl. Phys. **82**, 4153 (1997).
- [75] A. V. Bragas, S. M. Landi, and O. E. Martinez, *Laser Field Enhancement at the Scanning Tunneling Microscope Junction Measured by Optical Rectification*, Appl. Phys. Lett. **72**, 2075 (1998).
- [76] R. Moller, U. Albrecht, J. Boneberg, B. Koslowski, P. Leiderer, and K. Dransfeld, *Detection of Surface-Plasmons by Scanning Tunneling Microscopy*, J. Vac. Sci. Technol. B **9**, 506 (1991).
- [77] M. Rucker, W. Knoll, and J. P. Rabe, *Surface-Plasmon-Induced Contrast in Scanning Tunneling Microscopy*, J. Appl. Phys. **72**, 5027 (1992).
- [78] M. Specht, J. D. Pedarnig, W. M. Heckl, and T. W. Hansch, *Scanning Plasmon Near-Field Microscope*, Phys. Rev. Lett. **68**, 476 (1992).
- [79] S. Grafstrom, J. Kowalski, R. Neumann, O. Probst, and M. Wortge, *Analysis and Compensation of Thermal Effects in Laser-Assisted Scanning Tunneling Microscopy*, J. Vac. Sci. Technol. B **9**, 568 (1991).

- [80] V. Gerstner, A. Knoll, W. Pfeiffer, A. Thon, and G. Gerber, *Femtosecond Laser Assisted Scanning Tunneling Microscopy*, J. Appl. Phys. **88**, 4851 (2000).
- [81] Y. Inouye and S. Kawata, *Near-Field Scanning Optical Microscope with a Metallic Probe Tip*, Opt. Lett. **19**, 159 (1994).
- [82] S. Wang, S. Boussaad, and N. J. Tao, *Surface Plasmon Resonance Enhanced Optical Absorption Spectroscopy for Studying Molecular Adsorbates*, Rev. Sci. Instrum. **72**, 3055 (2001).
- [83] R. C. Reddick, R. J. Warmack, D. W. Chilcott, S. L. Sharp, and T. L. Ferrell, *Photon Scanning Tunneling Microscopy*, Rev. Sci. Instrum. **61**, 3669 (1990).
- [84] S. E. Sund, J. A. Swanson, and D. Axelrod, *Cell Membrane Orientation Visualized by Polarized Total Internal Reflection Fluorescence*, Biophys. J. **77**, 2266 (1999).
- [85] H. Raether, *Surface-Plasmon Resonance on Smooth and Rough Surfaces and on Gratings*; Springer-Verlag Berlin Heidelberg, 1988.
- [86] T. Tsang, T. Srinivasanrao, and J. Fischer, *Surface-Plasmon Field-Enhanced Multiphoton Photoelectric-Emission from Metal-Films*, Phys. Rev. B **43**, 8870 (1991).
- [87] D. Axelrod, *Total Internal Reflection Fluorescence Microscopy in Cell Biology*, Traffic **2**, 764 (2001).
- [88] P. Andrew and W. L. Barnes, *Energy Transfer across a Metal Film Mediated by Surface Plasmon Polaritons*, Science **306**, 1002 (2004).
- [89] D. Roy and J. Fendler, *Reflection and Absorption Techniques for Optical Characterization of Chemically Assembled Nanomaterials*, Adv. Mater. **16**, 479 (2004).
- [90] E. Kretschmann, *Determination of Optical Constants of Metals by Excitation of Surface Plasmons*, Z. Phys. **241**, 313 (1971).
- [91] E. Kretschmann, *Decay of Non Radiative Surface Plasmons into Light on Rough Silver Films. Comparison of Experimental and Theoretical Results*, Opt. Commun. **6**, 185 (1972).
- [92] A. Levy and N. M. Amer, *Time-Resolved Surface Expansion of Metals under Picosecond Laser Illumination* Appl. Phys. Lett. **66**, 3594 (1995).
- [93] D. A. Smith and R. W. Owens, *Laser-Assisted Scanning Tunneling Microscope Detection of a Molecular Adsorbate*, Appl. Phys. Lett. **76**, 3825 (2000).
- [94] E. Kroger and E. Kretschmann, *Scattering of Light by Slightly Rough Surfaces or Thin Films Including Plasma Resonance Emission*, Z. Phys. **237**, 1 (1970).
- [95] M. Yoshimoto, T. Maeda, T. Ohnishi, H. Koinuma, O. Ishiyama, M. Shinohara, M. Kubo, R. Miura, and A. Miyamoto, *Atomic-Scale Formation of Ultrasoother Surfaces on Sapphire Substrates for High-Quality Thin-Film Fabrication*, Appl. Phys. Lett. **67**, 2615 (1995).
- [96] S. Nakamura, T. Mukai, and M. Senoh, *High-Brightness InGaN/GaN Double-Heterostructure Blue-Green-Light-Emitting Diodes*, J. Appl. Phys. **76**, 8189 (1994).

- [97] M. Kawasaki, K. Takahashi, T. Maeda, R. Tsuchiya, M. Shinohara, O. Ishiyama, T. Yonezawa, M. Yoshimoto, and H. Koinuma, *Atomic Control of the SrTiO₃ Crystal-Surface*, Science **266**, 1540 (1994).
- [98] M. B. Lee, M. Kawasaki, M. Yoshimoto, M. Kumagai, and H. Koinuma, *Epitaxial-Growth of Highly Crystalline and Conductive Nitride Films by Pulsed-Laser Deposition*, Jpn. J. Appl. Phys., Part 1 **33**, 6308 (1994).
- [99] J. Cui, A. Sun, M. Reshchikov, F. Yun, A. Baski, and H. Morkoc, *Preparation of Sapphire for High Quality III-Nitride Growth*, MRS Internet J. Nitride Semicond. Res. **5**, 1 (2000).
- [100] G. Kastle, H. G. Boyen, B. Koslowski, A. Plettl, F. Weigl, and P. Ziemann, *Growth of Thin, Flat, Epitaxial (111) Oriented Gold Films on c-Cut Sapphire*, Surf. Sci. **498**, 168 (2002).
- [101] A. R. Wildes, J. Mayer, and K. Theis-Brohl, *The Growth and Structure of Epitaxial Niobium on Sapphire*, Thin Solid Films **401**, 7 (2001).
- [102] G. Gutekunst, J. Mayer, and M. Ruhle, *Atomic Structure of Epitaxial Nb-Al₂O₃ Interfaces. 1. Coherent Regions*, Philos. Mag. A **75**, 1329 (1997).
- [103] T. Wagner, *High Temperature Epitaxial Growth and Structure of Nb Films on α -Al₂O₃(0001)*, J. Mater. Res. **13**, 693 (1998).
- [104] A. Gibaud, R. A. Cowley, D. F. McMorro, R. C. C. Ward, and M. R. Wells, *High-Resolution X-Ray-Scattering Study of the Structure of Niobium Thin-Films on Sapphire*, Phys. Rev. B **48**, 14463 (1993).
- [105] A. R. Wildes, R. A. Cowley, R. C. C. Ward, M. R. Wells, C. Jansen, L. Wireen, and J. P. Hill, *The Structure of Epitaxially Grown Thin Films: A Study of Niobium on Sapphire*, J. Phys.: Condens. Matter **10**, L631 (1998).
- [106] M. Kitada, *Reactions in Au/Nb Bilayer Thin-Films*, Thin Solid Films **250**, 111 (1994).
- [107] D. Porath, O. Millo, and J. I. Gersten, *Scanning Tunneling Microscopy Studies and Computer Simulations of Annealing of Gold Films*, J. Vac. Sci. Technol. B **14**, 30 (1996).
- [108] R. R. Adzic, M. W. Hsiao, E. B. Yeager, and G. Pruett, *Scanning Tunneling Microscopy of Stepped Single-Crystal Surface of Gold*, Surf. Sci. **273**, L425 (1992).
- [109] J. Rundqvist, J. H. Hoh, and D. B. Haviland, *Substrate Effects in Poly(Ethylene Glycol) Self-Assembled Monolayers on Granular and Flame-Annealed Gold*, J. Colloid Interface Sci. **301**, 337 (2006).
- [110] M. H. Dishner, M. M. Ivey, S. Gorer, J. C. Hemminger, and F. J. Feher, *Preparation of Gold Thin Films by Epitaxial Growth on Mica and the Effect of Flame Annealing*, J. Vac. Sci. Technol., A **16**, 3295 (1998).
- [111] S. M. Landi, A. V. Bragas, J. A. Coy, and O. E. Martinez, *Avoiding Photothermal Noise in Laser Assisted Scanning Tunneling Microscopy*, Ultramicroscopy **77**, 207 (1999).
- [112] P. Chu and D. L. Mills, *Interaction of Adsorbates with Electric Field Fluctuations near Surfaces: Influence of the STM Tip and Plasmonic Effects*, Phys. Rev. B **79**, 115435 (2009).

- [113] J. B. Ballard, E. S. Carmichael, D. X. Shi, J. W. Lyding, and M. Gruebele, *Laser Absorption Scanning Tunneling Microscopy of Carbon Nanotubes*, Nano Lett. **6**, 45 (2006).
- [114] E. S. Carmichael, J. B. Ballard, J. W. Lyding, and M. Gruebele, *Frequency-Modulated, Single-Molecule Absorption Detected by Scanning Tunneling Microscopy*, J. Phys. Chem. C **111**, 3314 (2007).
- [115] K. S. Kim, M. S. Kang, H. Ma, and A. K. Y. Jen, *Highly Efficient Photocurrent Generation from a Self-Assembled Monolayer Film of a Novel C₆₀-Tethered 2,5-Dithienylpyrrole Triad*, Chem. Mater. **16**, 5058 (2004).
- [116] J. P. Ferraris and G. D. Skiles, *Substitutional Alloys of Organic Polymeric Conductors*, Polymer **28**, 179 (1987).
- [117] J. P. Ferraris and M. D. Newton, *Electrochemical and Optical Properties of Thiophene Alkylheteroaromatic Copolymers* Polymer **33**, 391 (1992).
- [118] Z. J. Donhauser, B. A. Mantooth, K. F. Kelly, L. A. Bumm, J. D. Monnell, J. J. Stapleton, D. W. Price, A. M. Rawlett, D. L. Allara, J. M. Tour, and P. S. Weiss, *Conductance Switching in Single Molecules through Conformational Changes*, Science **292**, 2303 (2001).
- [119] A. M. Moore, B. A. Mantooth, Z. J. Donhauser, F. Maya, D. W. Price, Y. X. Yao, J. M. Tour, and P. S. Weiss, *Cross-Step Place-Exchange of Oligo(Phenylene-Ethynylene) Molecules*, Nano Lett. **5**, 2292 (2005).
- [120] K. Sugawa, T. Akiyama, H. Kawazumi, and S. Yamada, *Plasmon-Enhanced Photocurrent Generation from Self-Assembled Monolayers of Phthalocyanine by Using Gold Nanoparticle Films*, Langmuir **25**, 3887 (2009).
- [121] R. F. Dou, X. C. Ma, L. Xi, H. L. Yip, K. Y. Wong, W. M. Lau, J. F. Jia, Q. K. Xue, W. S. Yang, H. Ma, and A. K. Y. Jen, *Self-Assembled Monolayers of Aromatic Thiols Stabilized by Parallel-Displaced π - π Stacking Interactions*, Langmuir **22**, 3049 (2006).
- [122] O. Takeuchi, S. Yoshida, and H. Shigekawa, *Light-Modulated Scanning Tunneling Spectroscopy for Nanoscale Imaging of Surface Photovoltage*, Appl. Phys. Lett. **84**, 3645 (2004).
- [123] R. Smoluchowski, *Anisotropy of the Electronic Work Function of Metals*, Phys. Rev. **60**, 661 (1941).
- [124] P. S. Weiss, M. M. Kamma, T. M. Graham, and S. J. Stranick, *Imaging Benzene Molecules and Phenyl Radicals on Cu(111)*, Langmuir **14**, 1284 (1998).
- [125] S. W. Sides, P. A. Rikvold, and M. A. Novotny, *Kinetic Ising Model in an Oscillating Field: Finite-Size Scaling at the Dynamic Phase Transition*, Phys. Rev. Lett. **81**, 834 (1998).
- [126] S. A. Claridge, A. W. Castleman, S. N. Khanna, C. B. Murray, A. Sen, and P. S. Weiss, *Cluster-Assembled Materials*, ACS Nano **3**, 244 (2009).

- [127] R. C. Jin, Y. W. Cao, C. A. Mirkin, K. L. Kelly, G. C. Schatz, and J. G. Zheng, *Photoinduced Conversion of Silver Nanospheres to Nanoprisms*, *Science* **294**, 1901 (2001).
- [128] L. J. Sherry, R. C. Jin, C. A. Mirkin, G. C. Schatz, and R. P. Van Duyne, *Localized Surface Plasmon Resonance Spectroscopy of Single Silver Triangular Nanoprisms*, *Nano Lett.* **6**, 2060 (2006).
- [129] L. Au, D. S. Zheng, F. Zhou, Z. Y. Li, X. D. Li, and Y. N. Xia, *A Quantitative Study on the Photothermal Effect of Immuno Gold Nanocages Targeted to Breast Cancer Cells*, *ACS Nano* **2**, 1645 (2008).
- [130] J. Zeng, Q. Zhang, J. Y. Chen, and Y. N. Xia, *A Comparison Study of the Catalytic Properties of Au-Based Nanocages, Nanoboxes, and Nanoparticles*, *Nano Lett.* **10**, 30 (2010).
- [131] J. D. Slinker, N. B. Muren, S. E. Renfrew, and J. K. Barton, *DNA Charge Transport over 34 nm*, *Nature Chemistry* **3**, 228 (2011).
- [132] J. C. Genereux and J. K. Barton, *Mechanisms for DNA Charge Transport*, *Chem. Rev.* **110**, 1642 (2010).
- [133] D. Venkataraman, S. Yurt, B. H. Venkatraman, and N. Gavvalapalli, *Role of Molecular Architecture in Organic Photovoltaic Cells*, *J. Phys. Chem. Lett.* **1**, 947 (2010).
- [134] G. Bottari, G. de la Torre, D. M. Guldi, and T. Torres, *Covalent and Noncovalent Phthalocyanine-Carbon Nanostructure Systems: Synthesis, Photoinduced Electron Transfer, and Application to Molecular Photovoltaics*, *Chem. Rev.* **110**, 6768 (2010).
- [135] A. Harootunian, E. Betzig, M. Isaacson, and A. Lewis, *Superresolution Fluorescence Near-Field Optical Microscopy*, *Appl. Phys. Lett.* **49**, 674 (1986).
- [136] K. Lieberman and A. Lewis, *Simultaneous Scanning Tunneling and Optical Near-Field Imaging with a Micropipette*, *Appl. Phys. Lett.* **62**, 1335 (1993).
- [137] F. Formanek, Y. De Wilde, L. Aigouy, W. K. Kwok, L. Paulius, and Y. Chen, *Nanometer-Scale Probing of Optical and Thermal Near-Fields with an Apertureless NSOM*, *Superlattices Microstruct.* **35**, 315 (2004).
- [138] A. Vaish, M. J. Shuster, S. Cheunkar, Y. S. Singh, P. S. Weiss, and A. M. Andrews, *Native Serotonin Membrane Receptors Recognize 5-Hydroxytryptophan-Functionalized Substrates: Enabling Small-Molecule Recognition*, *ACS Chem. Neurosci.* **1**, 495 (2010).
- [139] M. T. Cygan, T. D. Dunbar, J. J. Arnold, L. A. Bumm, N. F. Shedlock, T. P. Burgin, L. Jones, D. L. Allara, J. M. Tour, and P. S. Weiss, *Insertion, Conductivity, and Structures of Conjugated Organic Oligomers in Self-Assembled Alkanethiol Monolayers on Au{111}*, *J. Am. Chem. Soc.* **120**, 2721 (1998).
- [140] P. S. Weiss, *Functional Molecules and Assemblies in Controlled Environments: Formation and Measurements*, *Acc. Chem. Res.* **41**, 1772 (2008).
- [141] A. M. Moore, B. A. Mantooth, Z. J. Donhauser, Y. X. Yao, J. M. Tour, and P. S. Weiss, *Real-Time Measurements of Conductance Switching and Motion of Single Oligo(Phenylene Ethynylene) Molecules*, *J. Am. Chem. Soc.* **129**, 10352 (2007).

- [142] W. R. Browne, T. Kudernac, N. Katsonis, J. Areephong, J. Hielm, and B. L. Feringa, *Electro- and Photochemical Switching of Dithienylethene Self-Assembled Monolayers on Gold Electrodes*, *J. Phys. Chem. C* **112**, 1183 (2008).
- [143] A. S. Kumar, T. Ye, T. Takami, B. C. Yu, A. K. Flatt, J. M. Tour, and P. S. Weiss, *Reversible Photo-Switching of Single Azobenzene Molecules in Controlled Nanoscale Environments*, *Nano Lett.* **8**, 1644 (2008).
- [144] S. J. van der Molen, J. H. Liao, T. Kudernac, J. S. Agustsson, L. Bernard, M. Calame, B. J. van Wees, B. L. Feringa, and C. Schonenberger, *Light-Controlled Conductance Switching of Ordered Metal-Molecule-Metal Devices*, *Nano Lett.* **9**, 76 (2009).
- [145] K. Y. Wu, S. Y. Yu, and Y. T. Tao, *Continuous Modulation of Electrode Work Function with Mixed Self-Assembled Monolayers and Its Effect in Charge Injection*, *Langmuir* **25**, 6232 (2009).
- [146] H. Bouas-Laurent, A. Castellan, J. P. Desvergne, and R. Lapouyade, *Photodimerization of Anthracenes in Fluid Solution: Structural Aspects*, *Chem. Soc. Rev.* **29**, 43 (2000).
- [147] J. Reichert, R. Ochs, D. Beckmann, H. B. Weber, M. Mayor, and H. V. Lohneysen, *Driving Current through Single Organic Molecules*, *Phys. Rev. Lett.* **88**, 176804 (2002).
- [148] D. K. James and J. M. Tour, *Electrical Measurements in Molecular Electronics*, *Chem. Mater.* **16**, 4423 (2004).
- [149] J. E. Anthony, *Functionalized Acenes and Heteroacenes for Organic Electronics*, *Chem. Rev.* **106**, 5028 (2006).
- [150] D. Kafer, G. Witte, P. Cyganik, A. Terfort, and C. Woll, *A Comprehensive Study of Self-Assembled Monolayers of Anthracenethiol on Gold: Solvent Effects, Structure, and Stability*, *J. Am. Chem. Soc.* **128**, 1723 (2006).
- [151] M. H. Zareie, J. Barber, and A. M. McDonagh, *Structural Changes in Self-Assembled Monolayers Initiated by Ultraviolet Light*, *J. Phys. Chem. B* **110**, 15951 (2006).
- [152] M. A. Fox and M. D. Wooten, *Characterization, Adsorption, and Photochemistry of Self-Assembled Monolayers of 10-Thiodecyl 2-Anthryl Ether on Gold*, *Langmuir* **13**, 7099 (1997).
- [153] Z. J. Donhauser, D. W. Price, J. M. Tour, and P. S. Weiss, *Control of Alkanethiolate Monolayer Structure Using Vapor-Phase Annealing*, *J. Am. Chem. Soc.* **125**, 11462 (2003).
- [154] E. Delamarche, B. Michel, H. A. Biebuyck, and C. Gerber, *Golden Interfaces: The Surface of Self-Assembled Monolayers*, *Adv. Mater.* **8**, 719 (1996).
- [155] T. Ishida, S. Yamamoto, W. Mizutani, M. Motomatsu, H. Tokumoto, H. Hokari, H. Azebara, and M. Fujihira, *Evidence for Cleavage of Disulfides in the Self-Assembled Monolayer on Au(111)*, *Langmuir* **13**, 3261 (1997).
- [156] F. I. Ali, I. A. Hashmi, B. S. Siddiqui, and M. Rasheed, *Simple Method for the Preparation of Symmetrical Alkyl and Aryl Disulfides with Alkyl Sulfonyl Halides in Nitrogenous Base*, *Synth. Commun.* **37**, 2461 (2007).

- [157] M. Carril, R. SanMartin, E. Dominguez, and I. Tellitu, *A Highly Advantageous Metal-Free Approach to Diaryl Disulfides in Water*, *Green Chem.* **9**, 315 (2007).
- [158] T. Wolff, N. Muller, and G. Vonbunau, *Regioselective Photo-Dimerization of 9-Methylantracene in Homogeneous and Micellar Solutions*, *J. Photochem.* **22**, 61 (1983).
- [159] H. D. Becker and K. Andersson, *Photochemical Diels-Alder Dimerization of 9-Phenylethynylantracene*, *J. Photochem.* **26**, 75 (1984).
- [160] H. D. Becker, *Unimolecular Photochemistry of Anthracenes*, *Chem. Rev.* **93**, 145 (1993).
- [161] C. Gonzalez and E. C. Lim, *Electronic Spectra and Photophysics of the Two Stable Conformers of Anthracene Dimer: Evaluation of an Ab Initio Structure Prediction*, *Chem. Phys. Lett.* **322**, 382 (2000).
- [162] N. J. Brewer, S. Janusz, K. Critchley, S. D. Evans, and G. J. Leggett, *Photooxidation of Self-Assembled Monolayers by Exposure to Light of Wavelength 254 nm: A Static SIMS Study*, *J. Phys. Chem. B* **109**, 11247 (2005).
- [163] P. A. Lewis, C. E. Inman, Y. X. Yao, J. M. Tour, J. E. Hutchison, and P. S. Weiss, *Mediating Stochastic Switching of Single Molecules Using Chemical Functionality*, *J. Am. Chem. Soc.* **126**, 12214 (2004).
- [164] J. U. Nielsen, M. J. Esplandiu, and D. M. Kolb, *4-Nitrothiophenol SAM on Au(111) Investigated by in Situ STM, Electrochemistry, and XPS*, *Langmuir* **17**, 3454 (2001).
- [165] V. Iancu and S. W. Hla, *Realization of a Four-Step Molecular Switch in Scanning Tunneling Microscope Manipulation of Single Chlorophyll-a Molecules*, *Proc. Natl. Acad. Sci. U. S. A.* **103**, 13718 (2006).
- [166] Other proposed mechanisms for switching have included relative ring rotation. The calculated barrier to rotation about the ethynyl bond in **MPEA** is only ~1 kcal/mol (Figure 3.7), similar to the value calculated for phenyl ring rotation in **OPEs**, so the observed stability of the conductance status is inconsistent with ring rotation being responsible for conductance switching.
- [167] P. S. Weiss and D. M. Eigler, *Site Dependence of the Apparent Shape of a Molecule in Scanning Tunneling Microscope Images - Benzene on Pt(111)*, *Phys. Rev. Lett.* **71**, 3139 (1993).
- [168] I. B. Berlman, *Handbook of Fluorescence Spectra of Aromatic Molecules*; Academic Press: New York, 1971.
- [169] S. Olive and M. A. Fox, *Photooxidation of Anthracene on Atmospheric Particulate Matter*, *Science* **205**, 582 (1979).
- [170] M. A. Meador and H. Hart, *Substituent Effects on the Photoisomerization of Anthracenes to Their 9,10-Dewar Isomers*, *J. Org. Chem.* **54**, 2336 (1989).
- [171] M. J. Frisch, G. W. Trucks, H. B. Schlegel, G. E. Scuseria, M. A. Robb, J. R. Cheeseman, J. Montgomery, J. A. T. Vreven, K. N. Kudin, J. C. Burant, J. M. Millam, S. S. Iyengar, J. Tomasi, V. Barone, B. Mennucci, M. Cossi, G. Scalmani, N. Rega, G. A.

- Petersson, H. Nakatsuji, M. Hada, M. Ehara, K. Toyota, R. Fukuda, J. Hasegawa, M. Ishida, T. Nakajima, Y. Honda, O. Kitao, H. Nakai, M. Klene, X. Li, J. E. Knox, H. P. Hratchian, J. B. Cross, C. Adamo, J. Jaramillo, R. Gomperts, R. E. Stratmann, O. Yazyev, A. J. Austin, R. Cammi, C. Pomelli, J. W. Ochterski, P. Y. Ayala, K. Morokuma, G. A. Voth, P. Salvador, J. J. Dannenberg, V. G. Zakrzewski, S. Dapprich, A. D. Daniels, M. C. Strain, O. Farkas, D. K. Malick, A. D. Rabuck, K. Raghavachari, J. B. Foresman, J. V. Ortiz, Q. Cui, A. G. Baboul, S. Clifford, J. Cioslowski, B. B. Stefanov, G. Liu, A. Liashenko, P. Piskorz, I. Komaromi, R. L. Martin, D. J. Fox, T. Keith, M. A. Al-Laham, C. Y. Peng, A. Nanayakkara, M. Challacombe, P. M. W. Gill, B. Johnson, W. Chen, M. W. Wong, C. Gonzalez, and J. A. Pople, *Gaussian 03, Revision C.02*; Gaussian, Inc., Wallingford CT, 2004.
- [172] A. D. Becke, *Density-Functional Thermochemistry. 3. The Role of Exact Exchange*, J. Chem. Phys. **98**, 5648 (1993).
- [173] M. F. Perutz, A. J. Wilkinson, M. Paoli, and G. G. Dodson, *The Stereochemical Mechanism of the Cooperative Effects in Hemoglobin Revisited*, Annu. Rev. Biophys. Biomol. Struct. **27**, 1 (1998).
- [174] S. P. Sullivan, A. Schmeders, S. K. Mbugua, and T. P. Beebe, *Controlled Polymerization of Substituted Diacetylene Self-Organized Monolayers Confined in Molecule Corrals*, Langmuir **21**, 1322 (2005).
- [175] C. Chen, C. A. Bobisch, and W. Ho, *Visualization of Fermi's Golden Rule through Imaging of Light Emission from Atomic Silver Chains*, Science **325**, 981 (2009).
- [176] T. Ye, A. S. Kumar, S. Saha, T. Takami, T. J. Huang, J. F. Stoddart, and P. S. Weiss, *Changing Stations in Single Bistable Rotaxane Molecules under Electrochemical Control*, ACS Nano **4**, 3697 (2010).
- [177] L. H. Dubois and R. G. Nuzzo, *Synthesis, Structure, and Properties of Model Organic-Surfaces*, Annu. Rev. Phys. Chem. **43**, 437 (1992).
- [178] G. E. Poirier and M. J. Tarlov, *The $c(4 \times 2)$ Superlattice of n -Alkanethiol Monolayers Self-Assembled on Au(111)*, Langmuir **10**, 2853 (1994).
- [179] J. Noh and M. Hara, *Final Phase of Alkanethiol Self-Assembled Monolayers on Au(111)*, Langmuir **18**, 1953 (2002).
- [180] M. E. Anderson, R. K. Smith, Z. J. Donhauser, A. Hatzor, P. A. Lewis, L. P. Tan, H. Tanaka, M. W. Horn, and P. S. Weiss, *Exploiting Intermolecular Interactions and Self-Assembly for Ultrahigh Resolution Nanolithography*, J. Vac. Sci. Technol. B **20**, 2739 (2002).
- [181] H. M. Saavedra, C. M. Thompson, J. N. Hohman, V. H. Crespi, and P. S. Weiss, *Reversible Lability by in Situ Reaction of Self-Assembled Monolayers*, J. Am. Chem. Soc. **131**, 2252 (2009).
- [182] P. A. Lewis, R. K. Smith, K. F. Kelly, L. A. Bumm, S. M. Reed, R. S. Clegg, J. D. Gunderson, J. E. Hutchison, and P. S. Weiss, *The Role of Buried Hydrogen Bonds in Self-Assembled Mixed Composition Thiols on Au{111}*, J. Phys. Chem. B **105**, 10630 (2001).

- [183] R. K. Smith, S. M. Reed, P. A. Lewis, J. D. Monnell, R. S. Clegg, K. F. Kelly, L. A. Bumm, J. E. Hutchison, and P. S. Weiss, *Phase Separation within a Binary Self-Assembled Monolayer on Au{111} Driven by an Amide-Containing Alkanethiol*, J. Phys. Chem. B **105**, 1119 (2001).
- [184] P. V. Schleyer and M. M. Donaldson, *The Relative Stability of Bridged Hydrocarbons. II. Endo- and Exo-Trimethylenenorbornane. The Formation of Adamantane*, J. Am. Chem. Soc. **82**, 4645 (1960).
- [185] S. Fujii, U. Akiba, and M. Fujihira, *Geometry for Self-Assembling of Spherical Hydrocarbon Cages with Methane Thiolates on Au(111)*, J. Am. Chem. Soc. **124**, 13629 (2002).
- [186] T. Kitagawa, Y. Idomoto, H. Matsubara, D. Hobara, T. Kakiuchi, T. Okazaki, and K. Komatsu, *Rigid Molecular Tripod with an Adamantane Framework and Thiol Legs. Synthesis and Observation of an Ordered Monolayer on Au(111)*, J. Org. Chem. **71**, 1362 (2006).
- [187] S. Katano, Y. Kim, H. Matsubara, T. Kitagawa, and M. Kawai, *Hierarchical Chiral Framework Based on a Rigid Adamantane Tripod on Au(111)*, J. Am. Chem. Soc. **129**, 2511 (2007).
- [188] W. L. Yang, J. D. Fabbri, T. M. Willey, J. R. I. Lee, J. E. Dahl, R. M. K. Carlson, P. R. Schreiner, A. A. Fokin, B. A. Tkachenko, N. A. Fokina, W. Meevasana, N. Mannella, K. Tanaka, X. J. Zhou, T. van Buuren, M. A. Kelly, Z. Hussain, N. A. Melosh, and Z. X. Shen, *Monochromatic Electron Photoemission from Diamondoid Monolayers*, Science **316**, 1460 (2007).
- [189] T. M. Willey, J. D. Fabbri, J. R. I. Lee, P. R. Schreiner, A. A. Fokin, B. A. Tkachenko, N. A. Fokina, J. E. P. Dahl, R. M. K. Carlson, A. L. Vance, W. L. Yang, L. J. Terminello, T. van Buuren, and N. A. Melosh, *Near-Edge X-Ray Absorption Fine Structure Spectroscopy of Diamondoid Thiol Monolayers on Gold*, J. Am. Chem. Soc. **130**, 10536 (2008).
- [190] W. A. Clay, Z. Liu, W. Yang, J. D. Fabbri, J. E. Dahl, R. M. K. Carlson, Y. Sun, P. R. Schreiner, A. A. Fokin, B. A. Tkachenko, N. A. Fokina, P. A. Pianetta, N. Melosh, and Z.-X. Shen, *Origin of the Monochromatic Photoemission Peak in Diamondoid Monolayers*, Nano Lett. **9**, 57 (2009).
- [191] A. A. Dameron, L. F. Charles, and P. S. Weiss, *Structures and Displacement of 1-Adamantanethiol Self-Assembled Monolayers on Au{111}*, J. Am. Chem. Soc. **127**, 8697 (2005).
- [192] A. A. Dameron, J. R. Hampton, R. K. Smith, T. J. Mullen, S. D. Gillmor, and P. S. Weiss, *Microdisplacement Printing*, Nano Lett. **5**, 1834 (2005).
- [193] A. A. Dameron, J. R. Hampton, S. D. Gillmor, J. N. Hohman, and P. S. Weiss, *Enhanced Molecular Patterning via Microdisplacement Printing*, J. Vac. Sci. Technol. B **23**, 2929 (2005).
- [194] T. J. Mullen, A. A. Dameron, A. M. Andrews, and P. S. Weiss, *Selecting and Driving Monolayer Structures through Tailored Intermolecular Interactions*, Aldrichimica Acta **40**, 21 (2007).

- [195] C. Srinivasan, T. J. Mullen, J. N. Hohman, M. E. Anderson, A. A. Dameron, A. M. Andrews, E. C. Dickey, M. W. Horn, and P. S. Weiss, *Scanning Electron Microscopy of Nanoscale Chemical Patterns*, ACS Nano **1**, 191 (2007).
- [196] A. A. Dameron, T. J. Mullen, R. W. Hengstebeck, H. M. Saavedra, and P. S. Weiss, *Origins of Displacement in 1-Adamantanethiolate Self-Assembled Monolayers*, J. Phys. Chem. C **111**, 6747 (2007).
- [197] T. J. Mullen, A. A. Dameron, H. M. Saavedra, M. E. Williams, and P. S. Weiss, *Dynamics of Solution Displacement in 1-Adamantanethiolate Self-Assembled Monolayers*, J. Phys. Chem. C **111**, 6740 (2007).
- [198] P. E. Laibinis, R. G. Nuzzo, and G. M. Whitesides, *Structure of Monolayers Formed by Coadsorption of Two n-Alkanethiols of Different Chain Lengths on Gold and Its Relation to Wetting*, J. Phys. Chem **96**, 5097 (1992).
- [199] T. C. Zheng, M. Burkart, and D. E. Richardson, *A General and Mild Synthesis of Thioesters and Thiols from Halides*, Tetrahedron Lett. **40**, 603 (1999).
- [200] J. W. Greidanu and W. J. Schwalm, *Adamantanethione and Its Reduction to 2-Adamantanethiol*, Can. J. Chem. **47**, 3715 (1969).
- [201] J. W. Greidanu, *Chemistry of 2-Substituted Adamantanes. 2. Preparation of 2-Adamantanethiol and Some of Its Derivatives - Aromatic Solvent-Induced Shifts in Their NMR Spectra*, Can. J. Chem. **48**, 3593 (1970).
- [202] D. D. Tanner and B. G. Brownlee, *Free-Radical Substitution-Reactions of Sulfur Monochloride - Limited Synthesis of Mercaptans*, Can. J. Chem. **51**, 3366 (1973).
- [203] S. R. Wilson, G. M. Georgiadis, H. N. Khatri, and J. E. Bartmess, *Metalation of 1,3-Dithiolanes - Mercaptan Synthesis and Carbonyl Transposition*, J. Am. Chem. Soc. **102**, 3577 (1980).
- [204] D. Farcasiu, A. Ghenciu, and J. Q. Li, *The Mechanism of Conversion of Saturated Hydrocarbons Catalyzed by Sulfated Metal Oxides: Reaction of Adamantane on Sulfated Zirconia*, J. Catal. **158**, 116 (1996).
- [205] J. F. Moulder, *Handbook of X-Ray Photoelectron Spectroscopy: A Reference Book of Standard Spectra for Identification and Interpretation of XPS Data*; Perkin-Elmer Corporation, Physical Electronics Division: Eden Prairie, Mn, 1992.
- [206] N. Fairley, *CasaXPS*, 2005.
- [207] T. J. Mullen, Ph.D. Thesis, The Pennsylvania State University, University Park, PA, 2008.
- [208] T. J. Mullen, A. A. Dameron, and P. S. Weiss, *Directed Assembly and Separation of Self-Assembled Monolayers via Electrochemical Processing*, J. Phys. Chem. B **110**, 14410 (2006).
- [209] A. J. Bard and L. R. Faulkner, *Electrochemical Methods: Fundamentals and Applications*; John Wiley and Sons, Inc: Hoboken, 2001.
- [210] D. M. Collard and M. A. Fox, *Use of Electroactive Thiols to Study the Formation and Exchange of Alkanethiol Monolayers on Gold*, Langmuir **7**, 1192 (1991).

- [211] H. M. Saavedra, C. M. Barbu, A. A. Dameron, T. J. Mullen, V. H. Crespi, and P. S. Weiss, *1-Adamantanethiolate Monolayer Displacement Kinetics Follow a Universal Form*, J. Am. Chem. Soc. **129**, 10741 (2007).
- [212] J. Noh, T. Araki, K. Nakajima, and M. Hara, *Molecular Decomposition via Striped Phase in Self-Assembled Monolayers of Alkanethiols Adsorbed on Au(111)*, Mol. Cryst. Liq. Cryst. **371**, 95 (2001).
- [213] T. M. Willey, A. L. Vance, T. van Buuren, C. Bostedt, L. J. Terminello, and C. S. Fadley, *Rapid Degradation of Alkanethiol-Based Self-Assembled Monolayers on Gold in Ambient Laboratory Conditions*, Surf. Sci. **576**, 188 (2005).
- [214] E. Delamarche, B. Michel, H. Kang, and C. Gerber, *Thermal-Stability of Self-Assembled Monolayers*, Langmuir **10**, 4103 (1994).
- [215] N. Camillone, P. Eisenberger, T. Y. B. Leung, P. Schwartz, G. Scoles, G. E. Poirier, and M. J. Tarlov, *New Monolayer Phases of n-Alkane Thiols Self-Assembled on Au(111)-Preparation, Surface Characterization, and Imaging* J. Chem. Phys. **101**, 11031 (1994).
- [216] R. Yamada, H. Wano, and K. Uosaki, *Effect of Temperature on Structure of the Self-Assembled Monolayer of Decanethiol on Au(111) Surface*, Langmuir **16**, 5523 (2000).
- [217] L. Z. Zhang, W. A. Goddard, and S. Y. Jiang, *Molecular Simulation Study of the $c(4 \times 2)$ Superlattice Structure of Alkanethiol Self-Assembled Monolayers on Au(111)*, J. Chem. Phys. **117**, 7342 (2002).
- [218] W. Nowacki, *Die Krystall Struktur von Adamantan (Symm. Tri-Cyclo-Decan)*, Helv. Chim. Acta **28**, 1233 (1945).
- [219] B. Lussem, L. Muller-Meskamp, S. Karthaus, and R. Waser, *A New Phase of the $c(4 \times 2)$ Superstructure of Alkanethiols Grown by Vapor Phase Deposition on Gold*, Langmuir **21**, 5256 (2005).
- [220] S. J. Stranick, A. N. Parikh, Y. T. Tao, D. L. Allara, and P. S. Weiss, *Phase-Separation of Mixed-Composition Self-Assembled Monolayers into Nanometer-Scale Molecular Domains*, J. Phys. Chem **98**, 7636 (1994).
- [221] L. A. Bumm, J. J. Arnold, T. D. Dunbar, D. L. Allara, and P. S. Weiss, *Electron Transfer through Organic Molecules*, J. Phys. Chem. B **103**, 8122 (1999).
- [222] J. D. Monnell, J. J. Stapleton, J. J. Jackiw, T. Dunbar, W. A. Reinert, S. M. Dirk, J. M. Tour, D. L. Allara, and P. S. Weiss, *Ordered Local Domain Structures of Decaneselenolate and Dodecane-selenolate Monolayers on Au{111}*, J. Phys. Chem. B **108**, 9834 (2004).
- [223] J. D. Monnell, J. J. Stapleton, S. M. Dirk, W. A. Reinert, J. M. Tour, D. L. Allara, and P. S. Weiss, *Relative Conductances of Alkaneselenolate and Alkanethiolate Monolayers on Au{111}*, J. Phys. Chem. B **109**, 20343 (2005).
- [224] G. E. Poirier, W. P. Fitts, and J. M. White, *Two Dimensional Phase Diagram of Decanethiol on Au(111)*, Langmuir **17**, 1176 (2001).
- [225] W. P. Fitts, J. M. White, and G. E. Poirier, *Low-Coverage Decanethiolate Structure on Au(111): Substrate Effects*, Langmuir **18**, 1561 (2002).

- [226] W. P. Fitts, J. M. White, and G. E. Poirier, *Thermodynamics of Decanethiol Adsorption on Au(111): Extension to 0 Degrees C*, Langmuir **18**, 2096 (2002).
- [227] R. R. Kolega and J. B. Schlenoff, *Self-Assembled Monolayers of an Aryl Thiol: Formation, Stability, and Exchange of Adsorbed 2-Naphthalenethiol and Bis(2-Naphthyl) Disulfide on Au*, Langmuir **14**, 5469 (1998).
- [228] Y. S. Shon and T. R. Lee, *Desorption and Exchange of Self-Assembled Monolayers (SAMs) on Gold Generated from Chelating Alkanedithiols*, J. Phys. Chem. B **104**, 8192 (2000).
- [229] S. Imabayashi, D. Hobara, T. Kakiuchi, and W. Knoll, *Selective Replacement of Adsorbed Alkanethiols in Phase-Separated Binary Self-Assembled Monolayers by Electrochemical Partial Desorption*, Langmuir **13**, 4502 (1997).
- [230] M. M. Walczak, D. D. Popenoe, R. S. Deinhammer, B. D. Lamp, C. K. Chung, and M. D. Porter, *Reductive Desorption of Alkanethiolate Monolayers at Gold - a Measure of Surface Coverage*, Langmuir **7**, 2687 (1991).
- [231] D. Hobara, O. Miyake, S. Imabayashi, K. Niki, and T. Kakiuchi, *In-Situ Scanning Tunneling Microscopy Imaging of the Reductive Desorption Process of Alkanethiols on Au(111)*, Langmuir **14**, 3590 (1998).
- [232] D. Hobara, M. Ota, S. Imabayashi, K. Niki, and T. Kakiuchi, *Phase Separation of Binary Self-Assembled Thiol Monolayers Composed of 1-Hexadecanethiol and 3-Mercaptopropionic Acid on Au(111) Studied by Scanning Tunneling Microscopy and Cyclic Voltammetry*, J. Electroanal. Chem. **444**, 113 (1998).
- [233] K. M. Balss, B. D. Coleman, C. H. Lansford, R. T. Haasch, and P. W. Bohn, *Active Spatiotemporal Control of Electrochemical Reactions by Coupling to in-Plane Potential Gradients*, J. Phys. Chem. B **105**, 8970 (2001).
- [234] T. Kakiuchi, H. Usui, D. Hobara, and M. Yamamoto, *Voltammetric Properties of the Reductive Desorption of Alkanethiol Self-Assembled Monolayers from a Metal Surface*, Langmuir **18**, 5231 (2002).
- [235] C. A. Widrig, C. Chung, and M. D. Porter, *The Electrochemical Desorption of n-Alkanethiol Monolayers from Polycrystalline Au and Ag Electrodes*, J. Electroanal. Chem. **310**, 335 (1991).
- [236] M. D. Porter, T. B. Bright, D. L. Allara, and C. E. D. Chidsey, *Spontaneously Organized Molecular Assemblies. 4. Structural Characterization of n-Alkyl Thiol Monolayers on Gold by Optical Ellipsometry, Infrared Spectroscopy, and Electrochemistry*, J. Am. Chem. Soc. **109**, 3559 (1987).
- [237] J. J. Calvente, Z. Kovacova, R. Andreu, and W. R. Fawcett, *Numerical Simulation of Desorption Transients at Electrodes on the Basis of Non-Linear Adsorption Isotherms*, J. Chem. Soc., Faraday Trans. **92**, 3701 (1996).
- [238] J. J. Calvente, Z. Kovacova, M. D. Sanchez, R. Andreu, and W. R. Fawcett, *Desorption of Spontaneously Adsorbed and Electrochemically Readsorbed 2-Mercaptoethanesulfonate on Au(111)*, Langmuir **12**, 5696 (1996).

- [239] C. J. Zhong and M. D. Porter, *Fine Structure in the Voltammetric Desorption Curves of Alkanethiolate Monolayers Chemisorbed at Gold*, J. Electroanal. Chem. **425**, 147 (1997).
- [240] R. G. Nuzzo, L. H. Dubois, and D. L. Allara, *Fundamental-Studies of Microscopic Wetting on Organic-Surfaces. 1. Formation and Structural Characterization of a Self-Consistent Series of Polyfunctional Organic Monolayers*, J. Am. Chem. Soc. **112**, 558 (1990).
- [241] P. E. Laibinis, C. D. Bain, and G. M. Whitesides, *Attenuation of Photoelectrons in Monolayers of n-Alkanethiols Adsorbed on Copper, Silver, and Gold*, J. Phys. Chem **95**, 7017 (1991).
- [242] A. Snis and S. F. Matar, *Electronic Density of States, 1s Core-Level Shifts, and Core Ionization Energies of Graphite, Diamond, C₃N₄ Phases, and Graphitic C₁₁N₄*, Phys. Rev. B **60**, 10855 (1999).
- [243] O. M. Cabarcos, A. Shaporenko, T. Weidner, S. Uppili, L. S. Dake, M. Zharnikov, and D. L. Allara, *Physical and Electronic Structure Effects of Embedded Dipoles in Self-Assembled Monolayers: Characterization of Mid-Chain Ester Functionalized Alkanethiols on Au{111}*, J. Phys. Chem. C **112**, 10842 (2008).
- [244] R. G. Nuzzo, B. R. Zegarski, and L. H. Dubois, *Fundamental-Studies of the Chemisorption of Adsorbates on Well-Defined Organic-Surfaces*, J. Electrochem. Soc. **134**, C110 (1987).
- [245] A. S. Duwez, *Exploiting Electron Spectroscopies to Probe the Structure and Organization of Self-Assembled Monolayers: A Review*, J. Electron Spectrosc. Relat. Phenom. **134**, 97 (2004).
- [246] T. Ishida, M. Hara, I. Kojima, S. Tsuneda, N. Nishida, H. Sasabe, and W. Knoll, *High Resolution X-Ray Photoelectron Spectroscopy Measurements of Octadecanethiol Self-Assembled Monolayers on Au(111)*, Langmuir **14**, 2092 (1998).
- [247] T. Ishida, N. Choi, W. Mizutani, H. Tokumoto, I. Kojima, H. Azehara, H. Hokari, U. Akiba, and M. Fujihira, *High-Resolution X-Ray Photoelectron Spectra of Organosulfur Monolayers on Au(111): S(2p) Spectral Dependence on Molecular Species*, Langmuir **15**, 6799 (1999).
- [248] J. Noh, E. Ito, K. Nakajima, J. Kim, H. Lee, and M. Hara, *High-Resolution STM and XPS Studies of Thiophene Self-Assembled Monolayers on Au(111)*, J. Phys. Chem. B **106**, 7139 (2002).
- [249] C. D. Bain, H. A. Biebuyck, and G. M. Whitesides, *Comparison of Self-Assembled Monolayers on Gold - Coadsorption of Thiols and Disulfides*, Langmuir **5**, 723 (1989).
- [250] D. E. Weisshaar, M. M. Walczak, and M. D. Porter, *Electrochemically Induced Transformations of Monolayers Formed by Self-Assembly of Mercaptoethanol at Gold*, Langmuir **9**, 323 (1993).
- [251] C. J. Zhong and M. D. Porter, *Evidence for Carbon Sulfur Bond-Cleavage in Spontaneously Adsorbed Organosulfide-Based Monolayers at Gold*, J. Am. Chem. Soc. **116**, 11616 (1994).

- [252] D. G. Castner, K. Hinds, and D. W. Grainger, *X-Ray Photoelectron Spectroscopy Sulfur 2p Study of Organic Thiol and Disulfide Binding Interactions with Gold Surfaces*, *Langmuir* **12**, 5083 (1996).
- [253] M. T. Lee, C. C. Hsueh, M. S. Freund, and G. S. Ferguson, *Air Oxidation of Self-Assembled Monolayers on Polycrystalline Gold: The Role of the Gold Substrate*, *Langmuir* **14**, 6419 (1998).
- [254] C. M. Whelan, M. R. Smyth, C. J. Barnes, N. M. D. Brown, and C. A. Anderson, *An XPS Study of Heterocyclic Thiol Self-Assembly on Au(111)*, *Appl. Surf. Sci.* **134**, 144 (1998).
- [255] E. Sabatani, J. Cohenboulakia, M. Bruening, and I. Rubinstein, *Thioaromatic Monolayers on Gold - a New Family of Self-Assembling Monolayers*, *Langmuir* **9**, 2974 (1993).
- [256] Y. T. Tao, C. C. Wu, J. Y. Eu, W. L. Lin, K. C. Wu, and C. H. Chen, *Structure Evolution of Aromatic-Derivatized Thiol Monolayers on Evaporated Gold*, *Langmuir* **13**, 4018 (1997).
- [257] P. Kohli, K. K. Taylor, J. J. Harris, and G. J. Blanchard, *Assembly of Covalently-Coupled Disulfide Multilayers on Gold*, *J. Am. Chem. Soc.* **120**, 11962 (1998).
- [258] M. C. Bourg, A. Badia, and R. B. Lennox, *Gold-Sulfur Bonding in 2D and 3D Self-Assembled Monolayers: XPS Characterization*, *J. Phys. Chem. B* **104**, 6562 (2000).
- [259] J. R. I. Lee, T. M. Willey, J. Nilsson, L. J. Terminello, J. J. De Yoreo, and T. van Buuren, *Effect of Ring Substitution Position on the Structural Conformation of Mercaptobenzoic Acid Self-Assembled Monolayers on Au(111)*, *Langmuir* **22**, 11134 (2006).
- [260] L. Bistričić, G. Baranović, and K. Mlinarić-majerski, *A Vibrational Assignment of Adamantane and Some of Its Isotopomers - Empirical Versus Scaled Semiepirical Force-Field*, *Spectroc. Acta Pt. A-Molec. Biomolec. Spectr.* **51**, 1643 (1995).
- [261] J. J. Fox and A. E. Martin, *Investigations of Infrared Spectra. Determination of C-H Frequencies ($\sim 3000\text{ cm}^{-1}$) in Paraffins and Olefins, with Some Observations On "Polythenes"*, *Proc R. Soc. London, A* **175**, 208 (1940).
- [262] J. O. Jensen, *Vibrational Frequencies and Structural Determination of Adamantane*, *Spectroc. Acta Pt. A-Molec. Biomolec. Spectr.* **60**, 1895 (2004).
- [263] E. Delamarche, A. C. F. Hoole, B. Michel, S. Wilkes, M. Despont, M. E. Welland, and H. Biebuyck, *Making Gold Nanostructures Using Self-Assembled Monolayers and a Scanning Tunneling Microscope*, *J. Phys. Chem. B* **101**, 9263 (1997).
- [264] L. H. Dubois, B. R. Zegarski, and R. G. Nuzzo, *Fundamental-Studies of the Interactions of Adsorbates on Organic-Surfaces*, *Proc. Natl. Acad. Sci. U. S. A.* **84**, 4739 (1987).
- [265] D. J. Lavrich, S. M. Wetterer, S. L. Bernasek, and G. Scoles, *Physisorption and Chemisorption of Alkanethiols and Alkyl Sulfides on Au(111)*, *J. Phys. Chem. B* **102**, 3456 (1998).

- [266] D. L. Allara and R. G. Nuzzo, *Spontaneously Organized Molecular Assemblies. I. Formation, Dynamics, and Physical-Properties of n-Alkanoic Acids Adsorbed from Solution on an Oxidized Aluminum Surface*, *Langmuir* **1**, 45 (1985).
- [267] S. N. Patole, C. J. Baddeley, D. O'Hagan, and N. V. Richardson, *Reversible Exchange of Self-Assembled Monolayers of Semifluorinated n-Alkanethiols and n-Alkanethiols on Au/Mica Surfaces*, *J. Phys. Chem. C* **112**, 13997 (2008).
- [268] P. S. Weiss, *Nanotechnology - Molecules Join the Assembly Line*, *Nature* **413**, 585 (2001).
- [269] Y. H. Wang, C. A. Mirkin, and S. J. Park, *Nanofabrication Beyond Electronics*, *ACS Nano* **3**, 1049 (2009).
- [270] H. M. Saavedra, T. J. Mullen, P. P. Zhang, D. C. Dewey, S. A. Claridge, and P. S. Weiss, *Hybrid Strategies in Nanolithography*, *Rep. Prog. Phys.* **73**, 036501 (2010).
- [271] G. Benitez, C. Vericat, S. Tanco, F. R. Lenicov, M. F. Castez, A. E. Vela, and R. C. Salvarezza, *Role of Surface Heterogeneity and Molecular Interactions in the Charge-Transfer Process through Self-Assembled Thiolate Monolayers on Au(111)*, *Langmuir* **20**, 5030 (2004).
- [272] T. Base, Z. Bastl, Z. Plzak, T. Grygar, J. Plesek, M. J. Carr, V. Malina, J. Subrt, J. Bohacek, E. Vecernikova, and O. Kriz, *Carboranethiol-Modified Gold Surfaces. A Study and Comparison of Modified Cluster and Flat Surfaces*, *Langmuir* **21**, 7776 (2005).
- [273] J. Strutwolf and C. K. O'Sullivan, *Microstructures by Selective Desorption of Self-Assembled Monolayer from Polycrystalline Gold Electrodes*, *Electroanalysis* **19**, 1467 (2007).
- [274] T. Base, Z. Bastl, M. Slouf, M. Klementova, J. Subrt, A. Vetushka, M. Ledinsky, A. Fejfar, J. Machacek, M. J. Carr, and M. G. S. Londesborough, *Gold Micrometer Crystals Modified with Carboranethiol Derivatives*, *J. Phys. Chem. C* **112**, 14446 (2008).
- [275] A. Firagoso, H. Laboria, D. Latta, and C. K. O'Sullivan, *Electron Permeable Self-Assembled Monolayers of Dithiolated Aromatic Scaffolds on Gold for Biosensor Applications*, *Anal. Chem.* **80**, 2556 (2008).
- [276] O. Y. F. Henry, A. Maliszewska, and C. K. O'Sullivan, *DNA Surface Nanopatterning by Selective Reductive Desorption from Polycrystalline Gold Electrode*, *Electrochem. Commun.* **11**, 664 (2009).
- [277] R. S. Clegg and J. E. Hutchison, *Hydrogen-Bonding, Self-Assembled Monolayers: Ordered Molecular Films for Study of Through-Peptide Electron Transfer*, *Langmuir* **12**, 5239 (1996).
- [278] R. S. Clegg, S. M. Reed, and J. E. Hutchison, *Self-Assembled Monolayers Stabilized by Three-Dimensional Networks of Hydrogen Bonds*, *J. Am. Chem. Soc.* **120**, 2486 (1998).
- [279] R. S. Clegg and J. E. Hutchison, *Control of Monolayer Assembly Structure by Hydrogen Bonding Rather than by Adsorbate-Substrate Templating*, *J. Am. Chem. Soc.* **121**, 5319 (1999).

- [280] K. Slowinski, H. K. Y. Fong, and M. Majda, *Mercury-Mercury Tunneling Junctions. I. Electron Tunneling across Symmetric and Asymmetric Alkanethiolate Bilayers*, J. Am. Chem. Soc. **121**, 7257 (1999).
- [281] T. J. Lenk, V. M. Hallmark, C. L. Hoffmann, J. F. Rabolt, D. G. Castner, C. Erdelen, and H. Ringsdorf, *Structural Investigation of Molecular-Organization in Self-Assembled Monolayers of a Semifluorinated Amidethiol*, Langmuir **10**, 4610 (1994).
- [282] S. W. Tamchang, H. A. Biebuyck, G. M. Whitesides, N. Jeon, and R. G. Nuzzo, *Self-Assembled Monolayers on Gold Generated from Alkanethiols with the Structure $RNHCOCH_2SH$* , Langmuir **11**, 4371 (1995).
- [283] R. S. Clegg, S. M. Reed, R. K. Smith, B. L. Barron, J. A. Rear, and J. E. Hutchison, *The Interplay of Lateral and Tiered Interactions in Stratified Self-Organized Molecular Assemblies*, Langmuir **15**, 8876 (1999).
- [284] R. C. Chambers, C. E. Inman, and J. E. Hutchison, *Electrochemical Detection of Nanoscale Phase Separation in Binary Self-Assembled Monolayers*, Langmuir **21**, 4615 (2005).
- [285] M. H. Schoenfish, A. M. Ross, and J. E. Pemberton, *Electrochemical Cleaning of Surface-Confined Carbon Contamination in Self-Assembled Monolayers on Polycrystalline Ag and Au*, Langmuir **16**, 2907 (2000).
- [286] T. Kakiuchi, K. Sato, M. Iida, D. Hobara, S. Imabayashi, and K. Niki, *Phase Separation of Alkanethiol Self-Assembled Monolayers During the Replacement of Adsorbed Thiolates on Au(111) with Thiols in Solution*, Langmuir **16**, 7238 (2000).
- [287] T. Arakawa, D. Hobara, M. Yamamoto, and T. Kakiuchi, *Effect of the Charged State of Gold Substrates on the Surface Composition of Two-Component Alkanethiol Self-Assembled Monolayers*, Electrochem. Commun. **7**, 848 (2005).
- [288] N. S. Pesika, K. J. Stebe, and P. C. Searson, *Kinetics of Desorption of Alkanethiolates on Gold*, Langmuir **22**, 3474 (2006).
- [289] P. H. Phong, V. V. Sokolov, N. Nishi, M. Yamamoto, and T. Kakiuchi, *Concentration-Dependent Switching of the Mode of Phase Separation in Ternary Self-Assembled Monolayers of 2-Mercaptoethane Sulfonic Acid, 2-Aminoethanethiol and 1-Dodecanethiol on Au(111)*, J. Electroanal. Chem. **600**, 35 (2007).
- [290] P. H. Phong, H. Tomono, N. Nishi, M. Yamamoto, and T. Kakiuchi, *Artificially Phase-Separated Binary Self-Assembled Monolayers Composed of 11-Amino-1-Undecanethiolate and 10-Carboxy-1-Decanethiolate on Au(111): A Comparative Study of Two Preparing Methods*, Electrochim. Acta **53**, 4900 (2008).
- [291] N. A. Kautz and S. A. Kandel, *Alkanethiol Monolayers Contain Gold Adatoms, and Adatom Coverage Is Independent of Chain Length*, J. Phys. Chem. C **113**, 19286 (2009).
- [292] E. Torres, A. T. Blumenau, and P. U. Biedermann, *Mechanism for Phase Transitions and Vacancy Island Formation in Alkylthiol/Au(111) Self-Assembled Monolayers Based on Adatom and Vacancy-Induced Reconstructions*, Phys. Rev. B **79**, 075440 (2009).

- [293] S. J. Stranick, A. N. Parikh, D. L. Allara, and P. S. Weiss, *A New Mechanism for Surface Diffusion: Motion of a Substrate-Adsorbate Complex*, J. Phys. Chem **98**, 11136 (1994).
- [294] G. E. Poirier and M. J. Tarlov, *Molecular Ordering and Gold Migration Observed in Butanethiol Self-Assembled Monolayers Using Scanning-Tunneling-Microscopy*, J. Phys. Chem **99**, 10966 (1995).
- [295] F. T. Arce, M. E. Vela, R. C. Salvarezza, and A. J. Arvia, *Dynamic Characteristics of Adsorbed Monolayers of 1-Dodecanethiol on Gold (111) Terraces from in-situ Scanning Tunneling Microscopy Imaging*, Electrochim. Acta **44**, 1053 (1998).
- [296] R. L. McCarley, D. J. Dunaway, and R. J. Willicut, *Mobility of the Alkanethiol Gold(111) Interface Studied by Scanning Probe Microscopy*, Langmuir **9**, 2775 (1993).
- [297] P. Fenter, P. Eisenberger, and K. S. Liang, *Chain-Length Dependence of the Structures and Phases of $\text{CH}_3(\text{CH}_2)_{n-1}\text{SH}$ Self-Assembled on Au(111)*, Phys. Rev. Lett. **70**, 2447 (1993).
- [298] J. Noh, H. S. Kato, M. Kawai, and M. Hara, *Surface Structure and Interface Dynamics of Alkanethiol Self-Assembled Monolayers on Au(111)*, J. Phys. Chem. B **110**, 2793 (2006).
- [299] D. F. Yang, C. P. Wilde, and M. Morin, *Studies of the Electrochemical Removal and Efficient Re-Formation of a Monolayer of Hexadecanethiol Self-Assembled at an Au(111) Single Crystal in Aqueous Solutions*, Langmuir **13**, 243 (1997).
- [300] M. Byloos, H. Al-Maznai, and M. Morin, *Formation of a Self-Assembled Monolayer via the Electrospreeding of Physisorbed Micelles of Thiolates*, J. Phys. Chem. B **103**, 6554 (1999).
- [301] D. F. Yang, C. P. Wilde, and M. Morin, *Electrochemical Desorption and Adsorption of Nonyl Mercaptan at Gold Single Crystal Electrode Surfaces*, Langmuir **12**, 6570 (1996).
- [302] T. Sumi and K. Uosaki, *Electrochemical Oxidative Formation and Reductive Desorption of a Self-Assembled Monolayer of Decanethiol on a Au(111) Surface in KOH Ethanol Solution*, J. Phys. Chem. B **108**, 6422 (2004).
- [303] J. H. Kennedy and F. Adamo, *Controlled Potential Electrolysis - an Experiment for Elementary Quantitative Analysis*, J. Chem. Educ. **47**, 461 (1970).
- [304] G. E. Poirier, M. J. Tarlov, and H. E. Rushmeier, *2-Dimensional Liquid-Phase and the $(P \times \sqrt{3})$ -Phase of Alkanethiol Self-Assembled Monolayers on Au(111)*, Langmuir **10**, 3383 (1994).
- [305] H. Hagenstrom, M. A. Schneeweiss, and D. M. Kolb, *Modification of a Au(111) Electrode with Ethanethiol. 1. Adlayer Structure and Electrochemistry*, Langmuir **15**, 2435 (1999).
- [306] T. C. Cheam and S. Krimm, *Vibrational Analysis of Peptides, Polypeptides, and Proteins. 26. Infrared Intensities of Amide Modes in n-Methylacetamide and Poly(glycine-I) from Ab Initio Calculations of Dipole-Moment Derivatives of n-Methylacetamide*, J. Chem. Phys. **82**, 1631 (1985).

- [307] D. L. Allara and R. G. Nuzzo, *Spontaneously Organized Molecular Assemblies. 2. Quantitative Infrared Spectroscopic Determination of Equilibrium Structures of Solution-Adsorbed n-Alkanoic Acids on an Oxidized Aluminum Surface*, *Langmuir* **1**, 52 (1985).
- [308] S. Krimm and J. Bandekar, *Vibrational Spectroscopy and Conformation of Peptides, Polypeptides, and Proteins*, *Adv. Protein Chem.* **38**, 181 (1986).
- [309] M. D. Porter, *IR External Reflection Spectroscopy - a Probe for Chemically Modified Surfaces*, *Anal. Chem.* **60**, 1143A (1988).
- [310] Y. Ge, T. Weidner, H. Ahn, J. E. Whitten, and M. Zharnikov, *Energy Level Pinning in Self-Assembled Alkanethiol Monolayers*, *J. Phys. Chem. C* **113**, 4575 (2009).
- [311] T. L. Brown, H. E. Lemay, and B. E. Bursten, *Chemistry: The Central Science*; Pearson Publications Company: NJ, 2006.
- [312] D. Zahn, *Car-Parrinello Molecular Dynamics Simulation of Base-Catalyzed Amide Hydrolysis in Aqueous Solution*, *Chem. Phys. Lett.* **383**, 134 (2004).
- [313] D. Zahn, *On the Role of Water in Amide Hydrolysis*, *Eur. J. Org. Chem.* **2004**, 4020 (2004).
- [314] For a gold electrode modified with alkanethiolate SAMs, reductive desorption by applying a sufficient cathodic potential is a one-electron process. $\text{RS-Au} + 1\text{e}^- \rightarrow \text{RS}^- + \text{Au}_0$.
- [315] D. Hobara, M. Yamamoto, and T. Kakiuchi, *Reconstruction of Au(111) Following the Reductive Desorption of Self-Assembled Monolayers of 2-Mercaptoethanesulfonic Acid Studied by in Situ Scanning Tunneling Microscopy*, *Chem. Lett.* **30**, 374 (2001).
- [316] M. J. Esplandiu, H. Hagenstrom, and D. M. Kolb, *Functionalized Self-Assembled Alkanethiol Monolayers on Au(111) Electrodes: 1. Surface Structure and Electrochemistry*, *Langmuir* **17**, 828 (2001).
- [317] M. Schweizer, H. Hagenstrom, and D. M. Kolb, *Potential-Induced Structure Transitions in Self-Assembled Monolayers: Ethanethiol on Au(100)*, *Surf. Sci.* **490**, L627 (2001).
- [318] M. Schweizer, M. Manolova, and D. M. Kolb, *Potential-Induced Structure Transitions in Self-Assembled Monolayers: II. Propanethiol on Au(100)*, *Surf. Sci.* **602**, 3303 (2008).
- [319] S. Yoshimoto, E. Tsutsumi, R. Narita, Y. Murata, M. Murata, K. Fujiwara, K. Komatsu, O. Ito, and K. Itaya, *Epitaxial Supramolecular Assembly of Fullerenes Formed by Using a Coronene Template on a Au(111) Surface in Solution*, *J. Am. Chem. Soc.* **129**, 4366 (2007).
- [320] S. Yoshimoto, Y. Honda, O. Ito, and K. Itaya, *Supramolecular Pattern of Fullerene on 2D Bimolecular "Chessboard" Consisting of Bottom-up Assembly of Porphyrin and Phthalocyanine Molecules*, *J. Am. Chem. Soc.* **130**, 1085 (2008).
- [321] P. Zhou, Z. H. Dong, A. M. Rao, and P. C. Eklund, *Reaction-Mechanism for the Photopolymerization of Solid Fullerene C₆₀*, *Chem. Phys. Lett.* **211**, 337 (1993).

- [322] J. Y. Kim, K. Lee, N. E. Coates, D. Moses, T. Q. Nguyen, M. Dante, and A. J. Heeger, *Efficient Tandem Polymer Solar Cells Fabricated by All-Solution Processing*, *Science* **317**, 222 (2007).
- [323] T. Erb, U. Zhokhavets, G. Gobsch, S. Raleva, B. Stuhn, P. Schilinsky, C. Waldauf, and C. J. Brabec, *Correlation between Structural and Optical Properties of Composite Polymer/Fullerene Films for Organic Solar Cells*, *Adv. Funct. Mater.* **15**, 1193 (2005).
- [324] G. Dennler, M. C. Scharber, and C. J. Brabec, *Polymer-Fullerene Bulk-Heterojunction Solar Cells*, *Adv. Mater.* **21**, 1323 (2009).
- [325] J. J. Palacios, A. J. Perez-Jimenez, E. Louis, and J. A. Verges, *Fullerene-Based Molecular Nanobridges: A First-Principles Study*, *Phys. Rev. B* **64** (2001).
- [326] T. Shimada, T. Okazaki, R. Taniguchi, T. Sugai, H. Shinohara, K. Suenaga, Y. Ohno, S. Mizuno, S. Kishimoto, and T. Mizutani, *Ambipolar Field-Effect Transistor Behavior of Gd@C₈₂ Metallofullerene Peapods*, *Appl. Phys. Lett.* **81**, 4067 (2002).
- [327] N. Marjanovic, T. B. Singh, G. Dennler, S. Gunes, H. Neugebauer, N. S. Sariciftci, R. Schwodiauer, and S. Bauer, *Photoresponse of Organic Field-Effect Transistors Based on Conjugated Polymer/Fullerene Blends*, *Organic Electronics* **7**, 188 (2006).
- [328] A. Dzwilewski, T. Wagberg, and L. Edman, *C₆₀ Field-Effect Transistors: Effects of Polymerization on Electronic Properties and Device Performance*, *Phys. Rev. B* **75** (2007).
- [329] A. Dzwilewski, T. Wagberg, and L. Edman, *Photo-Induced and Resist-Free Imprint Patterning of Fullerene Materials for Use in Functional Electronics*, *J. Am. Chem. Soc.* **131**, 4006 (2009).
- [330] E. Kovats, G. Oszlanyi, and S. Pekker, *Structure of the Crystalline C₆₀ Photopolymer and the Isolation of Its Cycloadduct Components*, *J. Phys. Chem. B* **109**, 11913 (2005).
- [331] M. Nakaya, T. Nakayama, and M. Aono, *Fabrication and Electron-Beam-Induced Polymerization of C₆₀ Nanoribbon*, *Thin Solid Films* **464**, 327 (2004).
- [332] S. Tsukamoto, T. Nakayama, and M. Aono, *First-Principles Study on Electronic Responses of a C₆₀ Molecule to External Electric Fields*, *Chem. Phys.* **342**, 135 (2007).
- [333] R. Priefer, Y. J. Lee, F. Barrios, J. H. Wosnick, A. M. Lehuis, P. G. Farrell, D. N. Harpp, A. M. Sun, S. X. Wu, and J. P. Snyder, *Dicubyl Disulfide*, *J. Am. Chem. Soc.* **124**, 5626 (2002).
- [334] T. M. Swager, D. A. Dougherty, and R. H. Grubbs, *Strained Rings as a Source of Unsaturation - Polybenzvalene, a New Soluble Polyacetylene Precursor*, *J. Am. Chem. Soc.* **110**, 2973 (1988).
- [335] F. L. Klavetter and R. H. Grubbs, *Polycyclooctatetraene (Polyacetylene) - Synthesis and Properties*, *J. Am. Chem. Soc.* **110**, 7807 (1988).
- [336] P. E. Eaton and D. Stossel, *Synthesis of Alkynylcyclooctatetraenes and Alkynylcubanes*, *J. Org. Chem.* **56**, 5138 (1991).

- [337] J. N. Hohman, M. Kim, G. A. Wadsworth, H. R. Bednar, J. Jiang, M. A. Lethai, and P. S. Weiss, *Shaken Not Stirred: Liquid-Metal Nanoparticles by Molecular Disassembly*, submitted (2011).

Vita

Moonhee Kim

Education

Ph.D., Chemistry, The Pennsylvania State University, University Park, PA, August 2011
Dissertation Title: Beyond Molecular Assemblies and Scanning Tunneling Microscopy
Thesis Advisor: Paul S. Weiss,

B.S. and M.S., Chemistry, Korea University, Seoul, South Korea 2002
Thesis Title: Characterization of Polymer-SWNTs Nanocomposite Light Emitting Diodes
Thesis Advisor: Jong-Ho Choi,

Professional Experience

Research Scientist, Park Systems	2002, 2003
Graduate Research Assistant, The Pennsylvania State University; Advisor: Paul S. Weiss	2004 - 2010
Graduate Research Assistant, California NanoSystems Institute, University of California at Los Angeles; Advisor: Paul S. Weiss	2010, 2011
Teaching Assistant, The Pennsylvania State University:	
Honors General Chemistry	2006
General Chemistry Lab	2007
Physical Chemistry	2008
Honors General Chemistry	2009

Honors and Awards

ACS Division of Colloid & Surface Chemistry Best Student Poster	2010
Chemistry Travel Awards at Penn State	2007, 2008, 2009, 2010, 2011
Penn State Chemistry Graduate Student Award	2004, 2005
Penn State Chemistry Research Award	2010
Korea Science Foundation Fellowship	2004, 2005
Brain Korea 21 Fellowship	2000, 2001

Professional Membership

American Chemical Society
American Vacuum Society
Materials Research Society